Using Photoionization to Investigate Reactive Boron Species and the Kinetics of Hydrocarbon Radicals

Dissertation zur Erlangung des
naturwissenschaftlichen Doktorgrades
der
Julius-Maximilians-Universität Würzburg

vorgelegt von

Domenik Schleier

aus Geldersheim

Würzburg, Mai 2021

Eingereicht bei der Fakultät für Chemie und Pharmazie am 15.05.2021

Gutachter der schriftlichen Arbeit
1. Gutachter: Prof. Dr. Ingo Fischer
2. Gutachter: Prof. Dr. Holger Braunschweig

Prüfer des öffentlichen Promotionskolloquiums

1. Prüfer: Prof. Dr. Ingo Fischer
2. Prüfer: Prof. Dr. Holger Braunschweig
3. Prüfer: Jun. Prof. Dr. Ann-Christin Pöppler

Datum des öffentlichen Promotionskolloquiums: 09.07.2021

Doktorurkunde ausgehändigt am ____________________

"Hard work beats talent, when talent doesn't work hard."
Famous saying

List of Abbreviations

The following abbreviations are used.

AB	ammonia borane (NH_3BH_3)
AE	appearance energy
AI	allyl iodide
B. braunii.	*Botryococcus braunii*
BC	boron carbide
BD	breakdown diagram
BDE	bond dissociation energy
BO	Born-Oppenheimer
CAS-MRCI	complete active space - multi reference configuration interaction
CBS	complete basis set
CCD	charged coupled device
CI	conical intersection
(CRF-)PEPICO	(combustion reactions followed by) photoelectron photoion coincidence
CVD	chemical vapor deposition
CW	continous wave

DESIRS	Dichroisme et Spectroscopie par Interaction avec le Rayonnement Synchrotron
DFT	density functional theory
EPR	electron paramagnetic resonance
E-1MA	E-1-methylallyl radical
FC	Franck-Condon
FEL	free electron laser
FTS	fourier transform spectrometer
FWHM	full width half maximum
GC/MS	gas-chromatography/mass spectrometry
GGA	generalized gradient approximation
HACA	hydrogen abstraction acetylene addition
HOMO	highest occupied molecular orbital
HPL	high-pressure limit
KE	kinetic energy
LINAC	linear accelerator
LPL	low-pressure limit
LUMO	lowest unoccipied molecular orbital
MFC	mass flow controller
NIM	normal incidence monochromator

IE	ionization energy
IR	infrared
ISM	interstellar medium
JT	Jahn-Teller
MCP	microchannel plate
MS/MS	multiple start/multiple stop
m/z	mass to charge
Nd:YAG	neodymium-doped yttrium aluminum garnet
NMR	nuclear megnetic resonance
PAH	polycyclic aromatic hydrocarbon
PES	potential energy surface
PFI-ZEKE	pulsed field ionization-zero kinetic energy
PIE	photoionization efficiency
PIMS	photoionization mass spectrometry
PJT	Pseudo Jahn-Teller
(R)CSSD(T)	(restricted) coupled-cluster single-double-(triple)
REMPI	resonance enhanced multi-photon ionization
RRKM(/ME)	Rice Ramsperger Kassel Marcus(- master equation)
RT	Renner-Teller

SLS	Swiss Light Source
SOLEIL	Source Optimesée du Lumiére d'Énergie Intermédiare du LURE
SPES	slow photoelectron spectrum
TMB	trimethyl borane
TOF	time-of-flight
TOFMS	time-of-flight mass spectrometer
(T)PES	(threshold) photoelectron spectroscopy
UV/VIS	ultraviolet/visible
VMI	velocity map imaging
VUV	vacuum ultraviolet
Z-1MA	Z-1-methylallyl radical
Φ	quantum yield
Γ^{irrep}	irreducible representation
Γ^{red}	reducible representation
1-MA	1-methylallyl radical
2-MA	2-methylallyl radical

Abstract

Die vorliegende Arbeit lässt sich in zwei Unterkategorien gliedern. Sie befasst sich zum einen mit der isomerenselektiven Identifikation von hochreaktiven anorganischen Verbindungen. Zum anderen werden Ratenkonstanten für die Reaktionen verschiedener Kohlenwasserstoffradikale mit Sauerstoff ermittelt. Beide Bereiche sind durch die Frage der Energiespeicherung und -gewinnung in der Zukunft unmittelbar miteinander verbunden. Während bisher fossile Energieträger einen überdurchschnittlichen Anteil an der Energieerzeugung haben, sollen schon bald regenerative Quellen den Großteil ausmachen. Mittels Photovoltaik oder vergleichbarer Methoden ist es schon möglich einen Teil des akuten Energiebedarfs zu decken, allerdings sind mögliche Energiespeicher momentan noch zu ineffizient. Wasserstoff wird deshalb als vielversprechender Kandidat für Energieträger der Zukunft angesehen. Jedoch benötigt reiner Wasserstoff große Energiemengen um komprimiert zu werden und noch größere um ihn zu verflüssigen, weshalb andere Speicherformen notwendig geworden sind. Diese Wasserstoffspeichermaterialien sind noch nicht ausgereift, da es beim Abspalten von Wasserstoff oft zu Zersetzungsprozessen kommt.

Andere Methoden um vor allem flüssige Energieträger zu Gewinnen sind spezielle Mikroalgen, die große Mengen Öl produzieren können. Ähnliche Kohlenwasserstoffe benutzt man heutzutage bereits als Treibstoff für Autos, jedoch haben die aus Algen gewonnenen Verbindungen einen anderen chemischen Aufbau, wodurch neue Verbrennungsmodelle entwickelt werden müssen. Ratenkonstanten von Modellverbindungen stellen hierfür oft das Rückgrat dar, deren Kenntnis unverzichtbar ist.

Die Herausforderung reaktive Moleküle zu untersuchen, liegt oft darin sie in einer inerten Atmosphäre erzeugen zu müssen. Nur unter diesen Bedingungen hat ihre Reaktivität kaum Möglichkeiten sich zu entfalten. Hierzu wurden stabile Vorläufermoleküle in die Gasphase überführt und in einer verdünnten Umgebung möglichst selektiv in die gewünschte Radikalspezies überführt. Es konnte dafür auf drei verschiedene Methoden zurückgegriffen werden. Der Vorläufer wurde entweder thermisch gespalten, durch Lichtabsorption dissoziiert oder durch andere Radikale mittels Abstrak-

tionsreaktionen erzeugt. Jede dieser Methoden bietet Vor- und Nachteile je nachdem welche experimentelle Observable im Speziellen untersucht werden soll und wie der Vorläufer beschaffen ist. Sowohl die isomereselektive Identifikation als auch die Bestimmung der Ratenkonstanten wurde mittels Schwellenphotoelektronenspektroskopie durchgeführt. Mit Hilfe eines Photoelektron/Photoion Koinzidenz (PEPICO) Aufbaus konnten massenselektive Signale detektiert werden. Diese Methode benötigt eine Lichtquelle, die eine hohe Repetitionsrate aufweist und im VUV-Bereich komplett spektral durchstimmbar ist. Diese Voraussetzungen sind an Synchrotron-Strahlungsquellen verfügbar, weshalb die Experimente in dieser Arbeit an den entsprechenden Strahllinien an der SwissLightSource oder am Synchrotron SOLEIL durchgeführt wurden. Zur Unterstützung der experimentellen Daten wurden durch quantenchemische Rechnungen und Simulationen durchgeführt, aus denen eine klare isomerenselektive Zuordnung des jeweiligen Signals erfolgt. Die gesuchten Ratenkonstanten konnten mittels geeigneter Programme aus den Kinetikdaten extrahiert werden, wobei auch die Ratenkonstanten der Seitenreaktionen berücksichtigt wurden.
Die wichtigsten Erkenntnisse lassen sich wie folgt zusammenfassen:

- Die Ratenkonstante zwischen dem Allylradikal (C_3H_5) und Sauerstoff konnte von 0.8 - 3 mbar bei Raumtemperatur ermittelt werden. Das Radikal wurde hierfür auf zwei unterschiedlichen Wegen generiert, einmal durch direkte Photolyse von Allyliodid und einmal indirekt durch H-Abstraktion von Propen. Allyl konnte mittels Schwellenphotoelektronenspektroskopie eindeutig nachgewiesen werden. Zusätzlich konnte in den Experimenten mit Propen ein neues Reaktionsprodukt identifiziert werden. Die Druckabhängigkeit der Reaktion stimmte in etwa mit der Literatur überein, wobei die Vergleichbarkeit aufgrund eines anderen Badgases nur bedingt gegeben war.

- Im nächsten Schritt wurde versucht die isomerenselektive Kinetik der Methylallylradikale zu untersuchen. Während sich 1- und 2-Methylallyl unabhängig voneinander generieren lassen, besitzt 1-Methylallyl (1-MA) zwei Stereoisomere E-1-Methylallyl (E-1MA) und Z-1-Methylallyl (Z-1MA) die sofort isomerisieren. Mit Hilfe des CRF-PEPICO Setups konnten Ratenkonstanten für 2-MA zwischen 1 und 3 mbar aufgenommen werden. Für 1-MA wurden Abklingkurven ebenfalls zwischen 1 und 3 mbar aber bei zwei verschiedenen Photonenenergien aufgenommen, sodass die beiden Isomere anhand ihrer Io-

nisierungsenergie getrennt werden konnten. Beide Isomere zeigten ähnliche Ratenkonstanten im Rahmen der Fehlergrenzen. Die verschiedenen Druckabhängigkeiten zwischen Allyl, 1-MA und 2-MA konnten durch die größe der Moleküle, sowie deren Substitutionsmuster gut erklärt werden.

- Mit Hilfe des Photolysereaktors konnten sowohl das IO Radikal als auch Hypoiodige Säure (IOH) erzeugt und spektroskopiert werden. Die relativistischen Effekte in IO führten dazu dass sich bisherige experimentelle Studien mit den theoretischen Vorhersagen widersprachen. Das Schwellenphotoelektronenspektrum von IO zeigte zwei nicht komplett auflösbare Vibrationsprogressionen, die auf die zwei tiefsten Triplettzuständen zurückzuführen sind. Die beiden Zustände sind etwa 0.13 eV von einander getrennt und besitzen sehr ähnliche Vibrationsfrequenzen im Kation. Für IOH stimmten die Ionisierungsenergie und die Vibrationsfrequenzen im Kation mit denen von anderen Studien gut überein.

- Es konnte das echte Biradikal Diboren HBBH beobachtet werden. Seine Ionisierungsenergie wurde auf 9.08±0.015 eV bestimmt. Eine Progression der B-B Streckschwingung im Kation konnte beobachtet werden. Der kationische Grundzustand ist doppelt entartet, was zum Auftreten von Seitenbanden aufgrund des Renner-Teller-Effektes führt.

- Als weitere Borradikale konnten sowohl BH_2, BF und BH detektiert werden. Bei BH_2 wurde die Ionisierungsenergie, aufgrund übereinstimmender Simulationen, auf 8.12±0.02 eV bestimmt. Zudem wurden Banden der Biegeschwingung bis zu acht Niveaus über der Fundamentale registriert. BH wurde sowohl im Singulett als auch im Triplett Zustand generiert. Die Ionisierungsenergie von ^{1}BH konnte zu 9.82 eV bestimmt werden, wohingegen ^{3}BH einen Wert von 8.48 eV besitzt. In beiden Fällen wurden nur eine schwache beziehungsweise keine Vibrationsprogression beobachtet. Für das ebenfalls hergestellte BF Molekül konnten Werte von 11.11±0.02 eV und 1690 cm^{-1} früherer Messungen bestätigt werden.

- Es konnte ein hochaufgelöstes ms-TPES des Boran-Ammoniak-Komplexes H_3NBH_3 aufgenommen werden. Die Ionisierungsenergie konnte mit Hilfe von Simulationen auf 9.25 eV korrigiert werden und der erste Wasserstoffverlust tritt bei einer Energie von 10.00 eV auf. Iminoboran HBNH konnte aus Pyrolyse von Borazin hergestellt werden. Es besitzt eine Ionisierungsenergie von 11.31±0.02 eV und die Frequenz der Streckschwingung im Kation wurde auf 1530 cm^{-1} bestimmt. Für den Vorläufer Borazin konnte eine Ionisierungsenergie von 10.01±0.02 eV bestimmt werden, die mit bisherigen Werten gut übereinstimmt.

- Die Pyrolyse von Trimethylboran $B(Me)_3$ lieferte hauptsächlich CH_3BCH_2 durch Methanverlust. Dessen Ionisierungsenergie liegt bei 8.55±0.03 eV und eine ausgeprägte antisymmetrische CBC Streckschwingung mit einer Frequenz von 1450 cm^{-1}. Das ms-TPES lieferte aber auch Anhaltspunkte für die Anwesenheit anderer Isomere mit der Summenformel C_2H_5B. Außerdem konnte bei höheren Pyrolyseleistungen ein zweiter Abstraktionsweg identifiziert werden, der zur Bildung von CH_2BH führt. Das Isomer des Methylborylen CH_3B wurde mittels seiner Ionisierungsenergie von 9.37±0.03 eV und seiner kationischen BC-Schwiung von 1300 cm^{-1} von ebendiesen eindeutig unterschieden.

Keywords

Synchrotron Radiation, Kinetics, Spectroscopy, Photolysis, Radicals, Biradicals.

Contents

Publications

Parts of this thesis have been published in the following journals. Permission to re-use the published content was granted prior by the respective copyright holder.

(1) D. Schleier, E. Reusch, M. Gerlach, T. Preitschopf, D. P. Mukhopadhyay, N. Faßheber, G. Friedrichs, P. Hemberger and I. Fischer, Kinetics of 1- and 2-methylallyl + O_2 reaction, investigated by photoionisation using synchrotron radiation. *Phys. Chem. Chem. Phys.*, **2021**, *23*, 1539-1549.

(2) D. P. Mukhopadhyay, D. Schleier, I. Fischer, J.-C. Loison, C. Alcaraz and G. A. Garcia, Photoelectron Spectroscopy of boron-containing reactive intermediates using synchrotron radiation: BH_2, BH, and BF. *Phys. Chem. Chem. Phys.*, **2020**, *22*, 1027-1034.

(3) D. Schleier, E. Reusch, L. Lummel, P. Hemberger, I. Fischer, Threshold Photoelectron Spectroscopy of IO and HOI. *ChemPhysChem*, **2019**, *20*, 2413-2416.

(4) D. Schleier, A. Humeniuk, E. Reusch, F. Holzmeier, D. Nunez-Reyes, C. Alcaraz, G. A. Garcia, J.-C. Loison, I. Fischer, R. Mitric, Diborene: Generation and Photoelectron Spectroscopy of an Inorganic Biradical. *J. Phys. Chem Lett.*, **2018**, *9*, 5921-5925.

(5) D. Schleier, P. Constandinidis, N. Faßheber, I. Fischer, G. Friedrichs, P. Hemberger, E. Reusch, B. Sztáray and K. Voronova, Kinetics of the a-C_3H_5 + O_2 reaction, investigated by photoionization using synchrotron radiation. *Phys. Chem. Chem. Phys.*, **2018**, *20*, 10721-10731.

Publications outside of the scope of this work are:

(6) X. Tang, X. Lin, G. A. Garcia, J. C. Loison, C. Fittschen, A. Röder, D. Schleier, X. Gu, W. Zhang, and L. Nahon. Threshold photoelectron spectroscopy of the HO_2 radical *J. Chem. Phys.*, **2020**, *153*, 124306

(7) D. P. Mukhopadhyay, D. Schleier, S. Wirsing, J. Ramler, D. Kaiser, E. Reusch, P. Hemberger, T. Preitschopf, I. Krummenacher, B. Engels, I. Fischer and C. Lichtenberg, Methylbismuth: an organometallic bismuthinidene biradical. *Chem. Sci.*, **2020**, *11*, 7562-7568

(8) E. Reusch, D. Kaiser, D. Schleier, R. Buschmann, A. Krueger, T. Herrmann, B. Engels, I. Fischer, P. Hemberger, Pentadiynylidene and Its Methyl-substituted Derivatives: Threshold Photoelectron Spectroscopy of R_1-C_5-R_2 Triplet Carbon Chains. *J. Phys. Chem. A*, 2019, **122**, 9563-9571

(9) T. Bolze, J. Wree, F. Kanal, D. Schleier, P. Nürnberger. Ultrafast Dynamics of a Fluorescent Tetrazolium Compound in Solution. *ChemPhysChem*, **2018**, *19*, 138-147

(10) B. Gans, S. Boye-Peronne, G. Garcia, A. Röder, D. Schleier, P. Halvick, J. Loison. Unveiling the Ionization Energy of the CN Radical. *J. Phys. Chem. Lett.*, **2017**, *8*, 4038-4042

1. Introduction

Known for more than 50 years, climate change has become one of the major threats to not only the environment, but to mankind itself and is one of the defining challenges we face in the 21st century.[1] The proposed globally rising sea levels and temperatures will lead to loss of habitable land,[2] prolong and enhance extreme weather events and trigger more and more people to leave their homes.[3] Therefore, climate change is not restricted to the polar ice caps or alpine glaciers but will impact the lives of billions of people directly or indirectly. Science and engineering have grasped the severity of the situation and has dedicated serious efforts to combat climate change at its root, namely CO_2 emissions, by finding alternatives for fossil fuels to generate energy. Today the majority of our consumed energy still comes from non-renewable energy carriers like oil and natural gas, although renewable energy has an increasing percentage in our energy mix.[4] While wired objects like buildings and trains can be powered by solar cells and wind energy without any additional efforts, freely movable objects like cars, ships, and planes need to have an internal energy storage to function properly. Almost exclusively the automobile industry has decided that cars in the 21^{st} century will be powered by electricity that is stored in on-board batteries, moving away from the conventional combustion engine. Yet, battery technology faces a serious challenge in increasing the energy density to replicate previously known specifications.[5] Car manufacturers have circumvented this issue by building bigger and heavier devices needing large amounts of scarcely available resources.[6] Similar concerns arise for hydrogen-powered systems in which fuel cells containing platinum are required to generate power.[7] With large parts of the population and media ascribing transformative and almost unlimited power to the aforementioned technologies in the future, it feels like combustion processes are obsolete sooner than later. However, the search for new energy carriers could give combustion a second wind and also purge its name from the unsustainable and polluting technology it is associated with today, to being just another pillar of the energy sector.[8] Plant-based biofuels offer a sustainable alternative to conventional fossil fuels and can be produced

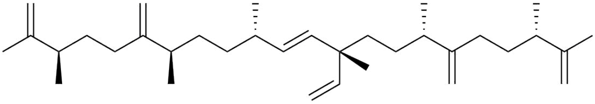

Botryococcene ($C_{34}H_{58}$)

Figure 1.1.: Major crude oil produced by the microalgae *B. braunii.*[14]

from leftover biomass.[9] The term biofuel is loosely defined and describes any compound that is synthesized using renewable methods and can be used for energy generation, with the most prominent representatives being bio-ethanol and long-chain esters used in bio-diesel.[10] Initially, biofuels were produced from food crops like wheat, sugarcane, or soybeans and directly competing with food production itself, thus posing a threat to world hunger especially in third world countries.[11] To maximize energy densities and reduce land usage, extremely durable, fast-growing, high-energy crops like switchgrass or *Miscanthus* have been investigated as potential feedstock.[12] In order to further commercialize this process upscaling is necessary, again creating a competition with agriculturally viable land. Later, the primary sources for biofuels were lignin, cellulose, and hemicellulose for which feedstock from abandoned agricultural land and food waste could be used, circumventing any competition with conventional food crops, but limiting expansion possibilities. Nowadays, third generation biofuels are produced by water-borne micro-algae, which eliminates any kind of competition with land-grown material, due to minimal land usage and great upscaling potential.[11] While there are drawbacks like low photosynthetic efficiency, high cost of cultivation and post-processing, as well as mediocre cell culture conditions, microalgeas represent a truely sustainable way to create biofuels.[13] However, the obtained products have a completely different composition with higher oxygen and nitrogen contents compared to fossil fuels that depends on the species of algae used for production.[14,15] Ethanol contains oxygen, whereas algae-synthesized long,chain hydrocarbons as well as fatty acids, used for the production of bio-diesel, often show branched substitution patterns and unsaturated chains, rendering previously established combustion models on saturated non-branched hydrocarbons outdated.[10] The major crude product of one of the most promising algae strains (*Botryococcus braunii*) is illustrated in figure 1.1.[14,16]

Biofuels can also be used as a short-term energy storage to absorb spikes in

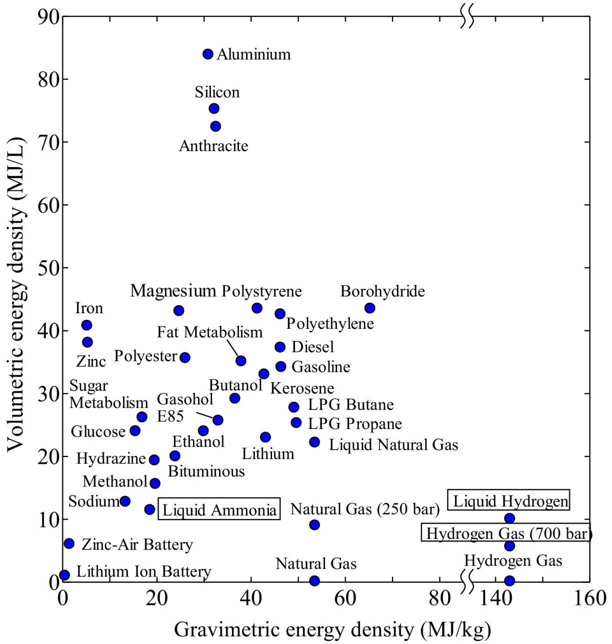

Figure 1.2.: Gravimetric and volumetric energy densities of some selected compounds.[18]

energy production from solar, wind and other environmentally dependent sources.[17] Until now, the main buffer molecule was proposed to be hydrogen because of its enormous gravimetric and moderate volumetric energy densities displayed in figure 1.2.[18] It can be produced everywhere using the electrolysis of water and either burned to generate heat or be used in fuel-cells for electricity. However, its neat storage and transport are difficult and consume a majority of its contained chemical energy rendering the process extremely inefficient.[19] Several routes were explored that tried to solve this problem ranging from liquification by cooling, over adsorption onto metals or metal-organic-frameworks, to chemical conversion that stores hydrogen in form of a different compound.[20] While its accessibility is better using liquification or adsorption methods, the highest density is found by chemically converting it into small molecules like ammonia or ammonia borane. Ammonia exhibits similar gravimetric energy density as hydrogen but much more favorable storage conditions, with a boiling point of −33.4° C and a condensation point of 9.90 atm.[18] This is similar to propane (−42.1° C; 9.40 atm) for which infrastructure for transportation and storage has already been developed and established. Just like hydrogen, it can be used directly in fuel-cells or burned, generating nitrogen and water in both cases. Ammonia fuel-cells have only recently emerged as a promising approach[21] and thus suffer from drawbacks like high platinum consumption as well as ammonia crossover through the ion exchange membrane, decreasing their efficiency.[22] In combustion, ammonia/air flames are less stable than methane/air flames, exhibit worse flame characteristics with higher ignition temperatures, and can create toxic NO_X species.[23] Currently, hydrocarbons are added to improve properties in ammonia combustion,[24] which the available models can only describe insufficiently. Yet ammonia-based technologies have already proven viable as well as cost effective in the near future and could soon be considered a vital component in biofuel technologies.[22]

With that being said, even CO_2 neutral combustion has some drawbacks, mainly the emission of NO_X and soot particles that lead to smog and pose serious health risks to humans, animals and plants.[25–27] Soot particles can be understood as aggregates of polycyclic aromatic hydrocarbons (PAHs) that form when hydrocarbons are not completely consumed by oxygen during combustion.[28] They are not only produced by combustion engines, substantial amounts of this particulate matter originate from wood or biomass burning stoves for cooking and ovens for heating.[29] These sources will continue to be used in Europe and throughout the western world but in particular in developing countries. Reducing soot formation has been the central point of combustion research in the last years and the accumulated knowledge has been gathered in several models with the most prominent being the hydrogen-abstraction acetylene addition (HACA) mechanism.[30] Interest in these combustion models also comes from astrophysics, where PAHs play crucial roles in the organic cycle of matter in the interstellar medium (ISM).[31] In this environment, PAHs are believed to be formed in the atmospheres of carbon-rich stars, where temperatures can reach several thousand Kelvin.[32] Therefore, it has been argued that reaction mechanisms responsible for interstellar PAH formation are similar to those encountered in the combustion community,[33] but their exact interstellar origin and structural characteristics remain largely unknown due to the lack of knowledge on possible formation routes. Estimations that up to 15% of all elemental cosmic carbon is locked-up in aromatic hydrocarbons emphasize the importance of understanding their chemistry.[31] While these models have come a long way, they still can only explain a fraction of the soot formation process and experimental evidence is only available for the first steps.[10] The newly emerging biofuels have the potential to exacerbate this problem in the nearby future with new and more complex mixtures of various compounds being used in combustion cycles.[8]

The foundation on which all combustion models are based, is the unambiguous identification of intermediates, that form when molecules decompose at high temperatures and pressures.[34] Under these conditions chemical bonds in the molecule are homolytically broken, creating at least two reactive radical species with unpaired electrons that can neither be isolated in a flask, nor probed using standard analytical techniques like gas-chromatography. Their high reactivity requires low molecular densities that need to be maintained during analysis, while multiple isomeric decomposition products in dozen of pathways lead to the convolution of signals in many spectroscopic techniques. The minimum requirements for any analytical technique aiding to elucidate these processes can only be met when:

- their sensitivity is high enough to detect trace amounts
- their resolution can distinguish between all available species
- various species can be detected simultaneously
- they are not restricted by selection rules and can be universally applied

Ionization techniques fulfill most of the listed points. They are sensitive, not confined by any spectroscopic selection rules and can unravel a wide variety of species simultaneously through their time-of-flight detection scheme.[35] The main spectral fingerprint used for identification is the ionization energy (IE), which requires a completely tunable light source in the vacuum-ultraviolet (VUV) region to measure. For many species, this is enough to unequivocally prove their existence, though many larger molecules have several isomers with close-lying IEs that require another analytical dimension for identification.[36] Since ionization processes do not only create a molecular cation but also a corresponding electron, the latter can be used to support or refute a specific assignment. Upon ionization, the molecular structure changes and bond lengths and angles get smaller or bigger depending on the nature and shape of the orbital the electron is ejected from. These changes are imprinted onto the electron that carries these information in the form of kinetic energy with respect to the incident wavelength of the light. This orbital specific information is unique for each isomer and offers an additional detectable parameter, that can be used for identification. The combination of mass spectrometry and photoelectron spectroscopy is called photoelectron photoion coincidence (PEPICO) spectroscopy and has been successfully used to identify compositions in flames, [37] heterogeneous catalysis, [38,39] and kinetic experiments. [40–42] Ultimately it yields a multidimensional data set consisting of mass to charge ratio (m/z), IE, and vibrational structure in the cation. [43] For the sake of completeness, it should be mentioned that high-resolution mass spectrometry can be used to identify isobaric species through their minor elemental mass differences, but this technique fails when isomers need to be distinguished.

In combustion and its related fields, it is not only important to identify the occurring species and the major pathways in controlled environments, but it is also necessary to rationalize their abundance under real conditions by measuring radical reactivity. For combustion processes, the main reactant for the radicals is oxygen because of its biradical nature and large presence in air. The reactivity of radicals can vary, depending on internal and external factors best explained using the most prominent example of an extremely stabilized radical, triphenyl methyl. [44,45] The three bulky phenyl groups prevent any reactant from reaching the central trivalent carbon atom carrying a majority of the radical spin density. This shielding of the radical site does not stabilize the molecule by lowering its thermodynamic potential energy but rather increases the barriers it needs to overcome to form any products and thus this method is referred to as kinetic stabilization. The phenyl groups also exhibit a second effect, that decreases the amount of spin density on the central carbon and transfers parts onto the substituents. This delocalization lowers the potential energy of a molecule and its propensity to react with any secondary molecules; it becomes thermodynamically stabilized. These two factors also govern the reactivity of smaller radicals that occur in combustion but their effects are much smaller, harder to estimate and, contrary to triphenyl methyl, might be working in opposite directions. Rate constants are a useful tool to classify and compare molecular reactivities. Their absolute value does not only depend on the involved species but also on ambient conditions like pressure and temperature. Although one would expect a straightforward relationship between these external factors and rate constants according to the Arrhenius equation, their true dependence can only be explained using potential energy surfaces of all involved intermediates and transition states.

Since radicals start reacting almost instantly, they need to be produced even faster and in a non-continuous way, so that the whole reaction can be observed. The two most frequently used methods for radical generation are pyrolysis and photolysis. Pyrolysis uses high temperatures to effectively break down a precursor molecule and generate the two fragments in large quantities.[46] When two radical precursors are co-pyrolyzed it can also form larger molecules, although only the most stable products are observed.[47] However, in certain cases the uncontrolled process of pyrolysis can lead to further reactions and prevent the selective generation of the desired intermediate. Photolysis can deposit a controlled amount of energy in a very specific mode of the precursor molecule, which is largely consumed in the ensuing bond scission, generating products with very little excess energy. The following reaction that forms the first stable intermediate can be monitored closely and subsequent steps can be excluded from the analysis under the right conditions. However, the amount of radicals is dependent on the absorption cross section of the precursor and thus lower compared to pyrolysis, which presents an additional challenge for the precursor selection. Photolysis experiments are performed in a suitable reactor in which all environmental parameters can be monitored and adjusted at will, which is usually not possible for non-preperative pyrolysis. The photolysis laser allows to know when the reaction has been initiated, record the whole decay by using a pulsed mode and offers a way to generate relatively cold radicals. Most photolysis setups are limited to a few selective energies they can use to induce a bond scission and thus have only a limited flexibility with respect to the precursor absoprtion. Therefore, pyrolysis and photolysis represent two complementary techniques, each with advantages and drawbacks for certain experiments. To paint a more vivid picture of the differences between pyrolysis and photolysis, they can be correlated to commonly available tools. Pyrolysis represents the sledgehammer approach, while photolysis can be compared to a pair of tweezers. Both can be applied to the same starting material, but one would use each to achieve something else.

A third approach is the radical generation inside a chemical reactor. Here, highly reactive atoms, usually hydrogen, oxygen, or halides, are mixed with precursor molecules which leads to a chemical reaction. The atoms, unsatisfied with their electronic situation, homolytically break element-hydrogen bonds to saturate themselves, leaving the precursor with a radical site. The thermodynamic driving force for such systems is usually the high thermodynamic stability of the generated compounds like H_2, H_2O, HCl, or HF. Depending on the molecular densities as well as the precursor molecule abstractions can happen multiple times and this approach is ideally suited to break down larger precursor molecules.

To better understand the upcoming data certain fundamental principles that have been mentioned in this introduction need to be examined more closely. Chapter 2 tries to bring the reader closer to the topics of synchrotron radiation, threshold photoelectron (TPE) spectroscopy and reaction kinetics. Afterward a quick overview of the unique properties of each relevant setup in this thesis is given and its advantages discussed (chapter 3). The results of this thesis are presented in chapter 4, where in section 4.1 the kinetics of the investigated hydrocarbon radicals are presented. The second part of this chapter (section 4.2) is dedicated to the spectroscopy of boron based radicals and biradicals. The chapter is brought to a finish by mentioning some miscellaneous projects.

2. Fundamentals

2.1. Symmetry

2.1.1. Symmetry of Molecules

In medieval times symmetry was viewed as a triumph of mankind over the chaos that is nature, which is best displayed at the Garden of Versailles. To the viewer symmetry represents beauty, it is aesthetic and unique. In chemistry one looks at a molecule in its ball and stick representation and intuitively knows if it is highly symmetric, meaning it can be rotated and mirrored in different ways to yield the same molecule or if those so called symmetry elements are absent. Based on decades of research that have lead to the nobel prize for Roald Hoffmann and Kenichi Fukui in 1982, science has found a way to relate the "beauty of molecules" to the electronic structure and thus to their chemical reactivity.[48,49] A major part of this thesis deals with the electronic character of neutral molecules and the effects that arise when one removes electrons from them. While these effects can hardly be quantified using symmetry arguments they can be qualitatively understood, which in most cases is good enough to predict them without having to go through highly complex and time-consuming potential energy surface (PES) calculations near conical intersections.
Every molecules symmetry can be classified depending on the number and kind of symmetry operations $\mathcal{R}$ it contains. These operations form a mathematical entity known as a group, that has to follow a given set of rules:[50]

- The product of two elements $\mathcal{AB}$ is also an element of the group.
- Multiplication of two elements is associative $\mathcal{A}(\mathcal{BC}) = (\mathcal{AB})\mathcal{C}$.
- There is a identity element E that does not change another element according to $\mathcal{A}\mathrm{E} = \mathrm{E}\mathcal{A} = \mathcal{A}$.
- There is an inverse to each element that transfers it back to the identity element according to $\mathcal{A}\mathcal{A}^{-1} = \mathcal{A}^{-1}\mathcal{A} = \mathrm{E}$.

These boundaries not only limit the number of avilable symmetry elements per group, they require certain elements to be present in them. For the sake of simplicity every symmetry operation can be written in matrix form $\boldsymbol{D(\mathcal{R})}$ given in equation 2.1, where $\vec{x}$ and $\vec{x'}$ are the vectors of all involved atoms before and after the operation has been carried out, respectively.

$$\vec{x'} = \boldsymbol{D(\mathcal{R})}\vec{x} \tag{2.1}$$

If the coordinate system is carefully chosen, the matrices $\boldsymbol{D(\mathcal{R})}$ only contain zeros and ones and all together form a *representation* Γ, with respect to the chosen basis. Since there is an infinite number of coordinate systems that all result in different matrices, the challenge is to define a new property that is uniform for every basis.[50] The character of an operation $\gamma(\mathcal{R})$ is equal to the sum of all diagonal matrix elements, also called its trace, which is independent of the coordinate system and suited to evaluate the found representations. In some cases the identified representation is multidimensional, meaning its character is greater than one. This is called a *reducible representation* Γ^{red} when it can be dismantled into several lower dimensional ones. According to equation 2.2 the matrix $\boldsymbol{D(\mathcal{R})}$ can be separated into two independent matrices $\boldsymbol{D'(\mathcal{R})}$ and $\boldsymbol{D''(\mathcal{R})}$.

$$\boldsymbol{D(\mathcal{R})} = \begin{bmatrix} \boldsymbol{D'(\mathcal{R})} & 0 \\ 0 & \boldsymbol{D''(\mathcal{R})} \end{bmatrix} \tag{2.2}$$

When the representation can no longer be cross-diagonalized it is termed an *irreducible representation* Γ^{irrep}, which have been determined previously for each point group, and are tabulated. Please note that there are groups that contain multidimensional Γ^{irrep}, which require at least one threefold rotational axis in the molecule. It is common to use the Mulliken terminology for molecular point groups, where A and B are one-, E is a two- and T is a three-dimensional representation. However, this can not be applied to linear molecules which have an infinite rotational axis and use labels from atomic spectroscopy.[50]

Breaking down reducible representations into irreducible ones follows equation 2.3, where g is the number of symmetry operations of a group and m_i determines how often Γ_i^{irrep} is contained in Γ^{red}.

$$m_i = \frac{1}{g}\sum_{\mathcal{R}} \gamma^{red}(\mathcal{R})\gamma_i(\mathcal{R}) \tag{2.3}$$

The symmetry of the molecule only gives hints at what the electronic structure coarsely looks like. Each molecule belonging to a group containing a multidimensional Γ^{irrep} has at least one set of degenerate orbitals, but up to this point it is unclear whether they are important for its reactivity. For chemistry and most spectroscopic methods, the frontier orbitals govern the properties and reactivity of a compound.[48]

Applying this principle to a single, or a set of orbitals, results in symmetry adapted molecular wavefunctions, which are used to construct the molecular orbital (MO) diagram. The symmetry of any state in this MO diagram is determined by multiplying the character of all orbitals with one unpaired electron in them. Since the direct product of completely filled orbitals is always the totally symmetric representation, they do not need to be taken into account. This is, strictly speaking, only true for one-dimensional point groups. In case of multidimensional point groups the direct product between two Γ^{irrep} can be a reducible one that contains more than one Γ^{irrep} after it has been broken down using equation 2.3. This means there are more electronic states for a single orbital occupation, some of which may be degenerate. This is the basis to explain vibronic interactions using symmetry arguments, and shows the difference between orbital and state pictures.[50]

2.1.2. Jahn-Teller Distortions and Symmetry

The Jahn-Teller (JT) effect[51] is a fundamental principle for molecules and states that: *"An orbitally degenerate electronic state of a nonlinear molecule is unstable with respect to a distortion, which removes the degeneracy."*[50]

There are various forms of the JT effect with different origins and prerequisites, yet all introduce a geometrical distortion q in the molecule.[52]

When a system is subjected to such a distortion, its electronic hamiltonian and corresponding energies can be expanded in a Taylor series using perturbation theory, given in equations 2.4 and 2.5.

$$H = H_i^0 + (\frac{\partial H}{\partial q})_i q + \frac{1}{2}(\frac{\partial^2 H}{\partial q^2})_i q^2 + ... \tag{2.4}$$

$$E_i(q) = E_i^0 + q\langle\psi_i|\frac{\partial H}{\partial q}|\psi_i\rangle + \frac{q^2}{2}\langle\psi_i|\frac{\partial^2 H}{\partial q^2}|\psi_i\rangle + q^2\sum_{j\neq i}\frac{\langle\psi_i|\partial H/\partial q|\psi_j\rangle}{E_i^0 - E_j^0} + ... \tag{2.5}$$

The energy of the undistorted molecule is given with E_i^0, while the next terms represent first- (q^1) and second-order (q^2) solutions. By applying symmetry arguments one can understand the molecular parameters required for a first-order JT effect without having to know what the wavefunctions of the involved orbitals ψ_i and matrix elements exactly look like. In case the two wavefunctions ψ_i are non-degenerate and of the same Γ^{irrep}, their direct product belongs to the totally symmetric representation. In addition the hamiltonian of a molecule depicted in equation 2.5 is always totally symmetric, since symmetry operations must never affect the electronic structure.[52] Consequently, the distortion q that changes the molecular shape has to be totally symmetric as well. Such distortions cannot switch the point group of a molecule, thus JT effects cannot occur in systems that have no degenerate pair of orbitals.

If Γ_{ψ_i} belongs to a multidimensional representation its direct product with itself is a Γ^{red} that yields more than one Γ^{irrep}. With some exceptions, the molecule is in a degenerate state and the distortion q can be of different symmetry without violating any symmetry arguments made before, resulting in a nonzero value for the first-order term in equation 2.5. The molecule becomes unstable with respect to its highly symmetric form along a degenerate coordinate q, whose symmetry corresponds to a certain vibration that is called the JT active mode. This lowers the symmetry of the molecule, lifting the degeneracy of the orbitals and stabilizes the system according to figure 2.1. Since the basis of first-order JT effects is a degenerate ground state, molecules must contain a rotational axis of three or greater, which is a necessary condition but not a sufficient one. A distortion in the neutral ground state can only occur in open shell species like radicals and biradicals since they exhibit an electronic state that is different from the totally symmetric one. The ground state symmetry of molecules that have an odd number of electrons in a degenerate pair of orbitals transform after the symmetry of the singly occupied orbital, and, if it is of E-character,

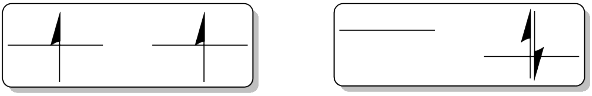

Figure 2.1.: Orbital changes from the undistorted (left) to the JT distorted molecule (right).

it is susceptible to a JT effect. Jahn and Tellers theories do not work on molecules that belong to linear point groups. These molecules have different symmetry properties compared to all other point groups and interactions in them are described by the related Renner-Teller (RT) effect.[53,54]

The last two terms in equation 2.5 belong to a second-order JT effect that consists of two components. The first of these two terms describes the nuclear motion of the undistorted molecule in electronic state $|\psi_i\rangle$, which can be interpreted as a force constant that forces the nuclei back into the more symmetric geometry. It is always totally symmetric, nonzero and positive, meaning it reduces the stability of the distorted system. The third overall term describes a mixing of two different electronic states, the ground state ψ_i and an excited state ψ_j. This renders the sign of this term negative since the value of E_i is always smaller than E_j and the stabilization is larger the closer the excited state is to the ground state. However, the two states can only interact under the symmetry conditions that the direct product of their symmetry representations contains the symmetry of the JT active mode. This second-order JT effect is more commonly termed pseudo-JT (PJT) effect.[50]

In point groups with a four-fold rotational axis or multiples thereof, direct products of two degenerate representations do not necessarily lead to a degenerate ground state. This means that the first-order JT effect is absent in these molecules, but second-order effects can still occur. The lowest excited states in these molecules usually originate from different electronic occupations of two degenerate orbitals and thus, they are energetically close to the ground state and can strongly interact with it. The symmetry condition for two states to mix and cause a PJT distortion is, that the direct prodcut of their representations must not contain the totally symmetric representation. In other point groups excited state mixing can be less effective and the third term in equation 2.5 might become negligible compared to the second, resulting in no PJT effect in these molecules.

It is important to understand the limitations of these symmetry-based arguments, so that reasonable assessments that are valid within the approach can be made. While symmetry can determine if a distortion occurs and what symmetry it has, the magnitude can not be determined. The spectral properties and how they change as a result of a distortion can also not be predicted, since at no point a PES is calculated.[50] Therfore, symmetry offers a first and easy estimate of the electronic situation in a molecule and can help explain divergence between experimental spectra and lower-level simulations.

2.1.3. Potential Energy Surfaces and Jahn-Teller Distortions

In order to get a more thorough understanding what a JT distortion actually represents one has to look at the PES around them, as well as the matrix elements that lead to the coupling between the two degenerate states. As depicted in the previous sections the nuclear motion causes a change in the electronic situation of a molecule. The corresponding couplings elements are vibronic, i.e. non-adiabatic, meaning, the commonly used Born-Oppenheimer approximation that allows the separation of nuclear and electron motions, is no longer applicable. In a diabatic picture, often used to illustrate these situations, the two states cross each other, creating a conical intersection (CI) based on symmetry arguments alone.[52] A complete mathematical description of JT CIs would exceed the limits of the thesis, but the interaction integrals and results give an excellent overview of the molecular dynamics near them.

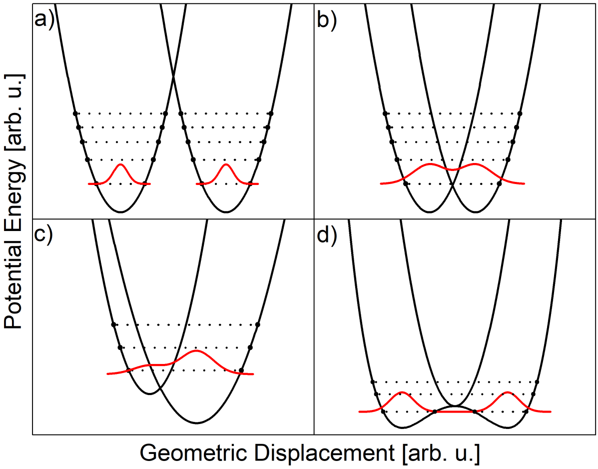

Figure 2.2.: Cuts through the 3D PES along the JT active mode for: a) a highly distorted first-order JT effect b) a slightly distorted first-order JT effect c) first- and second-order JT effect d) only second-order JT effect. Adapted with permission from Ref.[52]

For a more detailed description the interested reader is referred to the literature.[52,54–56]
Similar to equation 2.5 an analytical expression for a PES depending on a vibrational coordinate can be found by expanding it into a Taylor series. This results in two coupling elements g and k both depicted in equation 2.6 that determine the shape.[56]

$$k = (\frac{\partial E}{\partial \mathcal{L}_i}) \qquad g = (\frac{\partial^2 E}{\partial \mathcal{L}_i^2}) \tag{2.6}$$

Both represent different orders of derivatives of the energy with respect to the normal coordinate $\mathcal{L}_i$ and are consequently referred to as linear and quadratic coupling elements. Some cases for different values of g and k are illustrated in figure 2.2.
In the trivial case of both g and k being zero, the undistorted potential of a pair of degenerate electronic states can be approximated by one harmonic oscillator.
When linear coupling is turned on the two degenerate states split up horizontally along the JT active mode. This replaces the energetic minimum of the PES at the undistorted geometry with a crossing seam. Depending on the strength of the coupling the two wavefunctions can still interact and be delocalized over the CI or be completely separated by it (see figure 2.2 a) and b) respectively).[56] This picture is often referred to as JT effect and the corresponding PES are commonly found in the general chemistry literature, yet it is only one part of a more complicated situation.
To better understand this phenomenon it is necessary to expand the two-dimensional cuts through the PES depicted in figure 2.2 by another distortion coordinate into a three-dimensional surface plot. The region around a JT PES exhibiting linear coupling can be described using a "sombrero" potential. In the middle, the highest point of the PES, is the undistorted geometry of the molecule. When the two states are largely separated, the molecule can only be found there via tunneling effects.[56] The less symmetric molecule can "rotate" around the center as illustrated in figure 2.3 for a molecule with a threefold rotational axis. This motion is referred to as "pseudo-rotation", which can be misleading as the molecule does not rotate around a molecular axis, but rather the electronic situation in a valence bond picture rotates internally. In these cases the molecular wavefunction is completely delocalized between all occurring species and there is no angle dependency. An example for this case would be the cyclopentadienyl

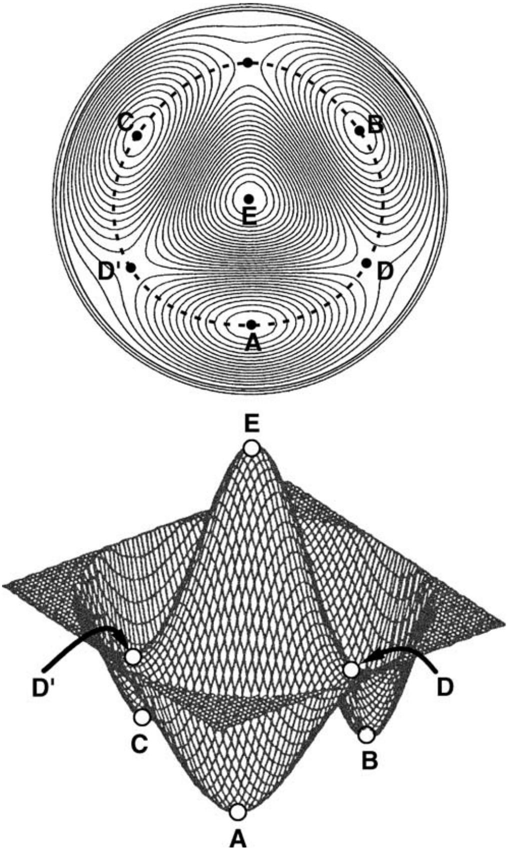

Figure 2.3.: Sombrero PES with linear and quadratic JT effects. The top picture is a contour plot of the bottom 3D picture. A, B, and C are the distorted intermediates, while D and D' are the respective transition states. E is the point of highest symmetry, or the undistorted molecule. Adapted with permission from Ref. [50]

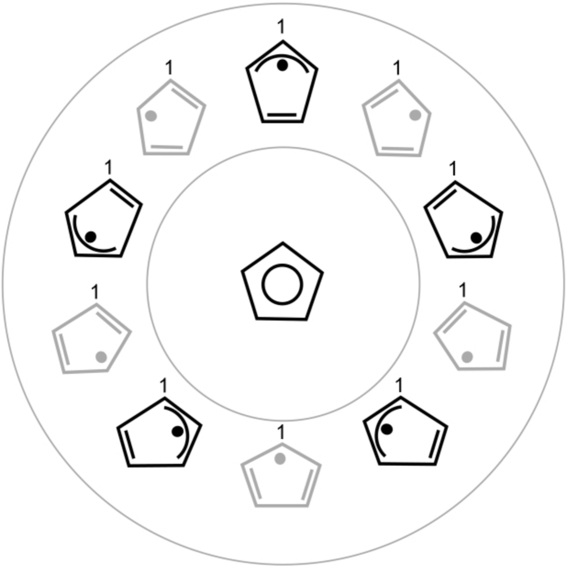

Figure 2.4.: Two-dimensional sombrero potential of the cyclopentadienyl radical. The delocalized structure in the middle is the highest point of the PES, while the distorted structures pseudo-rotate around it. Taken with permission from Ref.[52]

radical, whose two-dimensional sombrero potential is given in figure 2.4.[56] Quadratic coupling effects can further influence the PES, by introducing bumps on the pseudo-rotation coordinate, even though these can be neglected in most cases. When linear and quadratic coupling elements are nonzero, one electronic state gets lowered compared to its corresponding counterpart. This means that the wave function can be localized within one preferred structure and leads to a static JT effect.[52] The lower energetic distortion becomes an intermediate on the reaction coordinate around the center while the higher energetic distortion can be described as a transition state. The probed molecular properties exclusively correspond to the intermediate geometry as compared to an averaged situation in the linear only coupling. The number of intermediates and transition states of one complete pseudo-rotation is equal to the principle rotational axis of the molecule, and thus the PES has an angle-dependent component. Whether the wavefunction is localized or delocalized depends on the energy difference between the two species and on the zero-point energy of the molecule. In most cases, e.g. the benzene cation, the two species are energetically almost equivalent and the probed properties correspond to the averaged situation, when using a slow spectroscopic technique with respect to molecular vibrations. Thus, although the benzene cation exhibits a linear and quadratic JT effect, its photoelectron spectrum is equivalent to the undistorted molecule.[57]

In special cases the linear coupling element g can be zero but not the quadratic coupling k. In this case the PES exhibits two different gradients along two JT active modes but both have the same curvature, resulting in a double cone structure with a minimum energy for both at the highest point of symmetry. At this point the two surfaces touch and form a so called "glancing" conical intersection that becomes prominent in the Renner-Teller effect. When this coupling is strong a double well potential forms, which is the case for molecules with a four-fold rotational axis and is referred to as the PJT effect.[50,54,55]

2.1.4. Renner-Teller Effect

Jahn and Teller explicitly excluded linear molecules from their theorem, since in those the linear coupling element g always vanishes through symmetry arguments.[51] However, for the special case of a linear molecule the quadratic JT coupling can cause side bands in the spectrum that were first described by Renner in 1937 on the CO_2 cation.[53] In short, the RT effect describes the splitting of a degenerate electronic state along a bending vibration in linear molecules. Again, a complete mathematical description is not necessary in this thesis and can be found in much greater detail in the literature,[54,55] but a qualitative understanding of the effect is advantageous.

Linear molecules with N atoms exhibit a total amount of 3N-5 vibrations, and some are doubly degenerate, meaning they have the same frequency but different normal coordinates. These degenerate vibrations are of Π symmetry and ultimately lead to a splitting on the PES along their bending coordinate, similar to the degenerate modes in the first-order JT case (*vide supra*). For a splitting to occur the two Π vibrations need to be coupled to the electron movement in the molecule, which can be best expressed with the electron angular momentum along the z-axis of the molecule Λ. Thus, molecules without any angular momentum ($\Lambda = 0$) cannot exhibit any coupling between electron and vibrational degrees of freedom and no splitting is observed, which limits the effect in neutral species to radicals or excited states. In cases where $|\Lambda| = 1$, the electronic state of Π-symmetry is doubly degenerate ($\Lambda = \pm 1$) with two components called D_0 and D_1. They have the same number of vibrational modes, the same normal modes and the same vibrational frequencies, yet the two exhibit different PES along the same bending coordinate because of their vibronic couplings.[56]

Linear molecules that are positioned along the z-axis have two degenerate bending vibrations, one in the xz- and one in the yz-plane. When vibronic couplings are neglected, both D_0 and D_1 would have completely identical PES along any of the two Π vibrations with the same vibrational frequencies and normal modes. However, the appearance of these couplings lifts the degeneracy of the two bending vibrations in one component because the coupling between the $\Lambda = +1$ component and the xz-bending vibration is different from its coupling with the yz-bending vibration. In other words, the new vibronic wavefunction is now only an eigenfunction of the total angular momentum projected onto the z-axis and no longer an eigenfunction for either the electron angular momentum or the vibrational angular momentum. So changes in the electronic angular momentum have to be compensated in the vibrational angular momentum. Since both vibrations initially had the same frequency and the absolute value of $|\Lambda|$ is the same, both components split the vibrational frequency in the same amount but because their sign of Λ is opposite it is done in reverse order, best seen in table 2.1 for the ground state of HCCS. This results in two different bending frequencies along one bending coordinate where the two electronic states split up, albeit the geometry is not affected.[56]

It is worth noting that even though first-order JT effects are not present in linear molecules, the molecule can still be unstable with respect to its linear form due to PJT effects, even when only a weak RT effect is present. A prime example of this would be the BH_2 molecule, in which the bent ground state originates from mixing of an excited state into the ground state at linear geometry.[50] RT active molecules can be coarsely divided into three distinct groups depending on their coupling effects. This is given by three parameters, the strength of the RT splitting, the curvature of it, and the influence of the PJT effect, whose exact definition can be found in the literature.[54]

In the easiest case of weak coupling, the two PES touch at the point of highest symmetry and form a ”glancing” conical intersection, which is also the energetic minimum. This is also called the RT-only case since the molecule is not subject to a PJT effect. It is not distorted away from linearity, but the RT consideration is necessary to explain all experimentally observed signals.

When PJT effects are present as well their interaction can modify the PES and lead to a bent molecule. This leads to the conclusion that the RT effect alone can never lead to instability in a linear molecule.[58–60]

There are two situations that are created by PJT interaction on RT-active molecules. Either both PES are stabilized by the distortion or only one PES is stabilized and the second one is not changed leading to a new equilibrium geometry in both cases.

Table 2.1.: All vibrational modes of HCCS together with their corresponding symmetry and geometrical description. Values taken from Ref.[56]

D_0			D_1		
ω/cm^{-1}	Symmetry	Vibration	ω/cm^{-1}	Symmetry	Vibration
Non-degenerate modes					
761	Σ^+	Stretch	761	Σ^+	Stretch
1993	Σ^+	Stretch	1993	Σ^+	Stretch
3619	Σ^+	Stretch	3619	Σ^+	Stretch
Degenerate modes					
258	Π	yz-bend	258	Π	xz-bend
302	Π	xz-bend	302	Π	yz-bend
373	Π	yz-bend	373	Π	xz-bend
557	Π	xz-bend	557	Π	yz-bend

2.2. Synchrotrons

2.2.1. Generation of Synchrotron Radiation

Lasers emit light by creating a population inversion that leads to an amplification by a dominant stimulated emission process. This inversion is dependent on the wavelength of the emitted light and cannot be achieved easily for extremely high photon energies. Synchrotrons as well as their next generation counterparts, the free electron lasers (FEL) fill that gap perfectly and are ideal tools to study phenomenons at higher photon energies.[61,62] Although properties of laser light can be modified easily, the light from synchrotrons and FELs has become more versatile in its application, since their first discovery in 1944. Latest advancements successfully created defined ultrashort x-ray pulses at the European X-FEL, a time regime that was previously only covered by lasers.[63]
Charged particles that pass a static magnetic field are subjected to a force perpendicular to their propagation axis. The change in particle direction causes it to loose energy in the form of photons.[64] This, later called synchrotron radiation, was first theoretically predicted in 1898 by Lieard,[65] and first observed at the General Electric Synchrotron in 1947.[66] Calculations on electrons with relativistic velocities predicted a broad band emission from the infrared (IR) to the x-ray regime due to the uncertainty principle.[61] In order to accelerate electrons to relativistic speeds between 500 MeV and 20 GeV, three stages are used. First electrons get produced from a hot cathode and accelerated to several keV using simple electrostatic methods based on DC voltages. In the second stage a linear accelerator (LINAC) is used that increases their energy to several hundred MeV using so called cavities. In these a high frequency electromagnetic field oscillates. This forces electrons together in bunches, because only at specific times acceleration conditions are ideal. In short, particles ahead of the curve are getting decelerated until they are in resonance with the electromagnetic field and can be accelerated by it. The expensive cavities are rarely used alone to bring the electrons to their final velocities, rather a booster synchrotron is attached to the LINAC that forces the particles on a circular motion by bending magnets. In between the magnets the electrons are accelerated to their final energies by reusing the same cavities. Since the strength of the bending magnets has to be adjusted to account for the increase in energy of the electrons it has to increase synchronously, which was eponymous for synchrotrons.[61] In the last step, the completely accelerated

electrons are injected into a storage ring where their light can be used by the different beamlines attached to it. The electrons, previously bundled together by the LINAC, circle inside the storage ring in stable bunches, and their energy losses by photon emissions can be compensated by cavities. When the maximum number of bunches are used, the synchrotron operates in TOP-UP mode, which is the most common operational mode. The amount of particles inside the storage ring is proportional to the photon flux arriving at the beamlines. For electrons this equals the ring current. Another important aspect for this parameter is the kind of particle that is used in the snychrotrons. While in principle all charged particles exhibit synchrotron radiation, the radiation intensity P_S favors electrons and positrons according to equation 2.7.[61]

$$P_S = \frac{cq^2 E^4}{6\pi\varepsilon_0 r^2 (mc^2)^4} \tag{2.7}$$

The mass m is inverse proportional to P_S by its fourth power, diminishing the photon flux by thirteen orders of magnitude when using protons compared to electrons. Under certain considerations it is advantageous to use positrons, despite being more complicated to produce. Even under the ultrahigh vacuum conditions of the storage ring, particles can collide with residual atoms or molecules and can ionize them upon impact. The positively charged ion can attract other circulating electrons and throw them off their ideal track. Under the right conditions the ions can have a long residence time in the vicinity of the electrons, which leads to a decreased beam lifetime. Positrons also create positively charged ions when they collide with atoms, but their positive charge repels them, decreasing their residence time near the bunches.[61]

2.2.2. Properties of Synchrotron Radiation

From the point of view of the electron, the photon emission can be characterized by a Hertz dipole, meaning photons are emitted in all directions except towards their acceleration. For the steady observer, emission occurs in one direction with an opening angle of $2/\gamma$ according to the Lorentz-transformation of the coordinate system.[61] γ represents the Lorentz-factor and is defined according to equation 2.8 with the energy of the electron E_e, its mass m_0, the speed of light c and its relativistic velocity $\beta = v/c$.

$$\gamma = E_e/m_0 c^2 = 1/\sqrt{1-\beta^2} \tag{2.8}$$

Inside a storage ring electrons circulate in bunches that are several centimeters long, and the emission inside a bending magnet can occur for up to 100 ps for each bunch. The number of filled buckets inside the storage ring determines the time between the pulses which is between 2 - 500 ns. This repetition rate of up to several MHz creates a huge mismatch between synchrotrons and commercially available short pulse laser systems, e.g. titanium:sapphire, that are usually limited up to 10 kHz with experimentally usable pulse energies.[67] The light emitted by a bending magnet is linearly polarized in the plane of the storage ring, while light emitted above and beneath this plane is elliptically polarized. The spectral emission inside the opening angle exhibits a vertical distribution with high energy photons exhibiting a much narrower emission angle than lower energy photons.[61]
Bending magnets produce photons under a broad angle that can feed several beamlines at once, albeit their photon flux is relatively low. By forcing electrons on sinusoidal paths in the plane of the storage ring, they emit more photons under a slightly altered angle. This can be achieved by using *insertion devices* so called wigglers or undulators that are inserted into the storage ring and consist of a number of permanent dipoles. Wigglers have the same effect as several sequential bending magnets and lead to the addition of all photons created inside one device. The deflection parameter, often referred to as K-parameter (equation 2.9), describes the electron displacement and is linked to the strength of a wiggler as well as its opening angle.[61]

$$K = \frac{e}{2\pi m_e c} \cdot \lambda_u \cdot B_0 = 0.943 \cdot \lambda_u[cm] \cdot B_0[T] \tag{2.9}$$

One wiggler period λ_u is between 10-30 cm long and the magnetic field strength B_0 is about 1.5 T. The modified opening angle δ of the emitted light inside a wiggler is described by equation 2.10.

$$\delta \approx \pm K/\gamma \tag{2.10}$$

Wigglers usually have a K-parameter that is above 10, resulting in a broader emission angle. The photon flux increases proportional to the number of periods in a wiggler.

Undulators are conceptionally very similar to wigglers, but have a much lower K-value. Inside an undulator the amplitude of the electrons never exceeds the initial opening angle $1/\gamma$, leading to a K-value of ≈ 1. The period of an undulator is adjusted in a way that the initially created light waves can constructively interfere with other light waves that are generated one period later. Since electrons and photons have slightly different speeds, positive interference can only occur when the light emitted at the second period has a wavelength λ that is equal to the path difference within one undulator period. This means that undulators amplify light of a certain wavelength, as well as its higher harmonics, with respect to the undulator period while all other wavelengths are destroyed. The undulator periods for x-ray beamlines have lengths of several centimeters and wavelengths can be adjusted by moving the dipole magnets against each other. Another advantage of undulators is their variable polarization. For this the magnets have to be separated in two lengths along the electron propagation direction. The two components can be moved against each other creating a horizontal magnetic field, that can be altered in strength and in phase with respect to the vertical field.[61] Overall the quasi-continuous light, the broad spectrum as well as the variable polarization, offer a wide variety of options for spectroscopists, which will become even more important in the future.

2.3. Spectroscopic Techniques

2.3.1. Photoelectron Spectroscopy

The simplest ionization process of an atom or a molecule forms two particles, an electron and an ion. The minimum energy needed to eject the electron from the molecule is called ionization energy (IE) and is usually delivered by one or more photons. Any energy that exceeds the IE can be partitioned between electron ε_e and the different degrees of freedom of the ion E_{ion} according to momentum conservation laws. Since the ion is significantly heavier than an electron, the latter takes up almost all of this surplus in the form of kinetic energy according to equation 2.11.[68]

$$\varepsilon_e + E_{ion} = h\nu - IE \tag{2.11}$$

This allows the investigation of the electronic structure of a molecule, as electrons in different orbitals exhibit different binding energies, and the ions can occupy different states. In regular photoelectron spectroscopy high photon energies are used to eject electrons from different orbitals and separate them by their kinetic energy. In one-photon processes this requires monochromatic vacuum-ultraviolet (VUV) radiation historically provided by helium discharge lamps. The resolution of photoelectron spectra is intimately linked to the amount of excess energy that the electron carries away. In regular photoelectron spectroscopy high, non-resonant photon energies are used, which requires hemispherical analyzers that decelerate electrons and increase spectral resolutions. In small diatomic molecules the resolution is sufficiently high to not only resolve different electronic states but also molecular vibrations. Their intensity depends on the nature of the orbital the electron is ejected from. Ionization out of non-bonding orbitals does not change the molecular structure between neutral and cation much, leading to no or only marginal vibrational activity. The removal of electrons from bonding as well as anti-bonding orbitals changes molecular geometry parameters according to the shape of the orbital. The former usually leads to bond elongation and angle widening, while the latter show opposite behaviour. These geometry changes upon ionization lead to the excitation of a corresponding vibrational mode that can be seen in the spectrum.

2.3.2. Photoelectron Photoion Coincidence Spectroscopy

Photoelectron spectroscopy detects all electrons of a specific energy range, which includes any impurities that are ionized as well. For molecules that can be purified by other techniques and stored in flasks or gas bottles this is not a huge drawback. For radicals and other highly reactive species that need to be generated *in situ* from a stable precursor, the quality of the spectrum depends on the selectivity of the conversion process. The majority of radical generation methods are unselective by nature, as they either use too much force to destroy a precursor or not enough so that precursor and fragment signals are both detected. To exclude any unwanted products, different techniques have to be coupled together, to gain additional dimensions for separation. Photoelectron photoion coincidence (PEPICO) spectroscopy has a similar effect as the commonly used gas-chromatography/mass spectrometry (GC/MS) but does not require the separation of the gas mixture on a chromatography column first. Since most reactive species would not survive the latter separation process, PEPICO is an ideal tool for radical spectroscopy.[40] Upon ionization, electrons and ions are accelerated onto opposing detectors using electrostatic lenses. Because of their lower mass, electrons are detected almost instantly and provide the start time for an internal clock. The much heavier ion is detected after its time-of-flight (TOF) and triggering the stop signal. This single-start/single-stop acquisition scheme gives a mass information in conjunction with a complete characterization of the electron, resulting in mass selective photo-

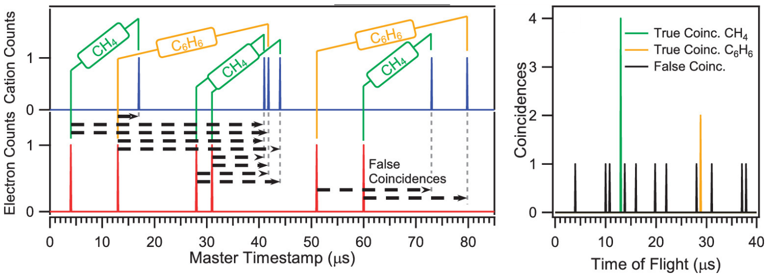

Figure 2.5.: True and false coincidences within a PEPICO experiment. The false coincidences are randomly distributed while true coincidences add up over time. Adapted with permission from Ref.[35]

electron spectra. An electron/ion pair that arises from the same ionization event is called a true coincidence, when both have different origins they contribute to the false coincidences. The TOF of the ions is usually several microseconds, which limits ionization rates to approximately 10^5 s^{-1} in order to suppress the false coincidence background as much as possible. Although the signal increases linearly with time, and the Poisson distributed background only by its square root, measurements would require tremendous amounts of time to achieve an acceptable signal/noise ratio. In order to increase throughput, a multiple-start/multiple-stop (MS/MS) scheme has been developed, as depicted in figure 2.5.[35] In MS/MS each electron and each ion that is detected during a specified time frame, e.g. 50 μs, is given a time stamp with respect to a master clock, which are then cross correlated. With four electrons and four ions in one detection window this would give four true and up to 12 false coincidences, the latter all with a different TOF. Although false coincidences are randomly distributed they ultimately scale linearly with the ionization rate in this detection scheme, identical to the signal. Simply adapting a MS/MS approach without changes does neither improve the signal/noise, nor reduce measurement time. This challenge can be overcome by adding an additional parameter.

By recording the ion impact coordinates on a position sensitive detector surface, in combination with a timely changing electric field, the ions can be deflected perpendicular to their flight axis. Hence, they change position as a function of time and the deflection field at the moment of their creation can be determined by using the TOF from the cross correlation. If the arrival position of the ion matches the deflection field arrangement at the time of its creation the electron/ion pair is termed a true coincidence and counted towards the signal. On the other hand, if the detected ion position does not match the deflection position it is a false coincidence and discarded. This method increases the dynamical range of PEPICO experiments by at least two orders of magnitude.[35]

2.3.3. Threshold Photoelectron Spectroscopy

Conventional photoelectron spectroscopy is not suited to resolve low frequency vibrations, molecular rotations and vibronic effects, because of the error prone measurements of kinetic energies. Other methods had to be developed that increase resolution powers significantly. Since monochromators and spectrometers offer a higher accuracy to determine the incident photon energy with respect to the analysis of electron kinetic energies by a hemispherical analyzers, it was apparent to change the variable parameter.[69] Starting with Baer *et al.*[70,71] the goal was to reduce the kinetic energy of the electron as much as possible while scanning the energy of the light source. Threshold electrons are only generated when the photon energy matches a molecular state in the cation, i.e. when the excitation is resonant. In order to discriminate between threshold electrons and kinetic electrons new setups were invented that relied on a constant electric abstraction field. This would guide electrons towards a pinhole and afterwards to the detector. Electrons with kinetic energy exhibit a momentum perpendicular to this field and cannot pass the pinhole, while threshold electrons with hardly any momentum can. However, kinetic electrons that are ejected directly towards the pinhole are also detected and inhomogenities in the electric field alter the electrons flight paths.[69] In principle, the resolution would only be limited by the accuracy of the energy calibration but including the unresolved issues no significant advantage was achieved. At that time, the light to ionize molecules came mostly from dye-lasers and a resonance enhanced multi-photon ionization (REMPI) scheme was applied, where an excited state was populated with one laser and another was scanned to create threshold electrons.[69] The lasers operated in a pulsed mode, which allowed the use for pulsed abstraction fields that offered another way to discriminate between kinetic and threshold electrons. After generation, the electrons were given some time to propagate in a field-free environment before the abstraction field was applied. Kinetic electrons with a momentum perpendicular to the abstraction field would still not be able to pass the pinhole and the ones ejected along the axis of the field would either be detected before or after the true threshold electron signal. The inclusion of the TOF for electrons lead to the prominent pulsed-field ionization zero kinetic energy photoelectron spectroscopy (PFI-ZEKE) used to this day to record rotational structures in cations.[72,73]

The advent of quasi-continuous synchrotron light sources allowed for a higher throughput and reduced measurement time, but not by using pulsed electron optics. The setup was reversed back to a continuous abstraction field, albeit in a slightly modified way. Known from ZEKE, the generated electrons spread uniformly in all directions, they create a Newton-sphere. Assuming an infinitely small ionization volume, the whole Newton-sphere can be recorded onto a position sensitive detector and electrons are separated by their initial kinetic energy. This technique is called velocity-map-imaging (VMI) and was pioneered by Eppink and Parker.[74] VMI setups do not use grid electrodes that deflect any kinetic electrons but rather curved electric fields, i.e. electrostatic lenses that focus the whole electron cloud onto a two-dimensional detector. In reality the ionization volume is made up of a finite interaction space between light- and molecular beam. In this arrangement, two particles can have identical vectors and still arrive at two different positions on the detector, depending on their exact point of creation. The solution is to merge all particles along the extraction coordinate, the Newton-sphere is pancaked. In this distribution two particles with the same ejection vector may still be separated in two dimensions. By taking advantage of the curved equipotential field lines, the particles within the pancaked distribution feel different field strengths, depending on their exact coordinates, leading to a focal point on the detector face that is only dependent on the initial vector. Threshold electrons lack any kinetic energy and hit the detector in the middle while kinetic electrons are detected in circles around the center. Simultaneous detection of different kinetic energies leads to a "matroshka-puppet" image, where multiple different circle sizes are displayed all centered around the threshold signal. The total energy that can be displayed on the detector can be varied by using different electric field strengths. VMI not only offered a way to increase throughput but also combined high extraction fields with high resolutions,[75] two conditions that were previously mutually exclusive. It is worth noting that the resolving capabilities of VMI setups could not match those from ZEKE. Yet, even the VMI arrangement suffered from "hot" electrons, that are ejected along the detector axis and accumulate together with the threshold signal.

The advantage of VMI is that the whole Newton-sphere is detected and thus a simple subtraction method was proposed by Sztaray and Baer.[76] The center of the image represents a circle and contains threshold and "hot" electrons. Its size depends on the desired resolution in the ensuing spectrum, as well as the signal strength. Usually circle sizes of 38 meV are chosen to resolve molecular vibrations without reducing the signal too much. Directly adjacent to the center circle a ring area is analyzed, for which the assumption is made that it contains only hot electrons. By simply subtracting the empirically weighted ring signal from the circle signal, contributions of hot electrons can be reduced to a minimum.

The high detection frequencies in synchrotron based experiments require different detectors than laser-based VMI experiments. The latter can use a CCD camera in combination with a phosphor screen, which can handle the low frequency of the pulsed setup.[77] For quasi-continuous experiments detectors with almost no downtime have to be used, which enforces the use of delay line anodes. These detectors consist of two perpendicular and intertwined electrodes X and Y. The position of a particle is measured by determining the difference in the arrival times of X_1, X_2, Y_1, and Y_2. These detectors are accustomed to the high count rates and well suited for synchrotron based setups.

For the sake of completion, it is also possible to record a threshold photoelectron spectrum (TPES) by not measuring electrons at all. By scanning the photon energy and measuring the photoion yield every new accessible state in the cation results in an increase in photoions. The ensuing photoion efficiency (PIE) curve exhibits the same structure as a TPES, but with steps in the photoion yield and maxima for a TPES. In general the two can even be converted into each other by integrating the TPES signal or by deriving the PIE curves, both with respect to the photon energy. The stepwise structure renders variables measure by PIE curves much more prone to errors, because the the exact location of one step is hard to determine. Most PIE curves use its first derivative, a TPES-like illustration, to reduce errors, demonstrating the superiority of the TPES method.[78]

2.3.4. Slow Photoelectron Spectroscopy

The principle of VMI can be used to stretch the boundaries of regular threshold photoelectron spectroscopy. By selecting only the threshold events in the middle of the detector the continued expansion of the Newton-sphere with increasing photon energy is not accounted for and this signal is thrown away. The so called slow photoelectrons can be just as useful for the spectrum when they are integrated correctly. One prerequisite before they can be used is the reconstruction of the 3D-Newton sphere from its 2D projection. There are several algorithms available to perform such a task, with the most widely used being pBasex developed by Garcia *et al.* and optimized by Röder.[79,80] Using such a method allows to plot the electron kinetic energy with respect to the photon energy in a 2D photoionization matrix, where each new state is depicted as a function of the photon energy with constant slope according to equation 2.12.

$$E_{kin}(e^{-}) = h\nu - IE \tag{2.12}$$

This matrix can be subjected to several mathematical transformations such as integration or rotation along either of the two axis. When integrating over all kinetic energies of the electrons the result is a resonant photoelectron spectrum, equivalent to a PIE curve, while integration up to a few meV leads to a TPES. The matrix can be rotated counterclockwise by 45°, which transforms the linearly increasing electron kinetic energies into vertical lines for each state. When this matrix is integrated up to KE$_{max}$ higher photonenergies also contribute to one specific state. The ensuing slow photoelectron spectrum (SPES) has a higher signal to noise ratio but broader bands depending on the reconstruction quality. In general the higher KE$_{max}$ is, the broader the bands get, limiting its integration space usually to around 50 meV for an acceptable signal/resolution trade-off. Fig-

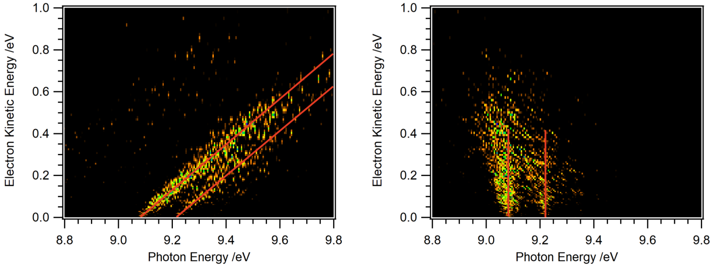

Figure 2.6.: Photoionization matrix (PES matrix) for the HBBH molecule. The matrix on the right has been rotated by 45° counterclockwise.

ure 2.6 shows an example of a normal (left) and rotated (right) PES matrix. Each vibrational state is clearly visible with increasing electron KE and a large broadening in each trace.

Autoionizing states spontaneously emit kinetic electrons and thus cannot be detected by a TPES method. They do appear in the PES matrix as circles, contrary to the diagonals for true vibrational states. They more likely occur in small molecules at photon energies significantly above the IE, in Franck-Condon gap regions. These regions are characterized by their high ionization rate but tiny threshold electron signal.

Overall the SPE technique offers an intriguing way to expand knowledge of photoionization processes, including a higher signal/noise and a more detailed characterization.

2.3.5. Franck-Condon Factors

As discussed in section 2.1, the symmetry or more precisely the geometry of a molecule is tightly connected with the structure of its (threshold) photoelectron spectrum. Within this thesis only a brief description of the necessary elements is given. The interested reader is referred to the literature for a more detailed discussion.[81–85]

The key to calculating and simulating (threshold) photoelectron spectra, which ultimately leads to a deeper understanding, is based on two approximations: the Born-Oppenheimer (BO) approximation and the Franck-Condon (FC) principle. The former states that electron and nuclear wavefunctions can be separated. The hamiltonian of a two particles system, an electron and a ”nucleus” given in equation 2.13 can be simplified to equation 2.14.

$$\hat{H} = -\frac{\hbar^2}{2m_x}\frac{\partial^2}{dx^2} - \frac{\hbar^2}{2m_R}\frac{\partial^2}{dR^2} + V(x,R) \tag{2.13}$$

$$\hat{H}_{el}(x;R) = -\frac{\hbar^2}{2m_x}\frac{\partial^2}{dx^2} + V(x,R) \tag{2.14}$$

The nuclear coordinates R influence the electronic wave function $\psi_{el}(x;R)$ only parametically, so the cores move in the potential that is determined by the electrons.

The FC principle states that during a vibronic transition the geometry and momentum of the nuclei do not change, since the nuclei are heavier and move significantly slower than electrons. The transition occurs vertically, when using the nuclear displacement as the x-axis. While the electronic excitation, or in the extreme case the ionization, does alter the equilibrium structure of the molecule, the nuclei do initially not move parallel to the electronic transition. In such a case the excitation can be depicted with a vertical line. The most interesting parameter for photoelectron spectra that needs to be calculated is the transition probability, which is equal to the square of its transition dipole moment R_{ev}.

$$R_{ev} = \int \psi'_{ev} * \mu \psi''_{ev} d\tau_{ev} \tag{2.15}$$

In equation 2.15 μ is the operator of the electrical dipole moment. ψ'_{ev} and ψ''_{ev} are the vibronic wavefunctions of the upper and lower state, respectively. Using the BO approximation one can separate the electronic and nuclear wavefunctions resulting in equation 2.16.

$$R_{ev} = \int \int \psi'_e * \psi'_v * \mu \psi''_e \psi''_v d\tau_e dr \tag{2.16}$$

Which leads to the expression for the electronic dipole moment:

$$R_e = \int \psi'_e * \mu \psi''_e \cdot d\tau_e \tag{2.17}$$

Please note that the electronic dipole moment depicted in equation 2.17 is strictly speaking only valid for bound-bound transitions. For ionization processes the wavefunction of the cation as well as the ejected electron have to be considered.[86] The overall transitional dipole moment can be expressed in terms of a nuclear and electronic part:

$$R_{ev} = R_e \int \psi'_v * \psi''_v dr \tag{2.18}$$

The integral in equation 2.18 is termed the vibrational overlap integral and its square represents the so called FC factors. When the geometries between the initial and the final state are very similar the wave function of ground and excited state have a large overlap and thus the largest FC-factor will be found at the 0-0 transition. If the geometries differ significantly the FC-factors for the lower transitions are small and thus they cannot be seen in the spectrum.

In polyatomic non-linear (linear) molecules the number of vibrations is 3N-6 (3N-5), so FC factors need to be calculated for each harmonic oscillator. However, through symmetry, specific selection rules can be invoked that exclude some vibrations from occurring in photoelectron spectra. As previously noted the intensity I of a transition is proportional to its electronic transition dipole moment R_e.

$$I \propto \int \psi_e' \mu \psi_e'' dq \tag{2.19}$$

In case of non-degenerate systems the direct product of all involved vibronic states ψ_e', ψ_e'' and the transition dipole moment μ has to be equal to the totally symmetric representation A.

$$\Gamma(\psi_e') \otimes \Gamma(\mu) \otimes \Gamma(\psi_e'') = A \tag{2.20}$$

In the special case of degenerate systems allowed transitions only need to *contain* the totally symmetric representation. The transition dipole moment is a three dimensional vector that can be separated into its three components μ_x, μ_y and μ_z and at least the direct product of one of the components needs to differ from zero for a transition to be allowed. In closed shell molecules the vibronic ground state is equal to the totally symmetric representation, which simplifies equation 2.20 to:

$$\Gamma(\psi_e') \otimes \Gamma(\mu) = A \tag{2.21}$$

Along with changes in the vibronic state, changes can also occur on rotational levels. Symmetry based selection rules for such rovibronic transitions have been formulated by Signorell and Merkt, but will not be further elaborated in this thesis.[86]

2.4. Kinetics

2.4.1. Pseudo-First Order Reactions

Reactions can be influenced by many internal factors, like reactant concentrations, as well as external factors, like pressure and temperature. In the simplest description the product formation rate of reaction (1) only depends on the concentration of the involved species and starting materials A and B are consumed with the rate k.[87]

$$\mathrm{A} + \mathrm{B} \xrightarrow{\mathrm{k}} \mathrm{C} \tag{1}$$

The change of the product concentration $[C]$ over time can be described using a differential equation 2.22.

$$\frac{d[C]}{dt} = k[A][B] \tag{2.22}$$

The sum of all exponents on the concentrations states the order of the reaction, which would be two in the above case. The integration of equation 2.22 allows to determine the rate constant of reaction (1) when the starting concentrations $[A_0]$ and the concentrations at time t, $[A]$ are known.

$$\frac{1}{[A]} - \frac{1}{[A_0]} = k_2 t \tag{2.23}$$

It is notable that equation 2.23 is only valid for equal starting concentrations of $[A]$ and $[B]$ and even then the determination process is impeded since absolute concentrations are hard to determine. Rate constants are easier to determine using the pseudo-first-order approximation, which uses one reactant is a large excess. This means that one concentration ($[B]$) can be seen as constant and can be merged with the rate constant, which changes equation 2.22 to 2.24.

$$\frac{d[C]}{dt} = k'[A] \tag{2.24}$$

The decay now follows first-order and after integration is described by equation 2.25.

$$[A] = [A_0] \cdot e^{-k't} \tag{2.25}$$

One has to note that in second-order decays the absolute concentrations have to be subtracted from one another while in a first-order decay, only relative concentrations at time zero and t are needed, which simplifies experimental setups. The second-order rate constants can be extracted using a linear plot of the pseudo-first-order constants over different concentrations of $[B]$ according to equation 2.26.

$$k' = k \cdot [B] + k_{Side} \tag{2.26}$$

The slope of this pseudo-first-order plot gives the second order rate constant, while the y-axis offset shows the neglected side reactions (k_{side}) that may also occur during the reaction. If these are accounted for in the reaction mechanism the y-axis intercept should be zero. Yet, even when these reactions are not quantified at all, the large excess of the reactant $[B]$ renders the probability of a reaction between any non-B molecules small and limits their influence on the rate constant k'.

2.4.2. Reactions with Pre-Equilibirum

Next to internal factors, ambient factors like temperature and pressure also play important roles in reaction kinetics.
The temperature dependence of a reaction is in most cases straightforward. The earliest description has been provided by Arrhenius who found that the rate constant of a reaction k_n is dependent on the activation energy E_A and the temperature T.[88]

$$k_n = A \cdot e^{-\frac{E_A}{RT}} \tag{2.27}$$

Equation 2.27 also contains a preexponential factor A as well as the gas-constant R. The former is dependent on the individual molecules and can be determined as the y-intercept of the plot $ln(k)$ versus $\frac{1}{T}$.
Within a single non-reversible reaction step the increase of T leads to an increase of the rate constant k_n. The only case when a temperature reduction exhibits the same phenomenon is when the activation energy E_A is negative, which is physically impossible. However, when reaction mechanisms become more complex negative temperature dependencies are not uncommon. Considering the reaction mechanism (2) , where k_1 and k_{-1} are both significantly greater than k_2.

$$\mathrm{A + B \underset{k_{-1}}{\overset{k_1}{\rightleftharpoons}} I \xrightarrow{k_2} P} \tag{2}$$

The reaction exhibits an equilibrium between the starting materials and the intermediate I, which only slowly can be consumed to form the product P. The concentration of I can be calculated using the equilibrium constant K.

$$K = \frac{[I]}{[A][B]} = \frac{k_1}{k_{-1}} \tag{2.28}$$

The equation for the product formation over time can be determined according to the reactions mechanism in (2) under the assumption that product formation does not disturb the equilibrium between A, B and I.

$$\frac{d[P]}{dt} = k_2[I] = k_2K[A][B] \tag{2.29}$$

The product formation is a second-order reaction with an effective rate constant of k.

$$k = k_2 K = \frac{k_2 k_1}{k_{-1}} \tag{2.30}$$

The temperature dependence of these reactions can be introduced by the Arrhenius equation 2.27 and together with 2.30 the activation energy is a sequentially dependent.

$$k = \frac{A_2 e^{-\frac{E_{A2}}{RT}} A_1 e^{-\frac{E_{A1}}{RT}}}{A_{-1} e^{-\frac{E_{A-1}}{RT}}} = \frac{A_2 A_1}{A_{-1}} \cdot e^{-\frac{E_{A2}+E_{A1}-E_{A-1}}{RT}} \tag{2.31}$$

The overall activation energy of reaction (2) consists of the sum of the three individual reaction steps, which under the right circumstances can become negative. One possible class of molecules for which negative temperature dependencies have been found are reactions between resonance stabilized radicals and oxygen. These reactions destroy the conjugation and will form an energetically unfavorable intermediate I. When barriers to other secondary products P are high, the rate constant of the reverse reaction k_{-1} is not negligible and the system exhibits an equilibrium. The system will predominantly react back to the starting materials upon increasing temperature, but eventual the minor non-reversible reaction pathway to the products P will have consumed all starting materials.[87]

2.4.3. Pressure Dependent Reactions

During the study of unimolecular dissociations such as the one shown in reaction (3), it has become apparent that the order of the reaction and thus the rate constant was pressure dependent. The same has been found to be true for their reverse reactions such as radical recombinations (4).[89]

$$\mathrm{AB\,(+M)} \longrightarrow \mathrm{A + B\,(+M)} \tag{3}$$

$$\mathrm{A + B\,(+M)} \longrightarrow \mathrm{AB\,(+M)} \tag{4}$$

Lindemann first described this behavior, using a pre-equilibrium distribution given in reactions (5) to (7) for a unimolecular dissociation.

$$\mathrm{A + A} \xrightarrow{\mathrm{k_1}} \mathrm{A^* + A} \tag{5}$$

$$\mathrm{A^* + A} \xrightarrow{\mathrm{k_{-1}}} \mathrm{A + A} \tag{6}$$

$$\mathrm{A}^* \xrightarrow{\mathrm{k_2}} \mathrm{B} + \mathrm{C} \tag{7}$$

Collisions between two A molecules create an excited A^* species that has enough energy to proceed via two possible routes. It can either get deactivated upon collisional energy transfer, or can undergo reaction to form the products B and C. Since (5) requires a certain energy to be present in the product molecules contrary to reaction (6), k_1 will always be smaller than k_{-1}. The rate of formation of the activated molecules A^* and its dissociation into the product B can be expressed with differential equations 2.32 and 2.33, according to the reaction mechanism.

$$\frac{d[A^*]}{dt} = k_1[A]^2 - k_{-1}[A^*][A] - k_2[A^*] \tag{2.32}$$

$$\frac{d[B]}{dt} = k_2[A^*] \tag{2.33}$$

Applying the steady state approximation, which states that the concentration of an intermediate species, in this case A^*, does not change over time, equation 2.32 is approximately zero and can be solved for $[A^*]$ to give equation 2.34.

$$[A^*] = \frac{k_1[A]^2}{k_2 + k_{-1}[A]} \tag{2.34}$$

This expression substituted in equation 2.33 yields the rate of formation for the product $[B]$.

$$\frac{d[B]}{dt} = \frac{k_2 k_1[A]^2}{k_2 + k_{-1}[A]} \tag{2.35}$$

Equation 2.35 is the most general approach and easiest way to illustrate the pressure dependency, since it allows the treatment of two extreme cases. At high pressures where $k_{-1}[A] \gg k_2$ one can neglect k_2 in the denominator so that it becomes equation 2.36 with a first-order rate constant.

$$\frac{d[B]}{dt} = \frac{k_2 k_1}{k_{-1}}[A] \tag{2.36}$$

At low pressures where $k_{-1}[A] \ll k_2$ is the case the reaction follows second-order, as in equation 2.37

$$\frac{d[B]}{dt} = k_1[A]^2 \tag{2.37}$$

The reaction has two critical steps and whichever is the slowest determines the overall rate as well as the reaction order of the whole process. In a first step the molecule takes up the required activation energy, which is initially distributed over the whole molecule. The accumulation into a critical mode, for dissociations this would be a critical vibrational mode, is the rate determining step to overcome this pre-activated complex. Under these conditions the rate constant can also be estimated by Rice-Ramsperger-Kassel-Marcus (RRKM) theory.[90]

At low pressures the probability of a pre-activating collission is low, so that once it occurs the reverse reaction (6) can not occur within the time frame of the competing product formation channel (7). The collision probability depicted by reaction (5) becomes the rate-determining step.

At high pressures collisions occur more frequently so that the deactivation process of $[A^*]$ becomes faster. The time the molecule needs to rearrange the energy into the critcal mode becomes the rate determining step, which in the reaction mechanism above is reaction (7).

The energy for the pre-activation can also come from collisions with other gaseous species, like bath gas atoms or molecules that can not react themselves. Reaction (5) can thus be expanded to a more general version, where the second A molecule is substituted by an inert collision partner M to yield equation 2.38 from 2.35.[87]

$$\frac{d[B]}{dt} = \frac{k_2 k_1 [M]^2}{k_2 + k_{-1}[M]}[A] = k[A] \tag{2.38}$$

All of the above listed equations are valid for molecular dissociations, but can be easily transformed to describe association reactions like radical recombinations using the following reaction mechanism.

$$\mathrm{A + M \xrightarrow{k_1} AM} \tag{8}$$

$$\mathrm{AM \xrightarrow{k_{-1}} A + M} \tag{9}$$

$$\mathrm{AM + B \xrightarrow{k_2} AB + M} \tag{10}$$

Equation 2.35 becomes:

$$\frac{d[AB]}{dt} = k[A][B] \tag{2.39}$$

Containing the pseudo-second-order rate constant:

$$k = k_1 (\frac{k_2[M]}{k_{-1} + k_2[M]}) \tag{2.40}$$

In association reactions the high-pressure regime is governed by a second-order rate constant, while at low pressures the rate constant is of third-order. Similar to dissociations, first attempts to describe the pressure dependency used a reduced form where a high- and low-pressure rate constant can be found by considering the two extreme cases with respect to $[M]$ in equation 2.40.

$$k_0 = \lim_{[M]\to 0} k = k_2(k_1/k_{-1})[M] \tag{2.41}$$

$$k_\infty = \lim_{[M]\to \infty} k = k_1 \tag{2.42}$$

Using the last two equations as basis for theoretical predictions means that the rate constant k is split up between two extreme cases. The kinetics at low pressures are exclusively governed by the bath-gas dependent k_0, which increases linearly with $[M]$ until the pressure is high enough so that the pressure independent k_∞ takes over. However, nature is rarely discontinuous and thus the region in between the two extremes is called "falloff" as the rate constant k decreases steadily from k_∞ to k_0. In other words, the influence of $k_0[M]$ on k grows while the pressure is decreased and vice versa. The point where the two extreme cases k_0 and k_∞ meet is called the center of the falloff. As a general rule the smaller the molecule is the more is k_∞ shifted to higher pressures. The challenge for the accurate theoretical description of the pressure dependency between the two regimes is, to find an expression that fulfills the requirements of a continuous falloff. [89] Using the definitions for k_∞ and k_0 from equations 2.41 and 2.42 one can rewrite the rate constant expression 2.40.

$$k = \frac{k_0 k_\infty}{k_0 + k_\infty} \tag{2.43}$$

Or for an easier handling, in its doubly reduced representation by deviding it by k_∞:

$$\frac{k}{k_\infty} = \frac{k_0/k_\infty}{1 + k_0/k_\infty} \tag{2.44}$$

The predictions made by equation 2.43, or 2.44 are dependent on the choice of k_0 and k_∞ but the experimental values are still consistently overestimated by theory. In order to account for this effect a "broadening factor" $F(k_0/k_\infty)$ has been introduced.

$$\frac{k}{k_\infty} = \frac{k_0/k_\infty}{1 + k_0/k_\infty} F(k_0/k_\infty) \tag{2.45}$$

The broadening factor is in between 0 and 1 and changes with respect to the pressure. It usually exhibits a minimum near the center of the falloff, which is why F_{cent} is especially dependent on the values for k_0 and k_∞. There are multiple explanations for broadening factors, such as the wide distribution of energies that are occupied in the excited species AB^*, which influences reactions (8) and (9). Further, single collisions do not provide enough energy to overcome the energy for reaction, but rather a whole sequence of collisions is required. These collisions do not all lead to an activation of the excited species, some might deactivate the molecule in a collision.[89]
It has to be noted that the understanding and modeling of pressure dependent reactions has improved, but it is still far from complete.

3. Experiment

Experiments presented in this thesis have been performed on two different setups, the microwave discharge fluorine reactor setup installed at the DESIRS beamline at synchrotron SOLEIL and the combustion-reactions-followed by PEPICO (CRF-PEPICO) setup at the SwissLightSource (SLS). The latter has two operational modes: A pyrolysis setup as well as a continous-flow photolysis reactor setup. These beamlines and setups will be described in this chapter.

3.1. Synchrotron SOLEIL

3.1.1. The DESIRS Beamline

The DESIRS (Dichroisme et Spectroscopie par Interaction avec le Rayonnement Synchrotron; dichroism and spectroscopy by the interaction with synchrotron radiation) beamline is dedicated to high resolution VUV spectroscopy with two separate permanent endstations, a VUV-Fourier-Transform spectrometer (FTS) and the PEPICO endstation SAPHIRS.[91] A third exit is reserved for endstations brought to the beamline by external users with special requirements and will be neglected in the upcoming description.

The storage ring at SOLEIL operates with electron energies of 2.75 GeV and feeds the DESIRS beamline with photons over the whole VUV region from 5 eV to 40 eV. Electrons inside the storage ring enter a 10.4 m long undulator (OPHELIE2) that uses 14 magnetic periods with a length of $\lambda_0 = 640\,\mathrm{mm}$ to amplify the photon flux and increase brilliance. Polarization of the synchrotron light can be changed to create linear, elliptic, and circular polarizations at the point of photon/matter interaction using independently variable vertical and horizontal magnetic fields created by three different sets of air coils. This non-mechanical scheme minimized energy losses and allows to adjust the three parameters, the horizontal magnetic field B_{0x}, the vertical magnetic field B_{0z} and the longitudinal phase shift ϕ independently. Compared to other VUV-beamlines, tunable polarizations

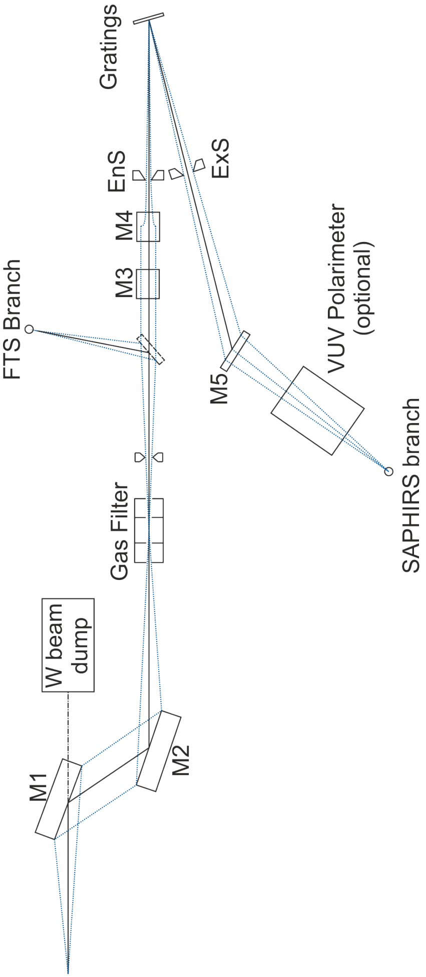

Figure 3.1.: Schematic illustration of the PEPICO branch of the DESIRS beamline. Adapted from ref.[91]

offer the possibility to perform photoelectron circular dichroism experiments on chiral molecules.

The schematic setup of all optical elements guiding the synchrotron light into the endstation is depicted in figure 3.1. After the undulator, the light is deflected horizontally by two mirrors to minimize heat stress on the upcoming optical elements, since they absorb light above 60 eV. A tungsten beam blocker is installed to take up high energy photons that are not yet absorbed by the first mirror. The second mirror focuses the beam into the middle of a gas-filter that is used to filter any higher harmonics that are created in the undulator. The gases, usually noble gases or mixtures thereof, can be varied to fit the energy range of the experiment. Afterwards, the beam width and hight can be tailored by using a four-blade aperture after which the light can be either inserted into the FTS apparatus or continue its way to the PEPICO endstation. To balance out any polarization effects induced by the the first two mirrors, the beam is deflected again using the same mirror setup. The beam is thus prefocused and can enter the 6.65 m long normal incidence monochromator (NIM) through an entrance slit. To optimize grating illumination inside the NIM, the beam is defocused vertically and slightly focused horizontally creating a thin line on the 7.5 m distant grating. This mirror setup also ensures a wavelength independent spot at the experimental focus points and maximizes the photon flux output of the NIM. The energy can be adjusted by rotation of the grating, with several gratings being available, ranging from high-resolution (2400 lines/mm, 4300 lines/mm) to high flux (200 lines/mm, 400 lines/mm), according to the needs of the experiment. Resolution and flux can also be traded for one another by using different entrance slit settings of the NIM. After the light passes the exit slit, a mirror focuses the beam into the experimental chamber of the SAPHIRS endstation. Experiments in this thesis used the 200 lines/mm grating and in combinations with the entrance and exit slits a spectral resolution of around 5 meV at the working energy range was achieved. The gas filter was filled with 0.25 mbar Ar to cut off the higher-order radiation from the undulator ensuring spectral purity.

3.1.2. The Fluorine Reactor Setup

A schematic picture of the microwave discharge fluorine reactor setup at the SAPHIRS endstation of the DESIRS beamline is given in figure 3.2. The setup consists of three chambers that are separated by Teflon skimmers with an internal diameter (i.d.) of 1 mm creating a pressure difference of at least three order of magnitude between each when in operation. In the first chamber, the main quartz tube with a 24 mm i. d. and 65 cm in length is positioned radially around the first skimmer opening while maintaining a 1 cm distance to it. The precursor molecules can be introduced into the tube by parallelly inserting a 6 mm i. d. and 190 cm long quartz sliding reactor into the main tube, while fluorine atoms can be fed through a side arm. The length difference between injector and main tube creates the hydrogen abstraction reaction zone, which can be varied at all times using an automatic 3D translational stage. Fluorine atoms are generated via a microwave discharge running at 2450 MHz outside of the first chamber from a diluted (≈ 5%) mixture of F_2 in helium and introduced into the main tube 50 cm in front of the reaction zone. The amount of fluorine can be adjusted by a needle valve and the discharge efficiency measured by F_2 detection is around 80%. Metered flows of gaseous samples are introduced into the injector by mass flow controllers (MFCs), while liquid samples are seeded in helium first to create a saturated vapor. The overall mass flow consisting of sample and helium for dilution is 1000 sccm. The molecules are adiabatically expanded through the first skimmer into a differentially pumped second chamber and through a second skimmer into the experimental chamber. This double skimmer setup reduces the amount of thermally excited molecules that are detected, thus increasing mass and kinetic energy resolutions. The pressure in the reaction chamber is regulated by a 600 m^3/h rootspump (Edwards GX600N) and can be adjusted by changing the overall flow coming from the MFCs. The second chamber is evacuated by three turbomolecular pumps (300 l/s, Edwards nEXT300D) and by a 120 m^3/h primary pump (Adixen ADP122), while the experimental cham-

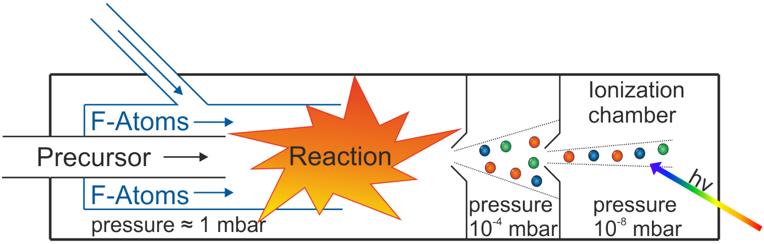

Figure 3.2.: Schematic picture of the fluorine reactor setup that was used in this thesis.

ber is attached to two turbomolecular pumps (1000 l/s, Leybold TurboVac 1000) as well as a $28\,\mathrm{m}^3/\mathrm{h}$ primary pump (Adixen ADP28G). This results in operating pressures of around 1 mbar, 10^{-4} mbar, and 10^{-8} mbar in the first, second and third chamber, respectively. The created molecular beam crosses the synchrotron light perpendicularly inside the double imaging PEPICO spectrometer DELICIOUS III.[92] After ionization, electrons are accelerated towards position sensitive velocity-map-imaging detectors and ions are guided by a modified Wiley-McLaren time-of-flight mass spectrometer (TOFMS). A continuous repeller voltage of 500 V corresponding to an extraction field of 89 V/cm guides the charged particles onto the detectors. Low electric fields are neceassary to be able to discriminate ions from a true ionization event from those originating from dissociative photoionization. It is worth noting that contrary to the electrons the ions are not velocity-map-imaged. Instead any energy transferred to an ion during (dissociative) photoionization creates a Newton-sphere, whose 3D momentum vectors can immediately be read out without the need for reconstruction. However, this requires translationally cold molecules in direction of the ion detector in order to have a reasonable mass resolution. In principle this is ensured by the double skimming setup, but upon significant kinetic energy uptake via dissociative photoionization, the mass resolution will deteriorate quickly. On cold molecules mass resolution at the half maximum is $\Delta m/m \approx 1000$ or $\Delta m/m \approx 100$ at 10% of the peak height. Electron resolution can be less than 1 meV,[92] which is needed to resolve molecular rotations, but is not required to record vibrationally resolved spectra. The DELICOUS III spectrometer offers the possibility of different analysis procedures that also impact the resolution of the obtained photoelectron spectrum. Standard threshold photoelectron analysis offers the highest resolution capabilities, albeit it needs a very large signal intensities to function properly. Slow photoelectron spectra can increase signal/noise ratios many times over by accounting for an expanding Newton-sphere with increasing photon energy, but lead to a minor broadening in the spectrum.

3.2. SwissLightSource

3.2.1. The VUV-X04DB-Beamline

The prime goal for the X04DB beamline at the SwissLightSource is to study chemical kinetics and thermochemical properties of molecules. For both of these applications separate setups have been developed and installed at the same endstation.[93] A second endstation is currently being commissioned that expands the use of the beamline to spectroscopy of clusters, but was not used in this thesis and will be neglected.

A complete schematic drawing of the optical elements that guide the synchrotron light to the endstation is depicted in figure 3.3. In the storage ring of the SwissLightSource (SLS) electrons circulate with an energy of 2.4 GeV and a ring current of 400 mA. Synchrotron light is provided to the VUV beamline via a bending magnet creating a horizontally diverging light beam with an angle of 8 mrad. The unfiltered light covers the whole spectral range of the synchrotron, but with unequal distribution. While emission in the horizontal plane is independent of the photon energy, higher energy photons in the X-ray region are almost exclusively emitted in the plane of the storage ring. Lower energy VUV photons have a trajectory above and below that plane, thus requiring a greater vertical acceptance angle of the upcoming optical elements. Contrary to the DESIRS beamline, the polarization of the light cannot be adjusted at will. The majority (75%) of the light is linearly polarized in-plane of the storage ring, with a minority being elliptically polarized above and below the plane. The light propagates through a pair of horizontal and vertical slits, which are used to adjust the photon flux. Higher energy radiation ($<$150 eV) is absorbed by a water-cooled copper rod in order to reduce heating stress on the optical elements, which would otherwise lead to an unstable beam profile. The blocker is placed in the center of the beam and cuts out everything within ±0.2 mrad, eliminating most of the x-ray photons while only 15% of VUV photons are lost.[93] The power of the light is consequently reduced from 240 W to 53 W after the blocker. The first, internally cooled, mirror absorbes another 51.8 W and reflects the rest onto a grating that acts as a dispersive element. The wavelength of the light can be adjusted by tilting the grating according to equation 3.1, where m is the diffraction order, λ

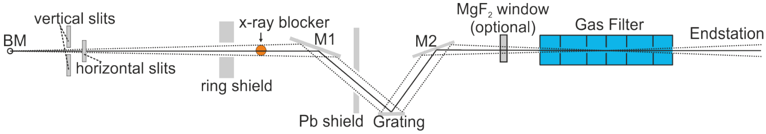

Figure 3.3.: Schematic frawing of the optical elements at the VUV beamline. Adapted with permission from Ref.[93]

the wavelength of the light, d the line spacing, ϕ the scan angle and Φ the constant deviation angle.

$$m\lambda = 2d \cdot cos\Phi \cdot sin\phi \tag{3.1}$$

Contrary to the DESIRS beamline, the light provided by the bending magnet is perfectly suited to be used in a monochromator setting without an entrance and exit slit. The resolution and photon flux can be tuned by different gratings (150 lines/mm, 600 lines/mm, 1200 lines/mm), that can be replaced without breaking vacuum. The measurements of this thesis have been performed using the 150 lines/mm grating. A second mirror refocuses the light inside the gas filter that is used to eliminate higher harmonics. The grating eliminates around 80% of the second harmonic and 95% of the third, but further suppression by a factor of 10^3-10^4 is needed. Higher harmonics are absorbed by the gas filter via ionization of the containing molecules or atoms, which limits the use of each substance to a specific energetic range. The operational range of each material can be coarsely estimated by its ionization energy (IE). The IE represents the upper limit for the usable energy of the synchrotron light, while the lower limit is at half of its value (IE/2). Interesting regions for radical spectroscopy are usually between 8 and 16 eV, which renders noble gases perfectly suited for gas filter applications. The efficiency is also dependent on the pressure inside the gas filter as well as its length. A second option to filter out higher harmonics is the use of an magnesium fluoride (MgF_2) window. This material is completely transparent up to 10 eV and quickly becomes opaque at 11 eV. Since the most common and cheapest gas filter material is argon, which has an IE of 15.75 eV, the MgF_2 window is perfectly suited for low ionizing molecules between 5.5 eV and 8 eV. The light is subsequently coupled into the CRF-PEPICO endstation.

3.2.2. The CRF-PEPICO Endstation

The CRF-PEPICO endstation is the advancement of the double imaging PEPICO apparatus that was previously described in detail.[94,95] Through its dynamic design it can incorporate a number of different experiments like laminar flames as well as catalytic, pyrolytic, and photolytic reactors. Experiments within this thesis have only been performed using the last two setups, which will be detailed in the next sections.

The apparatus consists of two chambers, a source chamber and an experimental chamber, that can either be separated by a skimmer or joined together depending on the type of experiment. Vacuum in the source chamber is provided by two turbomolecular pumps ($1200\,\mathrm{l\,s^{-1}}$, Pfeiffer) and one cryopump ($5000\,\mathrm{l\,s^{-1}}$, Leybold). The experimental chamber is evacuated by an extra turbomolecular pump ($600\,\mathrm{l\,s^{-1}}$, Pfeiffer) or a cryopump ($1200\,\mathrm{l\,s^{-1}}$, Leybold) creating a total vacuum when not in operation of about 5×10^{-8} mbar. The heart of the endstation is the double imaging PEPICO spectrometer that is located in the experimental chamber and intersects the synchrotron light beam. It consists of 26 independently controllable metal plates, 12 on the electron side, 14 on the ion side, for a maximum degree of flexibility on the shape of the electric lenses. The first two plates on each side have been cut to make room for the photolysis reactor that can be inserted for kinetic experiments. The electrons and ions created in the ionization event are velocity-map-imaged onto position sensitive delay-line detectors (Roentdeck DLD40). The PEPICO setup uses a multiple-start multiple-stop detection scheme as well as an alternating deflection field to reduce false coincidences. Within a TOF-MS, ions with the same mass have to have identical TOF, independent of their point of creation and initial kinetic energy they take up during ionization. These two effects are called space resolution and energy resolution and both are mutually exclusive to achieve within one region. The CRF-PEPICO setup uses a low extraction field with linear electric fields near the ionization volume, favoring space resolution, and curved, high electric fields later, to compensate for spreads in the kinetic energy. The strong and curved electric fields are also required for ion VMI. The relative lengths of these two regions can be adjusted at will without breaking vacuum, giving the setup two modes of operation; imaging and space focusing.[40] For experiments within this thesis, VMI conditions have been used for pyrolysis experiments to utilize the molecular beam, while photolysis experiments have been performed under space focusing conditions.

3.2.2.1. The pyrolysis setup

The pyrolytic microreactor developed by Chen and co-workers has been extensively used in the past and multiple, very detailed descriptions exist in the literature.[94–97] Therefore, only a brief description is given here.

To operate the endstation with a pyrolytic reactor a home-built pyrolysis source was attached to the source chamber perpendicular to the synchrotron beam. The source consists of a long metal tube on which a nozzle is mounted that has a small hole at its tip. The nozzle can be filled with precursor sample and by using different hole sizes from 100 μm to 300 μm the pressure inside the nozzle and the amount of bimolecular reactions in the pyrolysis reactor can be influenced. The nozzle is placed inside a copper block, which is used to heat the sample by circulating water through it. A silicon-carbide pyrolysis tube was mounted onto the copper block that could be resistively heated to several hundred Kelvin using an external power supply. The source was attached to an argon-backed MFC and a small flow of argon (5 sccm) was introduced into the nozzle creating a continuous molecular beam that passed a skimmer and crossed the synchrotron light. Highly volatile liquids can be placed in between argon bottle and MFC to create a sample/argon mixture of a few percent depending on the vapor pressure of the sample. Solid samples with low volatility can be placed inside the nozzle and heated to increase their vapor pressure.

3.2.3. The Photolysis Setup

The continous wave (CW) photolysis reactor setup is used to measure bimolecular rate constants as well as generate reactive intermediates that are not accessible otherwise. For this purpose a 57 cm long, 1.27 cm outer diameter (o.d.) quarz tube is used, which is coated using halocarbon wax to reduce wall losses. The coating is applied by pouring a saturated solution of the wax in acetone under constant rotation inside the reactor. After evaporation of the acetone the walls exhibit a constant blur, signaling an even coating. A schematic illustration of the photolysis setup is given in figure 3.4. The reactor tube is inserted in between the ion optics described in section 3.2.2 and the hole in its wall at the halfway point is placed in the middle of the ion optics pointing towards the synchrotron light. The hole size is a crucial parameter, that trades signal intensity for operable pressure range. For standard measurements a 300 μm hole is used. The exit of the reactor is 21±4 mm away from the ionization region, which minimizes the response time between laser trigger and signal detection. As photolysis laser a 10 Hz Nd:YAG laser (Quantel, Q-smart 850) was used and operated at either the second (532 nm), fourth (266 nm) or fifth (213 nm) harmonic, with photon fluxes of 190 mJ/cm^2, 150 mJ/cm^2 or 30 mJ/cm^2 respectively. After the photolysis laser has been aligned, the back of the reactor is attached to a pump and at the front a quartz mixing chamber is installed. It has four 5 mm o.d. gas inlets perpendicular to the reactor and is covered with a UV-transparent glass window, through which the laserlight can enter. The four gas-inlets can accomodate two different radical precursors, one reactant and a inert dilution gas, which come from calibrated MFCs. All joints are connected with Teflon tubing, to prevent precursor absorption inside the tubing, that alters its concentration over time. The pumping

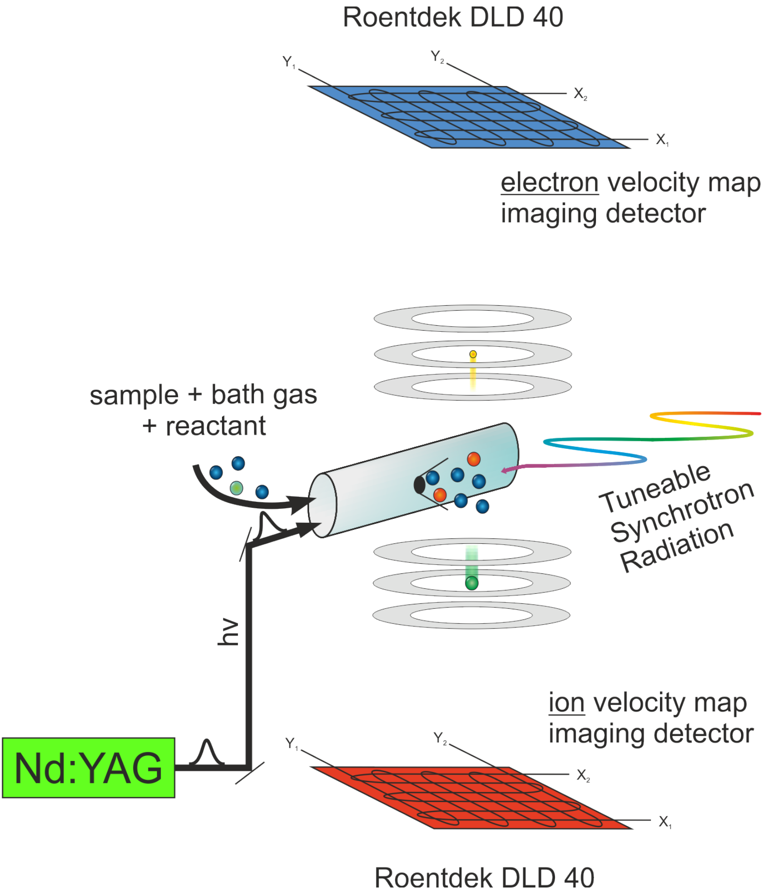

Figure 3.4.: Schematic illustration of the slow-flow photolysis setup at the VUV-beamline.

speed of the reactor pump can be adjusted by a regulatory valve and together with the overall gas flow entering the reactor the pressure can be set. When using a 300 μm hole the pressure range is usually between 1-3 mbar and limited by the pressure inside the experimental chamber, which must not rise above 6×10^{-6} mbar. For photolysis experiments the two chambers of the endstation are not separated by a skimmer to optimize pumping efficiency. By turning on the photolysis laser the light propagates down the reactor dissociating precursor molecules that absorb laser photons along the way. The high velocity of the generated radicals and low pressure inside the reactor lead to an uniform radical distribution directly after photolysis. The radicals generated right next to the hole can exit the tube, cross the synchrotron light and get ionized within 2 ms, which is the response time of the setup. Radicals that are closer to the mixing chamber have more time to interact with the reactant molecules, decreasing the initial radical signal. In principle rate constants can either be measured directly, using the formation of the product or indirectly by measuring the decreasing intensity of the radical signal. The first gives a rate constant that is unperturbed by any secondary reactions, while in the second method background reactions have to be accounted for. In both cases it is necessary to replace the photolyzed gas mixture inside the reactor in between laser pulses with a fresh one, to minimize any secondary effects. With a 10 Hz photolysis system at least half of the reactor volume, up to the pinhole, needs to be replaced within 100 ms. Assuming laminar flow conditions, meaning no perturbation by vortexes, this is dependent on the overall mass flow, temperature, reactor pressure and its inner diameter. The flow velocity in between laser pulses can be calculated using equation 3.2.

$$\frac{0.01\cdot(TotalFlow[sccm])\cdot\frac{Temp[K]}{298}\cdot\frac{1013.25\,mbar}{p_{Reactor}[mbar]}\cdot\frac{1}{60}}{\pi\cdot(\frac{ReactorI.D.[cm]}{2})^2}=Flow[\frac{m}{s}] \quad (3.2)$$

Thus, at room temperature, 50 sccm total flow, 3 mbar reactor pressure and an i.d. of 1.05 cm the gas travels 53.8 cm in between laser pulses, which is enough to photolyze a fresh mixture for each laser shot. Without any reactant the kinetic traces can exhibit a biexponential decay especially at lower pressures and high flow speeds. The reason for this is a ”pump-out” mechanism that replaces the photolyzed mixture with fresh gas before the reaction has been completed. In order to maximize signal intensity it is necessary to adapt the flow speed to the pressure so that radicals are detected in an almost constant fashion. Since the TOF of the ions is fast with respect to the kinetics, every ion has a detection time-stamp with respect to the laser trigger. By selecting a mass channel, these time-stamps can be used to plot the kinetic trace, which can consequently be analyzed in detail. In case the mass channel only contains one isomer, the photon energy for ionization does not have any impact on the kinetic traces with the exception of overlapping dissociative ionization channels of the precursor. When isomer selective rate constants need to be entangled, the photon energy has to be set so that only the lower ionizing isomer is detected. The higher ionizing isomer must be ionized at a photon energy where it exhibits a large threshold signal, to be able to discriminate the threshold signal from the background.

The photolysis setup can be expanded by a CW gas-phase UV/Vis setup to measure the precursor concentrations constantly according to the Beer-Lambert law. For this a separate light source (DH-2000-S-DUV-TTL, OceanOptics) with two different light bulbs, a Tungsten-halide as well as a deuterium lamp is used. The two lamps together cover a range between 210 nm and 2500 nm, ideal for hydrocarbon halide precursors that usually absorb between 300 and 200 nm. The outgoing light is coupled into a 200 μm light transmitting fiber (QP200-2-SR-BX, OceanOptics) which is connected to a gas absorption cell (Wavelength References) with a path length of 10 cm. The gaseous precursor flows through the absorption cell where the light can interact with it. Afterwards the light enters another fiber before being introduced into a UV/Vis spectrometer (Ocean HDX, OceanOptics). The spectrometer can resolve light from 200 nm to 1100 nm with a resolution of up to 0.61 nm (FWHM) and an integration time of 6 ms, which is well suited for real time measurements. The obtained optical density can be used to calculate the concentration of the precursor, which also requires its absorption cross section. For precursors where no absorption cross section in the gas phase is known it can be roughly estimated using different concentrations of the precursor in liquid hexanes. Although uncertainties in the concentration measurements increase the uncertainty in the rate constant, the error is very small as long as pseudo-first-order conditions are met.

3.3. Quantum Chemical Calculations

Quantum chemical calculations were performed using the *Gaussian 09* suite of programs.[98] A brief summary of the utilized density functional theory and complete basis set approaches (CBS-QB3) are presented in this section.

3.3.1. Density Functional Theory

Density functional theory is based on the theorem by Hohenberg and Kohn.[99] It states that the ground state of an electronic system is completely defined by its electron density and the corresponding ground state energy is only a functional thereof. The electron density of a system with N electrons $\rho(\vec{r})$ is the sum of all squared Kohn-Sham orbitals ϕ_i^{KS} according to equation 3.3.[100]

$$\rho(\vec{r}) = \sum_{i=1}^{N} |\phi_i^{KS}|^2 \tag{3.3}$$

Briefly, Kohn-Sham orbitals represent eigenfunctions of the Kohn-Sham (KS) equation 3.4, which gives comparable results as the Hartree-Fock (HF) method. However, KS orbitals take correlation effects into account, which are neglected in HF.[100,101]

$$\begin{aligned}[\widehat{T}_e + \widehat{V}_{Ne} + \widehat{V}_{ee} + \widehat{E}_{xc}]\phi_i^{KS}(\vec{r}_1) &= [h_1 + \int \frac{\rho(\vec{r}_2)}{\vec{r}_{12}} d\vec{r}_2 + v_{xc}(\vec{r}_1)]\phi_i^{KS}(\vec{r}_1) \\ &= \varepsilon_i \phi_i^{KS}(\vec{r}_1)\end{aligned} \tag{3.4}$$

In this $\widehat{T}_e$ is the operator of the electron kinetic energy, $\widehat{V}_{Ne}$ is the operator of the electron-core interaction, $\widehat{V}_{ee}$ is the operator of the coulomb-interaction of the electrons and $\widehat{E}_{xc}$ represents the operator for the exchange correlation interaction. The first two represent the single electron hamiltonian h_1, and the exchange-correlation potential v_{xc} results from the exchange-correlation energy according to equation 3.5.[101]

$$v_{xc}(\vec{r}) = \frac{\delta E_{xc}[\rho]}{\delta \rho(\vec{r})} \tag{3.5}$$

By exact determination of the exchange correlation energy E_{xc}, the exact energy of the whole system can be calculated. However, this is not possible, so methods have to be found that approximate the functional of E_{xc}, which is often done by separating the exchange- and the correlation parts (equation 3.6).[101]

$$E_{xc}[\rho] = E_x[\rho] + E_c[\rho] \tag{3.6}$$

Within the local density approximation it is assumed that the electron distribution can be approximated by a homogeneous electron-gas, which often overestimates the bond energy.[102] Another approach, the generalized gradient approximation (GGA), states that E_{xc} is not only dependent on the density, but also on its gradient. Expressions for the exchange term were provided by Becke in 1988 (B88),[103] while the work of Lee, Yang and Parr (LYP)[104] resulted in an expression for the correlation part. The obtained BLYP density functional method was later expanded to include HF exchange terms, which resulted in the ubiquitous B3LYP hybrid functional.[105]

3.3.2. The CBS-QB3 Method

Composite methods combine results of multiple calculations with minimal computational expense to approximate the results of time-consuming, more complex methods. Among the composite methods are the *Gaussian-n* methods[106] as well as the *Complete Basis Set* (CBS) methods,[107] which provide accurate results for thermochemical data. For computations the best result is achieved by an infinite basis set while simultaneously considering the correlation of all electrons. CBS methods try to converge on this limit by using a basis set extrapolation. Contributions to the overall energy of the system decrease with increasing order of perturbation theory, while their computational expense increases drastically. CBS methods exploit this issue, by reducing the basis set with each level of higher sophistication. The CBS-QB3 method uses geometry and frequency calculations on B3LYP/6-311G(2d,d,p) level as a basis and scales the zero point energy by a factor of 0.99. In addition single point calculations are performed on MP2/6-311+G (3d2f,2df,2p) level and corrected in second order by basis set extrapolation. To account for higher order correlation effects, terms from computations on MP4(SDQ)/6-31+G(d(f),p) and CCSD(T)/6-31+G(d') level are added as well. The calculated CBS-QB3 energy (equation 3.7) is corrected by an empirical term ΔE_{emp} and energy differences by spin contaminations (ΔE_{spin}) are considered as well.

$$\begin{aligned} E(CBS-QB3) = & E_{MP2} + \Delta E_{CBS} + \Delta E_{ZPE} + \Delta E_{MP4} + \Delta E_{CCSD(T)} \\ & + \Delta E_{spin} + \Delta E_{emp} \end{aligned} \tag{3.7}$$

Here, E_{MP2} represents the energy calculated on MP level, ΔE_{ZPE} is the scaled zero point enegry, ΔE_{CBS} originates from the extrapolation and ΔE_{MP4} is the energy difference between the MP4(SDQ)/6-31+G(d(f),p) level and the MP2 calculation using the same basis set. $\Delta E_{CCSD(T)}$ results from the analogous treatment of the MP4 and CCSD(T) calculations.

For the calculations of IEs the absolute CBS-QB3 energies at zero Kelvin of the neutral and the cation have to be subtracted. Experimental and theoretical values agree generally well with each other, with the exceptions of biradical systems. Since CBS-QB3 methods can only calculate the ground state of a molecule or ion any excited states with the same spin multiplicity that are visible in the spectrum cannot be calculated. It is also restricted to elements up to the third period. When molecules of higher periods are included, other methods and basis sets have to applied.

4. Results

The following chapter is separated in two main sections, divided by boron and non-boron containing compounds. In the first section, experiments involving photolysis on the CRF-PEPICO setup at the SwissLightSource are presented. First, the allyl radical and its methylated homologues and their pressure dependent kinetics with oxygen are investigated. The second part of the first chapter deals with the iodine monoxide radical and hypoiodous acid and their threshold photoelectron spectroscopy.
The second chapter is dedicated to boron containing molecules. Highly reactive boron compounds were investigated using the hydrogen abstraction of diborane at the french national synchrotron facility SOLEIL. Subsequently, the threshold photoelectron spectroscopy of borazine and trimethylborane and their respective pyrolysis products is detailed. The chapter will be concluded by a summary of various miscellaneous projects.

4.1. Photolysis and Kinetics

4.1.1. Kinetics of the Allyl Radical with Oxygen

4.1.1.1. Motivation and Background

The allyl radical is the smallest representative of resonance stabilization and therefore a model for many, more complex, compounds.[108] The ability to delocalize an unpaired electron over its multiple carbon atoms is intimately linked with its inherent stability relative to other non-stabilized congeners like alkyl radicals. Relative to those, allylic radicals exhibit alternating reaction pathways and an increased abundance in various environments,[109] which is the main motivation to investigate them. In the gas-phase they are detected in fuel-rich flames of different hydrocarbon precursors like 1-hexene, propyne, as well as allene and were found to play a crucial role in the formation of benzene.[110] The reaction between different C_3 radicals like propargyl and allyl is considered to be key step in the creation of polycyclic aromatic hydrocarbons (PAHs).[47,111–114] While the understanding of larger PAHs and their exact formation is incomplete, it is widely accepted that they represent molecular precursors of soot particles, a major concern for human health in modern societies.[115,116] Since PAHs are also found in carbon-rich stars[117] and other interstellar media[118] it can be deduced that the allylic radicals have contributed in some form to their formation in space. Allylic systems also play a role in the autoxidation of unsaturated fatty acids and esters, a mechanism leading to rancidity of fats.[119]

In the lab allyl radicals are usually generated by pyrolysis and photolysis of allyl halide precursors as well as in chemical reactors by H-atom abstraction of propene. Because of its aforementioned model character the allyl radical has been investigated by numerous spectroscopic methods, focusing on the structure and unimolecular reactions.[120,121] In detail, measurements of the ionization energy,[122] excited state lifetimes and couplings,[123] unimolecular reaction rates and reaction energetics[124,125] were performed. However, to understand the implications of allyl in PAH formation in particular under combustion conditions, bimolecular reaction rates have to be known. At these elevated temperatures and pressures two main branches determine their fate, the dimerization and the oxidation. The first leads to the formation of PAHs and has to be suppressed as much as possible, while the second ultimately produces carbon dioxide and water, the desired products of a complete combustion. Therefore, rate constants of the allyl dimerization were determined by multiple groups at various conditions.[126–129] On the other hand, reaction (11) has also been the focus of several experimental and theoretical studies.[130–136]

$$\text{a-C}_3\text{H}_5 + \text{O}_2 \underset{\text{k}_{-11}}{\overset{\text{k}_{11}}{\rightleftharpoons}} \text{a-C}_3\text{H}_5\text{O}_2 \qquad \Delta_R H^0 = -75.6\,kJ\ mol^{-1} \qquad (11)$$

With a reaction enthalpy at around 76 kJ mol^{-1} it is significantly less exothermic than for similar alkyl radical systems. The latter range at around 145 kJ mol^{-1}.[133] The reason for this major difference is a loss of resonance stabilization after O_2 addition, resulting in a relatively unstable allyl peroxy radical. The reverse reaction of (11) exhibits only a small barrier, while exit channels to secondary reaction products have to go through energetically unfavorable transition states.[130] In fact the elimination of HO_2 from the allyl peroxy radical has an activation energy of around 153 kJ mol^{-1} and isomerizations via H-shifts were calculated to be 121 kJ mol^{-1} or 159 kJ mol^{-1} for the (1,4) and (2,4) H-shifts, respectively.[130] With these high barriers the fate of the allyl peroxy radical is mainly determined by the loss of O_2, which becomes more important with higher temperature. The actual rate constant for reaction (11) is therefore decreasing when temperatures increase, resulting in no detectable product formation above 573 K.[131]

Recently Rissanen *et al.* studied the allyl + O_2 reaction over a wide pressure and temperature range.[137] They photolyzed allyl bromide at 193 nm and followed the allyl signal decay over time by photoionization mass-spectrometry. At lower temperatures up to 298 K they measured the respective rate constant of reaction (11) while between 320 K and 420 K they determined the equilibrium constant. It is worth noting that they did not observe a product signal from allyl peroxy, the presumed reaction product in the experiments, but suggested that their ionization technique is not mild enough.[137] Synchrotron based experiments offer a high photon flux and tuneability, which is perfectly suited to expand the investigation of reaction (11). They have previously been used to detect transient species in trace concentrations and are able to detect molecules with isomer selectivity based on their IE and vibrational fingerprint in the cation.[36,138–140] Photoionization mass spectrometry (PIMS) coupled to a slow flow reactor is regarded as the current gold standard for the study of chemical kinetics. A similar experiment has already been used by Osborn, Taatjes and coworkers,[141–143] who also investigated the allyl self reaction.[144]

4.1.1.2. Experimental

Experiments were performed on the photolysis setup at the VUV-beamline at the SLS described in section 3.2.3. Allyl radicals were generated directly by photolysis of allyl iodide and indirectly by H-atom abstraction of propene. In scheme 4.1 (A) allyl iodide (AI) was excited using either a 266 nm or 213 nm photon from the 4^{th} or 5^{th} harmonic of a Nd:YAG laser with a photon flux of $\approx$150 mJ cm^{-1} and $\approx$30 mJ cm^{-1}, respectively. Both photons lead to an electronic transition into the σ^* orbital of the carbon-iodine bond, decreasing the bond order and cleaving it directly. The H-atom abstraction was performed by generating chlorine atoms from oxalyl chloride $(COCl)_2$. After initiation by a 266 nm laser pulse one oxalyl chloride molecule ultimately forms two chlorine atoms and two inert carbon monoxide molecules. The chlorine atoms can then abstract a hydrogen atom from propene, generating allyl radicals. Vapors of the precursors and reactants were introduced into the reactor by calibrated MFCs. Their amount was determined by a combination of the individual gas flows and the respective vapor pressure of the precursor using the ideal gas law. For AI the vapor pressure was assumed at 51 mbar, while for oxalyl chloride it was 200 mbar. This resulted in total concentrations of 0.5% AI in scheme 4.1 (A) and 9% oxalyl chloride in scheme 4.1 (B) with 1% propene. At these concentrations the decay of the allyl radical decay did not depend on the precursor concentrations. The pressure in the reactor p_R was limited to a few mbar, based on the pressure in the ionization chamber, which had to be kept below 7×10^{-7} mbar. The photon energy was calibrated on the Ar 11s'-14s' autoionization lines in first and second order of the monochromator grating. Higher harmonics were filtered by a MgF_2 window or rare gas filters. The resulting ions and electrons were accelerated by a constant 125 V cm^{-1} extraction field in opposite directions onto position sensitive detectors. For the ms-TPES the VUV-photon energy was scanned between 8.0-8.5 eV and threshold electrons were collected with a 5 meV stepsize. The kinetic traces of allyl were obtained by plotting the signal of mass channel 41 as a function of reaction time relative to the laser trigger signal. The data were averaged for 13-90 minutes at a photon energy of 9.0 eV. The traces were analyzed using the CHEMKIN-II package[145] and the SENKIN routine.[146] For sensitivity analysis, the sensitivity coefficient $\sigma(i,j,t)$ for reaction i of species j at time t was normalized with respect to the maximum concentration c_{max} of the species j over the time history, resulting in $\sigma(i,j,t) = 1/c_{max} \cdot (\partial c(i,t)/\partial ln\, k_i)$. The time resolution of the experiment is determined by the time the molecules need to exit the flow tube and get ionized by the synchrotron light. It was accounted for by convoluting the concentration-time profiles with a Maxwell-Boltzmann function with 1 ms FWHM. Rate constants were optimized by a least-squares fit routine, with the rate constant value of reaction (11) being used a fit parameter.

Sources for errors can be summarized as follows. The gases were introduced by calibrated MFCs, which are correct within ±1% for pure gases like oxygen, argon and propene. Errors for saturated vapors like AI and oxalyl chloride are estimated to be slightly higher. The allyl radical concentration was determined indirectly based on the conversion efficiency of allyl iodide, which was accurate within up to 10%. These errors only have a minor influence on the rate constant of reaction (11), since oxygen is always used in large excess. The 2σ errors of the linear fit are within a few percent. External factors like reactor pressure and temperature provide more important sources for errors. The reactor pressure p_R was accurate within ±0.1 mbar, which leads to an error of ±19% at 0.8 mbar and 3% at 3.0 mbar. The temperature inside the reactor was assumed to be 298 K, which might be erroneous due to the energy deposited into the gas mixture being not be equally distributed. It can therefore deviate from RT, which causes reaction (11) to be slower since it exhibits a negative temperature dependence. Through the combination of all error sources the determined rate constants are estimated to be accurate within 25%.

4.1.1.3. Results

Starting with scheme 4.1 (A) allyl iodide was photolyzed at two different wavelengths (I) 266 nm and (II) 213 nm. In a first step a kinetic trace of the precursor was recorded to determine its depletion after every laser shot, as depicted in figure 4.1. The photolysis laser cleaves the C-I-bond of a specific amount of precursor molecules and after some time the signal recovers back to normal levels when new, unphotolyzed, gas flows through the reactor. A photolysis efficiency in scheme A (II) was derived, which estimated 5% of the precursor being photolyzed each time. With the measured cross sections of 16 Mb at 213 nm and 1.6 or 2.3 Mb at 266 nm for allyl iodide, the conversion was determined to be 0.5% for A (I).

With the photolysis laser present the recorded coincidence time-of-flight mass spectrum at 9.00 eV illustrated in figure 4.2 exhibits two main signals. At m/z 168 the precursor allyl iodide and at m/z 41 the allyl radical, both are visible. With the IE of allyl iodide being 9.30 eV the precursor

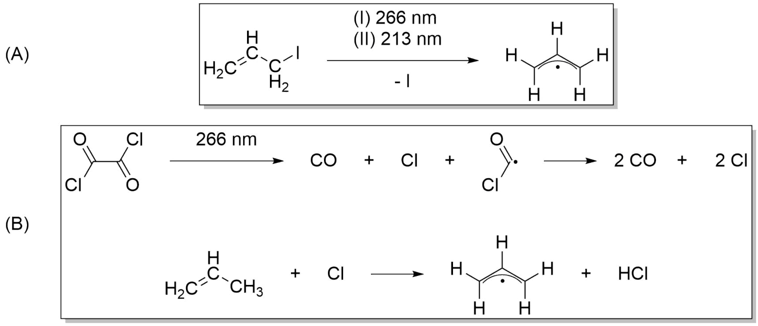

Scheme 4.1.: Generation of allyl radicals by (A) photolysis of allyl iodide and (B) H-atom abstraction by chlorine atoms.

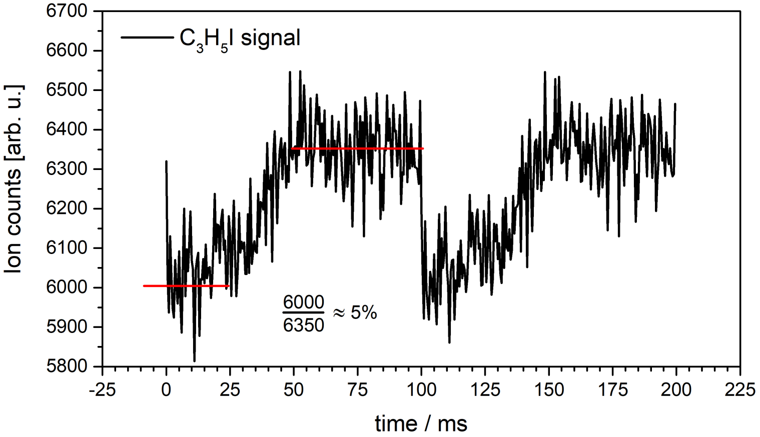

Figure 4.1.: Conversion efficiency of allyl iodide after excitation with 213 nm. The conversion of the precursor was determined to be 5%. The laser shots occur every 100 ms.

molecules can only get ionized by residual light of higher harmonic radiation or if they are vibrationally excited. Secondary processes like DPI can also contribute to the background signal of *m/z* 41 and have to be reduced as much as possible. The AE of the allyl cation from allyl iodide is 9.80 eV, which limits the background free detection to lower photon energies. Next to the precursor and the generated radical, iodine atoms were detected at photon energies of 10.50 eV and higher. Other secondary products, like 1,5-hexadiene and I_2 were observed above 9.5 eV, but with very low signal intensity, preventing the recording of a TPES. In the experiments where O_2 was added the direct reaction product, the allyl peroxy radical, could not be detected. While it could be detected using UV/VIS and IR spectroscopy,[136,147] all studies that ionized the reaction mixture failed to find any product signal. Calculations on the allyl peroxy cation reveal an IE of 8.89 eV with a triplet ground state exhibiting a drastically elongated C-O bond. The calculated binding energy of the O_2 fragment is only 60 meV and the FC-factors for transitions into the triplet ground state are small, because of the huge geometry change between neutral and cationic species. These effects can be explained in two ways: Firstly, ionization occurs from

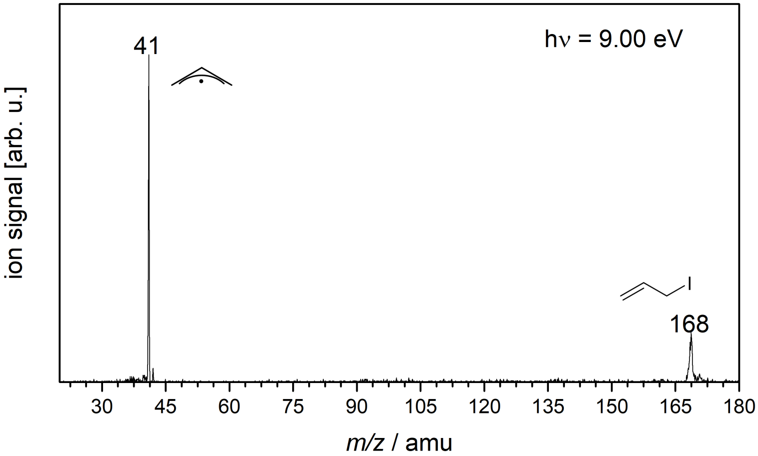

Figure 4.2.: Time-of-flight mass spectrum of allyl iodide photolysis at 266 nm recorded at 9.0 eV with the photolysis laser present.

the HOMO-1, a bonding orbital with its highest density in between the C-O bond, resulting in a reduced bond order in the cation and a loosely bound O_2 fragment. Secondly, the allyl cation exhibits a large resonance stabilization, which explains the low binding energy. As a result detection of the allyl peroxy radical by ionization is hardly possible. Other isomers of $C_3H_5O_2$ are presumably more stable but cannot be formed from allyl.
Although side products could only be detected in minor amounts, their reactions influence the decay of the allyl signal over time. As such, a typical decay profile for allyl without oxygen is displayed in figure 4.3 a) as red dots. These side reactions have to be quantified by recording kinetic traces without oxygen first, which allows an accurate determination of the rate constant for reaction (11). Table 4.1 presents the background reactions used to model the decay of allyl radicals without oxygen. The rate constants for reactions (12), (13), and (15) have already been established in the literature. The dimerization of two allyl radicals to form 1,6-hexadiene was investigated by Selby *et al.* between 1-6 Torr at RT.[144] The value was therefore taken without any corrections, even though one should note the

Table 4.1.: Background reactions considered in the decay of the allyl radical in scheme 4.1(A). All rate constants are given in $cm^3 mol^{-1} s^{-1}$ unless noted otherwise.

Reaction	No.	Rate constant k	Ref.
$2\,a\text{-}C_3H_5 \longrightarrow C_6H_{10}$	(12)	1.63×10^{13}	Selby *et al.*[144]
$a\text{-}C_3H_5 + I \longrightarrow C_3H_5I$	(13)	1.0×10^{14}	Jenkin *et al.*[136]
$a\text{-}C_3H_5 \longrightarrow \text{wall}$	(14)	9 (a)(c) 20 (b)(c)	This work
$I + I + M \longrightarrow I_2 + M$	(15)	2.96×10^{15} (d)	Baulch *et al.*[148]

(a) Scheme (I)
(b) Scheme (II)
(c) s^{-1}
(d) $cm^6 mol^{-2} s^{-1}$

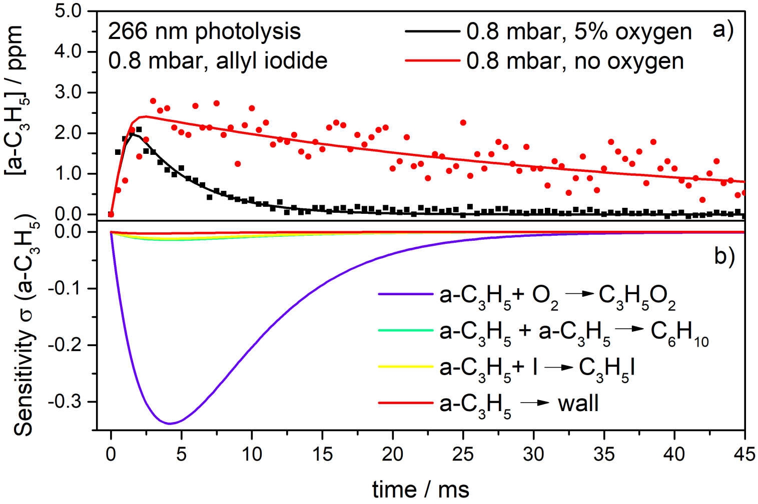

Figure 4.3.: a) Model kinetic trace for the allyl radical signal. Symbols represent experimental data points, and lines depict the numerical simulation. The rise in the beginning was accounted for by convolution with a response function. The sensitivity analysis for an experiment with 5% oxygen is presented in b) and illustrates the influence of the four most relevant reactions on the allyl signal, indicating only a minor importance of the background mechanism.

difference in the type of bath gas, which may influence the rate constant. The reported value for reaction (13) is 9.6 $\times 10^{13}\, cm^3 mol^{-1} s^{-1}$ by Jenkin *et al.* with similar values being obtained by Selby *et al.* between allyl and bromide atoms.[144] The used value of 1.0 $\times 10^{14}\, cm^3 mol^{-1} s^{-1}$ is in agreement with ref[136]. The dimerization of iodine atoms to I_2 (reaction (15)) was included due to its feedback effect on the recombination reaction (13). While all of these reactions represent major channels, radical chemistry often involves multiple minor pathways, due to their mostly barrierless nature. These reactions are summarized under the term *wall losses* originating from the main contribution by heterogeneous loss of the radicals in collisions with the reactor walls. Minimizing these reactions is often done by coating the inside of a reactor, which makes it dependent on several experimental parameters, like the ratio of wall surface area to gas volume, i.e. inner reactor diameter and coating quality. Thus, during the fitting routine the wall loss rate constant was used as a free fit-parameter which was optimized to fit the decay, wheras the literature known background reactions were not changed. In table 4.1 it can be seen that the rate for the wall losses was small and the other reactions described the decay well. However, for experiments with oxygen not only the forward reaction of (11) is added to the mechanism but since it is an equilibrium the reverse reaction (-11) can contribute to the allyl signal. Using thermodynamic data from the literature[137] it can be estimated that the rate of (-11) is between $0.25\,s^{-1}$ and $0.48\,s^{-1}$ at 0.8 mbar and 3 mbar, respectively. At these small rates the influence of (-11) can be neglected, in agreement with previous studies.[130,131,136] As soon as oxygen is added the decay of the allyl radicals gets faster, which indicates access to a new major reaction pathway as seen in the black trace in figure 4.3 a) for 5% oxygen. At longer reaction times the signal decays back to background level showing that allyl is completely consumed and secondary processes do not distort the allyl signal. The influence of reactions (11)-(14) on the allyl radical decay can be quantified by a sensitivity analysis, illustrated in figure 4.3 b). High numerical sensitivity values relate to a great influence of the chosen rate constant on the overall decay. As figure 4.3 a) already suggests, reaction (11) becomes the dominant pathway that influences the allyl radical decay, with the side reaction (12)-(14) becoming almost negligible. Possible deviations of the background rate constants given in table 4.1 have only a minor influence and the decay is determined by the chosen value for reaction (11).

The determination of bimolecular rate constants is usually done under pseudo-first-order conditions, thus in an excess of O_2. Changes in the concentration in the oxygen concentration over time can be neglected and it can be seen as constant during the experiment, resulting in pseudo-first-order rate constants like in equation 4.2a.

$$k^{2nd} = k \times [Allyl] \times [O_2] \tag{4.1}$$

$$k^{1st} = k' \times [Allyl] \tag{4.2a}$$

$$\text{with } k' = k \times [O_2] \tag{4.2b}$$

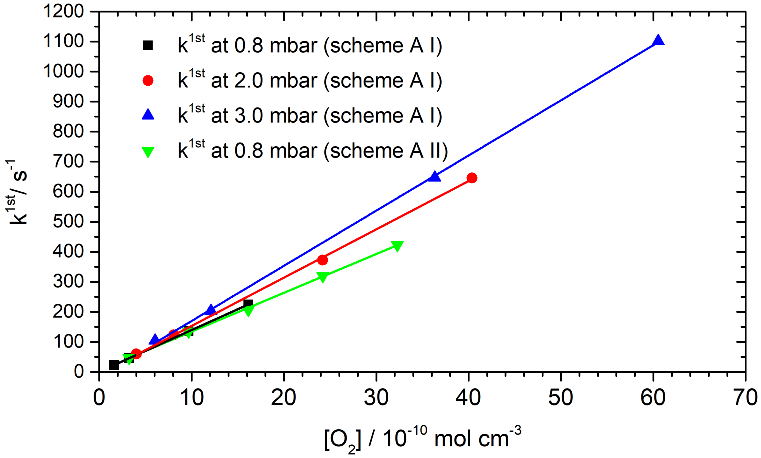

Figure 4.4.: Pseudo-first order plot of different allyl generation schemes for bath gas pressures of 0.8, 2.0 and 3.0 mbar.

Using this approximation, the pseudo-first order rate constants can be extracted from the kinetic traces using a exponential fit according to equation 2.24. The second order rate constants represents the slope of a linear plot of the pseudo-first order rate constants over different oxygen concentrations, with a y-axis offset of zero, as depicted in figure 4.4. It can be seen, that the pseudo-first-order rate constants are consistent with each other and show a small positive pressure dependence, which will be discussed later. For a reactor pressure p_R of 0.8 mbar and 266 nm photolysis wavelength the rate constant for reaction (11) is determined at $1.29 \pm 0.02 \times 10^{11}$ $\text{cm}^{\mathbf{3}}$ mol^{-1} s^{-1}. It is worth noting that CHEMKIN-II offers a way to directly yield second-order rate constants without having to determine the pseudo-first-order rate constants first. When these directly determined second-order rate constants are averaged the rate constant k_{11} would be $1.35 \pm 0.07 \times 10^{11}$ cm^3 mol^{-1} s^{-1}, which is in perfect agreement within error limits. The values of the determined second-order rate constants can be found in table 4.2.

Table 4.2.: Determined second-order rate constants for reaction (11).

Precursor	Pressure /mbar	Rate constant k_{11} /cm^{-3} mol^{-1} s^{-1}
C_3H_5I (266 nm)	0.8	1.35×10^{11}
C_3H_5I (213 nm)	0.8	1.40×10^{11}
	2.0	1.54×10^{11}
	3.0	1.75×10^{11}
$C_3H_6 + (COCl)_2$ (266 nm)	1.0	1.43×10^{11}

Allyl radicals can also be generated by H-atom abstraction according to scheme 4.1 (B). As a common photolytic precursor for chlorine atoms in kinetic experiments, the decomposition of oxalyl chloride has been investigated in great detail. Suits *et al.* found a two step mechanism after excitation at 235 nm[149] and 193 nm.[150] In a first, fast step the C-C bond breaks forming a chlorine atom, carbon monoxide and an excited COCl fragment. The latter can then dissociate in a slower process to form the second equivalents of chlorine and carbon monoxide.

The time scale on which the decomposition of COCl takes place depends on the excess energy carried by each radical, the temperature and pressure. A fourth parameter, the type of bath gas, influences the decay as well, though its quantification is not straightforward.[151,152]

Data by Gosh *et al.* proves that the dissociation of the intermediately formed COCl radical is dependent on the initially used photolysis wavelength.[153] In their experiments they saw evidence for COCl when photolyzing oxalyl chloride at 351 nm and 248 nm but none at 193 nm. They concluded that at higher photolysis energies the COCl fragment decays on a vibrational time scale, while at lower energies COCl lives longer and has the possibility to stabilize itself. Since their measurements provide a quantum yield (Φ) of 2 for the Cl atoms, COCl ultimately decomposes to form the second equivalents of Cl and CO. In line with these experiments Baklanov and Krasnoperov determined a Cl $\Phi = 2$ for $(COCl)_2$ dissociation at 193 nm.[154] The rate constants for this dissociation show a positive pressure and temperature dependence confirming that the lifetime of COCl is drastically reduced by increasing both parameters. Recently Huang *et al.* reinvestigated the chlorine formation and found a minor channel ($\Phi < 0.14$) that produces chlorine molecules right after excitation of oxalyl chloride.[155] The complex dissociation of oxalyl chloride and its influence on the kinetics has been widely neglected up to now. Within this thesis , the reported absorption cross section of 0.15 Mb at 270 nm by Gosh *et al.* was used.[153] Based on the absorption cross-section the Cl atom yield is estimated to be 15 times lower than that of allyl iodide. The conversion efficiency of oxalyl chloride to COCl, CO and Cl was therefore calculated to be 0.03% with $\Phi = 1$ and the subsequent thermal decomposition of COCl was taken into account in a separate background reaction (17), with a rate constant taken from Gosh *et al.*[153] The much more complex abstraction mechanism leads to multiple peaks in the time-of-flight mass spectrum at 9.0 eV, that have to be assigned to fully understand the kinetics inside of the reactor. Next to the dominant mass peak at m/z 41, masses 63 and 65 are major species at this photon energy. Both represent the COCl radical, 63 with ^{35}Cl and 65 with ^{37}Cl in a characteristic isotopic ratio of 3:1. Other, minor peaks, such as m/z 130 ($C_2O_2\,{}^{37}Cl_2$), 128 ($C_2O_2\,{}^{37}Cl\,{}^{35}Cl$), 126 ($C_2O_2\,{}^{35}Cl_2$), and 42 ($C_3H_6$) are not expected at this photon energy as their respective IEs

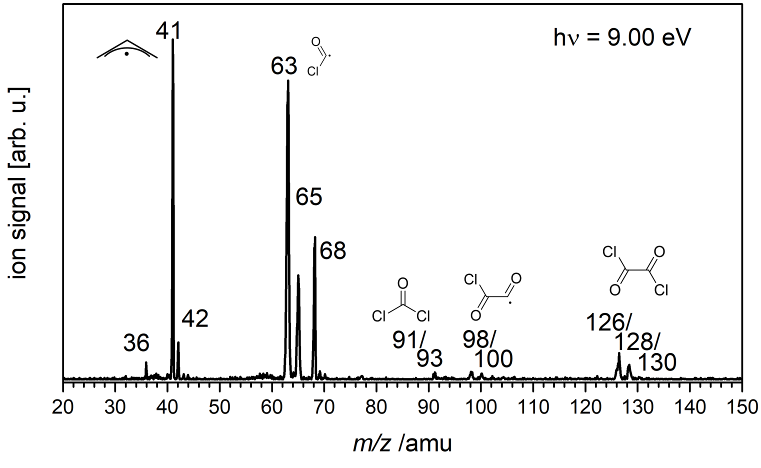

Figure 4.5.: Mass spectrum at 9.0 eV for the mixture of propene and oxalylchloride with the laser at 266 nm present. The reactor pressure p_R was set at 1.0 mbar.

are all above 9.5 eV. Similarly, m/z 36 can be attributed to $H^{35}Cl$ produced in the hydrogen abstraction of propene and with an ionization energy of 12.79 eV. Their presence can be explained by residual white light scattered by the gas filter as well as their high abundance in the reactor. Other direct photolysis products like $CO^{37}Cl_2$ (m/z = 102), $CO^{37}Cl^{35}Cl$ (m/z = 100), $CO^{35}Cl_2$ (m/z = 98), C_2O_2 ^{37}Cl (m/z = 93), C_2O_2 ^{35}Cl (m/z = 91) are also present in minor amounts. CO, Cl_2 and Cl have not been detected which is most likely due to their higher ionization energy and low abundance.

In addition the major peak at m/z 68 can not be attributed to any direct or indirect photolysis product. It exhibits no iostopic pattern and thus must consist of carbon, hydrogen and oxygen, as no other elements without major isotopes have been used in the experiment. It is therefore assigned to a C_4H_4O species, but the exact isomer cannot be extracted from the mass spectrum. Through the PEPICO setup and the possibility to record ms-TPES this issue can be resolved. In the ms-TPES of mass 68 a first peak at 8.41 eV representing the IE, can be seen as depicted in figure 4.6.

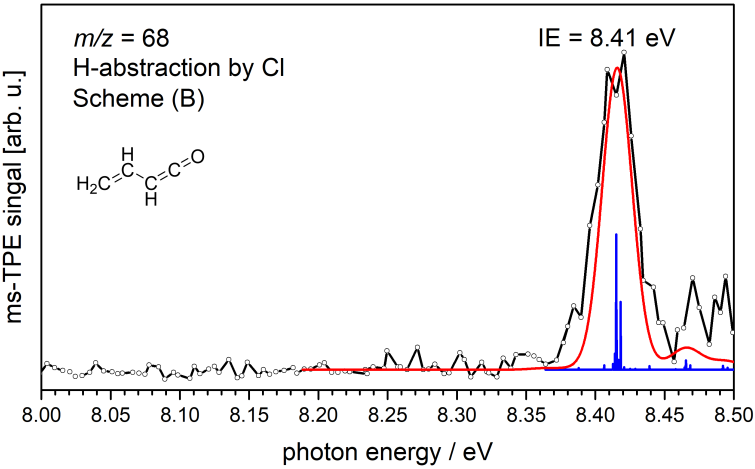

Figure 4.6.: ms-TPE spectrum of mass channel 68 between 8.00 and 8.50 eV. The simulation (red) and IE of 8.41 eV are in agreement with 1,3-butadienal.

With IEs being available for a number of C_4H_4O isomers, only the one for 1,3-butadienal fits well with the observed spectrum.[156] Furthermore, calculations on CBS-QB3 level of theory yield an computed IE of 8.41 eV and the FC-simulation fits well to the recorded spectrum. Its generation will be discussed later. As shown in figure 4.5 the abstraction of hydrogen atoms by chlorine works well. While the terminal methyl group is presumably the preferred abstraction site, in principle the three hydrogens located at the double bond can be cleaved off as well, forming two isomeric propylene radicals. As such, it is crucial to identify the generated molecules at $m/z = 41$ in this scheme using an isomer selective method. The IEs of the propylene radicals have been calculated to be 7.46 eV for the terminal and 7.65 eV for the central radical. A comparison between the ms-TPE spectrum of scheme (A) and (B) for the allyl mass channel is shown in figure 4.7, with the first peak being visible at 8.13 eV representing the IE of the observed molecule. Since no mass 41 signal was observed below this energy this channel can be exclusively attributed to the allyl radical, based on comparisons to the literature known IE_{ad} of allyl at 8.1309 eV.[122] A vibrational progression with spacings of 55 meV is visible and is assigned to the CCC bending mode ν_7^+ in the allyl cation. The multitude of identified species and the much more complex allyl generation, in conjunction with the convoluted multi-step photolysis of oxalyl chloride, requires several background reactions to be considered in the scheme. Since allyl radicals are not instantly produced, multiple reactions involving chlorine influence the generation indirectly, like the decomposition of the transient COCl radical (17), the recombination of chlorine atoms to Cl_2 (18) or their reaction with unphotolyzed oxalyl chloride.

$$\text{Cl} + (\text{COCl})_2 \longrightarrow \text{Cl}_2 + (\text{CO})_2\text{Cl} \tag{23}$$

The precursor for allyl radicals is propene, an unsaturated hydrocarbon on which chlorine atoms can also add to rather than cleave off a hydrogen atom. The two competing channels (19) and (20) have been investigated by Kaiser and Wallington, with regards to their pressure dependent branching ratios over a pressure range of 0.4 mbar up to 933 mbar.[157] At 1 mbar the allyl producing channel (20) is about four times faster than the addition route, yet both pathways are sufficiently relevant under our experimental conditions to be included in the reaction mechanism.

Allyl radicals can be consumed by dimerization (12), recombination with chlorine atoms or by reaction with hydrogen chloride. Other than the recombination reactions with bromine and iodine atoms, the rate constant for the chlorine pathway is not yet known. To account for these unknown allyl decomposition rates, they were integrated into a common loss reaction (21). While it is possible to include these reactions into the wall losses, the determined factor for the allyl iodide experiments originates almost exclusively from heterogeneous radical loss and was used without any changes. The above mentioned reactions are forming a background mechanism depicted in table 4.3, which was used to simulate the allyl concentration/time profiles for the oxalyl chloride/propene mixtures without oxygen. Other reactions like the formation of phosgene from COCl and Cl or the recombination of COCl were neglected due to their low significance for the allyl radicals. A typical kinetic trace is shown in figure 4.8 a), where dots represent experimental data points and lines are the result of the least square fit-routine using the respective mechanism with or without oxygen. As previously mentioned, one major species according to the mass spectrum is $m/z = 68$, which has been identified as 1,3-butadienal. The time trace of the mass channel shows that it is produced after the laser photolyzes the mixture inside the reactor as depicted in figure 4.9. It can be produced starting from propene by reaction with COCl or $COCl_2$, producing either

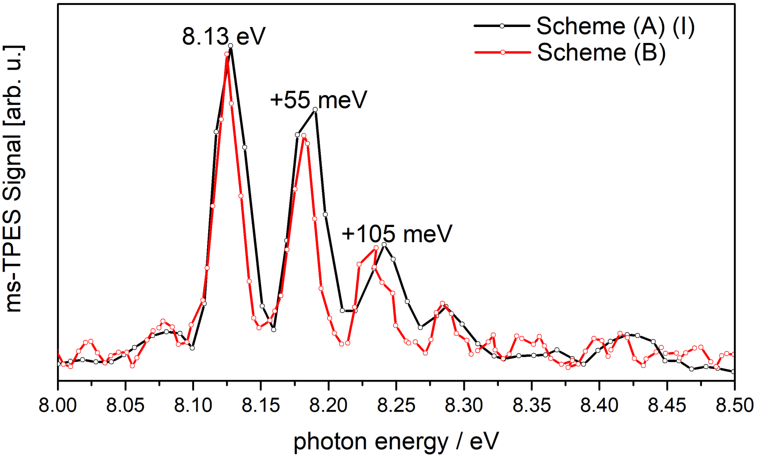

Figure 4.7.: ms-TPE spectrum of allyl using the photolysis of allyl iodide (black) and H-abstraction from propene (red).

hydrogen chloride and hydrogen atoms (24) or two equivalents of hydrogen chloride (25).

$$C_3H_6 + COCl \longrightarrow C_4H_4O + HCl + H \tag{24}$$

$$C_3H_6 + COCl_2 \longrightarrow C_4H_4O + 2\,HCl \tag{25}$$

These reactions have several drawbacks and will mostly likely not happen under the conditions of the experiment. Reaction (24) produces hydrogen atoms and thus it is forming thermodynamically unfavorable products

Table 4.3.: Background reactions considered in the decay of the allyl radical in scheme 4.1(B). All rate constants are in units of $cm^3mol^{-1}s^{-1}$ unless noted otherwise.

Reaction	No.	Rate constant k	Ref.
$2\,a\text{-}C_3H_5 \longrightarrow C_6H_{10}$		1.63×10^{13}	Selby *et al.*[144]
$a\text{-}C_3H_5 \longrightarrow wall$	(16)	20 (a)	This work
$COCl \longrightarrow CO + Cl$	(17)	1600 (a)	Ghosh *et al.*[153], extrapolated to 1 mbar
$Cl + Cl + M \longrightarrow Cl_2 + M$	(18)	4.6×10^{15} (b)	Baulch *et al.*[148]
$C_3H_6 + Cl \longrightarrow C_3H_6Cl$	(19)	5.12×10^{12}	Kaiser and Wallington[157]
$C_3H_6 + Cl \longrightarrow a\text{-}C_3H_5 + HCl$	(20)	2.23×10^{13}	Kaiser and Wallington[157]
$a\text{-}C_3H_5 + M \longrightarrow products + M$	(21)	1.3×10^{9}	This work
$O_2 + Cl + M \longrightarrow ClO_2 + M$	(22)	5.8×10^{14} (b)	Atkinson *et al.*[158]

(a) s^{-1}
(b) $cm^6mol^{-2}s^{-1}$

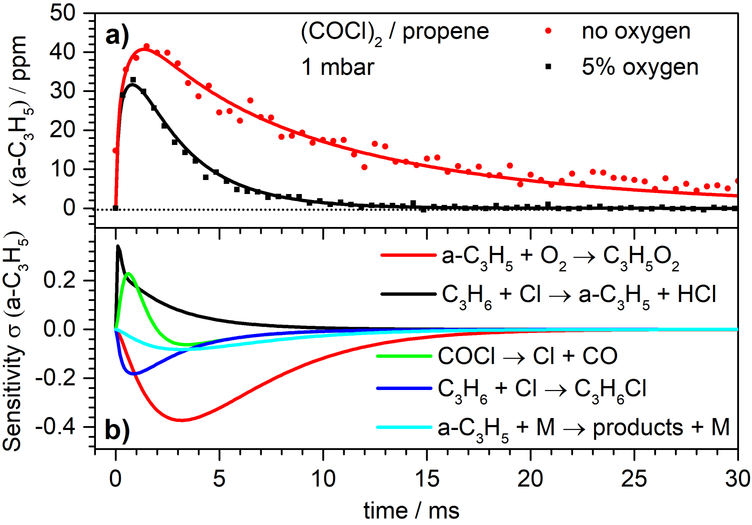

Figure 4.8.: a) Experimental time profiles of the allyl signal with (black) and without (red) oxygen using the H-atom abstraction of propene by chlorine atoms. Dots represent experimental data and solid lines are numerical simulations b) Sensitivity analysis of the hydrogen abstraction of propene by chlorine atoms with 5% oxygen added.

preventing their production in large quantities. One has to note that no thermodynamic data are available for 1,3-butadienal. Reaction (25) uses phosgene as starting material, which is only present in traces and can be excluded as the origin for the $m/z = 68$ peak.

The most promising route is a radical-radical reaction between the allyl radicals and the initially formed COCl. This reaction is almost barrierless based on the radical nature of both reactants, forming 1,3-butadienal under elimination of hydrogen chloride. Since the COCl molecule is vibrationally excited after photolysis it needs to be present sufficiently long time to react with the allyl radicals. With an estimated internal decomposition rate of

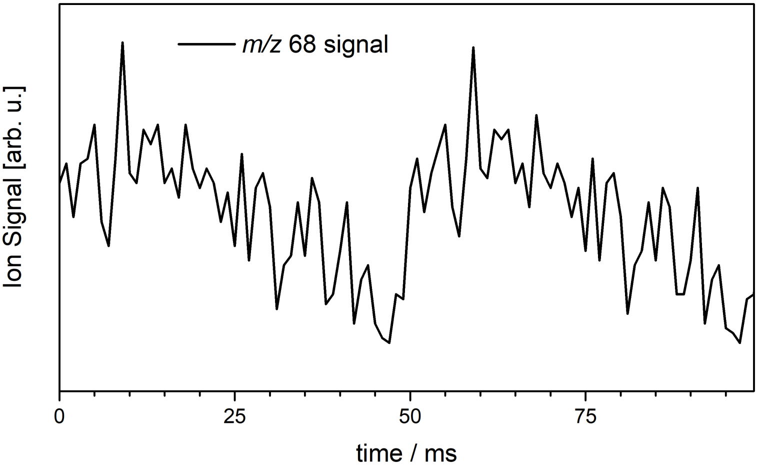

Figure 4.9.: Concentration/Time profile of mass channel 68.

$1600\,s^{-1}$ it has enough time to react and produce 1,3-butadienal according to reaction (26).

$$C_3H_5 + COCl \longrightarrow C_4H_4O + HCl \tag{26}$$

Even though reaction (26) is important to the background mechanism, its rate constant is not known and can not be considered directly. Indirectly it was accounted for by reaction (21) together with other relevant pathways. The above mentioned suitable kinetic model (see table 4.3) was used without correction in the experiments without oxygen, and the rate constant of (11) was adjusted in the least-square fit. A typical concentration-time profile is visible in figure 4.8 a), where dots represent the experimental data points and lines are the simulation. The literature known reaction (27) was also added, reflecting the fairly high oxygen concentrations in these experiments and account for the negative feedback this pathway could have on the chlorine concentration.

$$Cl + O_2 \longrightarrow ClO_2 \tag{27}$$

Figure 4.8 b) shows the sensitivity of the allyl radicals over time in an experiment with 5% oxygen present. Contrary to scheme 4.1 (A) various reactions influence the allyl decay in the first few milliseconds. After about 2 ms the main decomposition pathway is through reaction (11), highlighting it as the most important reaction at longer times. The rate constant for this scheme was determined to be 1.43 $\times 10^{13}$ cm^{3}mol^{-1}s^{-1} at 0.8 mbar.
In order to test the validity of the oxalyl chloride photolysis, and the influence compared to standard reaction schemes the analysis has been altered two more times. First by not separating the $(COCl)_2$ decomposition in two steps, and instead using a quantum yield of 2 for chlorine atoms. Secondly, the chlorine concentration can be deduced from the signal intensity of the allyl signal in the MS. Instead of assuming the conversion efficiency based on the relative cross sections of allyl iodide and oxalyl chloride, the factor to convert the MS counts in concentration from the allyl iodide experiments was used without correction. This required to double the chlorine concentration to simulate the kinetic traces. Both methods essentially yielded the same rate constants of 1.40 and 1.44 $\times 10^{13}$ cm^{3}mol^{-1}s^{-1}, respectively.

4.1.1.4. Discussion

The rate constants for reaction (11) were measured at four different reactor pressures p_R 0.8, 1.0, 2.0, and 3.0 mbar and the determined rate constants are displayed in figure 4.10 and summarized in table 4.2. Even with using different generation schemes the rate constants are highly consistent, although the preferred scheme should be the photolysis of allyl iodide at 213 nm as it is the simplest and least time consuming method. The hydrogen abstraction scheme is much more complex in its modeling of the results and experimental setup, nonetheless it offers the possibility to access radicals where no suitable direct precursor is available. The reaction of allyl radicals with oxygen initially produces an activated complex between the two reactants. In a next step this activated complex can either react to the products through collisional activation by the bath gas or transfer energy to the bath gas by collisions and reform the reactants. Reaction (11) is therefore a pressure dependent association reaction, underlined by the increasing second order rate constants displayed in figure 4.10.

$$\text{a-}C_3H_5 + O_2 + (M) \rightleftharpoons \text{a-}C_3H_5O_2 + (M) \qquad (28)$$

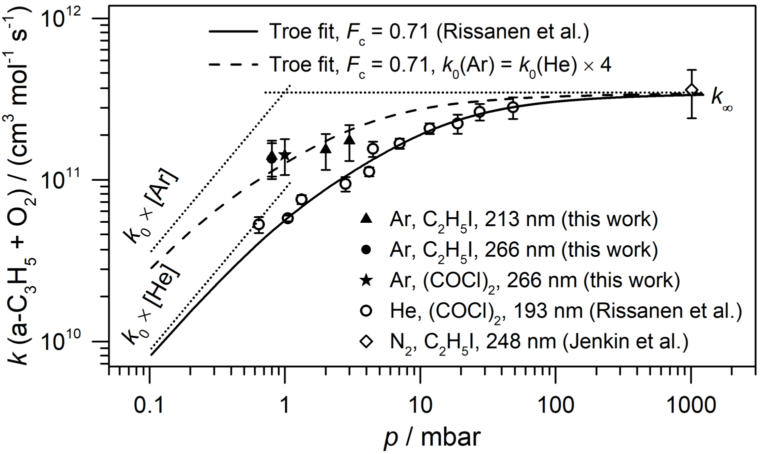

Figure 4.10.: Pressure dependent second-order rate constants of reaction (11) in the falloff region. The data are compared to the literature values by Jenkin *et al.*[136] and Rissanen *et al.*[137] (open symbols). The solid and dashed lines represent the Troe fit of the falloff behavior, using the dotted lines for high and low pressure limiting rate constants k_∞ and k_0. Errors correspond to the 2σ standard error for the Rissanen data, while the total estimated error is used for Jenkin *et al.* and this study.

Lee and Bozelli, studied reaction (11) at density functional level of theory as well as through CBSQ//B3LYP/6-31G(d,p) composite calculations and found that the association with oxygen dominates the fate of the allyl radicals at room temperature.[130] Further reactions of the peroxy radical species like H-atom shifts and cyclizations have to surmount high barriers of at least 59 kJ mol^{-1} with respect to the entrance level and are not accessible at room temperature. With increasing temperature the peroxy radical exhibits a propensity to dissociate back to the reactants, due to the relatively loosely bound (84 kJ mol^{-1}) oxygen fragment. The reverse reaction of (11) becomes more important until an equilibrium is reached, which has been observed by Walker *et al.*[135] as well as by Rissanen *et al.*[137]

The latter have investigated the reaction of allyl and oxygen over a broad temperature and pressure range and their room temperature data can be found in figure 4.10 as open circles. At very high pressures a single data point measured by Jenkin *et al.* is added in order to determine the rate constant in the limiting case of infinite pressure. The solid line represents the Troe-Fit by Rissanen *et al.* and their determined high-pressure rate constant is consistent with the atmospheric value of Jenkin *et al.* It is visible that the rate constants by Rissanen *et al.* is about a factor of 2 - 3 slower than the values determined in this study. In order to fit the rate constants consistently, using the same broadening factor ($F_c = 0.71$) and k_∞ value, the k_0 value for helium has to be multiplied by four. The broadening factor has been derived from a large data set by Rissanen *et al.* and since F_c is not dependent on the bath gas molecules taking the same value is in the best interest to compare helium and argon. One reason for this behavior could be the difference in the nature of bath gas. While the experiments in this thesis used argon, Rissanen *et al.* have used helium, and simply attributing the discrepancy of the studies to a higher collision efficiency is tempting. One can estimate the influence of the bath gas through two factors; the collision efficiency β_c and the Lennard-Jones collision frequency Z_{LJ} as depicted in equation 4.3. An increase of the energy transfer rate by a factor 2 - 3[159–161] leads to in increase in the collision efficiency of 1.3 to 1.5 based on equation 4.4. The estimation of Z_{LJ} can be done by looking at the tabulated values for the Lennard-Jones collision diameter σ_{LJ} and the Lennard-Jones well depth ε/k_B, which results in a ratio of $\mathrm{Z}_{LJ}(\mathrm{Ar})/\mathrm{Z}_{LJ}(\mathrm{He}) \approx 0.7$. Together with the value for β_c the influence of the bath gas on the rate constants can be quantified to be not more than 10 to 30%. These approximations also hold true if oxygen is added as well as in the propene and oxalyl chloride case. Oxygen has a very similar collision frequency Z_{LJ} relative to argon, and the rate constants for the propene experiments are consistent with the allyl iodide values, excluding large differences in β_c and Z_{LJ} in these experiments.

$$\frac{k_0(Ar)}{k_0(He)} = \frac{\beta_c(Ar)Z_{LJ}(Ar)}{\beta_c(He)Z_{LJ}(He)} \tag{4.3}$$

$$\beta_c/(1-\beta_c^{0.5}) \propto \langle \Delta E \rangle \tag{4.4}$$

$$\frac{k_0(Ar)}{k_0(He)} \approx 1.1 - 1.3 \tag{4.5}$$

Thus, there have to be other sources of this systematic difference in the studies, which most likely originate from unsolved experimental differences. One of these factors could be the Maxwell-Boltzmann function used as an instrument response function (IRF). Especially at high oxygen concentrations where the decay of allyl is finished within the first few milliseconds this function can become essential for the rate constants. Rissanen *et al.* neither fitted their data using an IRF nor did they explicitly consider individual background reactions and only summarized all available background reactions to a simple pseudo-first-order wall loss reaction. These assumptions, although commonly made, might not accurately reflect reality and therefore their analysis is less than ideal. However, the theoretical descriptions of the falloff behavior is far from complete. In the end, there are several differences in the parameters of the two studies that make it difficult to give a final conclusion, whose data points are more robust.

4.1.1.5. Conclusion and Summary

The kinetics of the reaction between allyl radicals and oxygen has been studied at the newly developed CRF-PEPICO apparatus at the VUV-beamline at the SLS. Allyl radicals were generated using two different generation schemes at 266 nm and 213 nm respectively. In the first scheme, allyl iodide was used as a precursor and in the second, a mixture of oxalyl chloride and propene served as a source for allyl radicals. Detection was provided by ionizing the radicals at a specific energy in a PEPICO scheme allowing to record kinetic traces and ms-TPE spectra at the same time. The concentration-time profiles were measured under pseudo-first order conditions and numerical simulations provided the second order rate constants. Photolyzing allyl iodide at 213 nm at 0.8 mbar resulted in a rate constant of $1.35\times10^{11}\,\mathrm{cm^3mol^{-1}s^{-1}}$ and very similar values were obtained for the other generation schemes. At higher pressures the rate constants showed a slight increase, in agreement with previous measurements and theoretical predictions. In the hydrogen-abstraction experiments, chlorine atoms created from oxalyl chloride were used to generate allyl radicals from propene. Although multiple abstraction sites are available, allyl was the only major product according to ms-TPE spectra. Another peak in the mass spectrum, which is exclusively present in this scheme could be identified as 1,3-butadienal formed by the reaction of the transiently present COCl with allyl radicals. Although modeling the kinetic traces is more complex using the hydrogen abstraction method, the obtained rate constants were consistent with the allyl iodide results. This prove-of-principle experiment underlines the possibility to measure radicals which have no suitable direct precursor, like the cyclopropyl radical which is known to isomerize upon direct photolysis of its halide precursors. In all cases the product of reaction (11) could not be detected. Unfavorable Franck-Condon factors, a propensity to dissociatively ionize, and a low binding energy for the oxygen fragment in the cation prevented the detection of the allyl peroxy radical. Comparing the determined rate constant values to the literature a small positive pressure dependence is found in both. However, the values in this study are 2 - 3 times higher than previously measured. This can be partly attributed to the difference in bath gas, but unresolved systematic differences, like the different treatment of side-reactions or the inclusion of an IRF can not be excluded. The falloff can be best described with the Troe parameters of $\mathrm{k}_0 = 2.2\times10^{18}\,\mathrm{cm}^6\mathrm{mol}^{-2}\mathrm{s}^{-1}$, $\mathrm{k}_\infty = 3.5\,\times10^{11}\,\mathrm{cm}^3\mathrm{mol}^{-1}\mathrm{s}^{-1}$, and $F_c = 0.71$.

4.1.2. Kinetics of the Methylallyl Radicals with Oxygen

4.1.2.1. Motivation and Background

The allyl radical received a considerable amount of attention over the last decades, due to its model character for spin delocalization (see section 4.1.1.1).[108] Its congeners, the C_4H_7 radicals like 1-methylallyl (1-MA), 2-methylallyl (2-MA) and cyclobutyl, have been relatively unnoticed and only recently attracted some interest. Based on their high structural analogies to the allyl radical, the methylallyl isomers have been found in similar environments. They are abundant in the interstellar medium[162] as well as in the combustion processes of isobutene and anti-knock additives like *tert*-butyl ethers.[163,164] Modern plant-based fuels can contain significant amounts of unsaturated fatty esters and branched hydrocarbons, which are prone to lose hydrogen atoms in α-position to the double bond forming intermediates that can be described as alkylated allyl radicals.[165] 1-MA and 2-MA can thus serve as suitable model compounds for the reactivity of sustainable, next-generation biofuels. The known spectroscopic properties for 1- and 2-MA are limited to excited state dynamics,[166] UV absorption and unimolecular decompositions.[167] Recently the IEs of both were investigated by ms-TPE spectoscopy, a central piece of information for this section.[168,169] The foundation to asess the reactivity of these radicals in different environments are bimolecular rate constants. In particular for

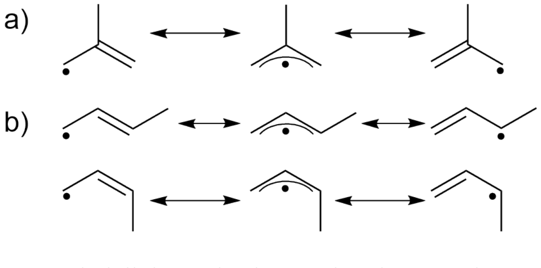

Figure 4.11.: Methylallyl radicals and their valence structures. a) 2-Methylallyl (2-MA) b) E-1-Methylallyl (E-1MA, upper trace) and Z-1-Methylallyl (Z-1MA, lower trace).

combustion processes the reaction between the 1- and 2-MA and oxygen is highly relevant and has hardly been investigated up to now.

$$\text{2-MA} + \text{O}_2 \rightleftharpoons \text{C}_4\text{H}_7\text{O}_2 \qquad \Delta_R H^0 = -90\,kJ\,mol^{-1} \tag{29}$$

$$\text{1-MA} + \text{O}_2 \rightleftharpoons \text{C}_4\text{H}_7\text{O}_2 \qquad \Delta_R H^0 = -82.6 \pm 5.3\,kJ\,mol^{-1} \tag{30}$$

The dimerization and dissociation rates for 2-MA have been reported at high temperatures in shock tubes[170,171] as well as in low temperature liquids,[172] but the rate constant of reaction (29) has only been estimated through canonical state theory.[173] For 1-MA, reaction (30) was investigated by Knyazev and Slagle over a broad pressure and temperature range.[174] They used crotyl bromide and generated 1-MA radicals through photolysis at 248 nm and 193 nm and detected them by photoionization with a bromide resonance lamp at 7.6-7.9 eV. They noted that 1-MA exhibits two chemically non-equivalent reactivitiy sites, a terminal and a non-terminal site, and attributed both an equal reactivity towards oxygen based on calculated spin density ratios of the two carbon atoms. However, the chemistry of 1-MA is more complex, as it exhibits two diastereomeric forms termed E-1MA and Z-1MA, depicted in figure 4.11, with a low barrier of isomerization calculated to be between 60-67 kJ mol^{-1}.[175] This prevents their separated generation and analysis, as they can freely interconvert between both forms. As such, methods that can distinguish signals from E-1MA and Z-1MA have to be employed in order to gain fundamental insight into their reactivity. Combining a PEPICO detection scheme with completely tunable synchrotron radiation allows the separation of the diasteroemeric forms by their IE and vibrational structure in the cation.[176] In the case of rate constants, contributions of one isomer can be isolated by choosing a photon energy below the IE of the respectively higher ionizing molecule. In principle it is also possible to investigate the latter, by utilizing the TPE signal to distinguish between both forms. In this scheme the photon energy from the synchrotron is chosen so that the higher ionizing isomer is resonantly ionized. The kinetic trace can then be extracted by selecting the threshold signal, and correcting it for statistical contributions of hot electrons. Several natural requirements have to be met that facilitate the measurement in this case. The ms-TPE signal of both isomers have to be energetically separated so that it can be attributed to one form rather than a mixture. Consequently, the higher ionizing molecule has to have at least one transition with favorable Franck-Condon factors, through which the signal to noise ratio can be increased.

4.1.2.2. Experimental

Methylallyl radicals were generated by photolyzing the respective halide precursors, 2-methylallyl iodide (2-MAI) or crotyl bromide (C_4H_7Br), using the 5^{th} harmonic of a Nd:YAG laser at 213 nm. The chemicals were purchased from Sigma-Aldrich and used without further purification. 2-MAI is available in a purity of >97%, while crotyl bromide is only technical grade (85%). The main impurity of the latter is 3-bromo-1-butene, which also yields 1-MA radicals upon photolysis. The pure gases like helium and oxygen were introduced into a mixing chamber by calibrated MFCs, which are correct within ±1%. The precursor was seeded in helium by flowing the gas through the respective liquid inside a glass sample container, which increased the error of the MFC calibrated on helium, to 1.5% based on the precursor enriched vapor. The final oxygen mole fraction was therfore accurate within 2%. Since the vapor pressures of the substances are not known, concentrations measurements were performed before the precursor gas stream entered the reactor via a gas-phase UV/Vis absorption setup using the Beer-Lambert law (see 3.2.3). The cross section for crotyl bromide ($390\,\mathrm{Lmol^{-1}cm^{-1}}$ at 230 nm) was taken from literature,[177] while 2-MAI was determined in liquid hexane under the assumption that the absorption in liquid hexane and the gas phase are identical. The latter method obtained a cross section of $720\,\mathrm{Lmol^{-1}cm^{-1}}$ at 270 nm. Overall the uncertainty for the concentrations is less than 10% for the 1-MA experiments but, most likely more for the 2-MA case. From the mixing chamber the gases can flow freely into the reactor, where the photolysis takes place. Radical concentrations in the reactor were estimated by the depletion of the precursor signal after each laser shot, similar to the allyl experiments (see figure 4.1). For 2-MAI a conversion of 5% was measured, while for crotyl bromide 4% 1-MA radicals were detected. Note, that all the above mentioned errors primarily influence the radical concentration, which under pseudo-first order conditions has only a minor influence on the rate constant. Increasing or decreasing radical concentrations by a factor of two, influences the rate constant only by 3%. To minimize radical losses inside the reactor, the tube was freshly coated with halocarbon wax prior to the experiments. The overall gas flow was set high enough so that each laser shot photolyzes a new precursor mixture to avoid radical accumulation, while keeping the reactor pressure between 1.0-3.0±0.05 mbar. The photolysis laser propagates down the reactor tube creating a uniform distribution of radicals within the time scale of the first radical detection. The mixture was sampled into the experimental chamber by a 300 μm hole in the wall of the reactor. The effusive molecular beam crossed the VUV light at a distance of 21±4 mm and a constant abstraction field of 218 V cm^{-1} accelerated the charged particles in opposite directions onto position sensitive detectors. For the ms-TPE measurements the photon energy between 7.3-8.0 eV and 7.7-8.6 eV for 2- and 1-MA respectively, with an energy resolution of 10 meV. Kinetic traces were obtained by plotting the coincidence intensities of one mass channel with respect to the laser trigger signal. In case of the 2-MA experiments laser shots were averaged for 120 minutes and the photon energy was set to 8.5 eV. For 1-MA each kinetic trace was obtained by integrating over 120-360 minutes and different ionization energies were chosen. At 1.0 mbar and 2.0 mbar photon energies of 7.54 eV and 7.59 eV were chosen to record kinetic traces of E-1MA and Z-1MA respectively. At 3.0 mbar a photon energy of 8.0 eV was chosen to unselectively ionize the mixture of E- and Z-1MA. Wall losses were quantified by recording kinetic traces without oxygen at the beginning and end of each experiment. Different MA decays were obtained by varying the oxygen concentration over a range of one magnitude, while maintaining pseudo-first order conditions. Kinetic traces were analyzed using the CHEMKIN-II package[145] and the SENKIN routine,[146] as described in section 4.1.1.2. The time resolution was accounted for by convoluting the kinetic traces with a Maxwell-Boltzmann type instrument response function with a rise time $\tau_{90-10} = 1.4$ ms. For comparison, rate constants were also obtained without the use of a convolution function, from monoexponential decays and linear fit routines. This analysis obtained up to 27% slower rate constants, since the fit began directly at the laser trigger.

The determined rate constants are correct within ±20% and error sources are as follows:

Inaccuracies in the concentrations of the reactants ($\approx \pm 2\%$) or radicals ($\approx \pm 10\%$) are common and cannot be avoided within the setup. Their influence on the rate constant is however negligible ($\approx \pm 3\%$) while working under pseudo-first-order conditions. Ambient parameters like pressure and temperature influence the rate constant to a larger extent. The pressure was accurate within 0.05 mbar which introduces an error of ±7% to the rate constant. Due to the absence of any heating elements on the reactor room temperature was assumed for all reactions. However, energy deposited into the molecules through the laser can influence their temperature if equilibration is not achieved instantly within the time scale of the experiment. Recent experiments of methylperoxy radicals using the same setup determined a radical temperature of 330±30 K, so slightly above room temperature.[178] Deviations of up to 20 K resulted in errors of the rate constant of up to 6%. It is worth noting that the reaction between methylallyl radicals and oxygen has a negative temperature dependence, thus resulting in smaller rate constants with increasing temperature.

4.1.2.3. Results

In figure 4.12 the different coincidence time-of-flight mass spectra for the 2-MA radical are shown. The two major peaks visible are at mass 182 and 55, representing the precursor 2-MAI and 2-MA respectively. At 8.90 eV the precursor also shows first decay towards mass 55 by dissociative photoionization. The difference spectrum 4.12 c) shows that radical generation by photolysis dominates the mass channel 55 at this energy. In figure 4.12 a) and b) there is one smaller peak visible at mass 110 which can be at-

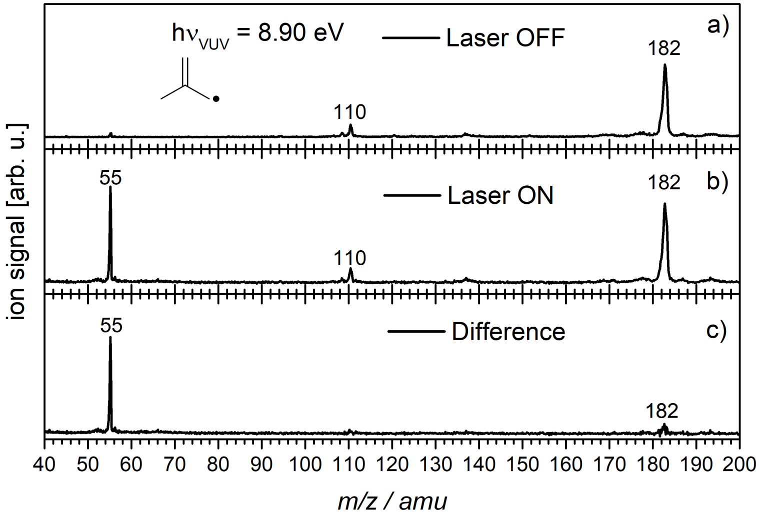

Figure 4.12.: Mass spectra recorded at 8.90 eV for the 2-MA experiments with a) laser off, b) laser on, and c) the difference between laser on and off.

tributed to the dimerization product of 2-MA. Since it is present when the laser is off it likely originates from decomposition of the precursor sample, which was indicated by an observed color change of the sample. Dimerization processes of two 2-MA radicals cannot be excluded but as the signal vanishes in the difference spectrum c) they do certainly not constitute a main reaction pathway. The mass 182 signal in figure 4.12 c) should be negative, since some of the precursor will be photolyzed when the laser is turned on. However, upon turning on the laser, a portion of the photons are deflected by the walls of the reactor and hit the inside the experimental chamber. At the used photon energy (213 nm) they can eject electrons from the metal surfaces, which can be accelerated by the electron optics and lead to a form of electron impact ionization of the gas mixture. This process creates a non-negligible background signal, which could be verified by closing the synchrotron light shutter without any effect on the background signal. So photolysis decomposes 5% of the precursor, which is convoluted with a higher background signal from secondary ionization processes, leading to a positive overall signal. In the experiments where oxygen was added the peroxy radical forming as the reaction product could not be observed via photoionization mass spectrometry. DFT calculations predict an ionization energy of 8.69 eV with a triplet ground state for the cation. The cationic structure exhibits a very long C-O bond (2.64 Å) with respect to the neutral (1.45 Å), resulting in unfavorable Franck-Condon factors as well as a low binding energy, similar to the allyl case. Hence, detection by photoionization is impeded by a combination of this large geometry change and low binding energies of the oxygen fragment between 75 - 85 $\mathrm{kJ\,mol^{-1}}$ in the cation.

The recorded photoionization time-of-flight mass spectrum for the 1-MA experiments is given in figure 4.13. Without the laser the precursor signals at mass 134 and 136 are dominant at 9.50 eV. Smaller peaks at 54 and 55 can be attributed to the onset of dissociative photoionization cleaving off HBr or Br, respectively. A small impurity occurring at mass 100 can not be explained by fragmentation or bimolecular reaction inside the sample, and is therefore attributed to an impurity originating from the experimental chamber. When the laser is turned on and photon energy is lowered to 8.50 eV, a single peak is visible with its $m/z = 55$ corresponding to the generated 1-MA radical. Neither the generated bromine atoms nor the precursor crotyl bromide get ionized at this photon energy and contributions from dissociative photoionization to the 1-MA signal can be excluded.

The recorded ms-TPE spectra of the produced radicals can provide insights

into the created isomers after photolysis of the precursors. The methylallyl spectra were previously measured under pyrolysis conditions and will be used to verify the identity of the isomers and compare the two generation methods.[168]
The ms-TPE spectrum displayed in figure 4.14 between 7.70 eV and 8.60 eV for 2-MA shows a generated species with an onset at 7.89 eV and a vibrational progression of 440 cm^{-1}. The first transition was assigned to the ionization energy into the cationic $X^+\ {}^1A_1$ ground state, which is in good agreement with the calculated value of 7.94 eV by CBS-QB3 composite calculations. The ms-TPES also agrees very well with previous experimental investigations, which found an IE of 7.88 eV with a vibrational progression of 440 cm^{-1}.[168] The vibrational peaks visible up to 8.05 eV could be attributed to the totally symmetric CCC bending vibration ν_{24}^{+} with a calculated vibrational frequency of 452 cm^{-1}. No other signals are observed up to 8.60 eV, showing that only the 2-MA isomer contributed to the recorded

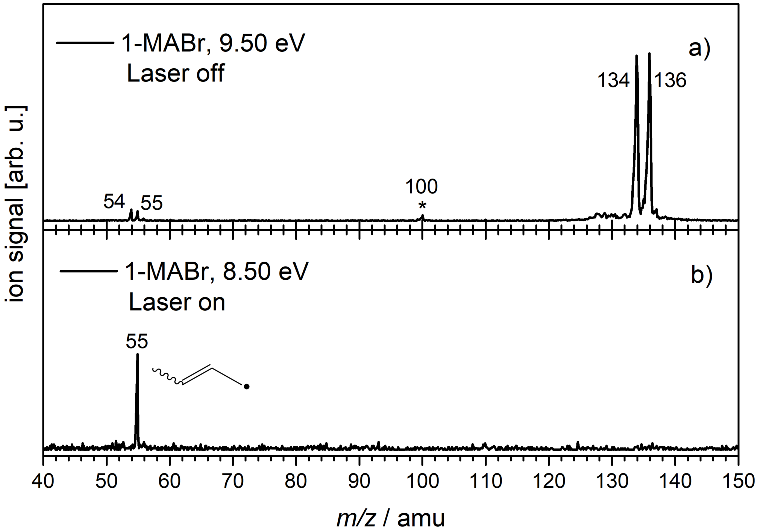

Figure 4.13.: Mass spectrum of the 1-MA experiments with a) the laser off and b) the laser on. Bromine atoms can not be detected due to their significantly higher ionization energy.

kinetic traces. The FC-simulation shows a very good agreement with the experimental data and the literature for the 2-MA radical.[168] The literature spectrum exhibits a pronounced hot band visible at 7.83 eV, which is less intense in the spectrum presented here. The primary reason for this are differences in radical generation, through which the radicals carry alternating amounts of internal energy. In the literature pyrolysis was used to generate 2-MA radicals at 450 °C, whereas in the photolysis reactor radicals can equilibrate by collisions with the bath gas before being ionized. Experimental factors, like differences in the setup or in the parameters, can influence temperature of the molecules as well. In the pyrolysis experiments the radicals have to pass a skimmer, which selects only coldest part of the molecular beam, while they are directly introduced into the experimental chamber from the photolysis reactor. This means that radicals produced in photolysis are thermally less excited than radicals in pyrolysis. In both cases cooling effects by supersonic beam expansion can be omitted in first instance, due to the small pressure differences in the respective reactors

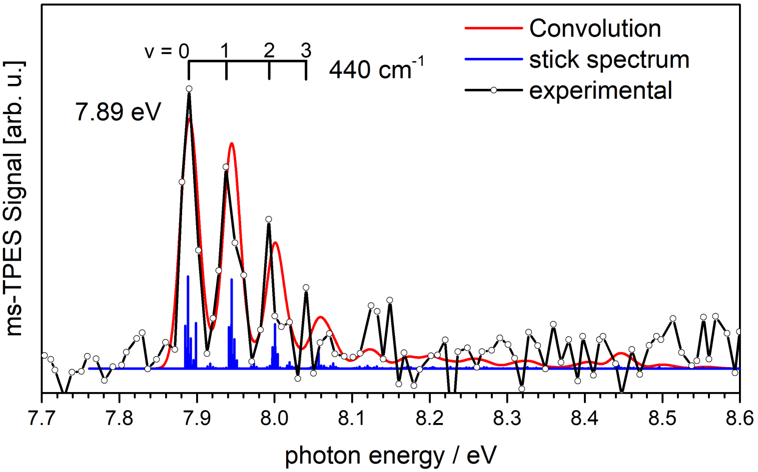

Figure 4.14.: Recorded ms-TPE spectrum of 2-MA between 7.70 eV and 8.6 eV. The radical was generated at 0.9 mbar through photolysis of 2-MAI at 213 nm. Every point was averaged for 390 s and the resolution is 10 meV.

and chambers. The comparison between these experiments showcase, that photolysis represents a softer approach to radical generation, with the possibility to limit secondary processes during the measurement.

The ms-TPES for 1-MA in figure 4.15 shows a more complex structure with multiple signals, which have been analyzed before.[168] The first major peak occurs at 7.48 eV and originates from E-1MA, agreeing with its calculated ionization energy of 7.54 eV. Transitions into two different vibrational modes of E-1MA can be seen, one being the CCC-bending mode ν_{25}^{+} (280 cm^{-1}, 35 meV) and the other the CC-stretching mode ν_{24}^{+} (565 cm^{-1}, 70 meV). The two peaks at 7.41 eV and 7.44 eV can be attributed to two hot bands from the same vibrations ν_{24}^{+} and ν_{25}^{+} respectively. At higher energies the second isomer Z-1MA is assigned to the peak at 7.59 eV in line with its computed ionization energy at 7.65 eV. It exhibits a vibrational progression originating from the CCCC bending mode ν_{23}^{+} (565 cm^{-1}, 70 meV) and the wagging mode of the terminal carbon atoms ν_{21}^{+}. Again a comparison between the previously recorded 1-MA TPES under pyrolytic conditions

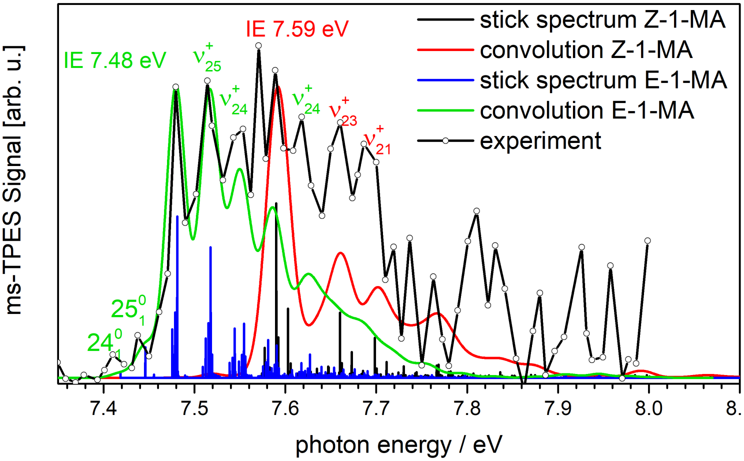

Figure 4.15.: The recorded ms-TPE spectrum of the 1-MA radical. Two isomers with two different ionization energies contribute the the experimental signal, the E-1MA starting at 7.48 eV and the Z-isomer at 7.59 eV.

reveals a better resolved and less broad spectrum in photolysis, mainly due to the lower temperature (*vide supra*). The ms-TPES proves that both conformers, E- and Z-1MA, are generated from a precursor, which is predominantly in E-conformation. Under pyrolytic conditions the isomerization barrier can be overcome by the high temperatures necessary to generate the radical, but photolysis ocurrs at room temperature. Photodissociation studies by Lau *et al.* showed that after photo exciting crotyl bromide at 234 nm the C-Br bond is cleaved and the hydrocarbon radical carries an internal energy between 29 kJ mol^{-1} and 126 kJ mol^{-1}.[177] This is not enough to surmount the barrier to isomers like 3-buten-1-yl (>201 kJ mol^{-1}), but sufficient to overcome the rotational barrier between E- and Z-1MA calculated to lie between 60-67 kJ mol^{-1}, resulting in a quick equilibration of the two isomers.[175] Computations using RRKM theory estimate the equilibration time for the E/Z isomerization at 1 atm at about 0.1 ns, much faster than the 100 ns it takes the radicals to transfer energy onto the bath gas through collisions.[175] Since in this study a photolysis wavelength of 213 nm is used, the radicals should form with a higher energy distribution, further facilitating the isomerization process. Predictions of the overall ratio between Z- and E-isomers ($R_{Z/E}$) at equilibrium were shown to be critically dependent on several parameters like computational method, temperature, pressure, and average internal energy of the radical.[175] At room temperature and 10.1 mbar, $R_{Z/E}$ was calculated to be between 1 and 2. For simplicity equal amounts of E- and Z-1MA were assumed directly after photolysis. According to the ms-TPES any contributions from the Z-isomer to the kinetic trace can be neglected below 7.55 eV and the E-isomer can be monitored exclusively. Isolating the signal originating from the pure Z-isomer is more challenging, as both isomers show overlapping transitions in the ms-TPES. Similar to the allyl experiments in section 4.1.1 the respective peroxy radicals could not be detected, due to their unfavorable Franck-Condon factors and low binding energies in the cation. Thus, the kinetics of the methylallyl radicals were determined by observing their respective radical decays over time.

Selected kinetic traces of the 2-MA radical are presented in figure 4.16 a). The radical signal decays over time even with no oxygen present, which is due to several side reactions the 2-MA radicals are invovled in. This background needs to be accounted for before the rate constant of reaction (29) can be determined relieably. Hence, kinetic traces without oxygen were recorded under the same conditions and analyzed using a reduced reaction mechanism, which did not include reaction (29). The most important side

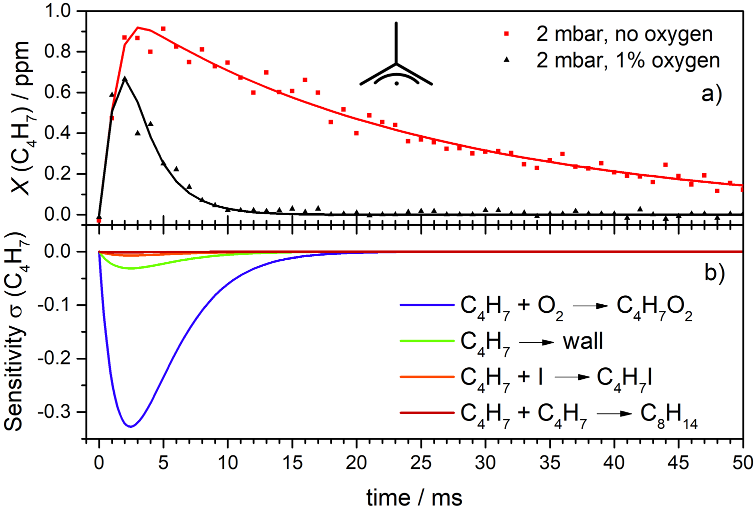

Figure 4.16.: a) Typical decay of the 2-MA radical with (black) and without (red) oxygen present. Dots represent experimental data points and lines show the result of the numerical simulation. b) Sensitivity analysis of the 2-MA radical with 1% oxygen present. The reaction between 2-MA and O_2 becomes the most important one once oxygen is added.

reactions are summarized in table 4.4 and include dimerization between 2-MA, recombinations between methylallyl radicals and halide atoms as well as formation of molecular iodine I_2. First-order heterogenous wall losses were included and the corresponding rate constant was treated as an independent fit parameter and optimized to reproduce the observed decay. As such the wall loss reaction also included any minor contributions that are yet unaccounted or mismatched in the other rate constants from extrapolation. In particular reactions of 2-MA with the precursor can be treated this way since these exhibit a pseudo-first order behavior because of the large excess of precursor molecules. All reactions together yielded a consistent background mechanism, which was used without changes in the oxygen measurements. Most rate constants in table 4.4 are not known

under the conditions of the experiments. Therefore, they need to be extrapolated or derived from allyl radical reactions, with the iodine and bromine atom dimerizations being the exceptions. The dimerization reaction of the 2-MA radical was studied by shock tubes at much higher temperatures and pressures.[170,171] A study performed at room temperature and 133 mbar total pressure[172] revealed a recombination rate constant for the 2-MA radical that is comparable to the allyl radical at pressures between 1.3-8.0 mbar.[144] Similarly, the values for the reactions between halide atoms and methylallyl radicals were derived from allyl and used without correction in the case of iodine and scaled by 0.8 in the case for bromine. The latter was done to better fit the experimental traces at longer reaction times. Figure 4.16 b) shows that the influence of reaction (34) on the decay is negligible. An increase of the rate constant by a factor of three changed the rate constant of reaction (29) only by 3%.
Consequently, different amounts of oxygen (0.25%-2.0%) were added to the

Table 4.4.: Background reactions considered in the decay of the methylallyl radicals. All rate constants are in units of $cm^3mol^{-1}s^{-1}$ unless noted otherwise.

Reaction	No.	Rate constant k	Ref.
$2\,C_4H_7 \longrightarrow C_8H_{14}$	(31)	2.6×10^{13}	Bayrakceken *et al.*[172]
2-MA $\longrightarrow$ wall	(32)	$32^{(a)}$	This work
1-MA $\longrightarrow$ wall	(33)	$15^{(a)}$	This work
2-MA + I $\longrightarrow$ 2-MAI	(34)	1.0×10^{14}	Jenkin *et al.*[136]
1-MA + Br $\longrightarrow$ 1-MABr	(35)	8.0×10^{13}	estimated, Jenkin *et al.*[136]
$I + I + M \longrightarrow I_2 + M$	(36)	$2.96\times10^{15\,(b)}$	Baulch *et al.*[148]
$Br + Br + M \longrightarrow Br_2 + M$	(37)	$1.02\times10^{15\,(b)}$	Baulch *et al.*[148]

(a) s^{-1}
(b) $cm^6mol^{-2}s^{-1}$

mixture and the trace for x(O_2)=1% is given as an example in figure 4.16 a) in black. The decay becomes visibly faster when oxygen is added, underlining the dominance of reaction (29) in the system.

Oxygen can attack all methylallyl radicals at different, non-equal, reaction sites. In the case of 2-MA there are two terminal and one central position, which cannot be distinguished based on the decay of the radical signal. The propensity of each site to react with oxygen can be evaluated by calculating the heats of reaction for the respective reaction. Reaction enthalpy values (ΔH_R) at 298 K on CBS-QB3 level of theory displayed in scheme 4.2 show that the formation of the 2-MA peroxy species at the central site is highly unfavorable and even endothermic compared to the terminal sites. Previously, the heat of reaction for 2-MA + O_2 has been calculated to be -90 kJ mol^{-1} using the MP2 method,[173] a difference of ≈10 kJ mol^{-1}, which can be explained by the different methods. The CBS-QB3 method gives excellent results for the allyl system (bottom trace) with a calculated value of -75.6 kJ mol^{-1} compared to an experimental value of -76.2 kJ mol^{-1}.[131] Therefore, it is assumed that the results for the MA systems also give very good predictions.

The decay of the formed peroxy species back to the reactants could also influence the decay of the radical species. The temperature dependent rate constants of the reverse reaction (-29) have been calculated by Chen and Bozzelli and resulted in values of 1.6×10^{-4}s^{-1} (CBS/MP2) and 1.5×10^{-3}s^{-1} (DFT/B3LYP) at 300 K.[173] Even the faster rate constant is tiny and its influence on the decay of the radical signal can be neglected under these conditions. Keeping the background rate constants, fit parameters, instrument response functions and initial radical concentrations constant, allows the concentration-time profiles to be fitted by optimizing the reaction rate with oxygen. As displayed in figure 4.16 b) reaction (29) becomes dominant once oxygen is added with only minor contributions from the wall losses to the decay, which is expected in a pseudo-first order system.

The pseudo-first order plots can be seen in figure 4.17 for the 2-MA radical. According to the equation $k^{1st} = k^{2nd} \times [O_2]$ the second order rate constant can be extracted as the slope of the pseudo-first order rate constants versus the oxygen concentration. When the background reactions are accounted for the slope has a y-intercept of zero, which is the case in figure 4.17. A standard pseudo-first order evaluation of the data set using a single monoexponential fit resulted in two different effects, a non-zero y-intercept and rate constants for (29) that are up to 27% slower. The former can be explained by unaccounted background reactions, while the latter is mainly caused by

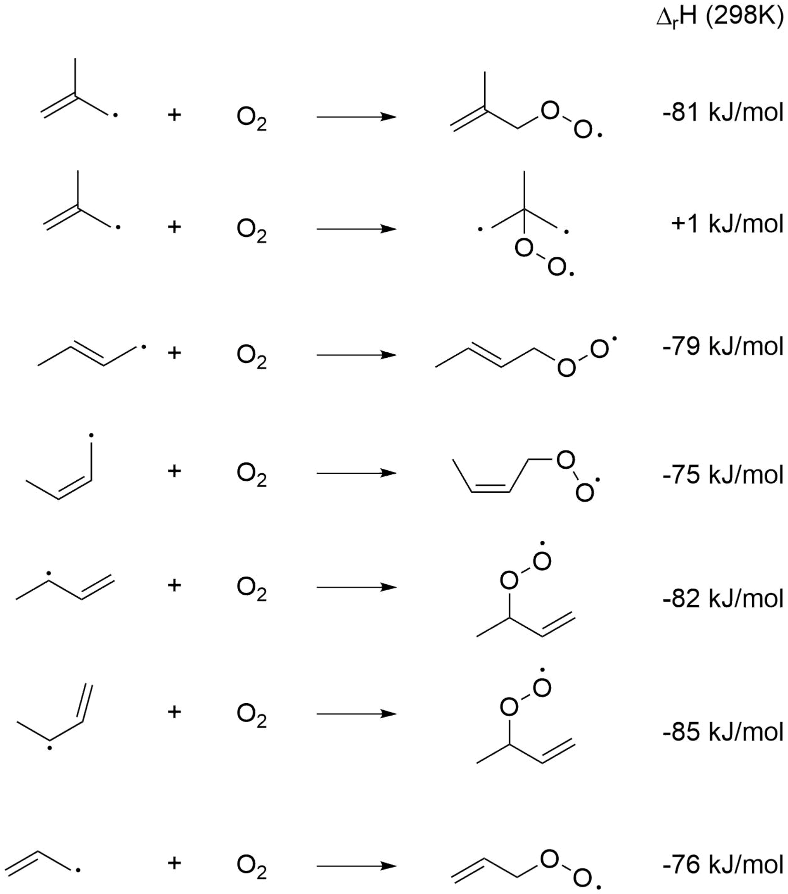

Scheme 4.2.: Possible reaction between methylallyl radicals and oxygen. The reaction enthalpies were calculated at 298 K using the CBS-QB3 method.

the neglection of the IRF. Especially at high oxygen concentrations where the 2-MA signal is back to background level within the first few milliseconds, the simple analysis yields systematically too low rate constants. A monoexponential analysis including the IRF, agrees with the full kinetic simulation within ±9% on average. This underlines the superiority of the numerical simulation compared to other analysis procedures. However, the different analysis also reveal a large influence of the IRF and its width, which is why an additional error of ±5% has been included into the error estimate discussed in section 4.1.2.2. The established rate constants from figure 4.17 are displayed in table 4.5. As one can see there is no pressure dependence of reaction (29) over the pressure range between 1 - 3 mbar. Thus, it can be assumed that the reaction is already at or close to its high pressure limiting rate constant k_∞ with a value of $5.1\times10^{11}\,cm^3mol^{-1}s^{-1}$.

The kinetics of the 1-MA radical were investigated at different photon energies. In order to observe the pure E-1MA signal the synchrotron light was set at 7.54 eV, as to not ionize the other isomer Z-1MA. It was also tried

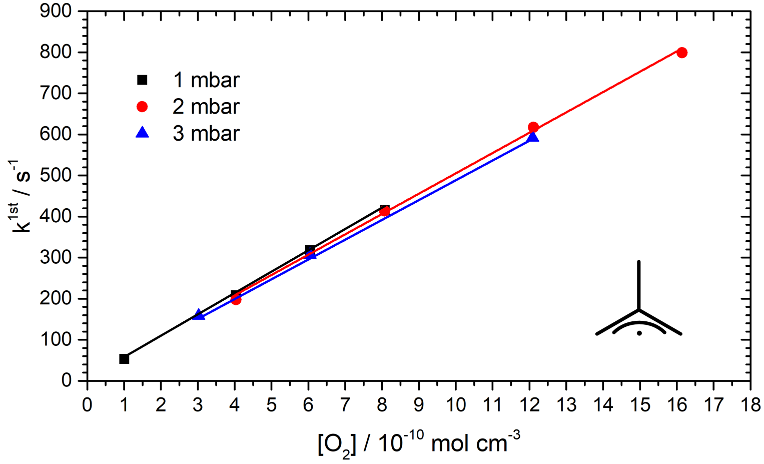

Figure 4.17.: Pseudo-first order plot of the 2-MA radical with oxygen between 1 - 3 mbar overall pressures. Within the experimental error no pressure dependence is found.

to obtain the isomer specific rate-constant of the higher ionizing Z-1MA radical. The concentration/time profiles at 1 mbar at various oxygen concentrations are displayed in figure 4.18. The mixture was ionized directly at the threshold of the Z-1MA at 7.59 eV and only the threshold signal was used by subtracting ring and circle contributions as depicted in section 2.3.3. Although the trend of each trace is clearly visible, the signal/noise ratio is poor and thus, the fits exhibit a huge standard error that ultimately

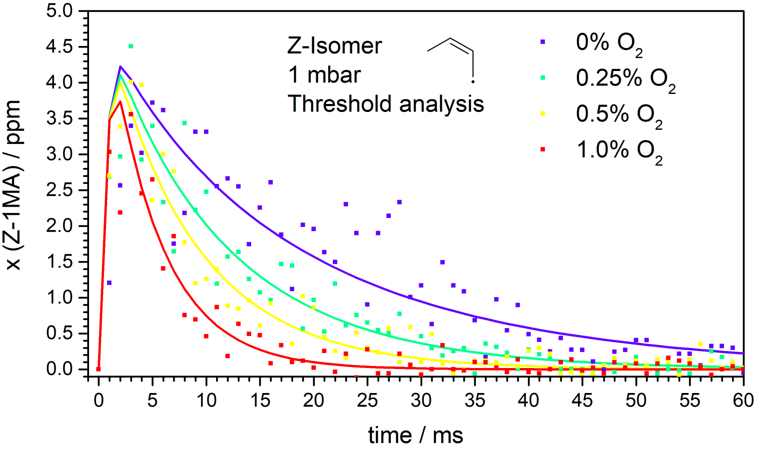

Figure 4.18.: Obtained concentration/time profiles for the Z-1MA isomer using threshold analysis. The dots represent the data points, while the solid lines are the least-square fits.

Table 4.5.: Pressure dependence of the second order rate constants for the 2-MA + O_2 reaction at 298 K.

pressure / mbar	k^{2nd} / $10^{11}\,cm^3mol^{-1}s^{-1}$
1	5.2±1.0
2	5.1±1.0
3	5.1±1.0

reflects on the validity of the obtained rate constant. In addition one has to keep in mind that even though Z-1MA exhibits a big FC-factor at 7.59 eV, the FC-factor of the lower ionizing E-1MA is not negligible, which introduces further error sources. Therefore, the threshold analysis was neglected on the 1-MA data.

Ultimately the complete signal at 7.59 eV was used, resulting in the determination of a rate constant for the mixture of E- and Z-1MA. A comparison between the two analysis methods shows no significant difference in the obtained pseudo-first order rate constants in both cases, but the reduction of the error bars by using all ions in the mass channel proved to be an advantage.

For the reactions of E-1MA without oxygen the concentration of the bromine atoms will be twice as high, because half of the generated hydrocarbon radicals will be present in the Z-form, which is not ionized. This has to be considered in the analysis of the kinetic traces. A typical decay of the

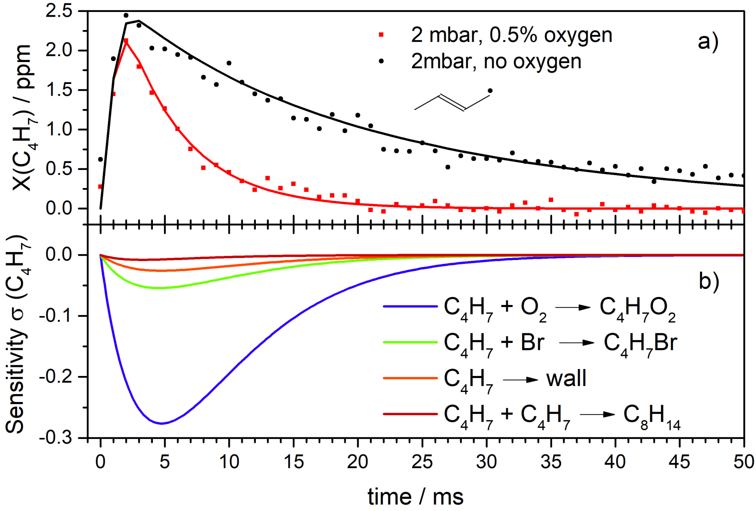

Figure 4.19.: a) Typical decay of the E-1MA radical signal over time with (black) and without (red) oxygen. b) Sensitivity analysis of the 1-MA radical over time.

1-MA signal is displayed in figure 4.19, where the initial rise of the radical signal exhibits the time resolution of the setup. The background reactions displayed in table 4.4 were derived from the allyl radical and the 2-MA radical with the reaction between 1-MA and bromine being multiplied with a factor of 0.8 to yield a better fit at longer reaction times.[136] The 1-MA radicals should exhibit multiple dimerization rate constants depending on the respective isomers (E/E), (E/Z), and (Z/Z) that are involved. These have not yet been determined, and thus the value for the 2-MA radical was used without any correction. The wall losses were optimized to fit the experimental data resulting in a value that is about twice as high as for 2-MA, due to the much higher uncertainties in the 1-MA case. After the background mechanism has been established, oxygen (0.25%-1.5%) was added to the mixture and the kinetic traces recorded. A typical decay curve with oxygen can be seen in figure 4.19 a) and the corresponding sensitivity analysis is displayed in figure 4.19 b). After the addition of oxygen, reaction (30) becomes the dominant decomposition pathway for E-1MA radicals, confirming the pseudo-first order conditions. It is notable, that

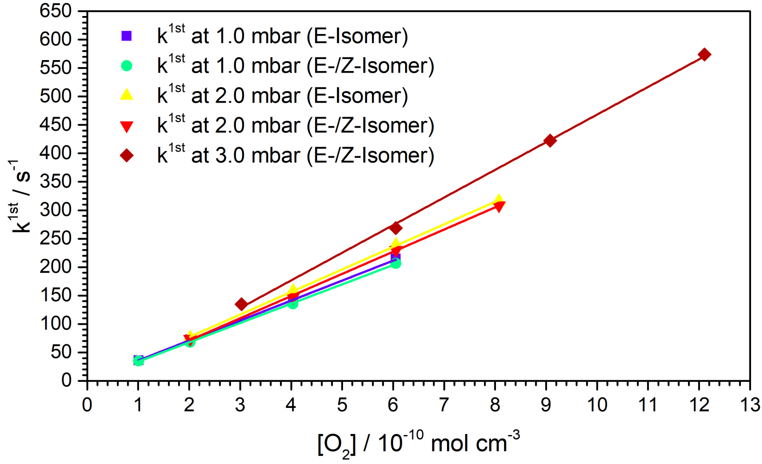

Figure 4.20.: Pseudo-first order plot of the reaction of 1-MA + O_2. The two isomers show almost identical rate constants and a weak positive pressure dependence is observed.

the second most important reaction is the recombination with the bromine atom, which can be rationalized by the higher concentration compared to the 2-MA experiments. The decomposition of the peroxy species back to the reactants was not considered based on similar assumptions as for the allyl and 2-MA radicals.
1-MA has three non-equivalent reaction sites, one of which is prochiral, resulting in a variety of formed reaction products displayed in scheme 4.2. Only the resonantly stabilized molecules were considered in the case of 1-MA, since the non-stabilized reaction products are assumed to be much higher in energy, similarly to 2-MA. Previous studies reasoned that the equal spin densities on the carbon atoms of the 1-MA radicals as well as insignificant sterical effects observed on similar alkyl radicals should result in similar rate constants for both sites. Stable neutral and cationic species were found for all three isomeric products. The neutral species have recently been detected by cavity ringdown IR spectroscopy,[179] but detection via photoionization is not possible as discussed above. Their IEs were com-

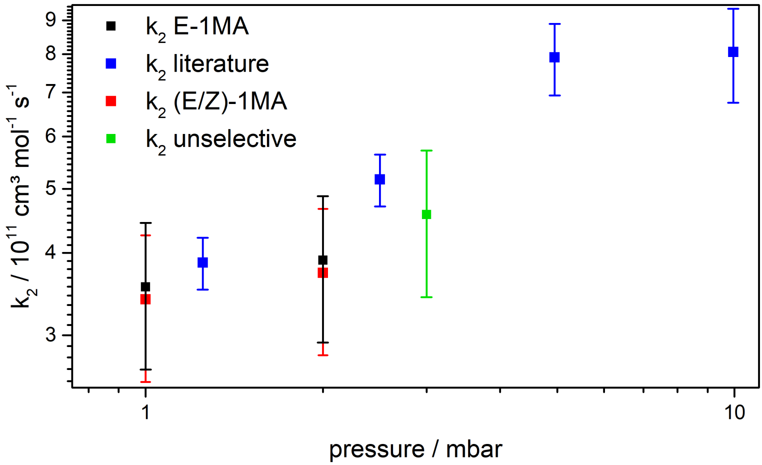

Figure 4.21.: Pressure dependent second-order rate constants of the 1-MA + O_2 reaction. Error bars correspond to the 2σ standard error from the linear fit. The overall experimental error was determined to be ±20%.

puted all to be around 8.30 eV with an almost planar CCCC framework in the cation. The pseudo-first order rate constants obtained by fitting the concentration-time profiles are displayed in figure 4.20. In all cases a linear dependence can be observed, with the each slope representing the second order rate constant of the respective experiment. No significant isomer dependency is found between the E- and E/Z-1MA experiments, with the direct comparison between the two showing a large overlap at 1 and 2 mbar. Similarly to 2-MA, the kinetic traces were also analyzed without accounting for the background mechanism, yielding consistent results.
The pressure dependence of the observed second order rate constants is depicted in figure 4.21 and for better comparison with the literature values their 2σ error from the linear fit is displayed. Their respective values are given in table 4.6 with an overall error estimated to be around ±20%. The determined rate constants are very close to the ones found by Knyazev and Slagle (blue squares).[174] They observed almost identical rate constants at 5 and 10 mbar respectively and thus their obtained rate constant of 8.06×10^{11} cm^3 mol^{-1} s^{-1} corresponds to the high pressure limit.

Table 4.6.: Pressure dependence of the second order rate constants for the 1-MA + O_2 reaction at 298 K. At 3 mbar the radicals were unselectively ionized.

pressure / mbar	k^{2nd} (E) / 10^{11} cm^3 mol^{-1} s^{-1}	k^{2nd} (E/Z) / 10^{11} cm^3 mol^{-1} s^{-1}	Ref.[174] / 10^{11} cm^3 mol^{-1} s^{-1}
1	3.6±0.7	3.4±0.7	-
1.25	-	-	3.87±0.35
2	3.9±0.8	3.7±0.8	-
2.5	-		5.17 ±0.47
3	4.6±1.0	-	-
4.95	-	-	7.91 ±0.98
9.95	-	-	8.06 ±1.31

4.1.2.4. Discussion

In order to put the presented results of the methylallyl radicals into a broader context, a comparison with their respective parent molecule allyl is warranted. The reaction mechanism of the latter has been studied extensively proceeding via a collisionally stabilized association intermediate. The respective rate constants for the high and low pressure regime have been determined to be $k_\infty=3.5\times10^{11}$ cm^3 mol^{-1} s^{-1} and $k_0=2.2\times10^{11}$ cm^6 mol^{-2} s^{-1} (in Ar). Less is known about the methylallyl radicals, with only reaction (30) being investigated experimentally by Knyazev and Slagle.[174] For the 2-MA radical only computational data for its reaction with oxygen (29) and their respective secondary products exist up to now.[173] Based on the strong similarity between the compared molecules it is very likely that the reaction of the methylallyl radicals with oxygen forms a transiently stabilized association complex according to reaction (38).

$$\mathrm{C_4H_7 + O_2 \rightleftharpoons [C_4H_7OO]^* \xrightarrow{M} C_4H_7OO} \tag{38}$$

As can be seen in figure 4.21 the measured rate constants for 1-MA in this study overlap with the literature within the respective error bars. Since the rate constant at 10 mbar does not differ from the one at 5 mbar this rate constant is attributed to the high pressure limit rate constant k_∞. The abrupt switch from falloff behavior starting at 5 mbar is uncommon and might be explained by a systematic overestimation of the 5 mbar rate constant. This would be in line with the values determined in this study and the rather small but nonetheless measurable rate constant increase of about 30% between 1 and 3 mbar.

On the other hand no experimental data are available for the 2-MA radical. Chen and Bozelli calculated k_∞ values of reaction (29) using different theoretical methods, and explored the potential energy surfaces of possible secondary reaction products. Their predictions for the high pressure rate constant for 2-MA depend strongly on the employed method and can be given in the general form in equation 4.6.[173]

$$k_\infty/cm^3mol^{-1}s^{-1} = A\cdot T^n\cdot e^{\frac{-E_a}{RT}} \tag{4.6}$$

$$k_\infty/cm^3mol^{-1}s^{-1} = 4.65\cdot10^8\cdot T^{1.19}\cdot e^{\frac{-2234\,J}{RT}} \tag{4.7}$$

$$k_\infty/cm^3mol^{-1}s^{-1} = 1.09\cdot10^{10}\cdot T^{0.57}\cdot e^{\frac{-9585\,J}{RT}} \tag{4.8}$$

Canonical transition state theory allows the calculation of the three parameters A, T^n and E_a, giving the k_∞ values at different temperatures. Using DFT methods the determined parameters can be seen in equation 4.7, while the CBS-q/MP2 gives results according to equation 4.8. At

Table 4.7.: High pressure limiting rate constants (k_∞) of three allylic radicals with oxygen.

	Allyl + O_2	1-MA + O_2	2-MA + O_2
k_∞ / $cm^3\,mol^{-1}\,s^{-1}$	3.5×10^{11} [136]	$\approx8.1\times10^{11}$ [174]	5.1×10^{11}

room temperature the two values for k_∞ are $1.60\times10^{11}\,cm^3\,mol^{-1}\,s^{-1}$ and $5.89\times10^{9}\,cm^3\,mol^{-1}\,s^{-1}$ for equation 4.7 and 4.8, respectively. The first value is in good agreement with the experimental findings, but the second is two order of magnitude lower, underlining the divergence in theoretical assesments and the importance of experimental studies. The barriers for the 2-MA peroxy species to form secondary products are all above the entrance level, and as such too high to play any role at room temperature. The only exception is an intramolecular H-shift that procedes via a stabilized six-membered ring, with a barrier of $83\,kJ\ mol^{-1}$ relative to the stabilized peroxy species.

A similar picture can be drawn for both isomers in the 1-MA case. Calculations by Dibble *et al.*[175] showed that both isomers can in principle undergo various isomerization processes after they have reacted with oxygen. The smallest barrier for Z-1MAOO is a 1,6 H-shift with a barrier of $87.4\,kJ\,mol^{-1}$ while for E-1MAOO it is a 1,5 H-shift at $104.6\,kJ\,mol^{-1}$. The barriers to form these secondary products are insurmountable at room temperature, but their contribution under combustion conditions may lead to several reaction products. A very common reaction under these conditions is a hydroperoxy HO_2 loss, which has been found to be endothermic for 1-MA. Therefore, the loss of oxygen is the exclusive decomposition pathway for 1-MAOO radicals under these experimental conditions.

The k_∞ for the different molecules are listed in table 4.7. The smallest value and largest pressure dependence is found for allyl.[137] The methylallyl species both being a factor of two to three higher, with 2-MA exhibiting no and 1-MA exhibiting only a small pressure dependence over the same pressure region. A clear trend is visible for k_∞ in the order of allyl<2-MA<1-MA, which needs to be understood in more detail. Obviously, an explanation based on sterical effects cannot rationalize the observed behavior and would even be counter intuitive.

It is well known, that the effect of pressure (and temperature) on the rate constants of recombination reactions is governed by a complex interplay between collissional activation and deactivation steps and microcanonical rate constants of each posssible reaction for the association complex.[180,181] These complex interactions can be treated using a RRKM/ME approach, but such calculations would be beyond the scope of this thesis when performed in detail. For that reason an analogy with the more simple alkyl radicals can be drawn. Miyoshi calculated systematic trends of the high- and low-pressure limiting rate constants for alkyl radicals with varying chain length and substitution patterns using the RRKM/ME approach.[182] He intentionally left out reactions to secondary reaction products, creating molecular size dependent "hypothetical" falloff plots for alkyl radicals. The neglected side reactions play crucial roles in alkyl radicals, but are not relevant in alkenyl radicals.[183,184] In this way the identified trends should be well transferable to the allylic systems discussed here, although one has to note that the well depth of alkenyl peroxy radicals and their association complexes are much more shallow than it is for their alkyl congeners.

The high pressure limiting rate constants depend almost exclusively on the substitution pattern of the respective radical reaction site and are largely independent from its chain length. In agreement with the experimental data the k_∞ values decrease from tertiary>secondary>primary. The reason for this is a more attractive PES at shorter internuclear distances resulting from a higher well-depth. In other words, the bond dissociation energy (BDE) decreases from tertiary to primary alkylperoxy radicals.[182] This observation is assumed to be transferable to alkenyl radicals, where their reactivity can be explained by a superposition of all reactive centers due to delocalization of the spin density. Since allyl and 2-MA have only primary sites, they exhibits smaller k_∞ values. Note that the central carbon atom of 2-MA does not produce a stabilized peroxy radical and can be neglected. On the other hand 1-MA has a primary as well as a secondary radical site both available for reaction with oxygen, hence should have the highest HPL rate constant in this series. In line with this qualitative treatment, using the BDEs can help further distinguish between the reactivities. The BDEs that are given in scheme 4.2 show the smallest one for allylperoxy with a significant higher value at 2-MA. Interestingly for 1-MA the BDEs for the secondary and primary sites give consistent values with this explaination.

In order to understand the falloff behavior of the radicals the low pressure limiting (LPL) rate constants become important, which Miyoshi also analyzed.[182] For k_0 the deciding factor is the amount of heavy atoms, which correlates directly with the density of states for the peroxy radicals around the threshold. This is independent of the substitution pattern and almost identical for same sized radicals. On this basis the k_0 of the radicals discussed here can be arranged in the order 1-MA≈2-MA>Allyl. The k_0 value is directly proportional to the size of the radical and therefore the falloff for allyl begins at higher pressures compared to the methylallyl radicals. This is commonly found in unimolecular dissociations and recombination reactions. Larger molecules reach their high pressure limit at overall lower pressures, due to their higher density of states.[185] Moreover, the same k_0 will cause the falloff to take place at higher pressures when k_∞ increases, as is the case going from 2- to 1-MA. Consequently the pressure dependency in the falloff region should increase in the order from 2-MA<1-MA<Allyl, again in qualitative agreement. However, one has to note that this behavior is only valid for low temperatures around 300 K and below, above 1000 K almost no dependency of k_0 can be observed.[182] In the 2-MA case, the already mentioned minor isomerization channel of the R-OO adduct to a R'-OOH radical structure via a six-membered transition state, followed by collisional stabilization of that product may contribute to the observed pressure dependence as well.

4.1.2.5. Summary

The isomeric methylallyl radicals 1-methylallyl (1-MA) and 2-methylallyl (2-MA) were generated using 213 nm laser photolysis of their halide precursors. Their rate constants with oxygen were measured in a slow flow reactor at pressures between 1 - 3 mbar and room temperature. The radicals were detected using synchrotron radiation at different energies using a PEPICO spectrometer. This allowed the determination of the identity of the generated species by recording ms-TPE spectra. The proposed reaction products, the methylallyl peroxy radicals could not be detected by photoionization due to their low stability in the cation, which causes dissociative photoionization. The second-order rate constants of the 2-MA oxidation reaction do not exhibit a pressure dependence in the investigated region. This resulted in the determination of the high pressure limiting rate constant k_∞ for this reaction at $5.1\times10^{11}\,\mathrm{cm^3\,mol^{-1}\,s^{-1}}$.
For 1-MA the two stereoisomers E-1MA and Z-1MA were produced upon photolysis, resulting in an isomer-selective rate constant for the lower ionizing E-1MA. Z-1MA was also observed according to ms-TPE spectra, but its rate constant could only be determined in a convolution with E-1MA, yet the rate constants are almost identical within the error limits. the 1-MA rate constants exhibit a small positive pressure dependence, with values

between $(3.5\pm0.7)\times10^{11}\,\mathrm{cm^3\,mol^{-1}\,s^{-1}}$ and $(4.6\pm0.9)\times10^{11}\,\mathrm{cm^3\,mol^{-1}\,s^{-1}}$ between 1 and 3 mbar. The difference in the pressure dependence between 1-MA and 2-MA can be rationalized by including their parent compound allyl. The k_∞ values depend mostly on the substitution pattern of the reactive radical site, whereas the k_0 values are influenced by the repsective chain length. For larger molecules the high pressure limit is reached at overall lower pressures as is the case for the methylallyl species compared to allyl. The falloff starts earlier for 1-MA because two out of its three radical sites are secondary versus two primary ones for 2-MA. This is based on the higher bond dissociation energies for higher substituted reaction sites, presumeably due to more attractive bonding potentials. Therefore, the k_∞ values grow in the order of $k_{Allyl} < k_{2-MA} < k_{1-MA}$. The experiments confirm the relationship between k_∞, radical size and substitution pattern for alkenyl radicals, which was previously predicted for alkyl radicals.

4.1.3. Iodine Monoxide and Hypoiodous Acid

Other than for kinetic studies, laser photolysis coupled to the CRF-PEPICO spectrometer can expand the avilable scope of spectroscopically investigateable molecules. In pyrolysis the high temperatures prevent the clean formation of oxygen centered radicals, especially hydrocarbon peroxy radicals. The latter exhibit rather small barriers for hydrogen elimination reactions or other hydrogen shifts. In these cases photolysis is often used, which forms radicals more cleanly. Especially the property of oxygen as a biradical renders its initial reaction barriers with other radicals very small. Through laser initiated bimolecular reactions molecules can be built up, rather than broken down as is common in conventional in pyrolysis. This scheme is particularly suited for investigations of molecules involved in atmospheric processes, where photons from sunlight influence the chemistry to a large extent.

4.1.3.1. Motivation

Iodine is a ubiquitous element in nature commonly found in aquatic life forms like algae from where significant portions can be emitted into the atmosphere.[186,187] These organic and inorganic species can then get photolyzed by sunlight producing iodine atoms, which can undergo several reactions. One of them is reaction (40) where IO is formed through the interaction with ozone, as illustrated in figure 4.22.

$$I_2 \longrightarrow 2\,I \tag{39}$$

$$I + O_3 \longrightarrow IO + O_2 \tag{40}$$

$$I + OH \longrightarrow HOI \tag{41}$$

IO can act as a catalyst to reform iodine atoms through several channels, refueling the destruction of ozone and leading to ultrafine iodine oxide particle (IOP) formation and aerosols. IOPs can act as cloud condensation nuclei, altering cloud lifetimes and thus influencing the radiative flux of the troposphere.[188] The two molecules that act as the starting point for this chemistry have been identified to be IO and HOI,[189–195] both of which have been studied using various spectroscopic techniques like UV/Vis,[196] IR,[197,198] EPR,[199] microwave spectroscopy[200] as well as photoelectron detachment.[201] However, thermodynamic properties as well as information on the cations are still scarce. Recently photoionization time-of-flight

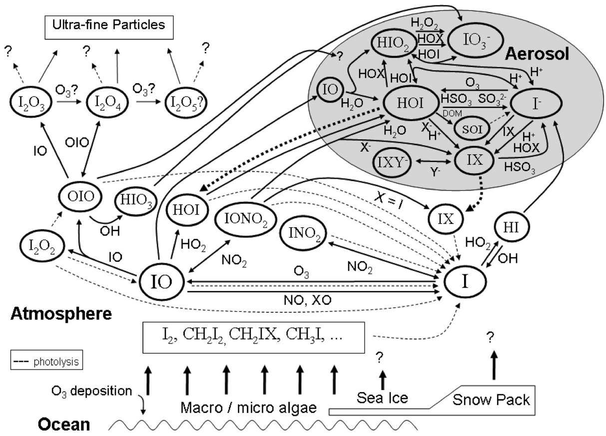

Figure 4.22.: Fate of emitted iodine molecules in the atmosphere. Photolysis by sunlight generates iodine atoms which can react with ozone, revealing a rich chemistry of iodine oxide species. Reprinted with permission from ref.[188]

mass spectrometry has been used to investigate the formation processes of IOPs,[202,203] but using this method requires accurate ionization energies of the respective species. Moreover, with increasing weight of the atoms, relativistic effects become increasingly important making spectral assignments more complex. A first photoionization study by Zhang *et al.* using photoion efficiency (PIE) curves determined the ionization energy to be at 9.74±0.02 eV.[78] Another band arose at 9.86 eV, which has been attributed to the vibrational overtone, but this assignment was questionable and did not match other higher transitions that were observed. Hassanzadeh *et al.* used high level relativistic computations to clarify the origin of the second band, and found an intense spin-spin splitting in the $X^+ \, ^3\Sigma^-$ ground state of IO^+, leading to a splitting of the $\Omega=0$ and $\Omega=\pm1$ levels.[204] Similar lower resolution PIE curves are available for HOI as well with an IE of 9.81±0.02 eV.[205]

In order to resolve the obvious discrepancies between experimental and theoretical data in IO^+ and determine accurate ionization energies for IO and HOI their respective threshold photoelectron spectra were recorded.

4.1.3.2. Experimental

For the iodine atoms, molecular iodine was used as a precursor. Iodine has a low vapor pressure of 35 Pa (0.35 mbar) and therefore the sample container was directly attached to the reactor and the iodine flow was regulated using a needle valve. The pressure inside the reactor was kept at 0.6 mbar at all times. Ozone was generated in a commercially available ozone generator (Fischer 502/10) by silent electric discharge of pure oxygen, creating a 5% mixture of ozone in oxygen. The latter was introduced into the reactor using a metered flow from a mass flow controller and the concentration of ozone inside the reactor was around $7{\times}10^{14}$ molecules cm^{-3}. Ozone only exhibits non-dissociative transitions at 532 nm and these have poor oscillator strengths, while iodine shows good cross sections into directly dissociative or pre-dissociative states.[206] This is why the 2^{nd} harmonic of the Nd:YAG laser described in section 3.2.3 at around 190 mJ cm^{-2} was used to cleave the I-I bond without any major interference from oxygen or ozone. Higher harmonic radiation from the synchrotron was suppressed by a MgF_2 window. Quantum chemical calculations on IO and HOI were performed using the B3LYP density functional. For iodine the correlation consistent polarized triple-ζ-PP basis set (aug-cc-pVTZ-PP) was employed. This basis set includes a relativistic pseudopotential for the inner shell electrons (1s-3d). For all other elements the aug-cc-pVTZ basis set was utilized.

4.1.3.3. Results

The iodine atoms were generated by photolyzing iodine molecules by the second harmonic of a Nd:YAG laser at 532 nm, creating two iodine atoms in two different spin states as depicted in reaction (42):[194,207]

$$\mathrm{I_2} \xrightarrow{\text{532 nm}} \mathrm{I\,(^2P_{3/2}) + I\,(^2P_{1/2})} \tag{42}$$

Collissions with the bath gas, containing mostly oxygen, quenches the iodine atoms in the excited $^2P_{1/2}$ state and through collissions with ozone they can undergo reaction to form IO, according to reaction (43).

$$\mathrm{I\,(^2P_{3/2}) + O_3 \longrightarrow IO + O_2} \tag{43}$$

The formation of HOI could be explained by either the abstraction of a

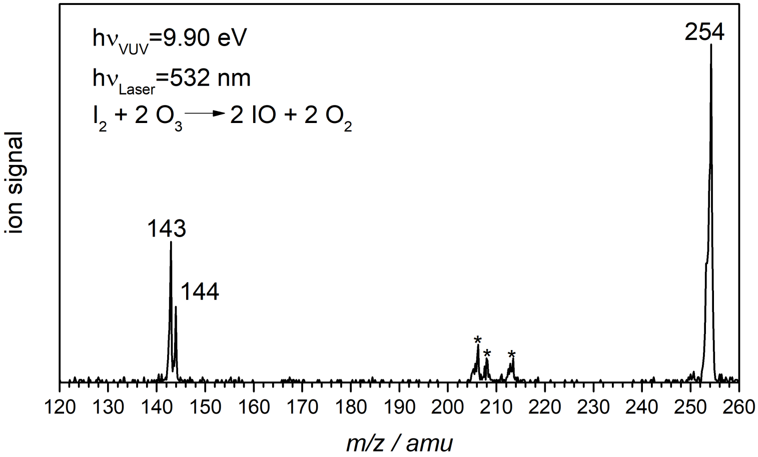

Figure 4.23.: Mass spectrum of the I_2 + O_3 mixture at 9.90 eV after photolysis at 532 nm. The peaks marked with asterisks are most likely impurities.

hydrogen atom from water by IO or by reaction of OH radicals with iodine atoms.

$$IO + H_2O \longrightarrow HOI + OH \tag{44}$$

$$I + OH \longrightarrow HOI \tag{45}$$

Since reaction (44) is endothermic by 86 kJ mol^{-1} it can be ruled out as a source for HOI and it is assumed that the sole origin is reaction (45), due to residual water adsorbed onto the walls of the reactor.
The TOF-MS at 9.90 eV of the $O_2/O_3/I_2$ mixture with the laser present can be seen in figure 4.23. It shows three distinct peaks at mass 254, 144, 143. The peaks marked with asteriks between 206 and 212 arise from previous experiments performed in the chamber and can be exluded as impurities. The dominant signal at m/z=254 can be attributed to the I_2 molecule used as precursor, while peaks at m/z=144 and 143 originate from HOI and IO, respectively. Up to 10.6 eV no presence of other species has been detected, including iodine atoms with an ionization energy of 10.43 eV. The large excess of ozone inside the photolysis reactor converts them instantly

to IO. While higher iodine oxide species have been detected at these photon energies in other experiments, the reactions forming them are apparently not fast enough to give rise to a detectable signal in the slow flow reactor. Higher photon energies were inaccessible due to a MgF_2 window that was used to filter higher harmonics, which is completly opaque above 11 eV.
Figure 4.24 shows the recorded ms-TPES of the IO radical with several distinct features. The IE can be attributed to the first peak visible at 9.71 ±0.02 eV representing the transition of the respective ground states $X^{+}\,{}^{3}\Sigma^{-} \leftarrow X\ {}^{2}\Pi_{3/2}$. This is in good agreement with theoretical predictions of 9.59 eV (Gaussian 2 procedure)[78] and 9.60 eV (CCSD(T) level of theory)[204] as well as calculations using the B3LYP/aug-cc-pVTZ-PP method yielding a value of 9.71 eV.[208] Compared to its lower homologue BrO the IE is lower by about 0.75 eV.[209] The HOMO of IO is a singly

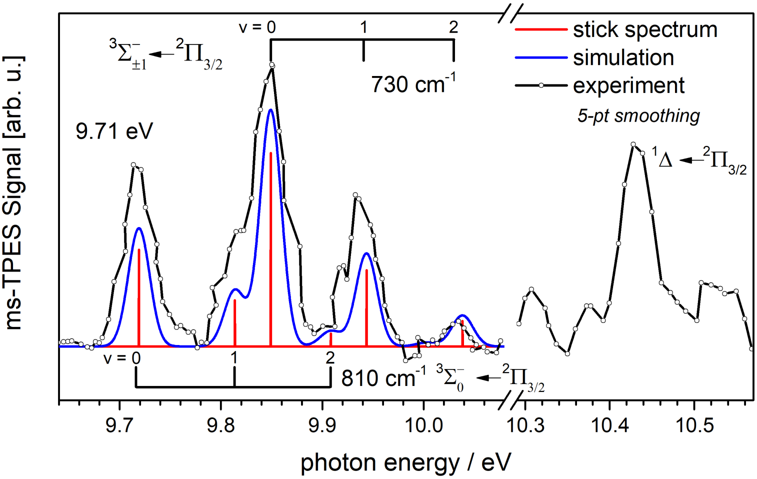

Figure 4.24.: Recorded ms-TPE spectrum of the IO radical. The ionization energy was determined to be 9.71±0.02 eV and assigned to the transition into the ${}^{3}\Sigma^{-}_{0}$ state. The spin-spin splitting can be resolved and at 10.43 eV the band of the first singlet state ($a^{+}\ {}^{1}\Delta$) can be seen. The red sticks represent the calculated Franck-Condon factors from Ref.[204]

occupied anti-bonding orbital from which an electron is ejected upon ionization leading to a pronounced vibrational structure in the cation. The computed bond length decreases from 1.868 Å [208,210] to 1.824 Å, [204] which is in agreement with the ejection of an antibonding electron. The second band is at 9.85 eV and represents the most intense transition, which has previously been attributed to the first vibrational overtone in the $X^+\,{}^3\Sigma^-$ state of IO^+. [78] This vibrational energy ($1130\,cm^{-1}$) is in stark contrast to the computed one ($764\,cm^{-1}$) and does not reproduce the third band at 9.94 eV. Hassanzadeh *et al.* suggested a different assignment based on their relativistic CCSD(T) calculations, which found a pronounced spin-spin splitting in the $X^+\,{}^3\Sigma^-$ ground state. Spin-spin splitting describes the interaction between the two spins of two separate electrons within one molecule. It is especially pronounced in molecules, with heavy elements and consequently large relativistic effects. Its mathematical description is the same as for spin-orbit couplings and leads to several energetically different components. [211] For a triplet state there are two possibilities. In the first case the two electron angular momenta initially couple together to give an overall spin angular momentum of zero. In the second case the spin angular momentum becomes ±1. The different energies of the two states can be best expressed using the total angular momentum Ω, similar to spin-orbit coupling schemes. The energy of a state is now not only dependent on its orbital- and spin angular momentum, but furthermore on the total angular momentum. In case of IO^+ this leads to a single lower lying ${}^3\Sigma_0^-$ and a doubly degenerate higher lying ${}^3\Sigma_{\pm1}^-$ component. [204] The second band is therefore assigned to the fundamental transition $X^+\,{}^3\Sigma_{\pm1}^- \leftarrow X^2\Pi_{3/2}$ and the energy difference between the two bands (0.14 eV, $1140\,cm^{-1}$) in the spectrum corresponds to the spin-spin splitting in the $X^+\,{}^3\Sigma^-$ state. This value is also in good agreement with the theoretically predicted one of $900\,cm^{-1}$, which is slightly dependent on the chosen computational method. The other bands at 9.94 eV and 10.03 eV represent the first and second overtone of the ${}^3\Sigma_{\pm1}^-$ state and reveal a vibrational frequency of $730\,cm^{-1}$. The vibrational progression of the ${}^3\Sigma_0^-$ state are convoluted with the much more intense transitions into the ${}^3\Sigma_{\pm1}^-$ state and can only be seen as shoulders in the experimental spectrum. The individual Franck-Condon factors are depicted as red sticks which were convoluted by a Gaussian with the FWHM of 25 meV (blue line) to generate the FC-simulation. The overall agreement is perfect, although the intensities of the individual transitions do not match exactly. This could originate from the assumption of a 1:2 statistical ratio for the two spin components in the calculations and might not necessarily reflect reality. Another band at 10.43 eV is visible and is assigned to the transition into the lowest singlet state $a^{+}\ {}^{1}\Delta \leftarrow\ X\ {}^{2}\Pi_{3/2}$ with no vibrational progression being visible. This value agrees well with the computed one at 10.45 eV but lacks the calculated intense FC factor. However, it is in line with observations from the previous PIE measurements, where no significant rise of the ion signal could be observed. The agreement between the two experimental studies points to an overall lower ionization cross section for the $a^{+}\ {}^{1}\Delta$ state. The absence of a vibrational progression can be derived from the calculations, which show a very small geometry change between the $X\ {}^{2}\Pi_{3/2}$ and $a^{+}\ {}^{1}\Delta$ state. The low signal/noise ratio is based on the diminishing transmission of the MgF_2 window as it is already close to the cutoff.

The ms-TPES of mass 144 is displayed in figure 4.25 and attributed to the $X^{+2}A'' \leftarrow X^{1}A'$ transition in the HOI molecule. The IE was determined to be 9.79±0.02 eV with a vibrational progression in intervals of 660 cm^{-1}. These values agree well with experimental literature data by

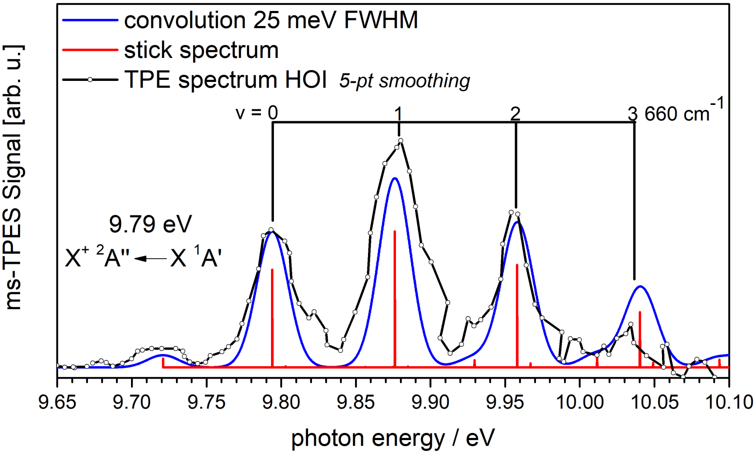

Figure 4.25.: Recorded ms-TPE spectrum of the HOI molecule. The IE was determined to be 9.79±0.02 eV with a vibrational progression originating from the I-O stretching mode with an energy of 660 cm^{-1}.

Monks *et al.*[205] who found an IE of 9.81 eV and a vibrational progression of 702 cm^{-1}, but is somewhat higher than the 9.70 eV in the most recent study by Wei *et al.* both using PIE curves.[203] DFT calculations using the B3LYP/aug-cc-pVTZ-PP method yield an IE of 9.82 eV and an vibrational frequency in the cation of 664 cm^{-1} , which are in perfect agreement with the experimental results. The computations reveal a shortening of the I-O bond length from 2.014 Å to 1.920 Å while the O-H bond and bond angle both increases slightly from 0.966 Å to 0.980 Å, and from 105.1° to 111.0°, respectively. This is in line with the computations by Ma *et al.* who found very similar parameters.[212] This behavior points to an occupied antibonding orbital with its highest density between I and O from which the electron gets ejected upon ionization. The FC-simulation based on the B3LYP/aug-cc-pVTZ-PP calculations coincides well with the experimental data. A small shoulder at 9.93 eV can be attributed to the ν_2^+ which corresponds to the bending mode with an energy of 1070 cm^{-1}. The small band at 9.72 eV is attributed to the 3_1^0 hot band, which is also well depicted in the FC-simulation.

4.1.3.4. Conclusion and Summary

IO and HOI are involved in the catalytic destruction of ozone especially in the marine boundary layer. Their investigated spectroscopic properties are limited and information on the cations is even scarcer. Both have been generated in a slow flow reactor by laser initiated reaction between iodine atoms and ozone or OH radicals according to reactions (43) and (41), respectively. The mass spectrum reveald the presence of IO, HOI and the precursor I_2, without any secondary products. The recorded ms-TPE spectrum for mass 143, corresponding to IO, shows an ionization energy of 9.71±0.02 eV and multiple distinct bands. While previous experimental studies attributed all bands to the $X^{+}\,{}^3\Sigma^- \leftarrow X\ {}^2\Pi_{3/2}$ transition, theoretical data questioned this assignment. Relativistic calculations found a significant spin-spin splitting due to the heavy iodine atom, breaking the degeneracy of the Ω=0 and Ω=±1 sublevels, with a calculated energy difference of 900 cm^{-1}. This could be confirmed by the ms-TPE spectrum where an experimental energy difference for the two sublevels of 1130 cm^{-1} is found. The vibration in the cation is determined to be 730 cm^{-1}, also in good agreement with the calculated value of 764 cm^{-1}. The vibrational progression into the ${}^3\Sigma_0^-$ state overlaps with the much more intense ${}^3\Sigma_{\pm 1}^-$ transitions. At higher photon energies a band at 10.43 eV reveals the first excited singlet state in IO^+ origination from the $a^+\ {}^1\Delta \leftarrow\ X\ {}^2\Pi_{3/2}$ progression.

The HOI^+ molecule has been investigated using PIE curves and an IE of 9.81 eV and a cationic vibration of 702 cm^{-1} was found. The ms-TPE data in this study agree with the existing data with a determined IE of 9.79 eV and a vibrational progression with spacing of 660 cm^{-1}. Calculations on B3LYP/aug-cc-pVTZ-PP level of theory revealed a shortening of the I-O bond while the bond angle and O-H bond both increase. This points to an occupied antibonding oribtal in the neutral species with its highest density in between the iodine and oxygen atoms. Overall the data presented here agree well with previous experimental and theoretical studies but offer a much higher accuracy.

4.2. Photoionization of Boron Compounds

4.2.1. Spectroscopy of a Boron-based Biradical

4.2.1.1. Motivation and Background

The research training school 2112 "Molecular Biradicals" aimed to investigate the properties of molecules containing more than one radical center. These molecules are often equally challenging for theoreticians, spectroscopists and synthetic chemists. Organic biradicals like the prominent benzyne (c-C_6H_4) represent crucial synthetic building blocks and have been the center of attention of multiple studies concerning their spectroscopic properties.[213,214] On the other hand their inorganic congeners have received significantly less attention, rendering spectroscopic and thermodynamic data on these compounds scarce. Boron compounds exhibit various binding motifs ranging from multicentered bonds in boron clusters,[215] over stabilized diborenes[216–218] and diborynes[219–223] with double and triple bonds, to borylenes with a lone electron pair at the boron atom.[224–226] All these species can be commonly found in chemical vapor deposition, production of boron-containing films,[227] and the doping of semiconductors[228,229] among other applications.[230] Non-stabilized diborenes R−B=B−R' are especially interesting, as their electronic properties can be changed by altering the substituents on the two boron atoms relative to the diborene parent compound H−B=B−H. Just recently it has been demonstrated that biradicalic diborenes can be synthesized and isolated,[231] underlining the necessity for fundamental spectroscopic data. So far HBBH has been almost elusive and only two experimental studies can be found in the literature investigating its properties. Knight *et al.* generated HBBH through dissociative photoionization of diborane B_2H_6 and trapped it in an neon matrix at 4 K, where an EPR spectrum revealed a triplet ground state.[232] The properties of HBBH in the infrared were asessed using the evaporation of boron atoms in a H_2 atmosphere, through which a vibrational frequency of $2679.9\,\mathrm{cm}^{-1}$ for the antisymmetric stretch mode ν_3 was found.[233] Several theoretical studies supported the EPR measurements[234] and focused on the unique electronic[235–238] and bonding properties[239] in the neutral ground state of HBBH. However, information on the cation is neither available through experimental nor through computational studies.

Diborene is a linear molecule with a $D_{\infty h}$ symmetry and a $^3\Sigma_g^-$ ground state.[234] The two highest orbitals are the degenerate π_x and π_y orbitals

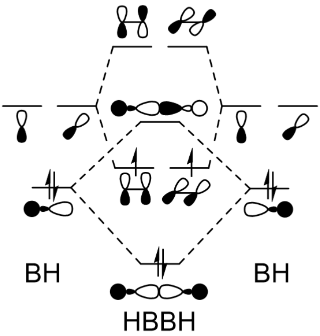

Figure 4.26.: MO diagram of diborene H–B=B–H·

each occupied by one electron, creating a bond order of two between the two boron atoms (see figure 4.26). All of these molecular properties cannot be translated into a single Lewis structure without omitting at least one crucial detail. Symbolizing the bond order of two by drawing HBBH with a double bond does not accurately reflect the triplet ground state, while a single bond with two radical centers at the borons fails to indicate the correct bond order. Since both versions are at least some degree of false, one can argue if Lewis structures should be used at all in this case. For the sake of simplicity the double bond structure will be used from here onwards.

4.2.1.2. Results and Discussion

Experiments were carried out on the DESIRS undulator beamline at the french national synchrotron facility SOLEIL using the double-imaging PEPICO spectrometer DELICIOUS III.[92] The unselective abstraction of hydrogen atoms from diborane through fluorine atoms generated diborene according to reaction (46).

$$B_2H_6 + 4\,F \longrightarrow HBBH + 4\,HF \tag{46}$$

This process is thermodynamically driven by the high formation enthalpy of HF ($\Delta H_f^0(298\,\text{K})$ = -272.775 kJ mol^{-1}).[240,241] The fluorine atoms for this process are generated in a microwave discharge of F_2 (5% in He) and mixed with the precursor (0.5% in Ar) at reduced pressures. The two reac-

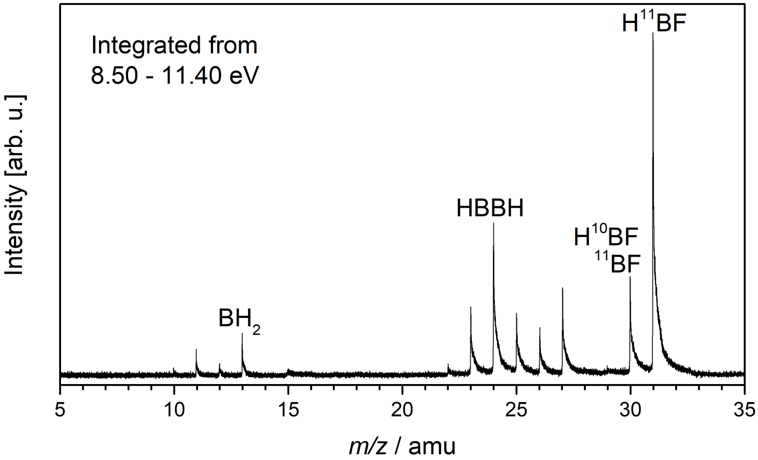

Figure 4.27.: Mass spectrum of the diborane, fluorine mixture with activated microwave discharge. The spectrum has been integrated from 8.50 eV to 11.40 eV.

tants were fed into the reaction chamber separately and mixed in a reaction zone at a pressure of 0.7-1.0 mbar. The gas mixture was expanded through two skimmers into the ionization chamber, where the molecules are ionized by the synchrotron light. The photon energy was scanned with steps of 5 meV and slow photoelectron spectra were obtained by integrating over all electron kinetic energies up to 50 meV. A similar approach has been pioneered in the groups of Dyke and Ruscic and used to determine IEs of BF,[242] B_2H_5[243] , B_2H_4[244] and others,[43,245,246] but its success has been limited based on the unselective nature of the approach. PEPICO can help to disentangle the signals of each species through its mass selective nature, gathering background free, isomer selective information.[176] Figure 4.27 shows a myriad of species being generated simultaneously, which can be coarsely segmented into three regions. The lower ($m/z < 20$) contains borane species with a single boron atom, a middle ($20 < m/z < 28$) with a mixture of B_2H_X molecules and a higher ($m/z > 28$) containing lower borane clusters and BF derivatives. The dominant peak is at $m/z = 31$ and can be attributed to HBF, while the second most intense signal is at

$m/z = 24$, corresponding to B_2H_2. The harsh abstraction conditions inside the reactor can cleave the diborane and form molecules with a single boron atom visible at $m/z = 10 - 13$, which can be identified as BH and BH_2. These molecules can subsequently react with the abundant fluorine atoms to form BF, HBF generating the dominant signals in the higher region. The lower and higher region of the mass spectrum will be discussed in section 4.2.2.

Other than regular TPE spectra, the DELICIOUS III endstation of the DESIRS beamline offers the possibility to record two-dimensional photoelectron matrices. In these the kinetic energy of the photoelectrons (E_{kin,e^-}) is plotted versus the photon energy of the synchrotron light. Starting at the ionization threshold the E_{kin,e^-} increases linearly according to the equation $E_{kin,e^-} = h\nu - IE$. Rotating the matrix counterclockwise

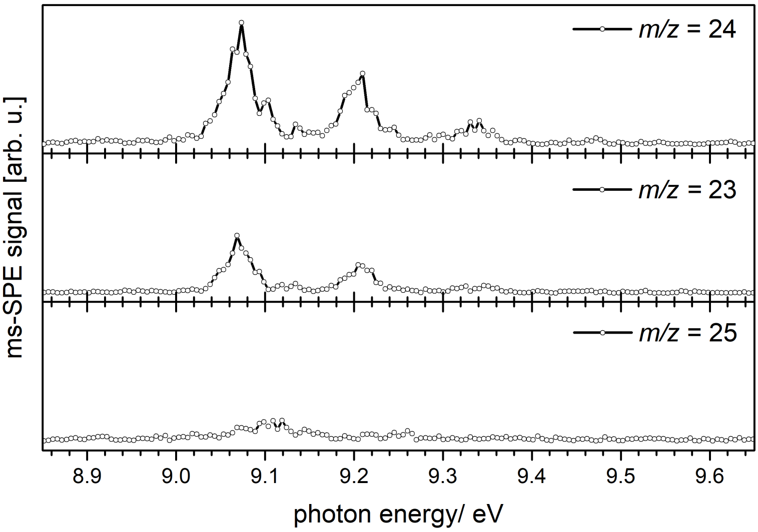

Figure 4.28.: ms-SPES of mass channel 24 (a) 23 (b) and 25 (c). The signal intensity in b) is approximately half of a) in line with the natural abundance of the boron isotopes. No corresponding signal can be found in c) underlining that a species with the highest mass of 24 is observed.

by 45° converts the diagonal slope of the signal into a vertical one, through which the signal to noise ratio can be increased by integrating over the E_{kin,e^-} signal.[247,248] At higher E_{kin,e^-} the signal diverges and the resolving power is significantly reduced. The trade-off between resolution and signal/noise can be optimized creating slow photoelectron (SPE) spectra with superior signal strength and comparable resolution to TPE spectra. A more detailed description is found in section 2.3.4.
The ms-SPE spectrum between 8.90 and 9.70 eV of $m/z = 24$ is displayed in figure 4.28 a) together with the signal in the mass channels 23 (b) and 25 (c). Several features point to an observed species with its highest mass in the m/z=24 channel. Other, heavier congeners like B_2H_4 and B_2H_3 can be excluded since mass 25 does not exhibit any corresponding signals. Considering the natural abundance of boron isotopes ($\frac{^{11}B}{^{10}B} = \frac{4}{1}$) the signal

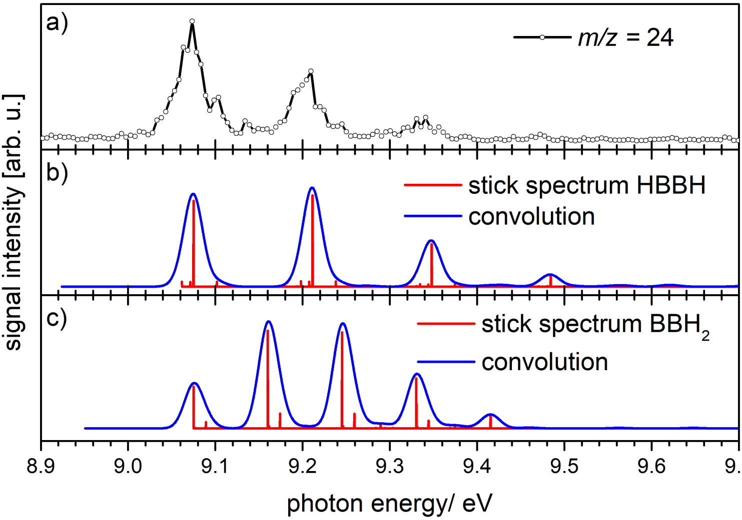

Figure 4.29.: Experimental SPES of mass channel 24 (a) together with the FC-simulations of HBBH (b) and BBH_2 (c). The simulation for HBBH fits the experimental spectrum very well, while no transitions for BBH_2 are found in the experimental spectrum.

at m/z=23 should be approximately half as intense as in 24, which is the case. B_2H_2 can have two different stable isomers, HBBH and BBH_2, with a third hydrogen bridging structure being identified as a transition state, by quantum chemical calculations. The computed IEs using the CBS-QB3 method are 9.02 eV (HBBH) and 8.97 eV (BBH_2) showing that both are very close and a precise distinction is only possible by comparing the vibrational progressions. However, several small features in the experimental spectra point to the dominant presence of diborene rather than BBH_2. The intensities in the mass spectrum for masses 24, 23 and 22 shows a typical boron isotopic pattern (16:8:1) contrary to masses 25, 26 and 27 which are of approximately equal intensity. The abstraction process seems to stop at the B_2H_2 stage and neither B_2H nor BB could be created in significant

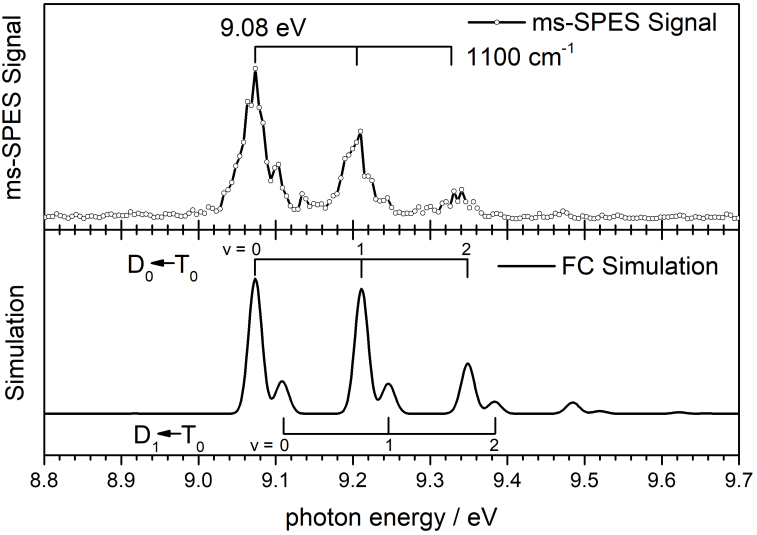

Figure 4.30.: ms-SPE spectrum of HBBH (upper trace) and the corresponding FC-simulation based on the CAS-MRCI computations (lower trace). The vibrational progressions arise from the excited B-B stretch mode in the $X^+\ ^2\Pi \leftarrow X\ ^3\Sigma_g^-$ transition. The simulation has been shifted by 0.195 eV to match the experiment.

amounts. This is in agreement with the calculated B-H bond strength in HBBH (555 kJ mol^{-1}), which is approximately equal to HF (559 kJ mol^{-1}) rendering the abstraction process close to thermoneutral at this stage. For BH_2 the abstraction process should continue, since it is 107 kJ mol^{-1} less stable than HBBH. The Franck-Condon simulations based on the CBS-QB3 calculations in comparison to the experimental spectrum are given in figure 4.29. In addition to the indications given by the mass spectrum, the HBBH simulation fits the experimental data significantly better, although it misses some small features. In cooperation with the group of Prof. Roland Mitric high-level complete active space multi reference configuration interaction (CAS-MRCI) were performed for HBBH yielding a perfect agreement with the experimental spectrum, depicted in figure 4.30.

According to the data in figure 4.30 HBBH has in IE of 9.08±0.015 eV with major vibrational peaks occurring in intervals of 1100 cm^{-1}. Upon ionization an electron is ejected from a bonding π orbital located between the two boron atoms. As a result the B-B bond length increases and the symmetric

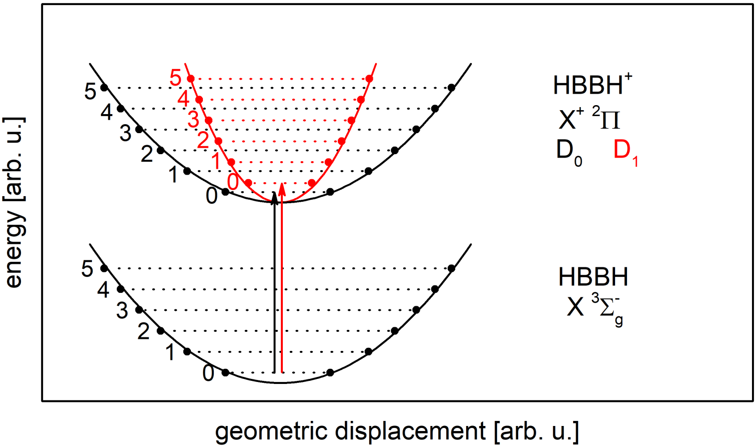

Figure 4.31.: Schematic illustration of the ionization process in HBBH. The cationic ground state is a doubly degenerate $^2\Pi$ state, in which the degeneracy can be lifted by exciting a bending motion. The different curvatures result in different zero-point energies and FC-factors.

stretching mode is excited in the HBBH cation. The latter has a doubly degenerate $^2\Pi$ ground state, in which a Renner-Teller splitting aggravates a straightforward analysis. The CAS-MRCI calculations showed that both components, referred to as D_0 and D_1, have their lowest energy at linear geometry for which the two are technically degenerate. However, at this geometry the D_1 state has a higher zero-point energy ($4801\,\mathrm{cm}^{-1}$) than D_0 ($4518\,\mathrm{cm}^{-1}$) ensuing in a second progression shifted by about $300\,\mathrm{cm}^{-1}$ (35 meV) to higher energies. The degeneracy of the two components is lifted by exciting a bending-motion, but the energetic minimum for the molecule remains linear. A visual representation of this behavior is given in figure 4.31, where D_0 and D_1 have different curvatures, resulting in different zero-point energies and FC-factors. The experimental ms-SPES cannot completely resolve the two progressions, but a defined shoulder is seen at the higher energy side of the bands. No significant hot band can be identified, indicating that the molecule is close to room temperature. The energy of the highly exothermic abstraction process is efficiently transferred to the vibrations of the HF molecules. While the CBS-QB3 method predicts the IE well within the standard error of computations, the CAS-MRCI calculations predict an IE of 8.865 eV, more than 0.2 eV below the experimental value. The bond length R_{BB} for the $X\ ^3\Sigma_g^-$ and $X^+\ ^2\Pi$ ground states were calculated to be 1.514 Å, and 1.606 Å comparable to other B=B systems. The most important parameters are summarized in table 4.8.

Table 4.8.: Important parameters for diborene HBBH.

	$X\ ^3\Sigma_g^-$	$X^+\ ^2\Pi$ (D_0)	$X^+\ ^2\Pi$ (D_1)	experiment
R_{BB}/Å	$1.514^{(a)}$ $1.506^{(b)}$	$1.606^{(a)}$ $1.604^{(b)}$	$1.606^{(a)}$	
ν_1/eV	$0.156^{(a)}$ $0.157^{(b)}$	$0.137^{(a)}$ $0.136^{(b)}$	$0.137^{(a)}$	0.14
ZPE/eV	$0.576^{(a)}$ $0.532^{(b)}$	$0.560^{(a)}$ $0.531^{(b)}$	$0.595^{(a)}$	
IE/eV	$8.865^{(a)}$ $9.019^{(b)}$			9.08±0.015

(a) CAS-MRCI
(b) CBS-QB3

4.2.1.3. Summary and conclusion

The parent diborene compound HBBH was generated through hydrogen abstraction by fluorine atoms from diborane B_2H_6. Atomic fluorine was generated in a microwave discharge of F_2 and mixed with diborane. The molecules were lead by a pressure gradient into the experimental chamber where they crossed the synchrotron light. The time-of-flight mass spectrum revealed the rich chemistry inside the fluorine reactor. The most dominant peak in the B_2H_X region was B_2H_2, which has been identified as HBBH by mass selected slow photoelectron spectroscopy. The IE was determined at $9.08\pm0.015\,\mathrm{eV}$ and the vibrational progression of $1100\,\mathrm{cm}^{-1}$ has been attributed to the symmetric stretching vibration in the cation. A second vibrational progression that is shifted by 35 meV with equal spacings is visible as shoulders on the most intense bands. The CAS-MRCI calculations proved a weak Renner-Teller effect in the cation, that splits the $^2\Pi$ ground state along a bending coordinate.

4.2.2. Slow Photoelectron Spectroscopy of BH_2, BH and BF

4.2.2.1. Motivation and Background

The presence of mass peaks in the lower and higher region of the mass spectrum in figure 4.27 was intriguing and lead to their investigation in a second set of experiments. Similar conditions were used to the previous experiments, but they were optimized for the BH_2, BH and BF signals by increasing the fluorine concentration. BH_2 is a textbook case for molecular orbital theory, in particular in conjunction with other elements of the second period, forming the famous Walsh-diagrams.[249] It exhibits a single unpaired electron which governs the structure depending on the level of excitation. The neutral ground state (X^2A_1) is bent (C_{2v}) with a bond angle of 129°, while the first excited state ($a^2\Pi_u$) exhibits a linear geometry ($D_{\infty h}$) and slightly shorter B-H bonds.[250–252] With only seven electrons BH_2 is very interesting for high level computations, thus studies on potential energy surfaces, rovibronic constants and estimations of the bent-to-linear barriers are available in abundance.[251–255] Its spectroscopic properties were first assessed in the visible and IR by Herzberg and Johns, who identified transitions of the vibronic bending mode between 11 500 cm^{-1} and 15 400 cm^{-1},[256] which were later corrected by computational methods.[252,253] Despite its model character, investigations of the IE of BH_2 are scarce and there is a significant mismatch between predictions by the calculations and experimental evidence.[257–259] First reports by Fehlner and Koski produced BH_2 by pyrolysis of diborane and found an IE of 9.8 ± 0.2 eV using electron-impact mass spectrometry.[257] However, two other studies failed to reproduce the generation of BH_2 in the thermolysis of diborane, citing thermodynamic and kinetic reasons, but one indirectly estimated an IE of 9.37 eV based on dissociation barriers.[258] In stark contrast to the experimental values, theoretical approaches predicted an IE of 9.18 eV with a bent geometry in the neutral and a linear structure in the cation.[259] Up to now, the huge difference in experimental and calculated values persist and no vibrational spectra for BH_2^+ have been reported.

The two diatomic borylenes BH and BF have been of greater interest in the recent past.[242,260–278] BH exhibits a singlet ground state $^1\Sigma^+$ and a stretching vibration of 2366.73 cm^{-1}.[250] Its first excited singlet state was determined by Fernando and Bernath to be 2.861 eV (23 073.97 cm^{-1}) above ground state level, featuring a reduced vibrational energy of 2251.46 cm^{-1}.[268] The potential energy surfaces of the triplet states were investigated by highly resolved emission spectroscopy, where an energy difference between the two lowest states $a^3\Pi \leftarrow b^3\Sigma^-$ was determined to be 3.355 eV (27 059.3 cm^{-1}) together with an elongated B-H bond of 0.03 Å in the b-state.[266] The same group also estimated the singlet-triplet gap ΔE_{ST} at 10410±300 cm^{-1} (1.29 eV) based on extrapolation of potential energy surfaces, that were derived from experimental data. Yet up to now no direct experimental values are available. The IE was measured via highly accurate Rydberg extrapolation at 9.81033 eV (79120.3 cm^{-1}) by Grant and co-workers along with a vibrational energy in the cation of 2526.58 cm^{-1}.[263]

BF is isoelectronic to CO and thus similar electronic properties are expected, however apart from the first excited states ($A^1\Pi$, $a^3\Pi$) as well as the ground state ($X^1\Sigma^+$) all other states have Rydberg character.[261,262] Due to the higher electronegativity difference in BF, its HOMO-LUMO gap and thus ΔE_{ST} is smaller than in CO (47 677 cm^{-1}) and was measured to be 29 105 cm^{-1}.[272] Investigations of the BF cation were performed by Caton and Douglas as well as by Dyke *et al.* who determined IEs of 11.115±0.004 eV[277] and 11.12±0.01 eV,[242] respectively. The vibrational frequency in the cation show greater divergence at 1680 cm^{-1}[277] and 1765 cm^{-1}.[242] Similar to CO, the bond length in BF becomes shorter upon ionization, although the HOMO is of bonding character. This effect has been well described for CO, especially in the context of π-backbonding in carbonyl complexes.[279] It is a result of electrostatic effects that increase the covalent bonding character in CO, and identical arguments have been made for BF. Theoretical predictions include accurate PES and spectroscopic constants for BF and BF^+ using high-level methods like multireference variational and single reference coupled cluster approaches.[262]

4.2.2.2. Results and Discussion

The mass spectrum displayed in figure 4.32 has been integrated over three different energetic intervals. In the lowest (7.5 - 9.0 eV) the dominant peak is at m/z=31 and 30 corresponding to $H^{11}BF$ and $H^{10}BF$ respectively. Several smaller peaks between masses 10 and 13 can be assigned to boron atoms, BH and BH_2. It is again worth noting that multiple species can be contained within one mass channel due to the two abundant boron isotopes ^{10}B and ^{11}B. In the intermediate region (9.0 - 11.0 eV) the main peaks occur in the B_2H_X section which was discussed in detail in the previous section 4.2.1. In between 11.0 and 11.2 eV the relation of peaks 30 and 31 change

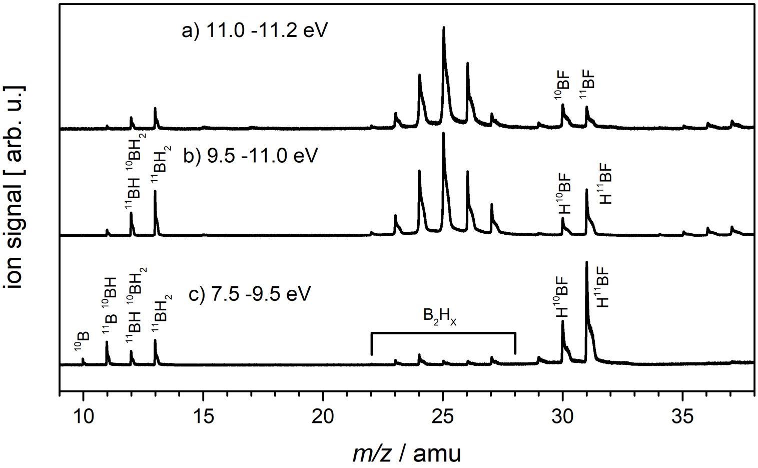

Figure 4.32.: Mass spectrum of the mixture created in the hydrogen abstraction of B_2H_6 by fluorine atoms. The spectra have been separated into three different energy regions.

to equal intensity, pointing to BF starting to get ionized, in line with the previously determined IE.

The ms-SPE spectrum of mass 13 is depicted in figure 4.33 a) together with two variants of the FC-simulation. The ionization sets in at 8.24 eV and numerous peaks up to 9.50 eV are observed in steps of 970 cm^{-1}. According to MO-theory the neutral ground state of BH_2 is bent with a single unpaired electron in a non-bonding p-orbital of A_1 symmetry. Upon ionization the electron from the SOMO is removed and BH_2^+ becomes linear with two paired electrons in its valence orbitals resulting in a singlet $(X^+\ ^1\Sigma_g^+)$ state. The most important geometry parameter that changes during the ionization process is thus the bonding angle, and the observed progression can be consequently assigned to the bending mode 2_0^n. The latter was determined to be 985 cm^{-1} in the neutral and 1012 cm^{-1} in the cation in conjunction with a shortening of the B-H bond length by 0.013 Å, although the removed electron originates from a non-bonding orbital. The most important parameters are summarized in table 4.9. Calculations on CBS-QB3 and G4 level of theory predict IEs of 8.21 and 8.28 eV in line with

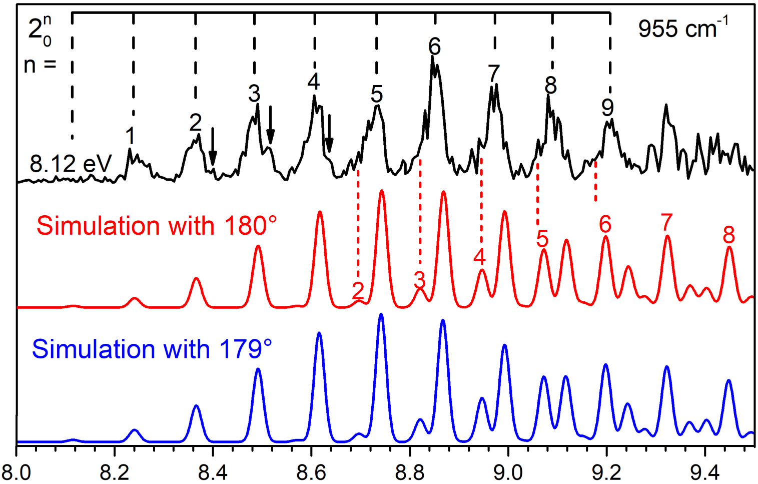

Figure 4.33.: SPES of $^{11}BH_2$ together with its FC-simulations. The simulation was shifted by 0.09 eV to fit the experiment. The IE is determined to be 8.12 eV. The pronounced vibrational activity is dominated by the BH_2 bending vibration ν_2^+.

the observed onset in the spectrum at 8.24 eV. However, when the geometry change is large, FC-factors are tiny at first and increase with transitions into higher vibrational levels, leading to a misinterpretation of the IE based on the onset in the spectrum. Since both simulations exhibit this behavior, the first peak in the spectrum is aligned with the second in the simulation resulting in a IE of 8.12±0.02 eV for BH_2 with the error estimated based on the FWHM of the other bands. Small shoulders on the lower energy side of the main bands can be observed at ∼0.75 eV above the IE, marked with red dotted lines. These can be assigned to the combination band of bending and an excited symmetric stretching mode ($1_0^1 2_0^n$), through which the vibrational frequency of the stretching mode can be estimated at ν_1^+=2680 cm^{-1} similar to the calculated value of 2664 cm^{-1}. Some additional small and not completely resolved features are marked with arrows and appear between 0.26 eV and 0.50 eV above the origin. They have no corresponding peak in the FC-simulation and have been tentatively assigned to a series of se-

Table 4.9.: Important experimental and computational parameters for $^{11}BH_2$, ^{11}BH, and ^{11}BF.

		Experiment		Theory (CBS-QB3), this work			
Spec.	E. State	IE/eV	ν/cm^{-1}	IE/eV	ν/cm^{-1}	r/Å	$\sphericalangle$
$^{11}BH_2$	X^2A_1	8.12	$2509^{(a)}$	8.21	2573	1.188	129°
			$974^{(a)}$		985		
			-		2739		
$^{11}BH_2^+$	$X^1\Sigma_g^+$	-	2680		2664	1.175	180°
			970		1012		
			-		1012		
					2953		
^{11}BH	$X^1\Sigma^+$	9.82	$2367^{(b)}$	9.84	2331	1.237	
	$a^3\Pi$	8.48	$2625^{(c)}$	8.42	2605	1.193	
$^{11}BH^+$	$X^2\Sigma^+$	-	2370		2531	1.205	
^{11}BF	$X^1\Sigma^+$	11.11	1410	11.19	1381	1.267	
^{11}BF	$X^2\Sigma^+$	-	1690		1668	1.216	

(a) Ref. [251]
(b) Ref. [268]
(c) Ref. [266]

quence bands representing the combination of asymmetric stretch (ν_3^+) and bending mode ($2_0^n 3_1^1$). In order to effectively populate the 3_1 level either temperatures of several thousand kelvin or a non-boltzmann distribution would be needed. In the upcoming paragraphs several pieces of evidence for the latter will be presented, which underline this assignment. This deviation from a boltzmann distribution can not be modeled using commonly available FC-simulation programs, and hence was neglected. The overall agreement of the simulations is perfect, with a small mismatch in the harmonically simulated progression contrary to experimental anharmonic spectrum at higher energies. With an unequal number of vibrational modes in the neutral and cation due to the bent to linear transition, simulating the spectrum is a general challenge. The two approaches used in this thesis are presented in figure 4.33, where a slightly distorted cationic BH_2 molecule with a bending angle of 179° is used (blue) or one vibrational mode in the linear BH_2 cation was deleted (red). Both produce comparable results by adjusting the number of vibrational modes in neutral and cation, albeit the latter method is more prone to errors, since two degenerate bending modes exist in the linear molecule. While deleting one component results in a perfect match for the experimental spectrum, the same treatment for the second component results in a totally different simulation as displayed in figure 4.34. Which component needs to be deleted cannot be determined *a priori*. Nearly all programs that calculate FC-factors use dushinsky rotations[280] or a variant thereof, where the normal modes of ground (Q'') and excited state (Q') are correlated by equation 4.9:

$$Q' = JQ'' + K \tag{4.9}$$

The geometry change is accounted for by K, while mixing between the modes of the ground and excited state is introduced by the parameter J. Q'' and Q' represent two column matrices with dimensions of (3N-6) and (3N-5) for neutral and cation respectively, and ultimately equation 4.9 does not work anymore when both have different dimensions. It is worth noting

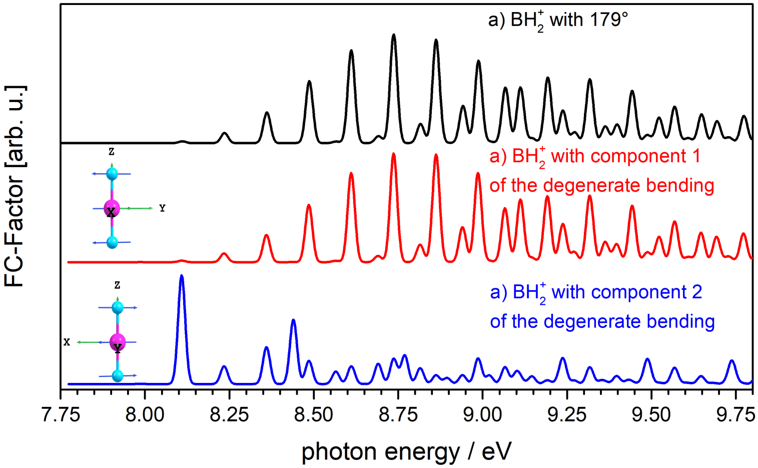

Figure 4.34.: Different FC-simulations for BH_2. a) With slightly distorted cation (179°) b) with component 1 of the degenerate bending mode c) with component 2 of the degenerate bending mode.

that the energies for the two cationic versions of BH_2 used to simulate are almost identical with differences in energy of 0.3 meV and bond lengths of 0.0004 Å. Other than the two options presented here, a meticulous analysis of the bent-to-linear transition can be carried out by accounting for the correlations between vibrational angular momentum in the linear geometry and the rotations in the bent state.[281,282] This would require highly expensive calculations, which are not necessary given the excellent agreement of the two other methods.

The ms-SPES of mass channel 12 between 9.50 and 10.70 eV is given in figure 4.35. It originates from ^{11}BH and the most intense band is visible at 9.82±0.02 eV, which is assigned to the $X^+\ ^2\Sigma^+ \leftarrow X\ ^1\Sigma^+$ transition. The previously determined experimental value of 9.81033 eV for BH was measured by Rydberg extrapolation and is in perfect agreement.[263] In addition, two more bands at +2370 cm^{-1} and +4500 cm^{-1} relative to the origin are visible and have been attributed to the BH-stretching mode based on previous reports (2526.58 cm^{-1})[263] as well as CBS-QB3 calculations (2530 cm^{-1}). The corresponding FC-simulation underestimates the

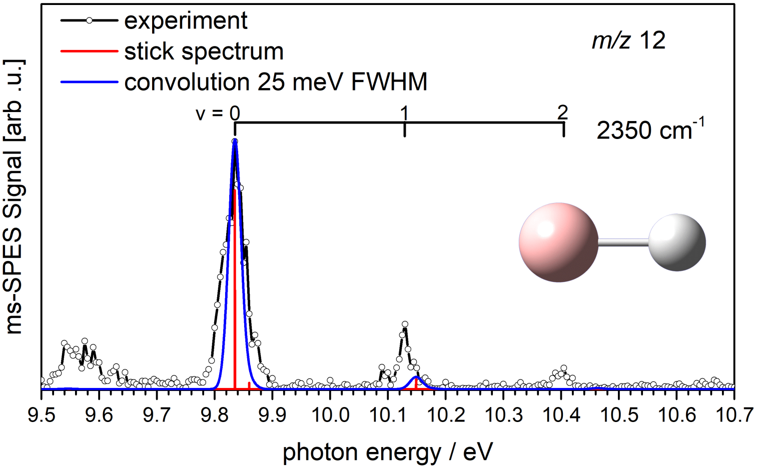

Figure 4.35.: ms-SPE spectrum of the $X^+\ ^2\Sigma^+ \leftarrow X\ ^1\Sigma^+$ transition in ^{11}BH. The IE was determined at 9.82±0.02 eV with a vibrational progression of ≈2350 cm^{-1}.

intensity of the vibrational progression, which could be caused by an underestimation of the geometry change between neutral and cationic species. At lower photon energies another band becomes visible in the same mass channel, which is displayed in figure 4.36. In this energy region several features of ^{10}BH$_2$ marked with asterisks can be seen but the peak at 8.48±0.02 eV has no corresponding signal in mass channel 13 in figure 4.33. Therefore, it must originate from a ^{11}BH species and is consequently assigned to the transition from the neutral excited state to the cationic ground state $X^{+}\ {}^{2}\Sigma^{+} \leftarrow a^{3}\Pi$. This is in very good agreement with the calculated value of 8.43 eV. Observing the aforementioned transitions in one experiment allows to determine the singlet-triplet gap ΔE_{ST} for BH at 1.34±0.03 eV (10 808±200 cm^{-1}). Using the more accurate IE by Grant *et al.*[263] this value is corrected to 1.33±0.02 eV (10 730±160 cm^{-1}). This is the first direct measurement of ΔE_{ST} within one experiment, although several calculated or indirect measurements of ΔE_{ST} exist in the literature. Brazier estimated ΔE_{ST} = 1.29 eV (10 410±300 cm^{-1}) by extrapolating potential

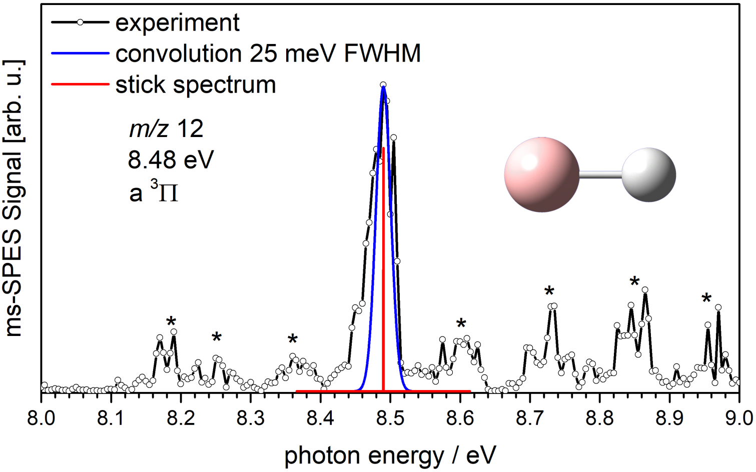

Figure 4.36.: ms-SPE spectrum of the $X^{+}\ {}^{2}\Sigma^{+} \leftarrow a^{3}\Pi$ transition in ^{11}BH. Through the IE of the $a^{3}\Pi$ state the singlet-triplet gap can be calculated at 1.34±0.03 eV using the experimental data of this study.

energy curves from experimentally observed vibrational frequencies.[266] In addition Miliordos *et al.* used high level multi-reference configuration interaction leading to a computed ΔE_{ST} value of 1.31 eV (10 588 cm^{-1}).[238] While some vibrational activity is observed when BH is ionized from the ground state, neither the simulation nor the experimental spectrum show any progression for the $X^+\ ^2\Sigma^+ \leftarrow a^3\Pi$ transition. The structure in the first triplet state ($a^3\Pi$) coincides almost completely with the cationic ground state including differences of only 0.012 Å in the B-H bond length (R_{BH}) and 74 cm^{-1} in the vibrational frequency. Contrary to that, the ionization from the $X\ ^1\Sigma^+$ ground state in BH leads to disparities of 0.032 Å in R_{BH} and 200 cm^{-1} between the neutral and the cationic species. The presence of the triplet state is a prime example of the unique conditions within the abstraction region. Although most of the energy released in the process is stored in the HF vibration, multiple, highly exothermic steps lead to the accumulation of a significant portion of energy in the generated molecules. The low pressure (∼ 1 mbar) reduces the number of collisions with the bath gas, which is due to the stored excess energy that cannot be transferred and converted. In order to detect triplet BH its lifetime has to be long enough to be generated and cross the synchrotron light in the more than 100 cm distant experimental chamber. Taking this into account and assuming similar conditions compared to the SLS photolysis setup, which has a time resolution of ∼ 1 ms for 2.1 cm, the lower limit of the lifetime is estimated to be in the range of tens of milliseconds. The double-skimming of the generated molecular beam, to select the coldest species seems to only affect the rotational temperature, with neither vibrational nor electronic excitations being sufficiently suppressed. Another explanation for this phenomenon could be the much higher efficiency in collision quenching for translational and rotational degrees of freedom. Previous measurements on the NH_2 radical show a significantly higher rotational cooling at the SOLEIL endstation, than at the SLS pyrolysis setup, with temperatures of 170 K and 300 K respectively.[283]

The ms-SPE spectrum of mass 30 (figure 4.37) originates from ^{11}BF, with the first band at 11.11±0.02 eV determined to be the IE and representing the $X^+\ ^2\Sigma^+ \leftarrow X^1\Sigma^+$ transition. This is in line with previous measurements, who measured 11.115±0.004 eV[273] and 11.12±0.1 eV.[242] Further major peaks are visible with spacings of 1690 cm^{-1} in agreement with the experimental findings of 1765 cm^{-1} by Dyke *et al.* and correspond to the BF^+ stretch mode. The Franck-Condon simulation based on CBS-QB3 calculations reproduces the experimental spectrum well and pre-

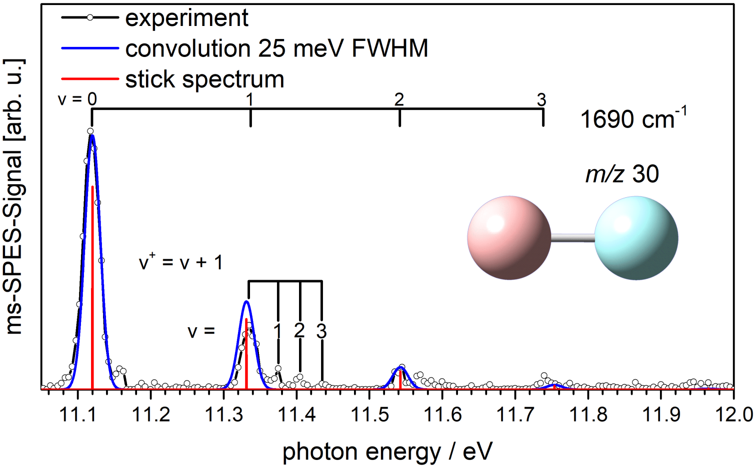

Figure 4.37.: ms-SPE spectrum of the BF molecule. The IE was measured at 11.11±0.02 eV, with a vibrational progression in the cation of 1690 cm^{-1}. Sequence bands can be seen up to $v'' = 3$ especially pronounced on the fundamental.

dicts a cationic vibrational frequency of 1668 cm^{-1}. Other, higher level methods, like MRCI and RCCSD(T), find slightly higher wavenumbers at 1700 cm^{-1} and 1699 cm^{-1}, respectively. Especially on the higher energy side of the first overtone transition several smaller bands can be identified, that have been assigned to sequence band transitions from the respective vibrationally excited ground state. They are small yet clearly distinguishable from the background and an energetic distance of 280 cm^{-1} can be measured. This value represents the difference in the vibrational energy of the neutral and the cation and thus a vibrational wavenumber of 1410 cm^{-1} can be derived, consistent with the $\omega_e = 1402.02\,cm^{-1}$ found by Zhang *et al.*[267] The presence of these sequence bands up to $v'' = 3$ proves the lack of vibrational cooling in the fluorine reactor and supports the non-boltzmann distribution seen in the species discussed previously. Due to the high vibrational excitation significant hot band activity should occur in the respective SPES. Unfortunately the appearance of the 1_1^0 band is calculated to be outside of the investigated energy region, while transitions from the

higher excited neutral vibrations overlap with the broad and more intense origin band.
The ms-SPES of HBF was also recorded, but shows no defined structure. It is displayed in figure A.4 in the appendix.

4.2.2.3. Conclusion and Summary

Next to HBBH the hydrogen abstraction from diborane produced BH, BH_2 and BF. All molecules were investigated using photoionization by synchrotron light in a i^{2}PEPICO scheme resulting in mass selected slow photoelectron spectra. The abstraction was performed by fluorine atoms produced in a microwave discharge and continuously driven by the high enthalpy of formation of the generated HF. The IE of BH_2 was extrapolated to 8.12±0.02 eV and up to 9 bands originating from the bending vibration with spacings of 970 cm^{-1} are visible in the spectrum. The origin transition has a negligible FC-factor and as such it is not observed. The first visible peak arises at 8.24±0.02 eV and belongs to the fundamental transition 2_0^1. At higher energies the progression changes and a combination band, consisting of bending and symmetric stretch (ν_1^+) vibration becomes visible. These features provide a tentative assignment of ν_1^+ at 2680 cm^{-1}. A combination of the asymmetric stretch (ν_3^+) and the bending mode is tentatively assigned to the shoulders in the bending mode progression at 2130 cm^{-1}, 3090 cm^{-1} and 4060 cm^{-1} above the origin. The existence of certain bands provides insight into the unique conditions in the abstraction region and the whole setup leading to vibrationally excited species. The most striking example of this is the BH radical. Its IE was determined to be 9.82 eV induced by the $X^+\ ^2\Sigma^+ \leftarrow X\ ^1\Sigma^+$ transition, while another band appeared at 8.48 eV assigned to an ionization process from the excited triplet state $a^3\Pi$. A vibrational activity with spacings of 2350 cm^{-1} was observed form ionization out of the $X\ ^1\Sigma^+$ state, but not for the $a^3\Pi$, as the latter has almost the same geometry as the cation. The existence of singlet and triplet states in one experiment allows the determination of the singlet-triplet gap ΔE_{ST} at 1.33±0.02 eV using the highly accurate IE measured with Rydberg extrapolation.
BF shows an IE of 11.11±0.02 eV and a vibrational progression of 1690 cm^{-1} in agreement with previous measurements. Due to the unique conditions inside the reactor sequence bands appear that offer the possibility to derive the vibrational frequency in the neutral at 1410 cm^{-1}.

All investigated molecules exhibit a non-boltzmann distribution and demonstrate that no efficient cooling can be achieved for vibrational and electronic excitations. This could be either due to the effusive molecular beam or more efficient translational and rotational cooling.

4.2.3. Threshold PES of NH_3BH_3, Borazine and HBNH

4.2.3.1. Motivation and Background

As described in the introduction of this thesis, hydrogen is investigated as one of the key energy carriers for the transition away from detrimental fossil fuels.[284–288] It exhibits an enormous gravimetric-, but a very low volumetric energy density, even when compressed at high pressures or liquefied.[18] Thus, several different materials have been designed to temporarily store and later release hydrogen when its contained chemical energy is needed. One of the most promising approaches is its chemical conversion and storage in form of ammonia borane H_3NBH_3 (AB).[284,288,289] Although the B-N unit is isoelectronic to C-C, these molecules exhibit a much higher polarity[290–293] and two sets of hydrogens, protic and hydridic, within the molecule.[294–297] As such, their properties and reactivity are vastly different compared to their hydrocarbon congeners. AB is a solid with a melting point between 97 – 119°C, more than 280°C higher than its related hydrocarbon ethane.[298–302] It is worth noting that the melting point is dependent on the heating rate, although such large melting range cannot be explained by this parameter alone and can be caused by different sample quality or experimental conditions. AB has a very high relative hydrogen content (19.6 wt%), and releases H_2 by thermolysis just over 120°C in a stepwise mechanism, forming H_2BNH_2, HBNH and BN.[301,303] The first two species could be identified by IR spectroscopy by co-pyrolysis as well as arc discharge of ammonia and diborane mixtures.[303,304] For a continuous usage, this process has to be reversible and consequently reactions must be well defined and thermoneutral. However, both amminoborane (H_2BNH_2) and imminoborane (HBNH) are highly reactive and readily polymerize to polyaminoboranes,[301] which can further decompose under elimination of more hydrogen gas to form borazine and other products.[298–300,305,306] Borazine in particular damages fuel cells and cannot be regenerated once produced, hence significant effort has been dedicated to avoid its formation in hydrogen storage systems. Nonetheless, borazine is a very attractive precursor for other material applications like in electroluminescent devices or the production of BN nanostructures.[307,308] In those fields the aforementioned differences between BN and CC subunits are exploited to help facilitate material modifications and create alternative designs, like BN-nanotubes, with superior properties like higher electron mobilities.[307] Recently it has been shown that imminoborane can interact with BN nanotubes, expanding their network by breaking B=N double bonds.[309,310] Yet, the remarkable interest in ammonia boranes and their derivatives is in stark contrast to the number of spectroscopic studies available for most of these species.

Although AB has been intensively investigated in the solid state,[311–323] gas-phase studies are scarce. Nearly all authors reported problems with tiny signals due to the extremely low vapor pressure and decomposition while trying to heat the samples.[324,325] The first gas phase study of AB was performed in 1970 by Lloyd and Lynaugh, who investigated its photoionization using regular photoelectron spectroscopy.[324] They found a vertical IE of 10.33±0.04 eV but noted that their spectrum is of poor quality as a result of partial degradation. Later they expanded their initial findings by measuring the adiabatic IE at 9.44±0.02 eV.[326] More than ten years later two microwave studies determined the B-N bond length, dipole moment, rotational barrier and zero-point structures in AB,[327,328] which were later expanded by the quadrupole splitting.[329] The first IR spectrum in the gas-phase was recorded by Sams *et al.* in 2012, who achieved rotational resolution ($>0.0035\,\mathrm{cm}^{-1}$) using a 68 m effective path length IR cell.[325] Until then the only relatable spectrum was available from a matrix isolation study,[330] that incorrectly assigned a band at $968\,\mathrm{cm}^{-1}$ to the N-^{11}B stretch mode, which was corrected to $603\,\mathrm{cm}^{-1}$ by Sams *et al.* combined spectroscopic and computational effort.[325,331] This proved that the N-B stretch reacts highly sensitive to the environment that AB is embedded in, and underlined the need for gas-phase studies on isolated molecules.

Imminoborane is the direct product when two moles of hydrogen are released by AB. It is highly reactive, isoelectronic to acetylene and has remained almost elusive so far. First computational studies rendered HBNH to be linear ($C_{\infty v}$) with a B-N bond length of 1.223 Å similar to a C-C triple bond (1.200 Å).[332,333] It was first produced by photolysis of AB in an Ar-matrix using a hydrogen discharge lamp and subsequently identified by IR spectroscopy.[334] Kawashima *et al.* managed to generate HBNH in an arc discharge of a diborane/ammonia mixture and probe it using IR spectroscopy as well.[304] The first successful gas-phase synthesis of HBNH was achieved by Zhang *et al.*, who used a cross beam experiment containing boron atoms and ammonia to detect HBNH using mass spectrometry.[335] They supported their experimental finding by quantum chemical calculations, that identified $HBNH_2$ as one possible intermediate, which can release one hydrogen atom. HBNH can also be seen as a structural variation of the diborene molecule, modifying its biradical character by substitution. Diborene was recently investigated by slow photoelectron spectroscopy (see section 4.2.1). This work offers fundamental insight into the differences between diborenes and imminoboranes.[336]

Borazine can be viewed as the cyclic trimer of imminoborane, forming as a side product in the dehydrogenation of AB. Its neutral ground state in the gas phase is planar leading to a D_{3h} symmetry, and therefore it is often referred to as the inorganic benzene, although that title is disputed.[337] Its isoelectronic properties suggest highly delocalized π-electrons and a similar, albeit lower, aromaticity to regular benzene resulting in a similar reactivity,[338] but spectroscopic observations based on nuclear independent chemical shift (NICS) values point to no aromatic character.[339] Even though borazine was first synthesized by Stock and Pohland almost one century ago,[340] its vibrational modes were only recently completely identified using inelastic neutron scattering.[341] The borazine cation was experimentally investigated multiple times resulting in two different IEs of 10.01±0.01 eV[342] and 9.88±0.02 eV,[343] but vibrations in the cation could only be tentatively assigned. Later it was recognized that the cationic ground state exhibits a Jahn-Teller splitting, similar to benzene, rendering its complete characterization difficult. Kato *et al.* used *ab initio* methods to calculate the geometries and energies of the distorted borazine cation in a C_{2v} geometry.[344] The reduced symmetry leads to a splitting in the two lowest cationic states. The $X^+\ {}^2E''$ splits up into ${}^2A_2$ and ${}^2B_1$ and the $A^+\ {}^2E'$ into ${}^2A_1$ and ${}^2B_2$. The IEs for every state were calculated to be 8.51 eV (${}^2B_1$), 8.92 eV (${}^2A_2$), 10.28 eV (${}^2A_1$) and 10.81 eV (${}^2B_2$) clearly underestimating the previous experimental results by up to 1.3 eV.

This brief overview of the available literature shows how important and fundamental these molecules are, yet their spectroscopic characterization in the gas-phase is incomplete at best. The following chapter elucidates the properties of NH_3BH_3, borazine and HBNH in the gas phase using mass selected threshold photoelectron spectroscopy.

4.2.3.2. Results and Discussion

The most tedious part before investigating the photoionization of AB is getting it into the gas-phase, which has been recognized by several authors in the past. For this reason the experiments were performed on the pyrolsis setup at the SLS, which is briefly described in section 3.2.2.1 and in detail elsewhere.[94,95] A few grams AB sample (ABCR, 99%) were placed inside a sample container with a 200 μm opening and mounted onto the pyrolysis source. The sample container was heated to 75°C at which point the vapor pressure was high enough to seed the molecular beam with AB. Higher temperatures up to 95°C were used as well but the signal did not increase, which is probably due to decomposition of AB. The mass spectrum of ammonia borane at 9.90 eV is displayed in figure 4.38 a). The dominant peak is at $m/z = 58$ which is attributed to acetone, used before to clean the sample container. Four smaller peaks appear at mass 45, 40, 31 and 30. The first two were identified as impurities originating from the chamber but no detailed characterization was performed, while the second two can be assigned to the ^{11}B and ^{10}B isotopes of AB, respectively. In figure 4.38 b) the synchrotron light was set to 10.50 eV. A new strong peak without isotopic pattern at $m/z = 17$ becomes visible, originating from ammonia (IE: 10.07 eV[345]) most likely forming as a decomposition product of AB that has been observed by others as well.[325] Although ammonia

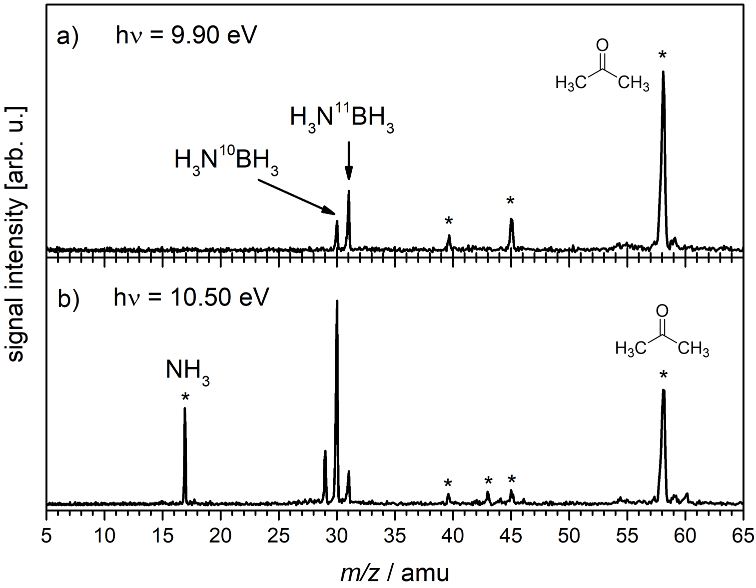

Figure 4.38.: Mass spectrum of ammonia borane (AB) at a) 9.90 eV and b) 10.50 eV. A hydrogen loss by dissociative photoionization is visible at 10.50 eV.

is a constant impurity inside the experimental chamber, ion imaging confirms the assignment as a decomposition product. The impurities above mass 40 remain negligible with an additional signal at mass 43 created by a methyl loss of acetone through dissociative photoionization (DPI). The molecule dissociates into two fragments after ionization producing a neutral, higher ionizing, and a charged, lower ionizing, species. At this photon energy mass 30 is the dominant peak in the spectrum, with masses 29 and 31 both being small, indicating the onset of a hydrogen atom loss by DPI at some point between 9.90 eV and 10.50 eV. The ms-TPE spectrum of AB is shown in figure 4.39 together with its FC-simulation. On the lower energy side the first two visible bands occur in the mass 30 channel at 9.26 eV and 9.55 eV and do not have any counterpart in the mass 31 channel. The isotopic pattern of boron rules out any contributions from AB and they have thus been linked to impurities in the chamber. At the

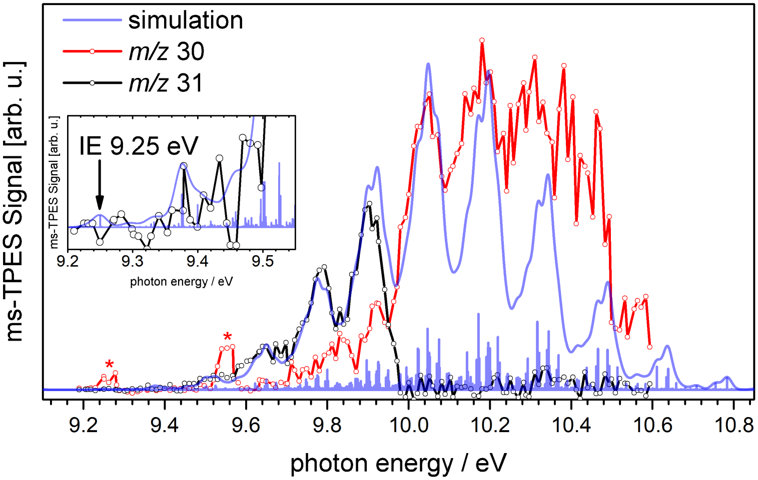

Figure 4.39.: Recorded ms-TPES of ammonia borane between 9.20 eV and 10.60 eV. The two peaks in the mass 30 channel marked with asterisks correspond to nitric oxide. The IE has been set to 9.25 eV in accordance with the vibrational progression of the FC-simulation.

end of the experiments mass spectra of the empty chamber at different ionization energies were recorded that showed a small signal at mass 30 starting to appear between 9.00 eV and 9.50 eV without the presence of mass 31. Molecules like formaldehyde and ethane can be excluded since their IEs are both above 10.50 eV,[346,347] while several CNH_4 species exhibit IEs significantly lower than 9.00 eV.[348,349] Nitric oxide has an IE of 9.26 eV[350] (74 721 cm^{-1}) and fits perfectly with the observations from the empty chamber measurements and the ms-TPE bands in mass 30. By manually selecting the molecular beam in the ion image, chamber background can be excluded from the analysis and consequently the bands disappear. However, since the overall signal intensity is small and both spectra largely coincide with each other, it was decided to use all detected coincidences in the ms-TPE spectrum. For mass 31 a first small rise can be seen at 9.47 eV with no clear vibrational structure up to 9.66 eV, afterwards broad bands appear in regular intervals of 1100 cm^{-1} up to 9.92 eV. At this photon energy the mass 31 signal decreases sharply to zero, while simultaneously the signal of mass 30 increases, underlining the hydrogen atom loss observed in the mass spectrum. The observed spectrum in mass 30 does therefore not originate from a BNH_5 species but rather represents the extended TPE spectrum of AB. Several more bands are visible, initially continuing in intervals of 1100 cm^{-1}, but getting increasingly broad and undefined at higher energies up to 10.60 eV. Similar to Lloyd and Lynaugh[326] it is tempting to attribute these bands to a single vibrational mode in the cation and determine the onset at 9.47 eV as the IE, yet ionization processes can be complex as seen in section 4.2.2. In order to get a more detailed insight into the spectrum, quantum chemical calculations on the CBS-QB3 level of theory have been performed. For simplicity, hydrogens at the boron atom will be numbered H_1 - H_3, while hydrogens attached to nitrogen will be H_4 - H_6 as depicted in figure 4.40. AB in its ground state exhibits a

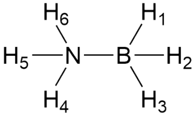

Figure 4.40.: Ammonia borane as described in this thesis. The boron hydrogens are numbered H_1 - H_3, while the hydrogens at the nitrogen are H_4 - H_6.

C_{3v} symmetry with staggered hydrogen atoms in line with previous high level computations,[325,331] although it exhibits a low rotational barrier of 8.66 kJ mol^{-1} around the B-N bond.[328] The B-H bond distances are all equal to 1.208 Å, whereas the N-H bond lengths are shorter at 1.017 Å. All HBH and HNH bond angles are identical and values of 113.67° as well as 107.81° have been determined respectively, pointing to a slightly larger pyramidalization for the NH_3 moiety compared to BH_3. The B-N bond is the longest in the molecule at 1.663 Å even longer than the C-C bond in its isoelectronic congener ethane (1.531 Å). Upon ionization the main geometry change occurs at the BH_3 group, where two bond angles increase to 119.81° each and the third decreases to 55.71°, bringing hydrogens H_1 and H_2 in close proximity to one another. The bond length of the latter two increases to 1.271 Å, while hydrogen atom H_3 is now bonded stronger to the boron with a distance of 1.173 Å. At the NH_3 subunit almost no change is observed with only small increases in the bond length and angle, however the distance between the two subunits, the B-N bond length, decreases by

Table 4.10.: Molecular parameters of AB, calculated using the CBS-QB3 method, and comparison to experimental values of ref.[328] determined by gas-phase microwave spectroscopy.

Parameter	Neutral	Experiment	Cation
d(B-N)	1.663 Å	1.6722 Å	1.555 Å
d(B-H_1)	1.208 Å	1.2102 Å	1.271 Å
d(B-H_2)	1.208 Å	1.2102 Å	1.271 Å
d(B-H_3)	1.208 Å	1.2102 Å	1.173 Å
d(N-H_4)	1.017 Å	1.0136 Å	1.024 Å
d(N-H_5)	1.017 Å	1.0136 Å	1.027 Å
d(N-H_6)	1.017 Å	1.0136 Å	1.027 Å
$\sphericalangle(H_1BH_2)$	113.67°	113.93°	119.87°
$\sphericalangle(H_2BH_3)$	113.67°	113.93°	55.94°
$\sphericalangle(H_3BH_1)$	113.67°	113.93°	119.85°
$\sphericalangle(H_4NH_5)$	107.81°	109.09°	107.20°
$\sphericalangle(H_5NH_6)$	107.81°	109.09°	105.67°
$\sphericalangle(H_6NH_1)$	107.81°	109.09°	107.20°

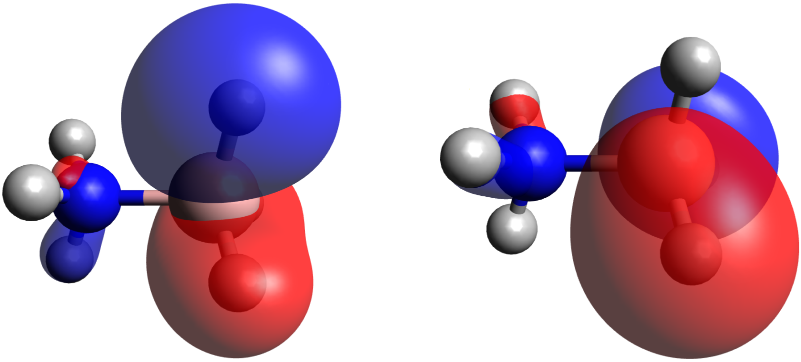

Figure 4.41.: Calculated frontier orbitals of NH_3BH_3. HOMO (left) and HOMO-1 (right).

more than 0.1 Å to 1.558 Å. The symmetry in the cation is reduced to the C_S point group. All important parameters are listed in table 4.10. To better understand the source of these geometrical changes the frontier orbitals have to be considered and analogies to the isoelectronic ethane have to be drawn. At first glance the orbitals of AB and ethane should be analogous to each other, with the only change being introduced by the different electronegativities of boron and nitrogen.[351] The two highest occupied molecular orbitals (HOMO) are displayed in figure 4.41. They have π_x and π_y character and represent bonding orbitals between the central atoms (B, N) and their respectively attached hydrogen atoms. HOMO and HOMO-1 have two nodal planes, one orthogonal to the symmetry plane (π_x) or in the symmetry plane (π_y) and one intersecting the boron-nitrogen bond. The latter renders both orbitals antibonding with respect to the B-N bond, in line with the predicted bond shortening in the cation. A third orbital, the HOMO-2 representing the bonding orbital between boron and nitrogen, is roughly 2.6 eV below the HOMO. It is clearly visible that the BH_3 moiety has an overwhelming contribution in the two HOMOs directly explaining the major geometry changes on the BH_3 site but almost none at the NH_3. Both HOMOs are completely degenerate in ethane and AB but have different symmetry characters, e_g for ethane and e for AB, due to the different point groups the molecules belong to. The MOs in the neutral only give hints which parameters are affected when an electron is removed from that orbital, they do not guarantee that the transition is intense in the ensuing TPE spectrum. For this the overlap of the nuclear wave functions of neutral and cation have to be compared, resulting in Franck-Condon factors that are dependent on the geometry of individual electronic states accessible in the cation. Since there are no detailed theoretical studies in the cationic potential energy surface of AB, and it is beyond the scope of this experimental work to perform such highly sensitive calculations, the complete ionization mechanism will be discussed on ethane. Although ethane is one of the simplest hydrocarbons its cationic energy surface has only recently been fully characterized in experiments and by theory.[347,352] The ionization can originate from three orbitals, the two degenerate C-H binding HOMOs of e_g symmetry or the C-C binding a_{1g} orbital around 0.6 eV below the first two.[347] The former is a prime example of a first-order JT effect, while for the latter no change in the molecular point group should occur. Due to the close energetic proximity in ethane the excited $^2A_{1g}$ state couples efficiently to the ^2E_g ground state, which results in a pseudo-Jahn-Teller (PJT) distortion. This leads to two slightly different equilibrium geometries with a "diborane-like" (DB) C_{2h} and a "long-bond" (LB) D_{3d} structure for the ^2E_g and $^2A_{1g}$ state respectively (see figure 4.42).[352] The energy difference between the two has been calculated to be around 250 cm^{-1} (3 kJ mol^{-1}),[353]. EPR experiments in low temperature matri-

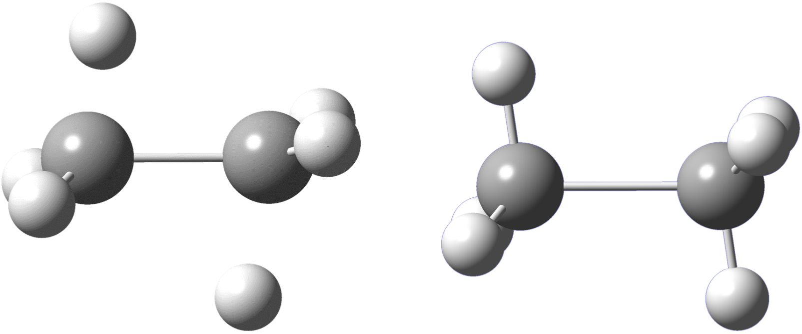

Figure 4.42.: Calculated geometries of the diborane-like (left) and long-bond structure (right) in the ethane cation. The bond lengths and angles were taken from ref.[352]

ces showed that the two structures both can exhibit pseudorotation on a sombrero PES.[354,355] The pseudorotation is completely frozen when measuring at around 4 K, which is suggested by a triplet signal in the EPR spectrum, where the spin density is located at the two longer C-H bonds of the DB structure. At 77 K the internal energy of the molecule is enough to overcome the barrier between DB and LB structure. This low barrier for DB↔LB interconversion has been confirmed by computational studies and is suggested to be between 1.2 and 6.7 kJ mol^{-1}.[353] Under these conditions the EPR spectrum shows a true septet signal, not a convolution between septet and triplet, which necessitates the fast interconversion between all DB and LB structures. The spin density is also equivalent to the charge in $C_2H_6^+$, which is completely delocalized at these temperatures. Interestingly, high resolution zero-kinetic-energy (ZEKE) photoelectron spectroscopy revealed no significant pseudorotation between the DB C_2H_6 molecules on experimental time scales (<100 ps).[347] Unfortunately, the latter study did not provide any details on the temperature of the molecules. By combining these results it was proposed, that each DB structure has access to its corresponding and higher lying LB structure. This allows interconversion between the structures since the LB structures have smaller barriers.[353,356] The final PES can be best described by a two-fold sombrero potential with each layer having three intermediates and the highest symmetry structure located in the middle. Such highly dynamical and intertwined situations cannot be simulated using conventional density functional theory and even highly sophisticated methods reach their limits in this particular case.[352]

The expected behavior of AB differs from ethane in some key aspects. Through the orbital energies, in particular the in comparison to ethane much lower HOMO-2, one can estimate that the PJT effect in AB is significantly less pronounced, shifting the corresponding $^2A_{1g}$ state upwards in energy. Therefore, the two-fold sombrero PES is significantly simplified. The barriers for the pseudorotation in the DB ethane cation originate from large geometry changes that need to be overcome, which is similar if not higher in AB. Especially the borane moiety, where large geometry changes upon ionization occur, should exhibit large pseudorotational barriers. This means that without the chance to access a LB state and with high barriers for pseudorotation, the AB cation is trapped in one specific energetic minimum. This facilitates the calculation of the cationic ground state and leads to a coinciding FC-simulation.

In order to match the experimental spectrum the IE has to be set to 9.25 eV. This value has to be handled with caution due to the complex electronic situation in AB, but is in agreement with the calculated values of 9.29 eV (G4) and 9.31 eV (CBS-QB3) as well as computational values in the literature (9.29 eV).[357] The first transitions have tiny FC-factors and can not be seen in the experimental spectrum, with the first recognizable feature at 9.37 eV being tentatively assigned to ν_{10}^{+}, the BH_3 bending vibration. The character description of some selected vibrations in the NH_3BH_3 cation is given in table 4.11. It is tempting to attribute the majority of the peaks to single vibrations or combinational modes in the cation, yet the stick spectrum shows that these bands do not originate from one single dominant transition. They rather represent a combination of different transitions, whose origins do not follow any regular pattern. A similar structure can be found in the photoelectron spectrum of ethane,[358] where a regular peak structure of 1170 cm^{-1} was initially attributed to the symmetric C-H deformation mode. High level computations by Lee *et al.* provided detailed insight into the ionization process and did not assign this structure to a single vibration, rather it is a result of a convoluted cationic potential energy surface with numerous strong vibronic interactions.[352] Exemplary for all other bands visible in the ms-TPES the most important transitions between 10.00 eV and 10.25 eV are listed in table 4.12, where a FC-factor of one has been arbitrarily assigned to the origin transition. The main vibration that is involved in most transitions is ν_{11} that can be described as a bending mode with major displacements at the boron site. By looking at the contributions of these bands it becomes clear that there is hardly any accumulation of quanta in one vibration when going to higher energies

Table 4.11.: Selected vibrations for the NH_3BH_3 cation together with their respective wavenumber $\tilde{\nu}$ and character. Please note, that the modes are sorted based on their wavenumber starting with the highest value.

mode number	wavenumber $\tilde{\nu}$ /cm^{-1}	character
ν_3^+	3389	NH_3 sym. stretch
ν_5^+	2229	BH_2 sym. stretch
ν_6^+	2010	BH_2 asym. stretch
ν_{10}^+	1023	BH_3 bending
ν_{11}^+	1211	BH_3 bending

and hence the visible pattern cannot be assigned to a single vibrational mode. The selected energy region in table 4.12 shows combinational bands of ν_{11} with ν_3, ν_5, ν_6 and ν_{10}, with a trend of including higher energetic vibrations when the energy increases while lower energetic bands show more contributions from lower energy vibrations. Because of the uncertanties and the complexity of the situation more detailed assignments in the AB spectrum would be ambiguous and require much higher resolution, thus the spectrum will not be further discussed. However, its good resolution, the intriguing peak pattern and challenging electronic situation in the cation are an excellent foundation on which high level theoretical investigations can build upon.

The recorded ms-TPES offers the possibility to determine the appearance energy (AE) of the hydrogen loss in AB. Molecules that interact with light absorb a specific amount of energy. When the initial process, e.g. the ionization, only consumes a portion of that, the surplus is distributed in the molecule. If accumulated in a specific vibrational mode it can lead to a dissociation. The AE is defined as the threshold at which dissociation of a molecule sets in. It is an important parameter, which can be used to determine the respective bond strength of a molecule or its formation

Table 4.12.: Most important FC-factors relative to the origin and the assigned vibrations for AB between 10.00 eV and 10.25 eV. Vibrational levels are given following the scheme Nν_X, with X representing the vibrational mode and N the number of quanta.

Transition energy	Assigned cationic vibrational level	FC-factor
10.03 eV	$2\nu_{11}$ $1\nu_6$ $1\nu_5$	118
10.05 eV	$1\nu_{11}$ $1\nu_{10}$ $1\nu_6$ $1\mathrm{v}_5$	117
10.06 eV	$2\nu_{11}$ $2\nu_5$	113
10.08 eV	$1\nu_{11}$ $1\nu_{10}$ $2\nu_5$	109
10.15 eV	$1\nu_{11}$ $2\nu_6$ $1\nu_5$	81
10.18 eV	$1\nu_{11}$ $1\nu_6$ $2\nu_5$	160
10.20 eV	$2\nu_{11}$ $1\nu_5$ $1\nu_3$	119
10.21 eV	$1\nu_{10}$ $1\nu_6$ $2\nu_5$	78
10.22 eV	$1\nu_{11}$ $1\nu_{10}$ $1\nu_5$ $1\nu_3$	108

enthalpy ΔH_f. To determine the AE, the fractional abundances of the parent molecule and the ionic fragment are plotted against the photon energy. Since different kinds of hydrogens exist in the molecule, it is important to determine which hydrogen bond is the weakest in the cation. While there are two sets of hydrogens in the neutral, protic (H_{4-6}) and hydridic (H_{1-3}), the cation exhibits four different hydrogens, two on each side. Scanning all B-H and N-H coordinates in AB^+ shows that the hydrogens at the nitrogen exhibit dissociation barriers of 2.5 eV (H_4) and 5 eV ($H_{5,6}$), while two hydrogens at the boron ($H_{1,2}$) need approximately 1 eV to initiate fragmentation. The third hydrogen (H_3) has a calculated dissociation barrier of 0.8 eV, which is in good agreement with the previously determined IE of 9.25 eV as well as the visible breakdown near 10 eV. It is worth noting that the literature gives values of 3.33 eV and 2.66 eV for the hydrogen loss barrier at the nitrogen and 0.67 eV for the easiest loss at the boron. This is in qualitative agreement with the values given in this thesis and discrepancies can be traced back to differences in the computational method (MP2/6-311++G(d,p) vs. CBS-QB3).[359]

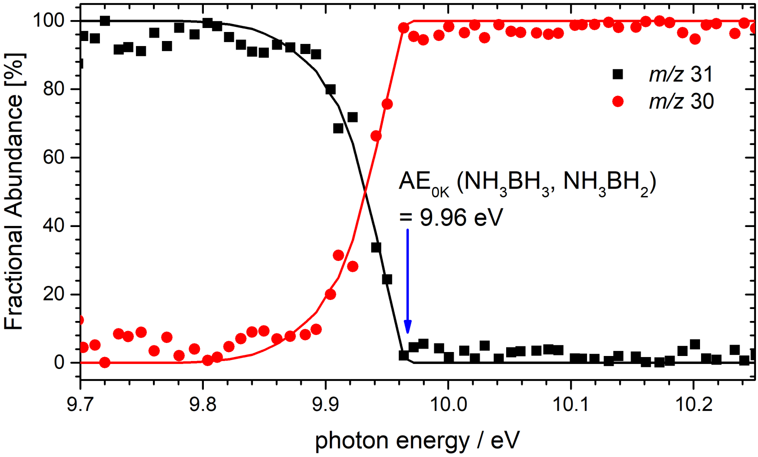

Figure 4.43.: Modeled breakdown diagram for the hydrogen loss of AB between 9.70 eV and 10.25 eV. The AE_{0K} has been determined to 9.96 eV.

Reaction (47) shows the hydrogen loss channel at the boron site, which is expected since the lone pair at the nitrogen can donate electron density to better stabilize the resulting cation.

$$\mathrm{H_3NBH_3} \xrightarrow{\mathrm{h}\nu} \mathrm{H_3NBH_2}^+ + \mathrm{H} + \mathrm{e}^- \qquad (47)$$

A hydrogen loss at the nitrogen would lead to a $\mathrm{BH_3NH_2^+}$ structure that has been found to be a transition state on the cationic PES, which isomerizes to the boryl structure without any barrier.[357] The corresponding breakdown diagram (BD) is depicted from 9.70 eV to 10.25 eV in figure 4.43. It was recorded with steps of 10 meV and integrated over 670 s each. It has been corrected for the two boron isotopes by eliminating all contributions from any ^{10}B species using the statistical abundances. Mass spectra at the dissociation threshold were symmetric, hence no kinetic shift of the AE is expected in the modeling using statistical rate theory. For the fit to have satisfactory agreement with the experimental data the temperature of the molecules has to be set to 220 K. The AE_{0K}, where the parent molecule is completely dissociated to the daughter has been determined to be 9.96 eV. Therefore, the cationic bond dissociation energy for a hydrogen loss at the boron site of $\mathrm{NH_3BH_3}$ is 0.71 eV when using the just determined IE and AE. Note that no reverse barrier was computed for reaction (47).

Borazine

Borazine was synthesized using protocols available in the literature[360,361] and characterized by ^{1}H-, ^{11}B-NMR, Raman and gas-phase IR-spectroscopy. At room temperature it is a liquid with a very high vapor pressure (113 mbar at 273 K[360]) readily available for gas-phase studies. It was introduced into the endstation through an effusive inlet to investigate its photoionization without any cooling effects from molecular beam expansion. Figure 4.44 shows the mass spectra recorded at different photon energies between 10 and 14 eV in 2 eV steps. Borazine exhibits a clear isotopic pattern with masses between $m/z = 81$ and $m/z = 78$, coming from $^{11}B_3N_3H_6$ and $^{10}B_3N_3H_6$, respectively. The relative intensities of the peaks can be deduced from the natural abundance of the two boron isotopes and were calculated to be 1.00/0.75/0.18/0.02 for masses 81 to 78 respectively. The theoretical intensities match the pattern at 10 eV but change afterwards with the dominant signal shifting to mass 80. This is a strong indication for a hydrogen loss

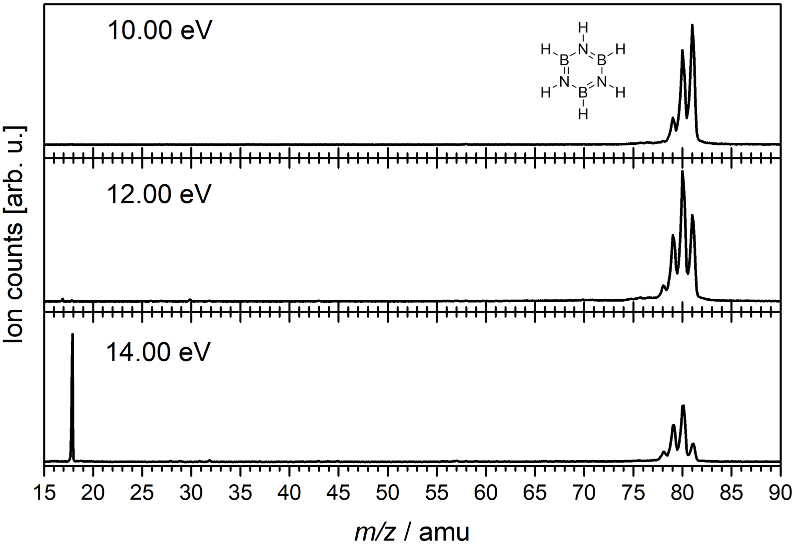

Figure 4.44.: Mass spectra of borazine at different photon energies between 10.00 eV and 14.00 eV.

by DPI, as previously found in AB. In principle other DPI channels can exist and have been observed previously using electron ionization at 70 eV, however they have not been found below hν=14 eV in this thesis. Next to the borazine signals, other mass peaks can be found, specifically at masses 18, 32 and 58, representing water, oxygen and acetone, respectively, which are all present as impurities in the chamber.

The ms-TPE spectrum of mass 81, the most intense borazine peak, can be found in figure 4.45. The first peak is visible at 10.01±0.02 eV with two more peaks in intervals of roughly 750 cm^{-1}. At higher energies the spectrum is mostly unstructured and decreases until 10.92 eV before showing another broad unstructured band at 11.34 eV, after which the signal declines to zero. It is worth noting that between the IE and 11.60 eV the spectrum never reaches the initial background levels. This indicates a convoluted PES with multiple low intensity transitions that cannot be resolved. Based on the ms-TPE spectrum the adiabatic IE of borazine was determined to be 10.01±0.02 eV. This is in perfect agreement with the results by Frost *et al.* of 10.01±0.01 eV[342] as well as the calculated IE of 10.03 eV (CBS-QB3), whereas the value of 9.88±0.02 eV found by Lloyd and Lynaugh is some-

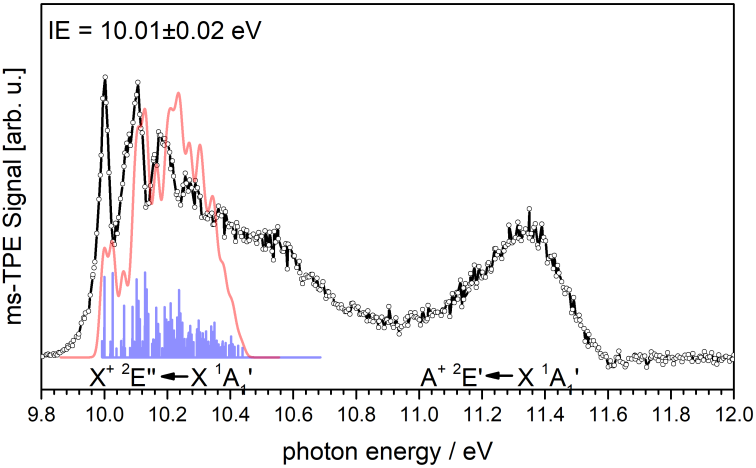

Figure 4.45.: ms-TPES of borazine. Only the most intense mass 81 was selected.

what lower.[343] The corresponding FC-simulation on CBS-QB3 level of theory shows an unsatisfactory agreement between experiment and theory for which a JT-distortion in the cationic ground state could be responsible. The sharp decline at 11.5 eV is identical to AB and shows the H-atom loss by DPI, from which a preliminary AE of 11.6±0.1 eV can be deduced. The complete breakdown diagram is illustrated in figure 4.46. There are two possible sites where a hydrogen can be lost, since two kind of hydrogens, hydridic and protic, exist in the molecule. Calculations showed that in the cation, hydrogens bound to a boron have a bond strength of 174 kJ mol^{-1} (1.80 eV), while the protic hydrogens bound to the nitrogens have a bond strength of 417 kJ mol^{-1} (4.32 eV), rendering a hydrogen loss on the boron atom more likely, as has been suggested by the literature.[344] In a qualitative way, a hydrogen loss leaves the boron atom with a positive charge that can be better stabilized by the adjacent nitrogens than the other way around. A complete analysis of this process using statistical rate theory is currently being performed by Marius Gerlach.

Upon closer inspection the spectrum of borazine offers a much more nuanced picture, as depicted in figure 4.47. Since the two visible peaks at

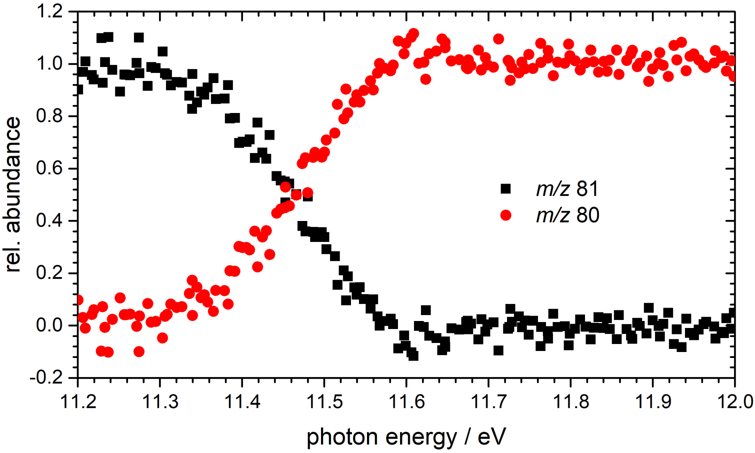

Figure 4.46.: Breakdown diagram recorded for the hydrogen loss of borazine between 11.20 and 12.00 eV.

10.11 eV and 10.20 eV are almost equidistant with respect to the origin, one can initially assume that they originate from the same vibration in the cation. However, the second band at 10.11 eV is asymmetric with a clear shoulder on the lower energy side and the previously identified third peak at 10.20 eV can be separated into two bands that are hardly resolved in the spectrum. In addition one finds several more, less intense bands that are clearly discernible from the background signal at higher energies, which have been marked with arrows up to 10.50 eV.

The FC-simulation given in figure 4.47 has been modified by multiplying the FC-factor of the origin transition by four. The simulation now agrees somewhat better, although its vibrational structure seems to be blue-shifted with respect to the experiment. A similar underestimation of the origin transition in the simulation was observed in the TPE spectra of adamantane and benzene.[362,363] In the former, the authors attributed this behavior to autoionization effects. They can be identified by looking at the PIE curve of

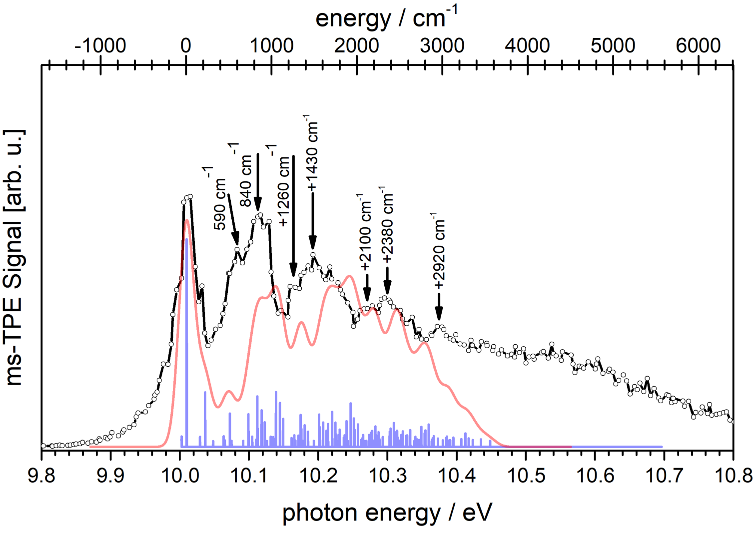

Figure 4.47.: ms-TPE spectrum of borazine between 9.80 and 10.80 eV. The corresponding FC-simulation has been modified by multiplying the origin transition by four.

mass 81, where the origin should exhibit a peak instead of a constant rise, if autoionizing states are present in borazine. However, this is not the case and consequently the mismatch between simulation and experiment cannot be explained by autoionization. A much more plausible explanation is the JT effect in the borazine cation, which is not considered in the CBS-QB3 calculations.

The previously recognized convoluted PES is, however, reasonably well reproduced in the simulation, which can be seen by the stick spectrum. Yet, due to the neglected JT effect, the assignment of the vibrational structure in the ms-TPE spectrum of borazine based on the FC-simulation has to be handled with caution. Thus, it is difficult to precisely attribute any band to one specific transition. The simulation suggests a clear peak at 10.06 eV, which would correspond to a ring twisting mode ν_{25}^{+}, but it is integrated into the second peak, which causes the asymmetry in the peak structure. The broadening is further amplified by several other intense vibrations, before the highest intensity is reached at $+840\,\mathrm{cm}^{-1}$. The third peak also consists of several overlapping transitions and afterwards the remaining peaks are only slightly above background levels. The spectrum requires a much higher resolution to identify these bands, which cannot be achieved with the utilized setup at the SLS. Reducing circle- and ringsize only lead to a minor improvement in spectral resolution. However, even with a well resolved spectrum assignments might be difficult to verify, especially with a FC-simulation on CBS-QB3 level.

At this point, a comparison with the organic counterpart of borazine, benzene, is warranted. The latter has been investigated in much greater detail and differences between the two spectra provide insights into the individual electronic structure of the molecules. For benzene numerous experimental studies using photoelectron,[363–366] EPR[367,368] and fluorescence spectroscopy[369,370] have focused on its cationic ground state equilibrium structure. In addition several theoretical approaches have been pursued to characterize the benzene cation completely.[371–373] Its lowest ground state geometry has been found to be of D_{2h} symmetry by high-resolution ZEKE-PFI experiments[57] in which two opposing C-C bonds either truncate or elongate. Both distorted benzene species exhibit only tiny barriers for interconversion, that proceeds via a pseudorotation on a sombrero-type PES, best illustrated in ref.[373] Thus, it was concluded that the structure is too fleeting and it should be treated as a symmetric species but without electronic degeneracies.[373] This observation has been supported by theory,

where the distortion away from the D_{6h} geometry stabilizes the cation by 0.18 eV but the barrier of pseudorotation is only 3 meV.[57]
The JT effect in the borazine cation was investigated by Kato *et al.*, who determined that the equilibrium structure for the ground state belongs to the C_{2v} point group, where one NH subunit is distorted out of the ring.[344] The E" and E' states consequently split up into two sublevels $^2B_1$ and $^2A_2$ as well as $^2A_1$ and $^2B_2$, respectively. Their energy difference with respect to the D_{3h} structure were calculated to be 0.42 eV for the X^+ ^{2}E" and 0.48 eV for the A^+ ^{2}E' set, although the splitting between the A and B states is very small with 0.03 eV and 0.02 eV, respectively. This also leads to a pseudorotation in the cationic ground state with a barrier lower than its zero-point energy, which therefore cannot be suppressed. As a result the three different C_{2v} structures are converted into each other on a vibrational time scale and so the borazine cation behaves like its highly symmetric D_{3h} structure.[57] In other words, the borazine and benzene cations have ground state wavefunctions that cannot be accurately described using a standard DFT approach, like CBS-QB3. It is worth noting that the calculated IEs

Table 4.13.: Selected vibrational modes in the borazine and benzene cation. For borazine all frequencies have been calculated using the CBS-QB3 method. Character assignments and vibrational frequencies for benzene have been taken from ref.[364] The vibrations were numbered in sequential fashion starting at the highest to the lowest wavenumber $\tilde{\nu}$.

	Benzene$^+$		Borazine$^+$	
Mode	$\tilde{\nu}$ /cm^{-1}	Character	$\tilde{\nu}$ /cm^{-1}	Character
ν_1	3191	C-H symm. (a_{1g})	3584	N-H stretch
ν_3	3168	C-H as. stretch (e_{2g})	3516	N-H as. stretch
ν_6	1610	C-C (e_{2g})	1440	H-B-N-H bend
ν_{13}	1178	H twist (e_{2g})	1043	(B-H) twist
ν_{19}	995	ring-breathing (a_{1g})	872	ring-deformation
ν_{20}	-	-	824	ring-breathing
ν_{25}	607	ring-twist (e_{2g})	503	ring-twist

for these transitions by Kato *et al.* differ significantly from experimental measurements and hence their splitting values could also exhibit large error bars.

The photoelectron spectrum of benzene has been simulated by Eiding *et al.* who used a multimode approach, that considers linear JT-coupling for totally symmetric and degenerate modes of E_{2g} symmetry all of which are listed in table 4.13.[364] They recognized that multimode JT problems are hard to analyze due to strong mode-mixing effects. By expanding a single-mode JT calculation into a two-mode JT problem, the intensities of individually computed bands can decrease due to mixing between the modes. The results are several partially resolved peaks and simulations get more convoluted the more degenerate modes are used for the multi-mode JT description. Eiding *et al.* used three degenerate (ν_6, ν_{13}, ν_{25}) and one totally symmetric (ν_{19}) mode to describe the vibrational progression in the benzene cation ground state. Later, Baltzer *et al.* recorded a well resolved photoelectron spectrum of benzene, and only identified two different vibra-

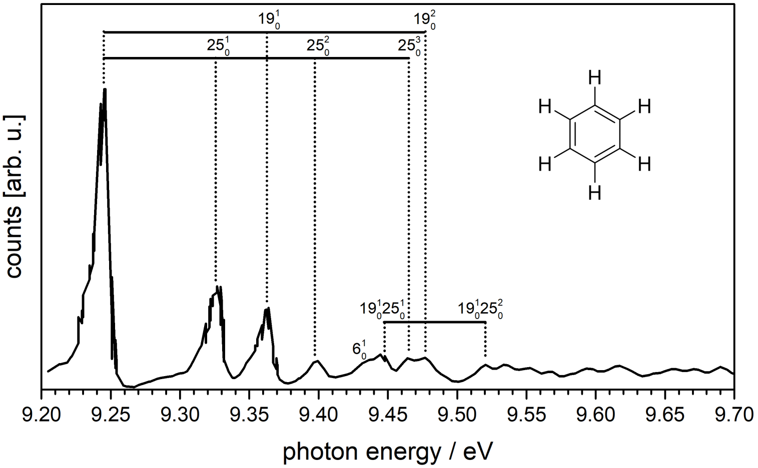

Figure 4.48.: Recorded photoelectron spectrum of benzene by Baltzer *et al.* and their vibrational assignments.[365] Note that the mode numbers have been altered with respect to the original paper to be consistent with the description in table 4.13.

tional modes ν_{19} and ν_{25} and combinations thereof (see figure 4.48). They found, that up to 0.3 eV above the origin, bands are clearly separated, while the vibrational structure gets more and more convoluted beyond that value, which is in perfect agreement with the established multi-mode approach.
The photoelectron spectra of benzene and borazine are compared in figure 4.49. They have been modified so that the origin transitions overlap but the corresponding x-axis cover the same absolute range, as to not distort the vibrational structure. The y-axis has been scaled, so that the background level for each spectrum is at zero and the intensities of the origin transitions match each other. For the sake of simplicity, the spectra will be divided into two sections: A lower energetic part, up to 0.3 eV above the respective origin and a higher energetic section starting at this value. In the latter no clear structure can be found in either molecule, pointing towards various low intensity transitions in both. Yet, while in benzene the signal is close

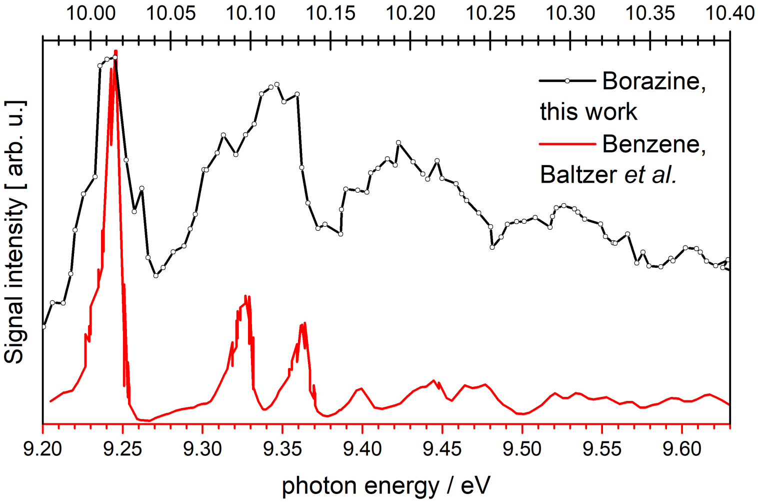

Figure 4.49.: Direct comparison between the photoelectron spectrum of borazine (black) and benzene (red). The bottom x-axis belongs to benzene, while the top one corresponds to borazine. Note that both spectra have been recorded using different methods (HeI vs. TPES).

to the background level, the borazine signal is at about half the intensity of the origin band. Hence, it is reasonable to assume that in this region borazine exhibits significantly more transitions of various different modes, possibly due to its lower symmetry. However, it could also be that the origin transition in borazine is less pronounced with respect to benzene, which could also explain the relative differences. This would mean that benzene undergoes a smaller geometry change upon ionization than borazine.

In the lower energy region benzene exhibits distinct bands, whereas borazine already shows asymmetric and overlapping peaks, which could be due to resolution differences between the two spectra. Baltzer *et al.* give a resolution of 4 meV (FWHM), while for borazine a resolution of 20 meV (FWHM) is achieved. These experimental factors certainly play a role, but citing them alone would be too narrow considering the complex situation of the molecules. Another possible cause for the broad borazine spectrum is the presence of other intense transitions. It has been assumed that such transitions exist in the higher energetic section based on the high signal intensity, and so their occurrence right above the origin is reasonable.

With that being said, overall the two spectra coincide very well on a qualitative level, but the vibrational structure of borazine seems to be red-shifted with respect to benzene. Some selected modes in benzene and borazine are juxtaposed in table 4.13. It can be seen, that the vibrational modes in borazine have lower frequencies, when the central ring atoms are involved. According to Baltzer *et al.* these are the most important vibrations to describe the ground state structure in cationic benzene. The lower frequency causes vibrations to be less separated and consequently the peaks will overlap more in the case of borazine. Yet, the exact origin of the discrepancy between the benzene and borazine photoelectron spectra cannot be identified at this point. The numerous plausible explanations and the high complexity of the electronic situation in the cation underline the need for a correct theoretical description in borazine, which includes the vibronic effects like in the well-established multi-mode JT approach. Hence, even though the simulation based on CBS-QB3 level is somewhat decent, assignments should not be made based on it, due to its failure to consider the JT effect.

It is also interesting to compare borazine to another, more similar molecule, s-triazine, which both belong to the same point group (D_{3h}), and possess less aromatic character than benzene. Ionization of triazine occurs from a non-bonding lone pair at one of the nitrogens, which represents a degenerate pair of orbitals of e'-symmetry.[374] The cationic ground state distorts away from the D_{3h} symmetry towards a C_{2v} geometry and is stabilized by 0.47 eV with respect to the conical intersection[374] (benzene 0.18 eV,[375] borazine 0.42 eV[344]). Like benzene and borazine, s-triazine exhibits a pseudo-rotation with a barrier of ≈10 meV, well below its zero-point-energy resulting in a similar dynamic in both cases. It would be an ideal target for comparison, to investigate the influence of JT-stabilization and point group dependence in the neutral on the performance of the FC-simulation, but unfortunately there are only low resolution photoelectron spectra of s-triazine to this date.[376]

One of the most interesting aspects during this project is the evaluation of FC-simulation performance based on DFT calculations in molecules with one or even multiple vibronic effects. This is best illustrated by looking at the FC-simulations of borazine based on the optimized structures of different computational methods depicted in figure 4.50. While CBS-QB3, MP2 and CCSD agree qualitatively with each other, G4 predicts a different onset and structure, demonstrating the high susceptibility to errors in the

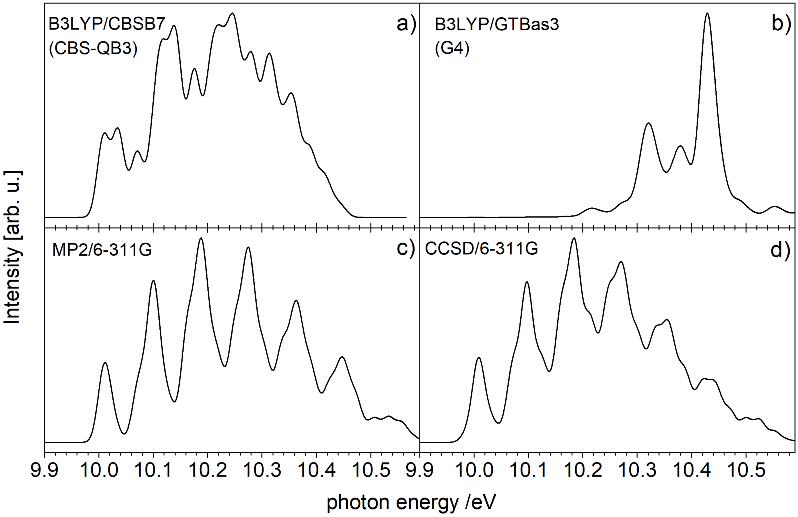

Figure 4.50.: FC-simulations of borazine using different computational methods.

calculations. In all cases the simulation does not accurately reproduce the experimental spectrum although the spacing up to 10.50 eV is somewhat best represented in the CBS-QB3 calculation. The CCSD and MP2 calculations are very similar to each other, but somehow fail to reproduce the complex PES.

In order to analyze transitions into excited cationic states the ms-TPE signal has to be integrated over all masses of borazine and borazine-H. The illustrated spectrum in figure 4.51 shows no intense peaks in the region above 11.5 eV, although some smaller bands at 12.8 eV and 13.7 eV can be seen. The spectrum has been multiplied by two from 12.50 eV onward to account for a change in integration time (1:2) during the measurement. To identify the source of all bands, the electronic situation in the neutral and the cation needs to be considered. The neutral borazine molecule exhibits a D_{3h} symmetry and possesses two sets of doubly degenerate HOMOs, one of π symmetry and one of σ symmetry, that are 1.7 eV apart. The HOMO and HOMO-1 have π character and transform as an E” representation, while HOMO-2 and HOMO-3 have σ character and transform as an E’ repre-

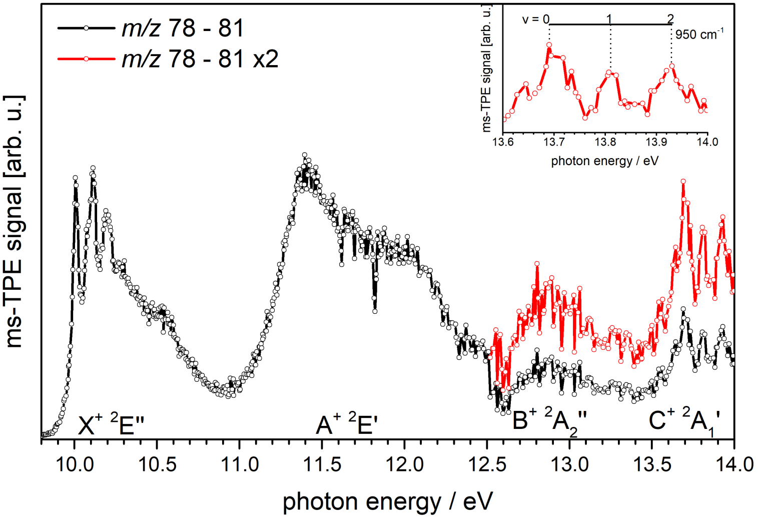

Figure 4.51.: ms-TPES of borazine integrated over masses 78 - 81.

Table 4.14.: Important experimental and computational parameters for borazine and benzene.

		Experiment	Theory	
Species	E. State	Rel. Energy/eV	Rel. Energy/eV	Ref.
Borazine	$X\ {}^{1}A_1'$	0	0	
Borazine^{+}	$X^{+}\ {}^{2}\mathrm{E}''$	$10.01^{(a)}$	$10.03^{(d)}$	this work
		$10.01^{(a)}$	$9.8^{(e)}$	[342]
		$9.88^{(a)}$	-	[343]
	$A^{+}\ {}^{2}\mathrm{E}'$	$11.34^{(c)}$	-	this work
		$11.42^{(b)}$	$10.4^{(e)}$	[342]
		$11.42^{(b)}$	-	[343]
	$B^{+}\ {}^{2}\mathrm{A}_2''$	$12.81^{(c)}$	-	this work
		$12.82^{(b)}$	$14.0^{(e)}$	[342]
		$12.83^{(b)}$	-	[343]
	$C^{+}\ {}^{2}\mathrm{A}_1'$	$13.69^{(a)}$		this work
		$13.98^{(b)}$	$14.8^{(e)}$	[342]
		$13.84^{(b)}$	-	[343]
Benzene	$X\ {}^{1}\mathrm{A}_{1g}$	0	0	
Benzene^{+}	$X^{+}\ {}^{2}\mathrm{E}_{1g}$	$9.243^{(a)}$	$9.12^{(f)}$	[365]
			$8.99^{(f)}$	[372]
	$A^{+}\ {}^{2}\mathrm{E}_{2g}$	$11.488^{(a)}$	$12.09^{(f)}$	[365]
			$12.03^{(f)}$	[372]
	$B^{+}\ {}^{2}\mathrm{A}_{2u}$	$12.3^{(b)}$	$12.37^{(f)}$	[365]
			$12.12^{(f)}$	[372]
	$C^{+}\ {}^{2}\mathrm{E}_{1u}$	$14.0^{(b)}$	$14.39^{(f)}$	[365]
			$14.31^{(f)}$	[372]

$^{(a)}$ adiabatic value
$^{(b)}$ vertical value
$^{(c)}$ peak of the band
$^{(d)}$ CBS-QB3
$^{(e)}$ INDO
$^{(f)}$ OVGF (outer valence Green's function)

sentation. Below these two sets of doubly degenerate orbitals lies a non-degenerate π-orbital of a_2" symmetry. Under the assumption of Koopmans theorem, the first three excited states would correspond to the symmetry of the orbital from which ionization takes place namely e", e' and a_2". Yet, as previously noted, ionization from completely filled degenerate orbitals causes adiabatic couplings between the cationic states and JT splittings. However, in zeroth order these effects can be neglected in the description of the excited states. Therefore, the first three states can be describes as $X^+\ ^2$E", $A^+\ ^2$E' and $B^+\ ^2A_2$", which is in agreement with the assignment from a combined experimental and theoretical study by Frost *et al.* One more peak can be seen starting at 13.69 eV, exhibiting a pronounced vibrational activity, which was also observed by others. Calculations by various authors independently suggest that this state originates from the ionization from an a_1' symmetric orbital. An energy of 13.83 eV has been calculated by Ortitz using partial third-order quasiparticle theory,[377] matching the experimental finding within 0.1 eV. Before the calculations were performed, experimental studies assigned the peak to different symmetries. Frost *et al.* attributed it to an E' symmetry,[342] while Lloyd and Lynaugh referred to it as A_1'.[343] The vibrational structure with a spacing of 950 cm^{-1} is significantly lower than the values of 1900 cm^{-1} and 2100 cm^{-1}, which have been found by other experimental studies.[342,343] Due to its A_1' character it is not subject to a JT distortion and the visible spacings might represent a ring-deformation mode, where one N-H subunit is distorted out of the ring. Using the CBS-QB3 calculations such a vibration has a frequency of 958 cm^{-1} in the cation.

The excited states of borazine can also be compared to its organic counterpart benzene, for which the excited state dynamics in the cation have been recently elucidated by femtosecond-resolved pump-probe experiments. A series of conical intersections determine the deactivation process from the fifth excited state on a vibrational time scale.[378] These strong vibronic interactions are caused by JT effects, which have been found in several excited states in a theoretical evaluation of the benzene cation PES.[372,373] Other non-adiabatic couplings, like mixing of excited states into lower lying ones lead to equally significant interactions that contribute to a highly convoluted PES with multiple electronic states mixing at the equilibrium geometry of the benzene cation. Döscher *et al.* explained this highly convoluted electronic situation by computations using a linear vibronic coupling approach.[372] In this approach diabatic wave functions are chosen and the off-diagonal electronic matrix elements, that induce couplings between two states are expanded into a Taylor series, proving that the complete characterization of such a PES is non-trivial. The state description for borazine given by the calculations predict a similar behavior, yet the much higher JT splitting in borazine might slow down the deactivation process. A summary of the ionization energies for borazine and benzene as well as the description of their cationic states is found in table 4.14.

HBNH

Borazine was pyrolyzed using the setup described in section 3.2.2.1. To identify the pyrolysis products several mass spectra have been recorded at various photon energies and pyrolysis powers. Figure 4.52 shows mass spectra at 11.50 eV and three different pyrolysis powers between 0 and 60 W. The signal of borazine constantly decreases towards higher pyrolysis powers but remains the most intense peak even at 60 W, rendering it extremely stable with respect to rapid thermal decomposition. The peak at mass 17, which has been identified as ammonia by its ms-TPES, already appears without

pyrolysis and increases significantly at higher pyrolysis powers. Masses 26 and 27 start to appear at 30 W and constantly increase up to 60 W. Their intensities resemble the typical boron isotopic pattern and can be assigned to iminoborane HBNH. In principle DPI processes can convolute

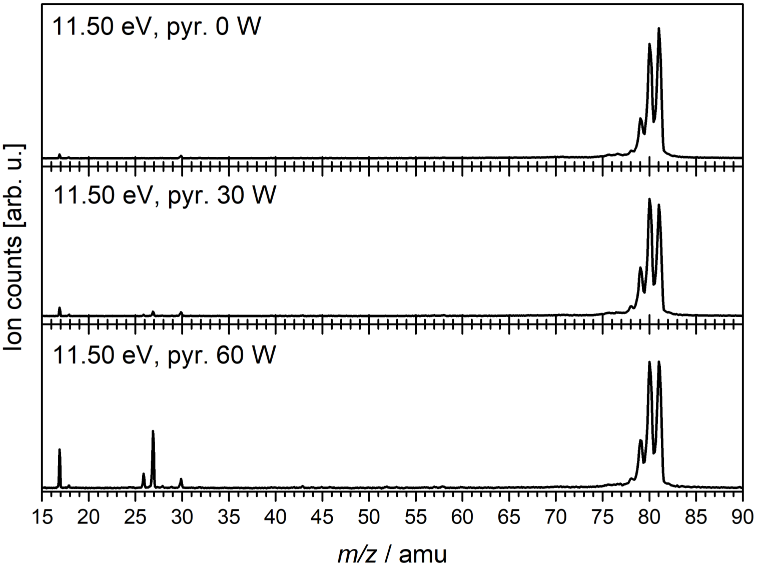

Figure 4.52.: Mass spectra of borazine at different pyrolysis powers up to 60 W.

the investigation of pyrolysis products when the precursor is not completely destroyed, but since no DPI channels have been found that produce HBNH up to 14 eV, left over borazine does not affect its investigation. Iminoborane is a linear molecule with $C_{\infty v}$ symmetry, a $^1\Sigma^+$ ground state and a BN bond order of 3. Its electronic configuration in the ground state is $...(3\sigma)^2(4\sigma)^2(5\sigma)^2(1\pi)^4$ with the two HOMOs being a degenerate pair of orthogonal BN-bonding π-orbitals with a higher contribution at the nitrogen.[332] The electronic situation is therefore similar to HBBH for which the MOs have been displayed in figure 4.26. The ms-TPES of HBNH was recorded at 60 W pyrolysis power between 11.10 eV and 12.00 eV in steps of 5 meV, which is illustrated in figure 4.53 for masses 26 and 27 to include both boron isotopes. Both ms-TPES show a relative intensity of 4:1 and largely coincide with each other, proving that they originate from a single boron containing species. In the mass 26 channel two peaks visible at 11.40 eV and 11.62 eV do not have a corresponding counterpart in mass channel 27. They have been attributed to residual acetylene inside the

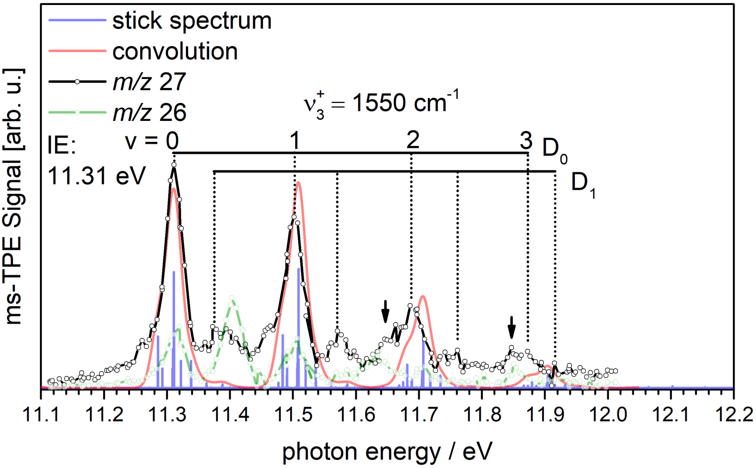

Figure 4.53.: ms-TPES of HBNH between 11.10 eV and 12.00 eV. Both mass channels show coinciding peaks, with acetylene peaks at 11.40 eV being visible in the m/z = 26 channel as well. The spectrum was simulated at 1000 K.

chamber. The peaks are in perfect agreement with TPES measurements available in the literature, which found an IE of 11.400±0.005 eV and a vibrational progression of 1811 cm^{-1} (224.6 meV).[379] Using the spectrum illustrated in figure 4.53, the IE, vibrational progression as well as possible vibronic interactions will be analyzed and compared to the simulated spectrum based on CBS-QB3 calculations. The ms-TPES of HBNH shows four intense bands in regular intervals with the peak of the first band at 11.31±0.02 eV, which has been assigned as the IE. This is in perfect agreement with the calculated value of 11.31 eV and originates from the ejection of an electron in one of the HOMOs in a $X^+\ ^2\Pi \leftarrow X^1\Sigma$ transition. The equidistant band structure can be explained by a pronounced vibrational progression in the cation with a spacing of 1550 cm^{-1} up to the second overtone. The removal of an electron from the BN-binding HOMOs reduces the bond order and the distance between the two atoms increases, resulting in a vibrational activity of the symmetric BN stretch mode (ν_3^+) in the cation. This is confirmed by computations where a B-N bond length of 1.234 Å is found for the $X^1\Sigma$ state and 1.307 Å for the $X^+\ ^2\Pi$ state. Accordingly, the energy of the B-N-stretch mode is lowered from 1780 cm^{-1} to 1533 cm^{-1} in the neutral and cationic ground states, respectively, which is almost identical to the experimentally determined value. The most important parameters of HBNH are summarized in table 4.15. The FC-simulation largely coincides with the experimental spectrum. Towards higher energies the harmonic simulation is increasingly blue-shifted with respect to the

Table 4.15.: Molecular parameters of HBNH, calculated using the CBS-QB3 method, and comparison to experimental values. The vibrational frequencies have been scaled by 0.96.[380]

Parameter	Neutral	Cation	Experiment
d(B-N)	1.234 Å	1.307 Å	-
d(B-H)	1.167 Å	1.169 Å	-
d(N-H)	0.990 Å	1.016 Å	-
$\sphericalangle$(HBN)	180°	180°	-
$\sphericalangle$(BNH)	180°	180°	-
ν_3	1780 cm^{-1}	1533 cm^{-1}	1530 cm^{-1}
IE	11.31 eV	-	11.31±0.02 eV

spectrum due to the anharmonicity of the potential well. The intensities in the experimental spectrum constantly decline, while the simulation predicts the fundamental transition to be the most intense, therefore overestimating the B-N bond length in the cation. Small shoulders on the lower energy side of the bands are especially prominent on the third and fourth band, where they have been marked by arrows, but are also present at the fundamental and origin transitions. In all cases they represent combinations of ν_3^+ with sequence band transitions of the form $7_1^1 3_0^n$ and $4_1^1 3_0^n$, to illustrate the two most intense. In the simulation they exhibit oscillator strengths of 39% and 33% of the respective higher lying main 3_0^n transition. By comparing the simulation and the experimental spectrum, one can see, that the broadening of the peaks is well represented by the simulation. However, the intensity of the sequence bands is somewhat underestimated, especially in the last two bands pointing either towards a greater thermal excitation in the experiment or an underestimation of the FC-factor by the simulation. Similar side bands arise at the higher energy side of all bands, which could have two different origins. Since HBNH has completely filled degenerate HOMOs with π symmetry, its situation is similar to borazine, where a JT effect leads to a distortion in the cationic ground state towards a C_{2v} geometry. Although Jahn and Teller explicitly excluded linear point groups from their first-order theorem, vibronic couplings between the degenerate bending vibrations and an electronic state in HBNH can still occur, similar to diborene.[336] This interaction is called the Renner-Teller effect and can only lead to a splitting in states where the electronic angular momentum is non-zero, so for $|\Lambda| \geq 1$. The electronic ground state of the HBNH cation is a $X^+ \ ^2\Pi$ state that can lead to the appearance of side bands, but does not necessarily distort the cation. A weak Renner-Teller interaction still results in a linear equilibrium geometry but with two electronically degenerate components at the potential minimum, called D_0 and D_1 for simplicity. The two potential energy surfaces touch each other in linear geometry and split up along a bending vibration, through which different zero-point energies and vibrational levels arise. Analogous to diborene the intense transitions can originate from transitions into the energetically lower D_0 state while the small side bands come from transitions into the D_1 state. The energy difference between D_0 and D_1 was determined to be 35 meV in diborene[336] and 70 meV for iminoborane, hence significantly smaller than the calculated JT splitting in borazine. The complete absence of this effect in iminoborane is impossible, but it could be convoluted with other vibrational transitions as indicated by the FC-simulation on CBS-QB3 level at

≈11.39 eV and ≈11.58 eV. The simulation can only reproduce transitions into the $X^+\ ^2\Pi$ state without any vibronic interactions so the bands may also represent a different vibrational transition. However, the electronic situation between HBNH and HBBH is almost identical and in the latter high level calculations unambiguously identified a Renner-Teller effect in the cation. Therefore, the assignment of the bands to a weak Renner-Teller splitting is completely justified and more plausible than to the very weak vibrational transitions suggested in the FC-simulation.

The results of iminoborane can be compared to two other linear congeners for which literature data are available - acetylene and diborene. All three species are parent compounds of their respective class and exhibit an identical orbital structure with a degenerate pair of π-HOMOs. By comparing them one can link their molecular properties to situations where B-B, B-N, or C-C subunits are interchanged in larger molecules.

Diborene has two fewer electrons than iminoborane and acetylene resulting in a reduced bonding character between the two central atoms. This is demonstrated best in its determined cationic vibrational energy of $1056\,\mathrm{cm}^{-1}$, more than $400\,\mathrm{cm}^{-1}$ and $700\,\mathrm{cm}^{-1}$ below iminoborane and acetylene, respectively. The absolute values are listed in table 4.16, and one can see that the B-N stretch frequency in iminoborane is at the halfway point between the B-B and C-C modes, visualizing the influence of the po-

Table 4.16.: Molecular parameters of HBBH, HBNH, and HCCH calculated using the CBS-QB3 method. The molecules are given in the form HXYH, where X and Y are placeholders for the respective heavy atoms (B, N, C). The vibrational frequencies have been scaled by 0.96.[380]

Parameter	HBBH	HBNH	HCCH	$HBBH^+$	$HBNH^+$	$HCCH^+$
d(X-Y)/Å	1.506	1.234	1.198	1.604	1.307	1.246
d(X-H)/Å	1.172	1.167	1.106	1.169	1.169	1.080
d(Y-H)/Å	1.172	0.990	1.106	1.169	1.016	1.080
∢(HXY)	180°	180°	180°	180°	180°	180°
∢(XYH)	180°	180°	180°	180°	180°	180°
ν_3 /cm^{-1}	1212	1780	1986	1056	1533	1813
IE/eV	9.08	11.31	11.44	-	-	-

larity on the bond strength. While diborene and acetylene do not have any dipole moment, the electronegativity difference between boron and nitrogen in iminoborane leads to a weakened triple bond character. Please note that these values are derived from the cations, yet a similar trend can be calculated for the neutral species, also seen in table 4.16. The computed cationic bond lengths of the respective heavy atoms further confirm this trend, as they increase in the order from acetylene<iminoborane<diborene. This influence of the polarity has been previously recognized by Paetzold and others[381,382] with respect to the reactivity of iminoboranes and linked to their inherent instability and propensity to oligomerize compared to alkynes. The discussion between hydrocarbons and their isoelectronic inorganic counterparts with respect to their IEs is difficult, since it represents the relative energy of neutral and cationic ground states, two factors that are not necessarily dependent and may vary in different amounts in each molecule. The overall very low IE of diborene HBBH can be understood by its open shell character, which results in a higher HOMO energy than the closed shell, singlet species HBNH and HCCH. One can tentatively attribute the lower IE of HBNH compared to HCCH to its higher polarity (*vide infra*).

It is also possible to discuss the direct relationship between BN and CC in a broader context by comparing the IEs of the H_xBNH_x species to their respective hydrocarbon counterparts. This is illustrated in figure 4.54, where the differences in IEs between the corresponding BN and CC species have been plotted against the number of hydrogen atoms. Please note, that red values have been calculated on CBS-QB3 level while black values are experimentally derived. The deviation between the experimental and computational values for X=3 and X=1 in figure 4.54 is -0.09 eV and -0.04 eV, respectively and thus can be neglected. It can be seen that with the exception of AB and ethane all other BN and CC compounds have approximately the same IE. Excluding the AB/ethane couple a clear trend is visible that starts at H_2BNH_2. The ΔIE(BN-CC) is lowered by about 0.2 eV for each two hydrogens cleaved off. This trend can be explained in two ways, by a destabilization of the BN neutral species relative to the CC compound with each added π-bond, and by a stabilization of the corresponding BN cations. Recalling the significantly reduced frequency of the BN-stretch mode in HBNH compared to HCCH, which can be related to a reduced orbital overlap between B and N due to differences in their electronegativities, it is reasonable to assume that BN species get less stabilized with each π-bond. This effect can be further amplified by an electrostatic interaction in the BN cations, which increases the bonding character, therefore stabilizing them. In BN compounds the charge is mostly located at the boron atom, which can be stabilized by the adjacent nitrogen atom, whereas in CC compounds the charge is completely delocalized, without any electron donating capabilities. Similar electrostatic arguments have been made to explain the increased bonding character of the carbonyl substituent in different transition metal carbonyl complexes as well as for the BF and BF^+ species.[262,279]

The exception to the rule is AB. Matus *et al.* tried to rationalize its significantly lower IE compared to ethane in a qualitative way based on computational results.[357] They took the IE of ammonia (10.07 eV[345]) as a standard reference and claimed that the BH_3 subunit stabilizes the ammonia cation, while for H_2BNH_2 the BH_2 substituent stabilizes the neutral by forming a strong π-bond. For ethane they suggested that the interaction of a methyl radical and methyl cation is less stabilizing ultimately resulting in a higher IE than in AB. Both of these effects can explain the differing behavior of the AB/ethane couple on a qualitative level.

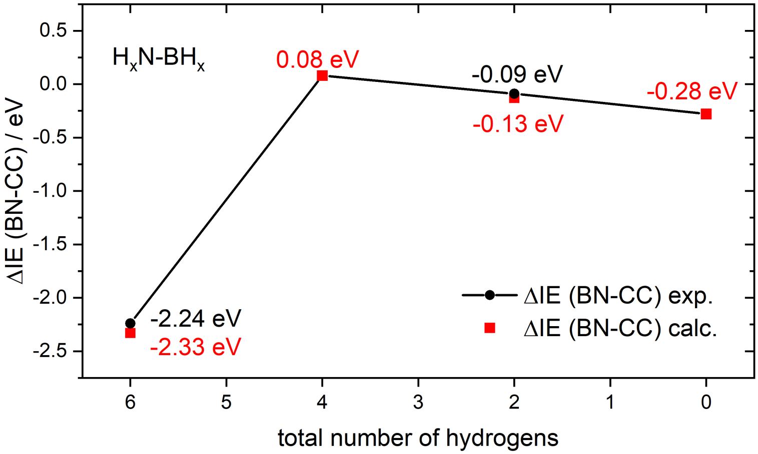

Figure 4.54.: Difference in IE between corresponding BN and CC compounds in the form H_xBNH_x. The red values have been calculated on CBS-QB3 level while the black resulted from experimental studies.

4.2.3.3. Summary

The cationic structures of ammonia borane, borazine, and imminoborane were investigated by mass selected threshold photoelectron spectroscopy. Ammonia borane exhibits a very low vapor pressure and therefore was placed inside a sample container and heated to 75°C while the evaporated molecules were taken up in an argon stream. A first featureless rise in the ms-TPES is found between 9.47 eV and 9.66 eV, after which peaks appear in a regular spacings of 1150 cm^{-1}. The regular pattern suggests a vibrational progression in the cation, but the cationic situation is more complex, which can be deduced from the isoelectronic ethane. The latter exhibits a similar progression, but mostly due to several vibronic effects like JT- and PJT-splittings that mixes its cationic PES with several states and lead to a geometric distortion in the ground state. The initial transitions in the ms-TPES have negligible FC-factors and no signal can be observed, however the IE of 9.25 eV could be determined by shifting the FC-simulation. This is in agreement with the calculated values of 9.29 eV (G4) and 9.31 eV (CBS-QB3). Yet, the DFT calculations do not consider the complex cationic structure in AB and consequently the simulation may not be accurately represent reality. At higher photon energies AB shows DPI by losing a hydrogen atom, the appearance energy was determined to be 9.96 eV.

The ms-TPES of borazine shows a first peak at 10.01±0.02 eV with a complicated vibrational activity. The origin transition is systematically underestimated in the FC-simulation, which is most likely due to autoionization effects. The JT distorted cationic ground state exhibits a low barrier for pseudorotation, which means that the calculated equilibrium geometry belonging to the C_{2v} point group is too fleeting and the borzaine cation can be treated as its highly symmetric structure. A similar feature has been observed for its organic counterpart benzene, although the frequencies of the corresponding vibrational modes are lower in borazine than in benzene. The distorted cationic structure leads to out-of-plane normal modes, which are most likely the reason for the convoluted cationic PES and the complicated vibrational activity in the cationic ground state. At higher photon energies three excited state can be observed, two broad bands with maxima at 11.35 eV and 12.79 eV and a well resolved third starting at 13.70 eV with two vibrational bands exhibiting spacings of 950 cm^{-1}. In between 11.5 eV and 12.0 eV a hydrogen loss is observed in borazine, that was calculated to occur on the boron atom because of the significantly lower B-H bond strength. A preliminary AE for this channel has been determined at 11.6±0.1 eV.

Borazine was used as a pyrolysis precursor to generate the highly reactive iminoborane, that is proposed to form during dehydrogenation of ammonia borane. At temperatures well above 1000 K borazine decomposes to ammonia and HBNH both of which were identified by ms-TPES. The IE of the latter has been determined to be 11.31±0.02 eV and it exhibits several pronounced vibrational bands in intervals of 1530 cm^{-1}. Since the cation is linear, it does not exhibit any JT or PJT effects, but vibronic coupling can occur in the form of a Renner-Teller splitting, similar to diborene or its organic congener acetylene. The latter effect causes side bands in the spectrum that were identified 70 meV above the respective vibrational bands, pointing to two components of doublet states with different zero-point energies. When the observed vibrational energies of diborene, acetylene, and iminoborane are compared, one can see not only a difference based on the bond order of the respective molecule but also due to the polarity of the bonds. Comparing the corresponding organic and inorganic compounds, i.e. ethane and ammonia borane, ethene and aminoborane as well as acetylene and iminoborane, with respect to their IE, declining differences can be found when the amount of hydrogens is lowered. The AB/ethane couple does not follow this trend. This observation has been attributed to a stronger stabilization in the AB cation with respect to the ethane cation.

4.2.4. Threshold PES of BMe_3 and its Pyrolysis Products

4.2.4.1. Motivation

Boron carbide (BC) exhibits remarkable properties like a high melting point, low density, extreme hardness, and small band gaps rendering it a potent candidate in material applications that range from bullet proof vests to high temperature semiconductors.[383] It is often applied as a coating by chemical vapor deposition (CVD),[384,385] in which a stable precursor molecule is decomposed by heating or in a plasma to form atoms that can create a thin film.[386] Trimethylborane (TMB) has been investigated with respect to BC CVD applications and although decomposition under plasma conditions has been proven to be effective,[387] it was not used in thermal processes due to unfavorable B/C ratios.[385] The reason was suggested to be the over-reactive character of the intermediates, that also render their observation extremely demanding.[386] Thus, the gas-phase chemistry of TMB has only been poorly understood and mostly investigated by computations or deduced from the final deposition products.[386,388] Imam *et al.* examined TMB decomposition under CVD conditions in different bath gases using a combined experimental and theoretical approach.[388] Their computations found high initial barriers to any secondary reaction products that are in agreement with previous calculations on B-C bond dissociation energies.[389] At lower temperatures a concerted loss of methane via an α-H elimination has the smallest barrier, forming $H_3C{-}B{=}CH_2$. This is thought to be a dead end for decomposition when argon is used as bath gas, but a parallel pathway with a higher barrier exists that produces $H_3C{-}BH_2$ and $H_2C{=}BH$ via the sequential loss of ethene and molecular hydrogen. These transient boron-carbon species have already been generated in co-deposition experiments of boron atoms with both ethane and methane and characterized by matrix isolation IR spectroscopy.[390,391] It has to be noted that these assignments have been made based on convoluted spectra, due to the unselective nature of the approach. In line with these results, Schleyer *et al.* predicted that the most stable BCH_3 species is CH_2BH, which is $102\,\mathrm{kJ\,mol^{-1}}$ more stable than methylborylene. However, they also find high rearrangement barriers of $105\,\mathrm{kJ\ mol^{-1}}$ in BCH_3 and conclude that, under the right conditions, it should be observable.[392] The thermal decomposition of a similar congener, trimethylbismuth, was recently investigated, where multiple sequential methyl losses lead to the observation of the biradicalic methyl bismuthinidene.[393] The complete lack of experimental knowledge on the gas-phase chemistry of trimethylborane and the properties of its predicted intermediates prompted us to investigate its thermal decomposition.

4.2.4.2. Results and Discussion

The recorded mass spectra at different photon energies and pyrolysis powers are displayed in figure 4.55. Without pyrolysis, the precursor starts to get ionized at around 10.00 eV, where no other signals are present (top left trace). It exhibits a typical boron iostopic pattern but a small peak at mass 57 can be identified due to the ^{13}C isotopes. At 10.50 eV TMB shows DPI, fragmenting to form a neutral methyl radical and a dimethylboryl cation (bottom left trace). The main pyrolysis products are observed between masses 39 - 41, which is in line with either a methyl or methane loss from TMB. Their IE is well below that of TMB and so a background free detection of the pyrolysis process is possible when the synchrotron en-

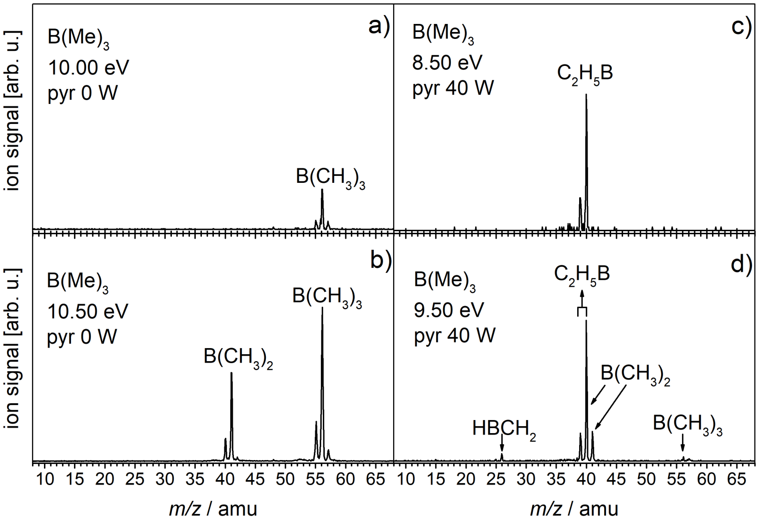

Figure 4.55.: Mass spectra of trimethylborane (TMB) at different photon energies and pyrolysis powers.

ergy is reduced to 8.50 eV (top right trace). While at 8.00 eV only trace amounts of products were detected at any pyrolysis power, the mass spectrum at 8.50 eV shows two main signals at masses 40 and 39 in a typical boron isotopic ratio of 4:1. These masses indicate that the main pyrolysis product at 40 W is CH_2BCH_3 that is formed via an α-H elimination of methane as proposed by theory.[388] In order to detect other possible products the photon energy is increased to 9.50 eV (bottom right trace), where another small peak at mass 26 can be identified, which can be attributed to a BCH_3 species. At this photon energy and high pyrolysis powers TMB can be ionized, and immediately decomposes via DPI to a dimethylboryl cation. These two competing processes are juxtaposed in the two bottom traces of figure 4.55 and schematically illustrated in figure 4.56. The methane loss by pyrolysis and methyl loss by DPI overlap in mass channel 40 due to the boron isotopes ^{10}B and ^{11}B, and, almost negligible, in mass channel 41 due to the carbon isotopes ^{12}C and ^{13}C. Using their natural abundances one can estimate the contributions that each species has in one mass channel, by comparing their intensities in the mass spectrum. The unperturbed distribution of masses 41 and 40 is displayed in the bottom left trace of figure 4.55, where a typical 4:1 pattern resulting from DPI can be seen. The picture gets more complex when the pyrolysis is turned on as illustrated in the bottom right trace. Since mass 39 can only originate from one species, $C_2H_5^{10}B$, its intensity can be multiplied by 4 to determine the contribution of its ^{11}B isotope. Similarly, the contributions of $C_2H_6^{10}B$ can be determined by dividing the mass signal of its ^{11}B isotope in mass channel 41. Since the mass 39 signal and mass 41 signal are about equally high one can estimate that the pyrolysis products are about 16 times more abundant in mass 40 than the DPI products. However, one has to note that this distribution is only valid for photon energies of 9.50 eV and a pyrolysis power of 40 W. At lower photon energies DPI should contribute less, while at higher energies DPI may at some point become dominant.

Intrigued by the rich chemistry that was indicated in the mass spectra, we investigated the temperature dependency of the TMB pyrolysis. Therefore, figure 4.57 shows TMB decomposition at different pyrolysis powers at 10.50 eV. First thermolysis products were already observed at 10 W pyrolysis power including a peak at mass 15, which started to appear in between 9.50 eV and 10.00 eV. It exhibited no significant isotopic pattern, is a product of the pyrolysis, and was identified as methyl radical by ms-TPES. Its source is ambiguous, as it can originate either from a methylated boron species or from methane that is cleaved off in the first step from

TMB. Methane itself could not be observed because of its much higher IE (12.61 eV[394]) and the use of a MgF_2 window that becomes opaque above 11 eV. Yet, a pyrolysis power of 10 W is significantly below the expected temperature for methane decomposition and thus it has to originate from other channels. It is possible, that TMB can decompose in two subsequent steps within the pyrolysis, first towards methyl and dimethylboryl radicals and the latter release a hydrogen atom in a second step. Theoretical studies predict the B-C bond dissociation enthalpy in TMB at 434.7 kJ/mol (298 K),[395] while the concerted loss of methane has a activation energy of 288.6 kJ/mol (673 K).[388] Therefore, it is more likely that impurities like acetone are responsible for the methyl radicals. Acetone was used prior to the experiment to clean the pyrolysis source and was identified by ms-TPES. Starting at 30 W mass 28 becomes visible that increases up to 50 W and can be assigned to ethene based on its IE (10.5138 ± 0.0006 eV[396]). These conditions revealed the presence of another species with a boron isotope pattern at mass 26, which was already seen in figure 4.55. The simultaneous rise of the ethene signal and CH_3B suggests that it is formed directly from TMB. For this process to occur, TMB also has to lose H_2, which is unlikely to happen in a concerted mechanism. Imam *et al.* proposed a sequential mechanism, first by elimination of ethene to form a CH_3BH_2 intermediate, and secondly the loss of molecular hydrogen to form a CH_3B isomer. According to the mass spectra this mechanism seems likely, although the presence of CH_3BH_2 should result in an isotope peak at mass 27, which is not visible. This means that the mass 28 signal is exclusively from ethene. Our own calculations predict an IE of 11.11 eV for CH_3BH_2, which is above the transmission window for MgF_2 and thus it could not be detected within this experiment. Another possibility for ethene formation is the loss of molecular hydrogen from ethane. The latter can be produced

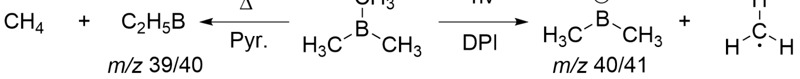

Figure 4.56.: The two competing channels for TMB decomposition, that lead to peaks between 39 - 41. The DPI channel has to be suppressed as much as possible to reduce background noise.

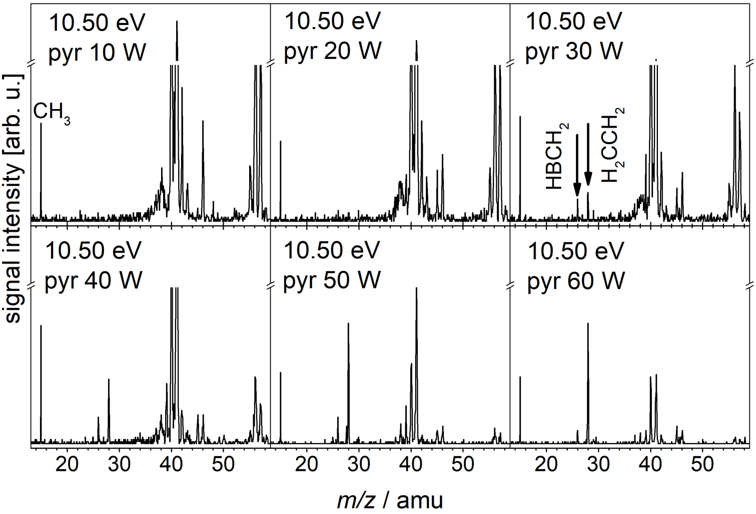

Figure 4.57.: Mass spectra of trimethylborane (TMB) at 10.50 eV with different pyrolysis powers. Please note that the y-axis is interrupted for better visibility of the small peaks.

from a dimerization of two methyl radicals and has an IE of 11.4902 eV [347] so it cannot be detected within this experiment either.

The ms-TPES of TMB is presented in figure 4.58 has been recorded from 9.50 eV to 10.60 eV in steps of 5 meV and integrated over 60 s. The first onset in mass 56 is visible at 9.84 eV and rises without any structural features up to 10.32 eV. At that point DPI towards the dimethyl boryl cation visibly sets in, giving rise to the mass 41 curve and at 10.60 eV the ms-TPE signal of TMB is completely at zero. The broad and structureless spectrum is characteristic of a large geometry change in the cation. Ionization from the E' symmetric HOMO, representing the B-C σ-bonds, leads to a JT-splitting and a symmetry reduction from the neutral D_{3h} to the cationic C_S. Due to this vibronic effect, standard DFT calculations do not accurately describe the ionization process. In conjunction with this, the large geometry change upon ionization leads to small FC-factors further aggravating any simulation efforts. Another effect that may lead to

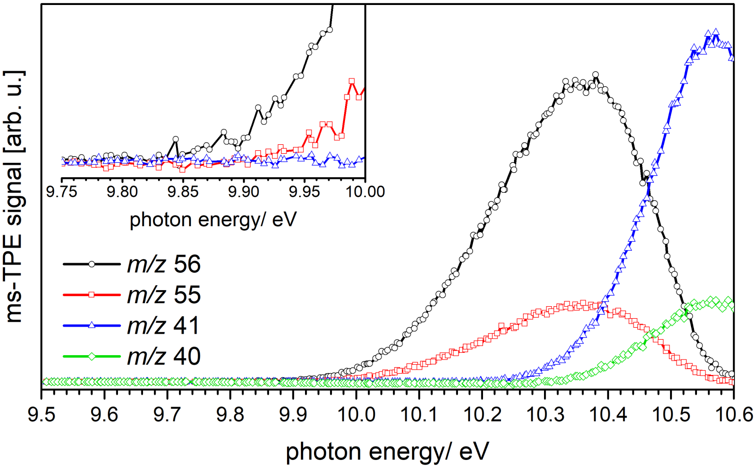

Figure 4.58.: ms-TPE spectrum of TMB between 9.50 and 10.60 eV recorded with steps of 5 meV and integrated over 60 s.

the broadening in the spectrum might be due to rotational activity of the methyl groups. Similar effects have been observed in the ms-TPES of R-C_5-R' species with different degrees of methylation. While H-C_5-H has clear and distinct peaks, the ms-TPE signal gets increasingly broad when the hydrogens are substituted by methyl groups. The IE was determined in previous studies using photoelectron spectroscopy and PIE curves yielding a value of 10.01±0.01 eV,[397] slightly higher than the results presented here, although electron impact studies found an IE of 8.8 eV.[397] Through the ms-TPE data in this study the IE of TMB can be further refined to the first discernible signal at 9.84±0.05 eV. The breakdown diagram of TMB can be found in figure A.5 in the appendix. It is well resolved and shows a clear breakdown towards the dimethylboryl cation. However, due to the cutoff of MgF_2 it could only be recorded up to 10.60 eV, which is slightly below the desired value to unambiguously identify the AE. An earlier study by Law *et al.* determined the $AE_{0K}(B(CH_3)_3 \rightarrow B(CH_3)_2)$ at 10.3±0.2 eV using electron impact ionization.[398]

The ms-TPES of mass 40 presented in figure 4.59 shows multiple distinct peaks in a regular pattern. Between 8.20 eV and 8.50 eV there is a broad and unstructured rise after which the signal increases sharply to the first peak. The featureless first part of the spectrum is caused by the high temperatures in the pyrolysis tube and inefficient cooling during the expansion into the vacuum leading to the appearance of several hot bands. Alternatively it could be caused by the appearance of another unstructured electronic state or other C_2H_5B isomers that might contribute. While Imam *et al.* predict a methane loss towards CH_3BCH_2, other isomers might still be formed due to the high temperatures in the pyrolysis. There are five different C_2H_5B isomers and their relative stabilities as well as IEs are given in figure 4.60. The relative stability of these molecules agrees with previously theoretical investigations,[399] which found the most stable isomer to be vinylborane (CH_2CHBH_2), and CH_3BCH_2 slightly higher in energy. However, the IE of vinylborane (10.18 eV) is too high to be detected in the investigated region. Two other isomers, ethyl borylene (CH_3CH_2B) and CH_3CHBH, are around 185 kJ/mol and 69 kJ/mol higher in energy than CH_3BCH_2, respectively, but their IEs (8.66 eV, 8.70 eV) are just slightly above the latter and their contribution cannot be excluded at this point. The illustrated FC-

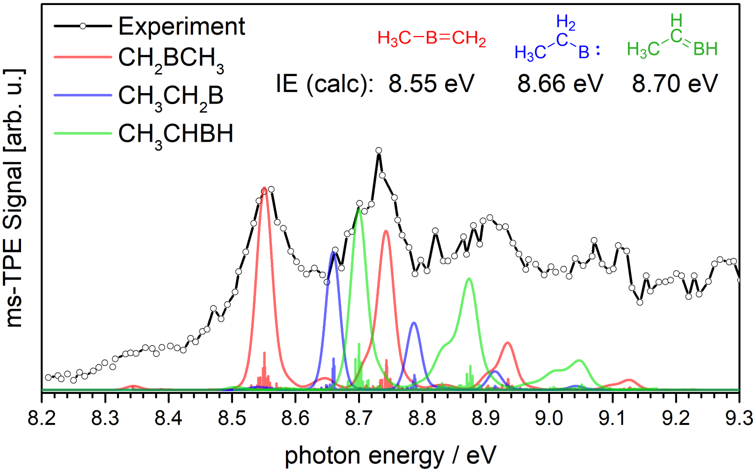

Figure 4.59.: ms-TPE spectrum mass 40 at 40 W pyrolysis power. The IE and vibrational progression agree well with CH_2BCH_3. The corresponding FC-simulation was performed at 1000 K.

simulations were modeled using a temperature of 1000 K, and even at this value the hot bands are significantly underestimated. Higher temperatures are not expected during pyrolysis at 40 W. The first peak at 8.55 ± 0.03 eV was attributed to the IE of CH_3BCH_2, which agrees well with the calculated value of 8.55 eV. Another peak can be identified at 8.73 eV ($+1450\,\mathrm{cm}^{-1}$) that can have different origins. It can either be assigned to a vibrational mode (ν_5^+) of CH_3BCH_2 representing the antisymmetric CBC stretch mode, or to the IE of CH_3CHBH, which is off by just 0.03 eV with respect to the calculated value. The high signal background above 8.80 eV indicates that either a second unstructured state becomes accessible, the signal is convoluted with secondary processes like DPI, or that other isomers are present. While the first can be proven using time-dependent calculations on the excited states of all present isomers, the second and third options seem much more plausible. The FC-simulations agree well with the spectrum but even together do not correctly reproduce the signal intensities in the spectrum at higher photon energies. Therefore, the high background levels are partially attributed to other isomers that are formed in the pyrolysis as well as to a rise in DPI when going to higher photon energies.

The mass spectrum at 10.50 eV reveals another small signal at mass 26, the ms-TPES of which is depicted in figure 4.61. Since it exhibits a typical boron isotopic pattern it can be attributed to a BCH_3 species, of which two stable isomers exist, methylborylene BCH_3 and methyleneborane CH_2BH. The latter was calculated to be $102\,\mathrm{kJ\,mol}^{-1}$ more stable but both have predicted IEs that are in close proximity to one another at 8.93 eV (BCH_3) and 9.35 eV (CH_2BH). The third isomer $CHBH_2$ was identified as a transition state on the PES.[392] The calculated geometries of the two stable isomers BCH_3 and CH_2BH are listed in table 4.17. Methylborylene be-

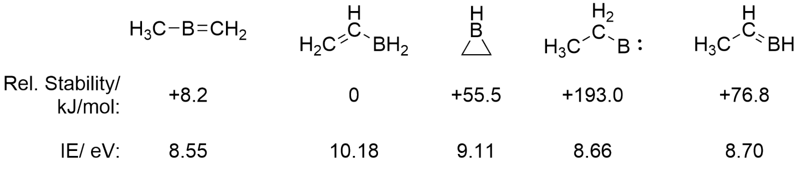

Figure 4.60.: Different C_2H_5B isomers with their relative stability (0 K) and IE. The values were calculated using the CBS-QB3 method.

longs to the C_{3v} point group and exhibits a singlet state in the neutral. The C-H bonds are all equal and have a bond length of 1.099 Å, as well as

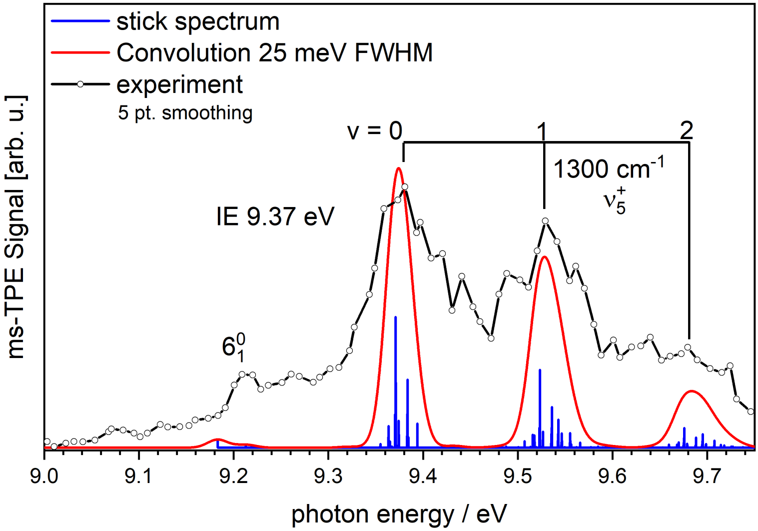

Figure 4.61.: ms-TPE spectrum mass 26 at 40 W pyrolysis power. The IE and vibrational progression coincide with CH_2BH. The corresponding FC-simulation was performed at 1000 K.

Table 4.17.: Molecular parameters of CH_3B and CH_2BH in their neutral and cationic ground states. The parameters have been calculated using the CBS-QB3 method.

Parameter	CH_3B	CH_3B^+	CH_2BH	CH_2BH^+
d(B-C)/Å	1.548	1.781	1.374	1.451
d(C-H)/Å	1.099	1.105	1.087	1.092
d(B-H)/Å	-	-	1.170	1.170
∢(HCH)	108.45°	110.08°	114.85°	115.78°
IE/eV	8.93	-	9.35	-

the same HCH bond angle at 108.45°. The B-C bond is longer at 1.548 Å and is significantly elongated to 1.781 Å upon ionization, while the CH_3 moiety hardly changes. Methyleneborane exhibits C_{2v} symmetry and is completely planar in its neutral and cationic ground states. The former is a singlet with a B-C bond length of 1.374 Å and a B-H bond length of 1.170 Å. The CH_2 unit has bond lengths of 1.09 Å for both C-H bonds and a bond angle of 114.85°. In the respective cationic structure only the B-C bond length is altered to 1.451 Å. The HCH bond angle increases slightly to 115.78 Å, while the C-H bonds are also slightly elongated to 1.092 Å. The B-H bond length stays the same, which indicates ionization from an orbital without any contribution at the B-H bond.

The ms-TPES shows that below 9.00 eV no signal is present, excluding the existence of the lower ionizing isomer methylborylene. The first band appears at 9.20 eV and can be attributed to a hot band of the CH_2 bending mode in the CH_2BH molecule. Similar to CH_3BCH_2 the FC-simulation agrees well with the spectrum but underestimates the hot band intensity even at 1000 K. Since there is no DPI process that leads to mass 26, this indicates a general underestimation of hot bands in the simulations. The first major peak is at 9.37 ± 0.03 eV was identified as the IE of CH_2BH, which is in agreement with the computed value of 9.35 eV. Calculations predict that upon ionization the B-C bond is elongated by almost 0.1 Å from 1.374 Å to 1.451 Å while all other parameters hardly change suggesting a strong activity of the B-C stretch mode ν_5^+. This vibration corresponds to another band that is shifted by 1300 cm^{-1} from the origin, albeit there are several side bands in the spectrum their origin cannot be determined unambiguously, due to the high temperature and low signal intensity.

The corresponding nitrogen compound methanimine (CH_2NH) exhibits contrasting effects in the cation, where an increased C-N-H bending angle and thus vibrational activity of the HNC bending mode ν_1^+ is found.[400] The lone pair at the nitrogen represents the HOMO and results in two isomeric forms, which have a low barrier for isomerization in the cation. The HOMO in methyleneborane is located mainly between the B-C bond and the lone pair is missing, explaining the differences in the respective electronic structures and ms-TPES.

The presence of both CH_3BCH_2 as well as CH_2BH provides first direct experimental proof for the calculated decomposition pathway for TMB. From the relative signal intensities in the mass spectra it can be deduced that the major decomposition occurs towards CH_3BCH_2. A smaller portion of TMB molecules can overcome the 93.1 kJ mol^{-1} greater barrier towards the CH_2BH decomposition pathway. The latter cleaves off ethene in a first step forming the stable intermediate CH_3BH_2. Its mass signal could not be detected during the experiments, which can be explained by its calculated IE of 11.11 eV. Hence, it cannot be observed using a MgF_2 window. However, the decomposition of TMB seems to be more complex than previous experimental and theoretical studies suggest. The ms-TPES of mass 40 demonstrates that other isomers than CH_3BCH_2 play a crucial role in the decomposition. It indicates that at least two more species, ethyl borylene (CH_3CH_2B) and CH_3CHBH, may be formed at some point. The exact formation pathways of the two energetically higher isomers are currently subject to theoretical calculations. Previous computational studies found that all C_2H_5B isomers are more stable than their separate components BH and C_2H_4.[399] For ethyl borylene a preliminary mechanism can be proposed that includes other pyrolysis products of TMB. In a first step the cleaved off ethene can undergo hydroboration with the intermediately formed methylborane CH_3BH_2 producing ethylmethyl borane. The latter is isomeric to the precursor TMB and has a calculated IE of 9.88 eV. The ms-TPE data are available for energies up to 10.00 eV, however the FC-simulation predicts very small FC-factors near the origin so unambiguous detection was not possible. Through a terminal methane loss of ethylmethyl borane the borylene can be formed. The proposed mechanism depicted in figure 4.62 is not yet supported by theoretical calculations and other pathways might exist. The absence of atomic boron during thermolysis indicates that mainly species with boron, carbon, and hydrogen are formed, rendering TMB an unsuitable source for boron atoms in thermic CVD applications. This has been first recognized by Lewis *et al.*[386] and recently it was suggested that the main film forming species below 900°C is CH_3BCH_2, which was deduced from the B/C ratio of 0.5 in CVD products.[388] When temperatures were raised to 1000°C the B/C ratio increased to 1.5 accounting for the increased significance of the second pathway gen-

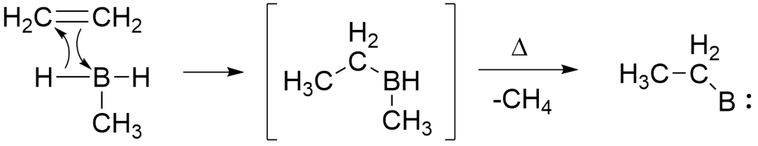

Figure 4.62.: Proposed mechanism of the ethyl borylene formation.

erating CH_3BH_2 and CH_2BH as well as additional surface chemistry eliminating hydrocarbon species from the films. This hypothesis can be partially confirmed when the signal of mass 28 is followed in mass spectra at different pyrolysis temperatures (figure 4.57), where ethene elimination becomes increasingly important above 30 W. Interestingly, the ethene signal does not scale with the CH_2BH signal visible at mass 26, suggesting that either the intermediately formed CH_3BH_2 has access to other reaction pathways or that CH_2BH is an intermediately formed species that can react further. Reactions like the elimination of either methyl or methane from CH_3BH_2 would be plausible, but the direct products BH_2 and BH have IEs of 9.21 eV and 9.82 eV, respectively and were not detected. The elimination of dihydrogen from CH_2BH would either form CBH or HCB for which the calculated IEs are 10.59 eV and 10.32 eV respectively, around the threshold of the highest used photon energy (10.50 eV). Since no mass 24 signal was detected, the elimination of dihydrogen from the CH_2 site of CH_2BH is the most plausible reaction mechanism and agrees with the decreased intensity of mass 26 in the mass spectrum at 60 W. Further decomposition is unlikely to occur at these temperatures, since the direct reaction product BH should have been detected otherwise. However, the increased ethene signal intensities could also be derived from a more abundant ethane signal, which is formed from the dimerization of methyl radicals. A final conclusion can only be drawn when higher photon energies are investigated as well.
The decomposition of TMB is in stark contrast to other $M(CH_3)_3$ compounds with elements of higher periods like bismuth or phosphorous. The much weaker C-Bi bond yields exclusively bismuth-centered radicals and biradicals upon thermolysis, while its methylene type structure CH_2BiH is higher in energy and no hydrogen rearrangement or methane elimination have been observed. This behavior is not valid for elements of the third period, although their methyl structures exhibit significant kinetic stabilization by high isomerization barriers like 225 kJ mol^{-1} for methyl phosphinidine.[401] Thone *et al.* proposed that the first step in the decomposition for trimethylamine pyrolysis in deuterium gas is the loss of a methyl group but noted that their dimethylamino signal was below the error limit.[402] They also found CH_3NCH_2, which was isolated as the trimer triazine and characterized by ^{1}H-NMR, thus being one of the major products. Its source was suggested to be a hydrogen loss from the dimethylamine radical but due to its high signal intensity and the comparability with TMB, it is more likely to originate directly from trimethylamine. When two carbons are

cleaved off of trimethylamine the only observable product is methanimine CH_2NH analogous to its boron congener.

4.2.4.3. Summary

The pyrolysis of the CVD precursor TMB was investigated using mass selected threshold photoelectron spectroscopy. TMB itself exhibits a broad and unstructured TPE spectrum due to a pronounced Jahn-Teller splitting in the cation that reduces the initial D_{3d} symmetry to C_S in the cation. The large geometry change upon ionization and the rotational activity of the methyl groups impede FC-simulation efforts. Dissociative photoionization causes TMB to fragment into a neutral methyl radical and a dimethylboryl cation with no other channels being observed until 10.60 eV. Pyrolysis at low temperatures reveals the presence of methyl radicals, indicating either minor channel for methyl abstraction in TMB or secondary pyrolysis channels due to impurities. Through theoretical studies the former can be excluded due to much higher activation barriers. The main decomposition channel is the loss of methane to form C_2H_5B species. The ms-TPES reveals a first band at a photon energy of 8.55±0.03 eV coinciding with the CH_3BCH_2 molecule. The spectrum is rather broad, which could be either due to DPI, rotational broadening of the methyl substituents or other C_2H_5B isomers. Calculations reveal that two other C_2H_5B isomers can be ionized in the same energy region: ethylborylene, CH_3CH_2B, with an IE of 8.66 eV and CH_3CHBH with an IE of 8.70 eV. Both are less stable than CH_3BCH_2, but might form via different routes. At higher pyrolysis temperatures a second pathway becomes visible that cleaves off ethene and molecular hydrogen in a sequential mechanism. The intermediately formed CH_3BH_2 could not be detected as its calculated IE of 11.11 eV is above the transparent window of MgF_2, but the latter can create a BCH_3 species that was identified as CH_2BH by its ms-TPES. Its IE of 9.37±0.03 eV is in perfect agreement with the calculated value of 9.35 eV and another band that can be assigned to the B-C stretch mode is shifted by 1300 cm^{-1}. The identification of these intermediates confirms the previously proposed decomposition mechanism based on calculations and reveals that the decomposition of TMB in argon is unlikely to be limited to the identified intermediates and pathways at these temperatures.

4.3. Other Projects

Other projects that did not lead to a publication or did not work as originally intended will be described in the next sections.

4.3.1. Kinetics of the Cyclopropyl Radical

Since the kinetic investigation of the allyl radical with oxygen constituted a proof of principle for the newly established CRF-PEPICO setup, generation of the isomeric cyclopropyl radical was the next step. Because of its ring strain it is thermodynamically unstable and has a propensity to isomerize to the allyl radical when generated with high excess energies, rendering mild formation approaches the only viable source. Figure 4.63 shows several direct photolytic precursor that were evaluated for their ability to generate cyclopropyl radicals without isomerization, yielding mixed results. Arnold *et al.* investigated the direct photolysis of cylpropyl iodide at 266 nm and 279.7 nm using a VMI coupled REMPI scheme, imaging the resulting iodine atoms as well as the electrons.[403] They found that in gas- and solution-phase the allyl radical is the only detectable product from photoexcited cyclopropyl iodide and provide computational evidence of a ring opening mechanism via a double-surface crossing mechanism. Dicyclopropylketone (DCPK) was investigated as another possible photolytic precursor by Clegg *et al.*, who also found a direct isomerization upon photolytic bond cleavage at 193 nm.[404] Engel and Bodager used diazocyclopropane and irradiated the molecule at 254 nm in a hydrocarbon bath gas and detected cyclopropane in a broad mixture of products using gas chromatography from which they deduced the existence of cyclopropyl radicals.[405] Bicy-

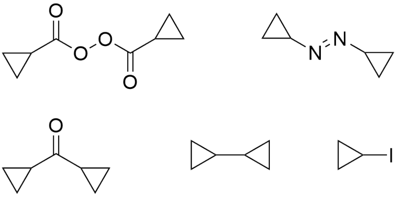

Figure 4.63.: Selected precursors for direct generation of cyclopropyl radicals that were already investigated prior to this study.

clopropyl was used as a precursor in an IR multi-photon dissociation study to reveal the ring opening to a 1,3-biradical species.[406] The most selective direct photolytic precursor for cyclopropyl radicals was determined to be bis(cyclopropylformyl) peroxide, which was irradiated at 308 nm in solutions of several hydrocarbons and trapping reagents to yield exclusively cyclopropyl radicals.[407,408] Dyke *et al.* used the hydrogen abstraction from cyclopropane by fluorine atoms to provide the first photoelectron spectrum of the cyclopropyl radical, in which they assigned an ionization energy of 8.18 ± 0.02 eV and found spacings of $1000\,\mathrm{cm}^{-1}$.[409] Similarly DeSain *et al.* investigated the HO_2 and OH production after the reaction of cyclopropyl radicals, which they generated by hydrogen abstraction using chlorine atoms, with oxygen and deduced several rate constants from this but did not characterize the radical itself.[410] Overall the hydrogen abstraction route using chlorine and fluorine atoms provides high radical yields and excellent selectivity, needed for kinetic experiments according to the literature. Nonetheless, direct photolysis precursors are more desireable because of the less convoluted background reactions, which are difficult to determine and are hardly literature known.

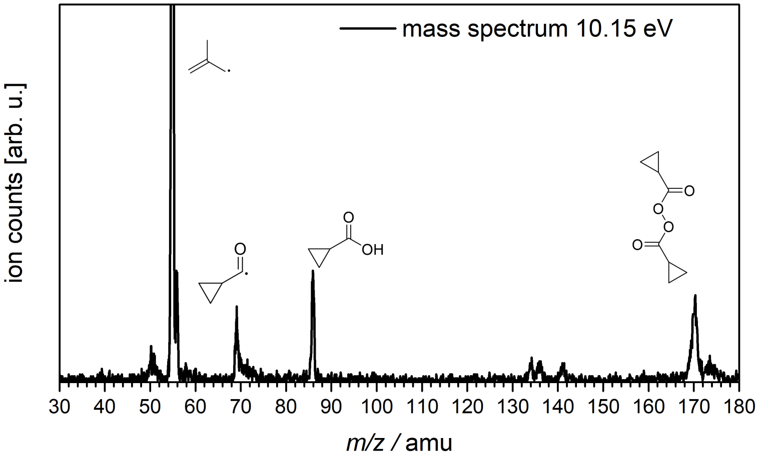

Figure 4.64.: Mass spectrum of bis(cyclopropylformyl) peroxide at 10.15 eV without the photolysis laser.

Within this work two different approaches, one direct and one indirect, have been used to generate cyclopropyl radicals. The direct approach used the bis(cyclopropylformyl) peroxide because of its high reported selectivity, [408] which was synthesized according to literature procedures [411,412] and photolyzed at 213 nm. The mass spectrum without the photolysis laser is presented in figure 4.64 and shows the precursor at mass 170 proving that its vapor pressure is high enough to get into the gas-phase. The mass peak at $m/z = 86$ is due to cyclopropylcarboxylic acid, which was used to synthesize the precursor. The peak at $m/z = 69$ is due to cyclopropylformyl most likely a product of DPI from either the precursor or the corresponding carboxylic acid. When the laser is turned on using a wavelength of 213 nm, no mass 41 signal can be identified rendering the precursor unsuitable for the generation of cyclopropyl radicals under these conditions. The second scheme has been based on the approach described by DeSain *et al.* where chlorine atoms were used to abstract hydrogen atoms from cyclopropane. [410] This reaction is only slightly exothermic and results in a quasi non-excited cyclopropyl radical that cannot undergo isomerization. As source for the chlorine atoms the photolysis of oxyalyl chloride has been

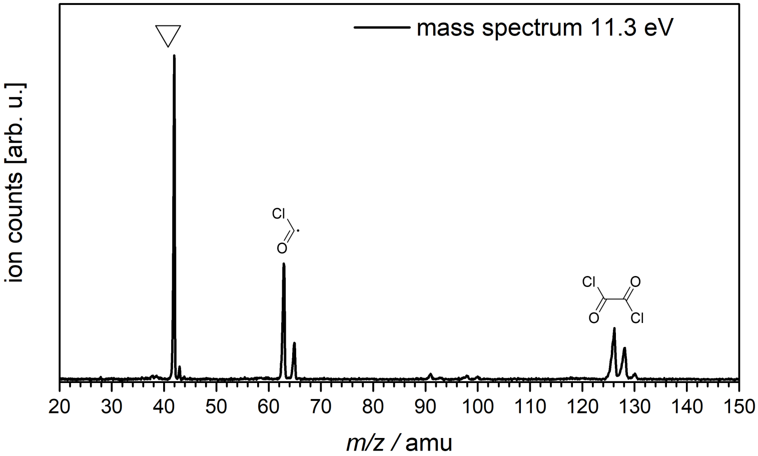

Figure 4.65.: Mass spectrum of cyclopropane and oxalyl chloride at 11.30 eV without the laser present.

used similar to the hydrogen abstraction from propene to create allyl radicals. The background reactions of oxalyl chloride photolysis could be well described in the allyl experiments and a mass spectrum of its mixture with cyclopropane is shown in figure 4.65. However, after turning on the laser at 213 nm no significant signal of m/z 41 could be observed. Scattered light by the laser created surface electrons inside the experimental chamber, which were accelerated by the ion optics and ended up ionizing bath gas argon atoms in an electron impact like ionization procedure. This led to significant noise peaking at around m/z 40 making it hard to detect small amounts of 41. A rough ($\Delta E = 0.015\,\mathrm{eV}$) TPES scan displayed in figure 4.66, revealed a very small signal at m/z 41, however its signature is very similar to the allyl radical. Therefore, it can be assumed that some of the cyclopropyl radicals isomerize to allyl radical under our experimental conditions.

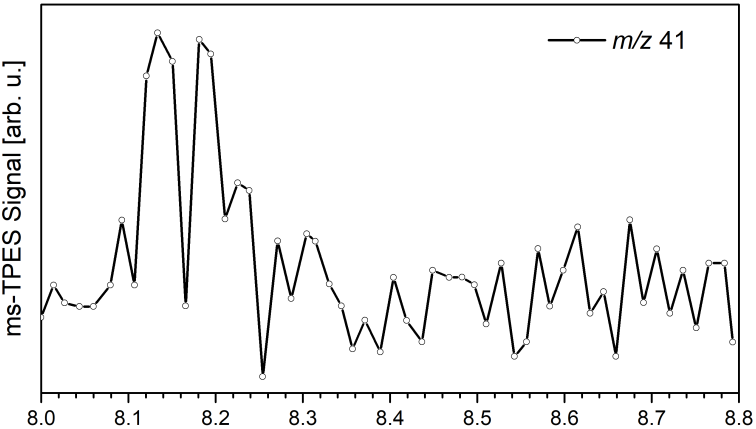

Figure 4.66.: ms-TPES of mass 41 using the hydrogen abstraction scheme from cyclopropane. The generated radical could be identified as allyl.

4.3.2. Generation of a Stabilized Diborene

Substitution of the hydrogens on the parent diborene HBBH is an intriguing way to change the electronic situation of diborenes. Contrary to the parent diborene other precursors have to be found and other generation schemes applied to produce these species in the gas-phase and probe them spectroscopically. A promising candidate is the bicyclic boron species that was first synthesized by Pospiech *et al.* in 2012 with the specific intention to liberate the dimethylamino substituted diborene under elimination of anthracene.[413] For this study the compound was synthesized in the group of Prof. Holger Braunschweig by Alexander Okorn and measured using the pyrolysis setup at the VUV-beamline of the SLS. The compound is air- and moisture sensitive and was placed in 20 mg portions into the nozzle while under argon atmosphere using a glovebag. The source was attached to the endstation and momentarily evacuated to limit decomposition through contact with air. Although its molar mass is quite high, heating the precursor to 95°C increases the vapor pressure enough to yield a good signal as displayed in figure 4.67.

Even without pyrolysis a strong signal at mass 178 can be identified as

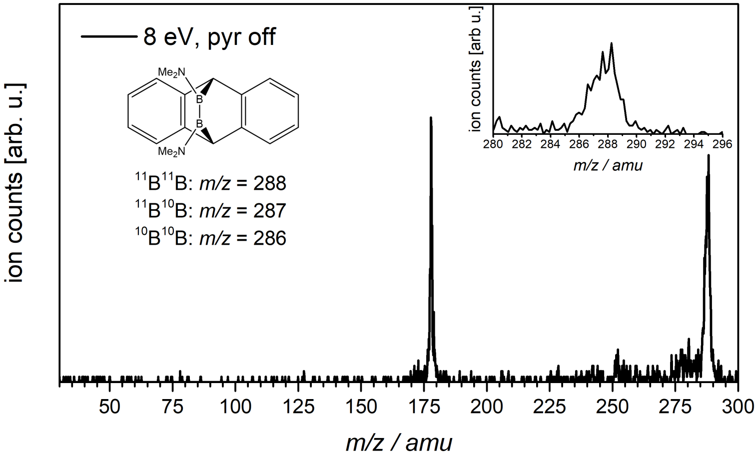

Figure 4.67.: Mass spectrum of the bicyclic boron precursor at 8.00 eV and no pyrolysis.

residual anthracene, with an IE of 7.415±0.010 eV, most likely formed as a byproduct of the synthesis or as a decomposition product with air. Next to the anthracene signal figure 4.67 shows a strong mass peak at 288 at 8.00 eV, which can be assigned to the bicyclic boron precursor. When the pyrolysis is turned on, the precursor signal intensity is lowered, while strong peaks at mass 110 and 45 are formed as displayed in figure 4.68. The latter does not exhibit an isotopic pattern and can be assigned to dimethylamine (IE 8.20 eV). The peak at 110 is in perfect agreement with the mass for the doubly substituted dimethylamino diborene and exhibits a strong isotopic pattern that matches the expected diborene structure. Its intensity is equal for 15 and 18 W pyrolysis power but diminishes significantly above 20 W although the precursor signal does not completely vanish. The IE of the corresponding diborene was calculated to be only 5.80 eV, however no signal could be detected at around 6 eV. Another signal at mass 273 also increases in intensity when pyrolysis is turned on that can be attributed to a methyl loss from the precursor showing another possible decomposition channel.

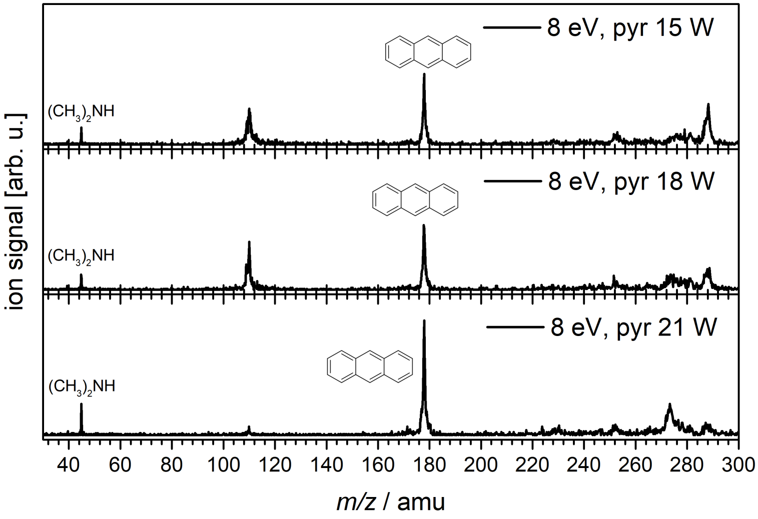

Figure 4.68.: Mass spectrum of the bicyclic boron precursor at 8.00 eV and different pyrolysis powers.

The precursor cannot be destroyed completely at these temperatures, and no signal can be observed near the calculated IE of the diborene. Thus, the precursor does not seem to liberate the diborene in the pyrolysis. The mass 110 signal is rather formed by DPI, which is in line with its decreased intensity at higher pyrolysis powers and the relative intensities of the precursor and mass 110 in electron impact studies. However, this channel does not exist up to 10.50 eV when pyrolysis is turned off. During thermolysis the relatively weak C-N bond can be broken before anthracene is cleaved off, destroying the diborene structure in the process, which is proven at pyrolysis powers of 30 W where a broad mass peak around mass 230 is observed that could correspond to a variety of methyl or alkyl amine losses from the precursor. The B-C bond towards the anthracene seems to be relatively stable an is thus unsuitable to cleave off the proposed diborene compound. In principle this scheme could be successful when the dimethylamino groups and anthracene can be substituted by other functional groups and the ring strain and resulting aromaticity could be increased by incorporating smaller rings like benzene into the molecule.

4.3.3. Photolysis of Borane Carbonyl

Boranes have a unique electronic situation with less valence electrons than orbitals for bonding. This inherent electron deficiency leads to an unstable borane molecule BH_3, which can stabilize itself by dimerization to diborane B_2H_6, with two three-center-two-electron bonds. The kinetics and thermodynamics of this dimerization are largely unkown and have only been partially derived from measurements using PIE curves.[414,415] Finding a precursor that selectively generates BH_3 through photolysis can open up an experimental pathway to determine the kinetics of its dimerization and help to elucidate other crucial thermodynamic parameters like dimerization energies. Borane carbonyl (BH_3CO) has been identified to liberate borane and inert carbon monoxide molecules upon photolysis at 193 nm.[416–419] However, it is gaseous and metastable at room temperature making it hard to handle and store for longer periods. It was first synthesized by Burg and Schlesinger in 1937 by co-condensation of diborane and carbon monoxide,[420] an unpractical, highly toxic and dangerous way for regular synthetic chemists. Parry *et al.* developed an easier method for storing

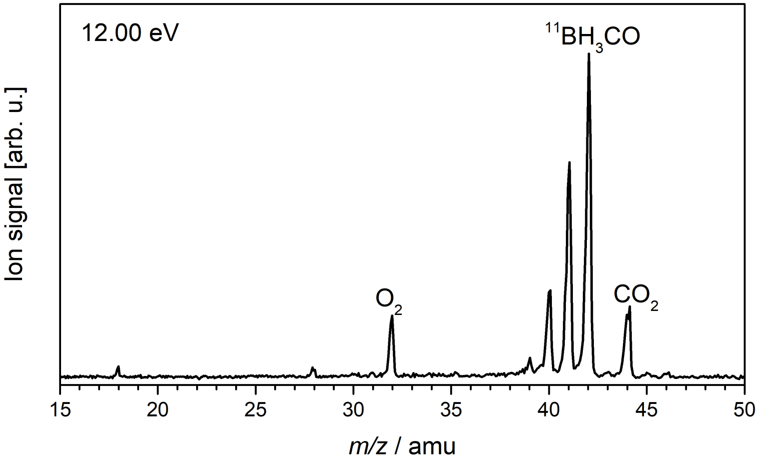

Figure 4.69.: Mass spectrum of borane carbonyl at 12.00 eV without photolyis laser.

and handling BH_3CO by converting it to a carboxide salt ($BH_3CO_2^{2-}$), which releases borane carbonyl upon treatment with concentrated phosphoric acid.[421] Their method still involved the tedious synthesis of borane carbonyl, which could be avoided by Schubinger *et al.* in 2001.[422] They used the loosely bound borane-tetrahydrofurane complex as starting material, through which they bubbled carbon monoxide to generate BH_3CO as an intermediate that can be separated by cold trap destillation because of its much lower boiling point. Subsequent introduction of borane carbonyl to a cooled ethanolic potassium hydroxide solution generates the carboxide salt that can be isolated as a colorless solid. Figure 4.69 shows the mass spectrum of BH_3CO at 12.00 eV well above the calculated IE of 10.58 eV using the CBS-QB3 method. Two minor peaks at masses 32 and 44 can be assigned to oxygen and CO_2 respectively occurring as impurities inside the chamber. The major peak is located in the mass 42 channel that corresponds to borane carbonyl, while three more peaks between 41 and 39 can be attributed to a combination of hydrogen loss by DPI and the ^{10}B isotopes of the respective species. The precursor was characterized by ms-TPE spectroscopy in combination with quantum chemical calculations on CBS-QB3 level of theory as illustrated in figure 4.70. Borane

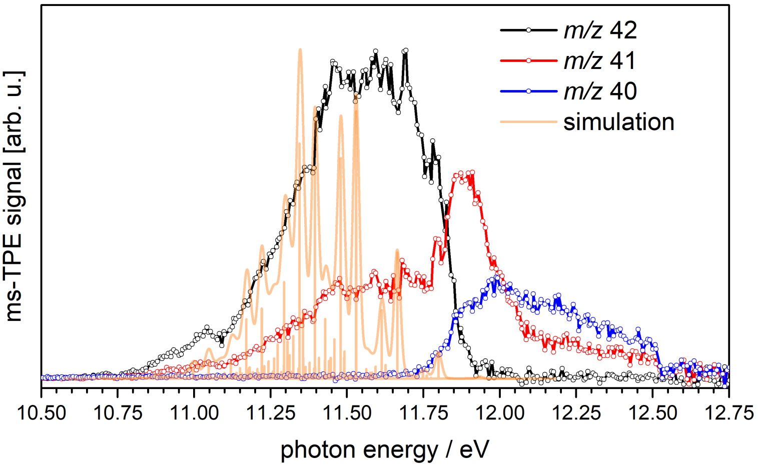

Figure 4.70.: ms-TPES of borane carbonyl between 10.5 eV and 12.75 eV.

carbonyl exhibits a C_{3v} symmetry and its orbital structure is thus very similar to ammonia borane. The two HOMOs represent a doubly degenerate pair of π_x and π_y orbitals with e-character and major contributions at the boron, from which ionization to the electronic ground state of the cation occurs. This results in a Jahn-Teller effect through which the lowest state splits up and causes a broadening in the spectrum that was first recognized by Lloyd and Lynaugh.[324] As previously mentioned this effect cannot be accurately described by single-reference quantum chemical calculations, which is why the FC-simulation does not fit the experimental spectrum very well. Between 11.75 eV and 12.00 eV a sharp decrease in the mass 42 signal can be seen that corresponds to a hydrogen loss by DPI. The mass 41 signal peaks at around 12.00 eV before decreasing while the signal in mass channel 40 becomes the most dominant indicating another hydrogen loss channel. The corresponding breakdown diagram is displayed in figure 4.71 and has been corrected for the respective ^{10}B isotopes. Upon photolysis at 213 nm the signals do not change and no borane mass peak could be identified. Rice *et al.* describe the absorption spectrum of BH_3CO containing a first peak at 55 800 cm^{-1} ($\approx$ 179 nm) with

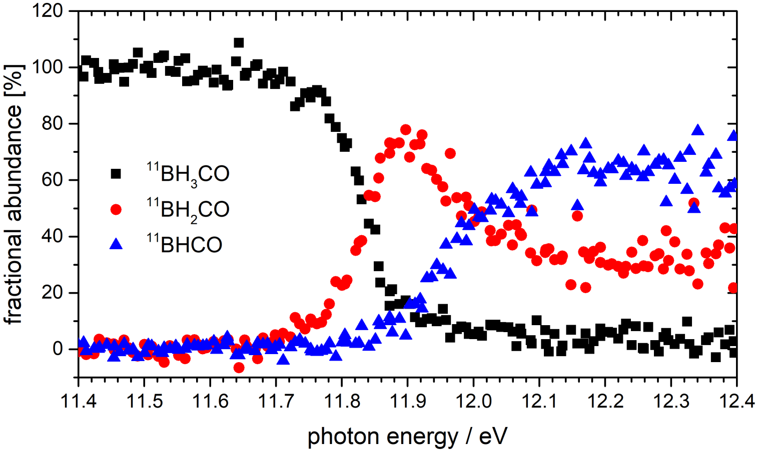

Figure 4.71.: Breakdown diagram of borane carbonyl between 10.50 eV and 12.75 eV.

a second, more intense, transition peaking at $63\,800\,\mathrm{cm}^{-1}$ ($\approx 157\,nm$).[416] Therefore, it is likely that the cross section at 213 nm is too small to generate borane in sufficient amounts.

4.3.4. Pyrolysis of $Bi(NMe_2)_3$

Reactive bismuth species have been proven to exist as part of catalytic processes, and only recently the first free bismuthinidine BiMe has been spectroscopically characterized.[393] By using IEs and AEs the Bi-C bond strength could be revised and selective bond breaking in $BiMe_3$ can start only slightly above room temperature. In order to expand the scheme to other substituents tris(dimethylamino)bismuth ($Bi(NMe_2)_3$) has been investigated as a possible pyrolysis precursor for similar bismuth radicals and biradicals. The compound itself is air, moisture, light and temperature sensitive and is thus very difficult to handle in the non-inert atmosphere necessary to get it into the sample container of the pyrolysis setup and the endstation. After 300 mg of the compound were placed inside the container,

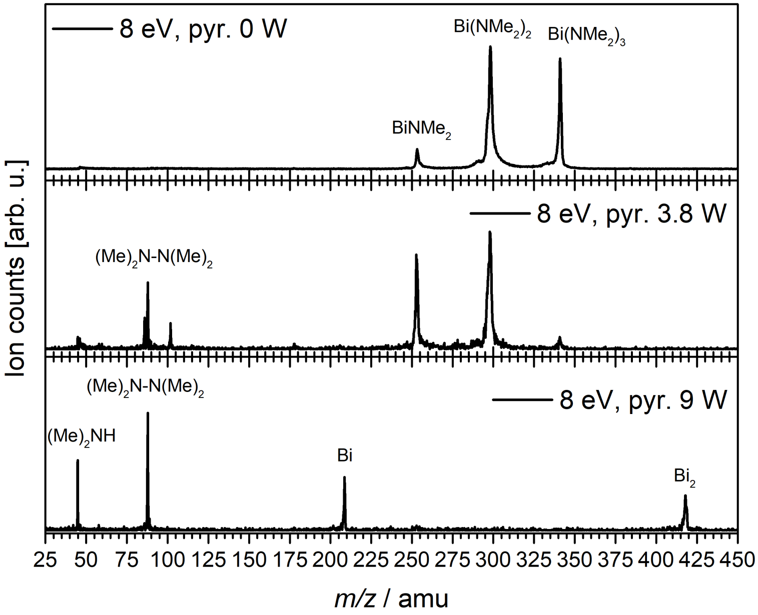

Figure 4.72.: Mass spectra of $Bi(NMe_2)_3$ at different pyrolysis temperatures.

the source was attached to the endstation and evacuated. Without heating the vapor pressure of the compound is too low and therefore it was heated to 40°C at which the signal sharply increased. The mass spectrum of the compound at 8.00 eV without pyrolysis is shown in the upper trace in figure 4.72 and exhibits three distinct peaks. The precursor mass is 341, corresponding to the highest peak, whereas the two others can be explained by the loss of one and two dimethylamino groups through DPI, respectively. Even at very low pyrolysis powers the precursor signal drops in intensity and the other two signals gain intensity relatively to it illustrated in the middle trace of figure 4.72. Several lower mass peaks can be identified either as dimethylamine or its dimer tetramethylhydrazine indicating an abstraction in the pyrolysis tube and a high bimolecular reactivity in the molecular beam. The latter originates from the sharp gas-phase transition and the uncontrollable vaporization mechanism the precursor exhibits, rendering a more diluted gas-phase one further challenge of this compound. At these pyrolysis temperatures the precursor signal does not get destroyed completely and the apparent DPI channels forming the respective radicals and biradicals prevent the analysis with a partially decomposed precursor. Increasing the pyrolysis power destroys the precursor completely but no

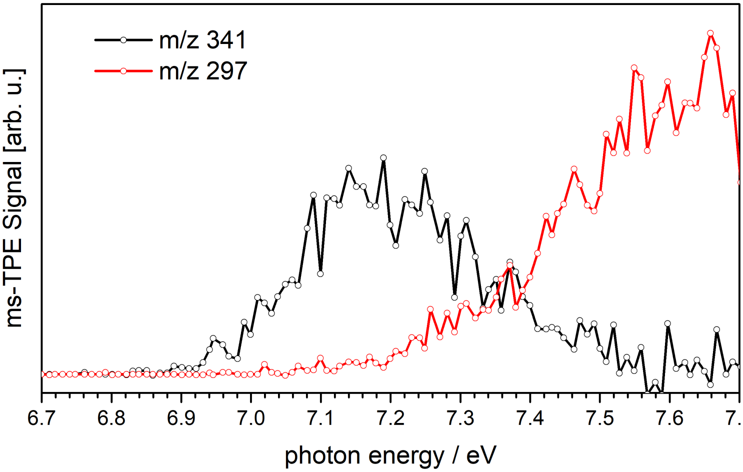

Figure 4.73.: ms-TPES of Bi(NMe$_2$)$_3$ and its dimethylamino loss channel.

signal from either radical or biradical can be detected, instead at 9 W two other signals start to appear that can be attributed to Bi atoms and Bi_2 molecules. This proves that a selective and sequential abstraction mechanism similar to $BiMe_3$ is not possible with its dimethylamino congener. The reason for this are either secondary processes like coatings inside the pyrolysis tube, which have been observed for some iron complexes or the extremely weak Bi-N bond so that all three bonds are cleaved almost simultaneously. The precursor could be characterized by ms-TPES which is shown in figure 4.73 and the corresponding breakdown diagram is depicted in figure 4.74. Its IE was calculated to be 6.71 eV, which is slightly below the first observable rise in the spectrum at around 6.95 eV. The spectrum itself is broad without any prominent features and the signal starts to decline between 7.20 and 7.30 eV representing the onset of DPI, which is only slightly above the IE and can be explained by a shallow potential well of the precursor cation and the low binding energy of the dimethylamino groups to the central atom.

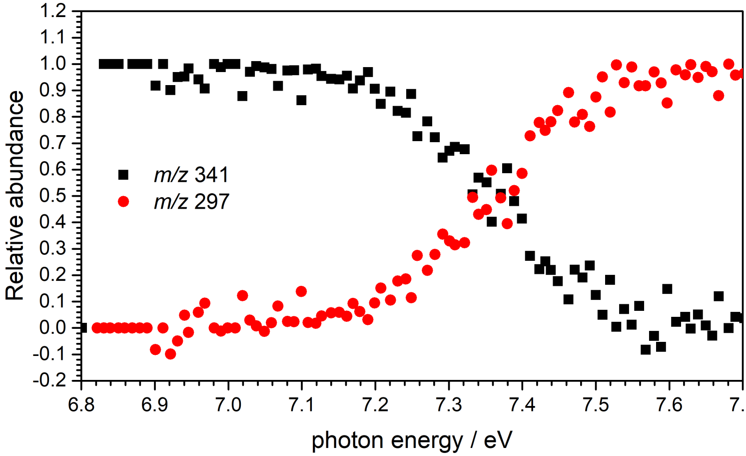

Figure 4.74.: Breakdown diagram of the dimethylamino loss channel in $Bi(NMe_2)_3$.

4.3.5. Hydrogen Abstraction by Xenon Difluoride

Fluorine atoms are an excellent initiators for hydrogen abstraction reactions. However, their generation is not straightforward and usually requires the handling of a microwave generated plasma.[423] In addition these setups require a large amount of substance, limiting their application to either commercially available precursors or easily scaleable synthesis procedures. A softer and more selective approach is their photolytic generation using a suitable and stable precursor molecule. Usually fluorine exhibits strong bond dissociation energies with almost all elements, which prevents their use as easily cleaveable precursors. This strong oxidizing capability of fluorine has been exploited to generate noble gas compounds that are only stable with fluorine substituents. These molecules have low bond energies and are excellent precursors for fluorine atoms, especially xenon difluoride XeF_2, containing a total bond energy of $265\,\mathrm{kJ\,mol^{-1}}$. While the first fluorine in XeF_2 is bound with $252\,\mathrm{kJ\,mol^{-1}}$, the second exhibits only a bond energy of $13\,\mathrm{kJ\,mol^{-1}}$, and is quasi non-bonding.[424] Thermally XeF_2 it is stable up to several hundred kelvin, but the fluorine atoms can be selectively cleaved off by exciting a dissociative state with a UV photon.[425] Using this

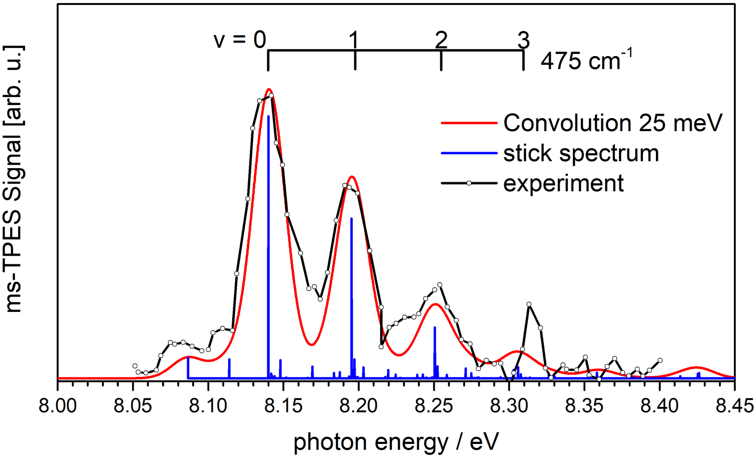

Figure 4.75.: Allyl radical TPES generated by the abstraction of hydrogen atoms from propene.

scheme, the first fluorine atom is directly cleaved off, creating the excimer XeF, which is often used as a source in excimer laser systems.[424] Since it is only stable in the excited state, it decomposes rapidly, ultimately generating two fluorine atoms and one inert xenon atom per absorbed photon. XeF_2 has a good vapor pressure (5 mbar[424,426]) and a decent photolysis cross section in the UV ($2.56 \pm 25 \times 10^{-19}$ cm^2 at 206 nm[427]), rendering it an ideal precursor for photolytic gas-phase experiments. For chemical kinetics this approach has been pioneered by Fittschen and co-workers.[428–430]

For a first proof of principle experiment XeF_2 was used in the abstraction of hydrogen atoms from propene, similar to the already established chlorine route. For this XeF_2, propene and argon were introduced into the photolysis reactor described in section 3.2.3. As a photolysis wavelength the 5^{th} harmonic of a 10 Hz Nd:YAG laser at 213 nm was used and the products characterized by ms-TPE spectroscopy.

The corresponding ms-TPES of the abstraction mass channel 41 is displayed in figure 4.75. It shows a first strong peak at 8.13 eV which is the IE of the allyl radical, providing evidence for a working abstraction route. The high formation enthalpy of HF could also lead to the creation of the isomeric propenyl radicals, where a hydrogen is abstracted directly at the carbon-carbon double bond. These species are much higher in energy than allyl and have calculated IEs of 7.65 eV ($CH_3{-}C^{\bullet}{=}CH_2$) and 7.46 eV ($CH_3{-}CH{=}C^{\bullet}H$) with a singlet ground state in the cation. Both molecules exhibit a linear CCC framework in the cation, so geometry change is rather large compared to the bent neutrals. The absent mass signal below 8.13 eV proves that the propenyl radicals are not generated in large amounts during the abstraction process.

5. Summary and Conclusion

This thesis highlights the importance of isomer-selective approaches for the complete analysis of chemical processes. The method of choice is photoelectron/photoion coincidence (PEPICO) spectroscopy, which allows simultaneous detection of electrons and ions coming from a single ionization event. Ionization techniques are sensitive and can record a number of species simultaneously, rendering them ideal tools to probe single steps in molecular transformations. Coupling these setups to completely tunable, high flux, synchrotron radiation allows one to analyze complex mixtures with isomer selectivity based on ionization energies and vibrational structure in the cation, without any prior separation steps. To make full use of this, threshold photoelectron spectra have to be recorded. Up to now, only very few setups exist that can be used to gather these data, although their impact and applicability is growing steadily in a number of different fields. Within the realm of closed-shell species an easier and more widely used method is gas-chromatography, but most open shell species would not survive the separation process. Since radicals cannot be stored under ambient conditions, they have to be created by selectively converting stable precursor molecules. Depending on the radical generation method different properties can be investigated ranging from thermodynamic data, over concentrations in high temperature environments, to chemical kinetics.

The main focus of the first part of this thesis is the determination of bimolecular rate constants. Isomeric hydrocarbon radicals were generated by a high intense UV light pulses and their kinetics with oxygen was measured. The conditions were chosen so that the oxygen concentration can be seen as constant throughout the experiment, i.e. so called pseudo-first-order conditions. The pressure dependence of different isomers in the falloff region was compared to theoretical models, and their reactivity could be explained.

The second part deals with boron containing compounds in various electronic situations. The corresponding precursors were successfully synthesized, according to literature procedures or could be commercially bought. They were subjected to fluorine atoms in chemical reactors or destroyed pyrolytically at high temperatures. Most investigated species exhibited vi-

bronic effects that could be elucidated using high level computations.
The key findings of this thesis can be summarized as follows:

- The allyl radical was successfully generated using direct and indirect photolytic schemes and its pressure dependent rate constants with oxygen were investigated. Precursors were allyl iodide or propene, which was subjected to chlorine atoms that could abstract the terminal hydrogen at the methyl site. The rate constants exhibited systematically lower rate constants compared to the literature, which was partly explained by experimental differences.

- The methylallyl radicals 1-methylallyl (1-MA) and 2-methylallyl (2-MA) were generated from their corresponding halide precursors. Their isomer selective rate constants with oxygen were measured at different pressures. The high pressure limiting rate constants increases with molecular size, and radical substitution site, which is in line with the experimental observations.

- The radical IO has been generated by bimolecular reaction between ozone and iodine atoms. Its IE of $9.71 \pm 0.02\,\text{eV}$ fits well to the previous experimental measurements, although its vibrational structure differs significantly. The relativistic effects in IO^+ lead to a spin-spin splitting that creates two close lying triplet states, which are split by $\approx 0.13\,\text{eV}$. The vibrational progressions could be identified at $810\,\text{cm}^{-1}$ and $730\,\text{cm}^{-1}$ for the lower and higher state respectively, which is in agreement with theoretical predictions.

- The hydrogen abstraction of diborane (B_2H_6) created a number of reactive boron species, which were identified by the related slow-photoelectron spectroscopy technique. Among the identified molecules were BH, BH_2, HBBH, and BF. The highly exothermic abstraction process created BH in the ground and first excited triplet state and through the two IEs at $9.82 \pm 0.02\,\text{eV}$ and $8.48 \pm 0.02\,\text{eV}$ a Singlet-Triplet gap of $1.34 \pm 0.03\,\text{eV}$ was measured.

  The intense vibrational progression of the bending mode in BH_2 ($955\,\text{cm}^{-1}$) made it possible to determine its IE at $8.12 \pm 0.02\,\text{eV}$, although no transition can be seen at this energy due to small Franck-Condon factors.

  HBBH, a prime example of a biradical, was identified and an IE of $9.08 \pm 0.015\,\text{eV}$ with a vibrational progression of $1100\,\text{cm}^{-1}$ from the

symmetric stretching mode. It is a linear molecule with a Π ground state in the cation that exhibits a Renner-Teller effect.
BF was identified as a side product inside the fluorine reactor and its IE has been measured at 11.11±0.02 eV in perfect agreement with previous experimental data. Large discrepancies exist in the vibrational frequency in the cation, where a wavenumber of 1690 cm^{-1} was measured to improve previous values.

- The nitrogen-boron pair (NB) is isoelectronic to the CC unit, which has created a lot of interest in a variety of different fields. NH_3BH_3 has been investigated as a potential hydrogen storage system, but very few gas-phase studies exist to date. Its IE was determined to be 9.25 eV which is very close to the computed one, and a Jahn-Teller effect has been recognized in the cation.
  Borazine is the inorganic analogue of benzene, however its characterization is far less complete than its hydrocarbon congener. The IE has been determined at 10.01±0.02 eV with a pronounced and convoluted vibrational activity in the cation, that is different from benzene itself. The parent iminoborane HBNH was generated by pyrolysis of borazine and exhibits an IE of 11.31±0.02 eV and a vibrational frequency in the cation of 1550 cm^{-1} originating from the symmetric stretching mode. A Renner-Teller effect has been identified in the spectrum similar to HBBH.

- The pyrolysis of trimethyl borane (TMB) resulted in a temperature dependent decomposition in two parallel pathways. At lower temperatures the loss of methane dominates, that leads to CH_3BCH_2 with an IE of 8.55±0.03 eV. Other C_2H_5B isomers cannot be excluded in the formation as well. At higher temperatures ethene is cleaved off from TMB. This creates CH_3BH_2 with a computed IE of 11.11 eV and can further decompose by splitting off hydrogen to create a CH_3B species. From the two isomers CH_3B and CH_2BH the latter could be identified by its IE (9.37±0.03 eV) and vibrational structure in the cation (1300 cm^{-1}).

A. Appendix

A.1. Synthesis

The following chapter describes the synthetic procedures used to synthesize some precursor molecules. All chemical were bought either at the *Chemikalienausgabe der Fakultät für Chemie und Pharamzie der Universität Würzburg* or from commercial vendors like *Sigmal Aldrich* or *ABCR* and used without further purification.
Unless otherwise noted, the following conditions apply. Each reaction was performed using standard Schlenk techniques or glovebox techniques under argon. Glassware was heated under vacuum conditions prior to use. Solvents used for reactions (ethanol, tetraglyme) were dried, deoxygenated, and argon saturated using the freeze-pump-thaw method. ^{1}H, ^{11}B and ^{11}B{^{1}H} NMR were recorded at 296 K on a Bruker *Advance 400* (operating at 400.1 MHz for ^{1}H and 100.6 MHz for ^{11}B). All chemical shifts (δ) were referenced to solvent peaks via residual solvent peaks acetone-d$_6$ (^{1}H, 2.05 ppm) and D_2O (^{1}H, 4.79 ppm). Coupling constants (J) are given in Hertz. Peak multiplicities are given with the following abbreviations: s = singlet, d = doublet, t = triplet, q = quartet.

A.1.1. Synthesis of K_2BH_3COO

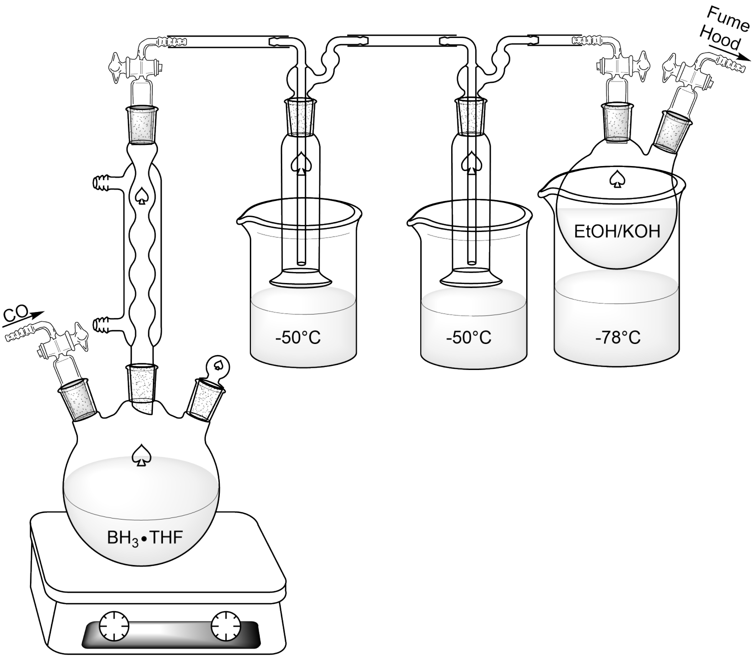

Figure A.1.: Experimental setup for the synthesis of K_2BH_3COO.

A three-necked round bottom flask equipped with a reflux condenser and gas inlet was charged with 30 mL $BH_3 \cdot THF$. The gas inlet was attached to a CO bottle with a pressure regulator and needle valve. The reflux condenser was cooled to -50°C and the CO bottle opened so that each second one bubble was produced. The gas stream was held constant for 120 min and afterwards slightly increased (30 min). At all times the temperature of the reflux condenser was between -30 and -50°C. The gas passed two cold traps held at -50°C and was inserted in a ethanolic potassium hydroxide solution (2.8 g KOH; 200 mL ethanol). There was no difference between dried ethanol and commercially available ethanol (96%). After 2.5 h the CO stream was stopped and the ethanolic solution heated to reflux for 1 h.

The BH_3COO^{2-} salt precipitated during reflux. It was collected using a frit and washed with cold ethanol and diethyl ether. It was characterized by ^{1}H, ^{11}B, and ^{11}B{^{1}H}. Please note that the corresponding sodium salt is easily soluble in ethanol and does not precipitate.[421] A major factor for the success of the reaction is the quality of the commercially bought BH_3·THF. Some batches are unsuited for this reaction, and no product formation was observed.
^{1}**H NMR** (400.1 MHz, D_2O, δ [ppm]): 0.79 (q, 1:1:1:1, $^1J(^1H\text{-}^{11}B)=80\,Hz$).
^{11}**B NMR** (100.4 MHz, D_2O, δ [ppm]): 32.09 (q).

A.1.2. Synthesis of BH_3CO

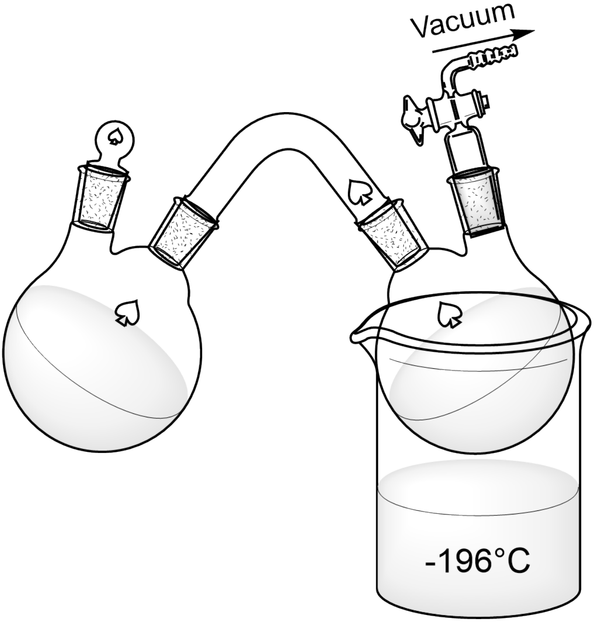

Figure A.2.: Experimental setup used to liberate BH_3CO from K_2BH_3COO.

10 mL concentrated phosphoric acid were filled in a 100 mL schlenk tube and frozen using liquid N_2. 1 g of K_2BH_3COO was placed on top of the frozen acid and the tube attached to a bridge that lead to a nitrogen cooled empty flask. The system was evacuated and the melting phosphoric acid reacted with the K_2BH_3COO generating BH_3CO and water. The much more volatile BH_3CO gas was trapped in the liquid nitrogen cooled flask, which could be used for later experiments and characterized by gas-phase IR.[431]

A.1.3. Synthesis of Borazine

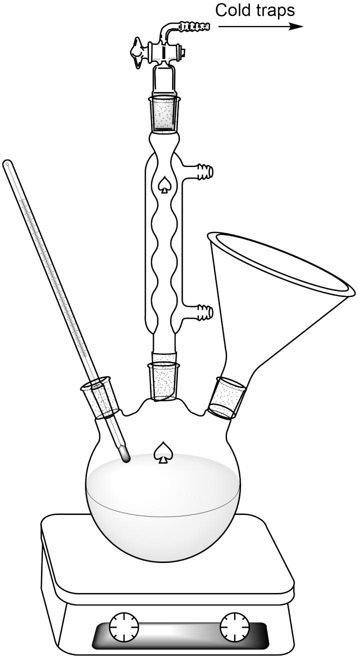

Figure A.3.: Setup used for the synthesis of borazine. The product was isolated at -78°C in the cold traps.

Borazine was synthesized according to reaction (48) and protocols are available from the literature.[360,361]

$$3\,(NH_4)_2SO_4 + 6\,NaBH_4 \xrightarrow[\text{tetraglyme}]{} 2\,B_3N_3H_6 + 3\,Na_2SO_4 + 18\,H_2 \qquad (48)$$

A 2 L three necked round bottom flask was equipped with a thermometer and fractionating coloumn. The exit of the coloumn was attached to a T-piece where one end lead to a pressure gauge and the other to a cold trap. A second cold trap was installed before the system was attached to the manifold. The round bottom flask was charged with 350 mL tetraglyme and a blended mixture of $(NH_4)_2SO_4$ (30.7 g) and $NaBH_4$ (82.3 g) was added. Upon addition, gas evolution started from the suspension. It was carefully heated to 40-50°C under constant stirring and subsequently to 80°C until hydrogen evolution subsided. The reaction mixture was extracted under a dynamical vacuum between 6-20 mbar for one hour and in addition 20 min at 135°C and full vacuum. The raw product could be isolated from the cold traps.

The raw product was a colourless suspension and according to ^{1}H and ^{11}B was contaminated with another boron compound. Multiple purification steps by recondensation did not yield any improvement in product quality, however photoionization mass spectra indicated that the impurity did not have a high vapor pressure. The tetraglyme could be reused up to three times until the solid side products made stirring the mixture impossible.

Borazine was characterized by IR, Raman, photoionization mass spectrometry, ^{1}H and ^{11}B-NMR spectroscopy.

^{1}**H NMR** (400.1 MHz, acetone-d_6, δ [ppm]): 5.38 (t, 3H,), 4.38 (q, 3H).
^{11}**B NMR** (100.4 MHz, acetone-d_6, δ [ppm]): 30.57 (d).
^{11}**B{^{1}H} NMR** (100.4 MHz, acetone-d_6, δ [ppm]): 30.57 (s).

A.2. Spectra

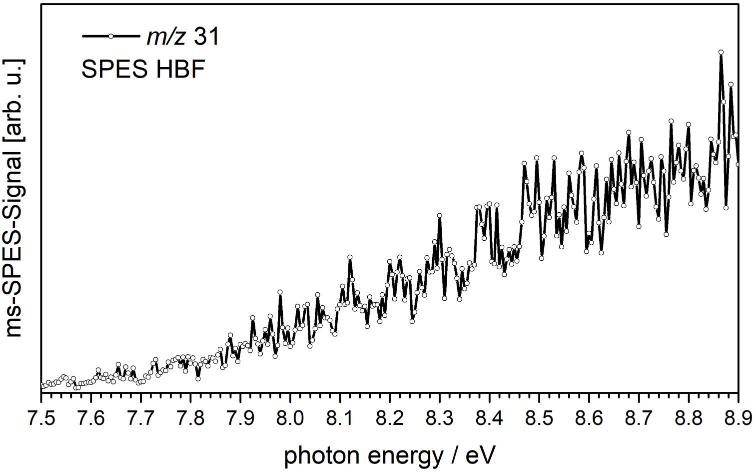

Figure A.4.: ms-SPES of HBF between 7.50 and 8.90 eV.

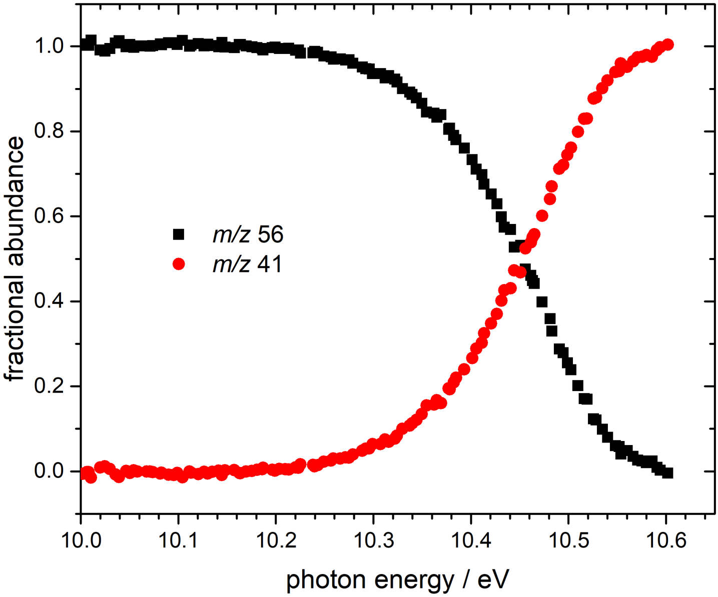

Figure A.5.: Breakdown diagram of trimethylborane between 10.00 and 10.65 eV. Data were recorded up to 10.60 eV due to the MgF_2 cutoff.

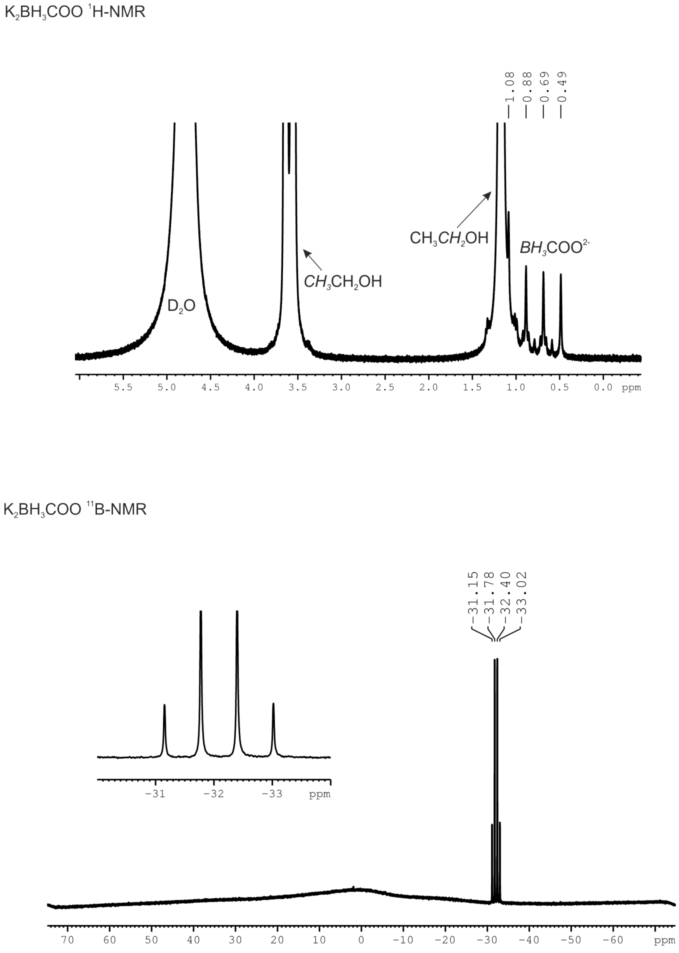

Figure A.6.: ^{1}H and ^{11}B NMR of K_2BH_3COO.

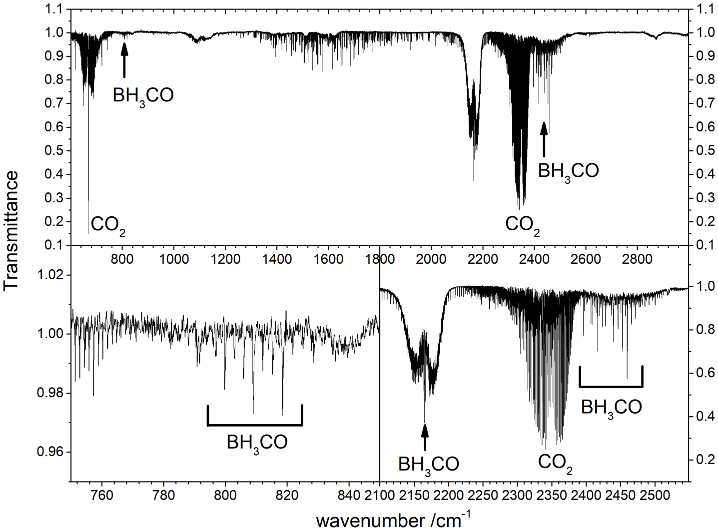

Figure A.7.: Gas-phase IR spectrum of BH_3CO.

Borazine ^{1}H NMR

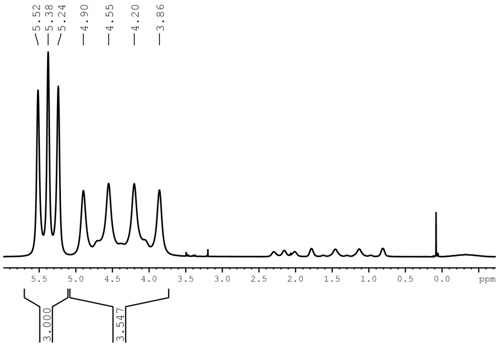

Borazine ^{11}B NMR

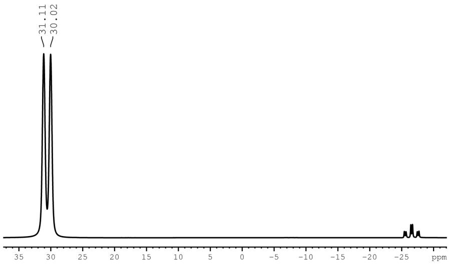

Borazine ^{11}B{^{1}H} NMR

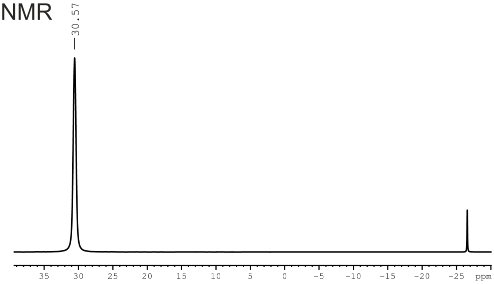

Figure A.8.: ^{1}H (top), ^{11}B (middle) and ^{11}B{^{1}H} (bottom) NMR of borazine.

B. Acknowledgements

Diese Arbeit in ihrer jetzigen Version wäre so nie zustande gekommen, hätte ich nicht über viele Jahre die Unterstützung einiger ausgewählter Personen erhalten.
Zunächst möchte ich mich natürlich bei meinem Chef und Mentor PROF. DR. INGO FISCHER bedanken. Meine Masterarbeit in der Anorganik hat mir einiges abverlangt, aber du hast nicht eine Sekunde gezögert mich bei dir aufzunehmen, obwohl mein Wissen und meine Expertise in der Gasphasenspektroskopie damals quasi gleich Null waren. Allein für diesen unglaubliche Vertrauenvorschuss bin ich dir auf ewig dankbar. Meine fehlende Expertise in dem Feld hat sich öfters in, im Nachhinein, komischen und abenteuerlichen Ideen geäußert. Ich hatte aber niemals das Gefühl, dich damit zu nerven und du hast mir eins um andere Mal in deiner umsichtigen Art verständlich gemacht, wo mein Fehler liegt. Manchmal hast du mich aber auch diese Holzwege bis zu Ende gehen lassen, woraus ich viele neue Erkenntnisse mitgenommen habe und jedes mal etwas gewachsen bin. Ich glaube diese Freiräume und dein stets offenes Ohr haben mich in den letzten Jahren maßgeblich geprägt. Du hast uns Doktoranden alles ermöglicht was sich ein junger Wissenschaftler wünschen kann: Eine harmonische Gruppe, internationale Forschungsaufenthalte, die Teilnahme an nationalen und internationalen Konferenzen und weitsichtige wissenschaftliche Leitung. Dazu gehört natürlich auch die Freiheit mit seinen Kollegen manchmal etwas länger zusammen sitzen zu können und an wenigen Tagen im Jahr die Arbeit hinten anzustellen.
Vielen Dank dafür!
An zweiter Stelle muss natürlich eine ganz spezielle Person kommen: Mein guter Kollege ENGELBERT REUSCH.
Du warst der einzige der mich "interviewt" hat bevor ich überhaupt in die Gruppe gekommen bin. Zum Glück hab ich anscheinend von Anfang an einen relativ guten Eindruck bei dir hinterlassen :)
Du hast mir alles beigebracht was ich an der SLS wissen musste und unsere Messzeiten waren dank dir nie langweilig. Viel wichtiger, wir sind uns währenddessen nie an die Gurgel gegangen, ganz im Gegenteil. Du hast

mir in deiner Arbeit für mein Engagement gedankt und dieses Kompliment kann ich nur genau so zurück geben. Deine ”Hands-On” Mentalität hat mir gezeigt, dass es nicht reicht nur ein gut durchdachtes Experiment zu haben, sondern, dass man für den Erfolg immer auch selbst mit anpacken muss. Ohne diese Art wären wir bestimmt mehrmals aufgeschmissen gewesen und hätten nur die Hälfte von dem gelernt was wir jetzt wissen. Du warst immer Feuer und Flamme für das was du tust und konntest mich für jedes Experiment begeistern.

Marco Flock, dir habe ich nach nur zwei(!) Monaten schon den Titel als Juniordoktorand abgenommen und ihn dann 1 3/4 Jahre behalten. Gern geschehen übrigens. Für mich unvergessen ist die Zeit mit dir auf den Konferenzen, bei denen du trotz wenig Schlaf meistens trotzdem in den morgendlichen Vorträgen saßt. Du hast mich damit immer wieder daran erinnert, dass sich harte Arbeit und Spaß nicht zwangsläufig ausschließen und beides gleichermaßen wichtig ist. Unsere gemeinsamen Schafkopfabende mit Engelbert und Max waren immer lustig und haben mir einiges außerhalb der Wissenschaft beigebracht. Nachdem Engelbert und Flo zuletzt nicht mehr im AK waren haben wir zwei das Ruder ein bisschen an uns gerissen und versucht die nächste Generation etwas lockerer zu machen. Ich denke wir haben zusammen einen guten Job gemacht, aber ob es gereicht hat wird sich wohl erst in Zukunft zeigen. Für deine persönliche Zukunft bei deinem neuen Job wünsche ich dir alles Gute.

Mein Dank geht natürlich auch an Florian Hirsch, der mir immer mit Rat und Tat zur Seite stand besonders in der Anfangszeit an der ich noch viel im IR gemessen habe. Genauso wie bei Marco werde ich unsere gemeinsame Zeit im AK und auf Konferenzen nie vergessen. Bleib so wie du bist!

Ihr drei habt so ziemlich den harten Kern der Arbeitsgruppe gebildet zumindest für fast die ersten zwei Jahre. Es gibt so viele positive Erinnerungen und keine schlechte. Wie Engelbert schon gesagt hat: Ihr wart nicht nur Arbeitskollegen, ihr seid schnell zu sehr guten Freunden geworden!

Natürlich gibt’s da noch die nächste Generation: Marius Gerlach, Tobias Preitschopf und Christian Matthaei.

Marius du hattest es nicht immer leicht mit mir und Engelbert. Auf Messzeiten haben wir dir einiges Abverlangt, aber dass du uns trotzdem weiterhin treu geblieben bist zeichnet dich eigentlich nur noch mehr aus. Ich bin mir sicher, dass die Synchrotronprojekte bei dir in fähigen Händen sind und hoffe, dass dich das Thema genauso reich belohnt wie Engelbert und mich.

Tobi und Christian: Ich hoffe wir älteren haben euch gut in die Arbeits-

gruppe integriert. Es hat immer Spaß gemacht mit euch zusammen zu arbeiten! Bleibt so wie ihr seid! Christian wenn ich die Arbeitsgruppe verlasse, dann überreiche ich dir feierlich den Titel als Seniordoktorand, wie er mir schon von Marco übergeben wurde.

Floriane Sturm und Lea Bosse, auch wenn unsere Zeit zusammen in der Gruppe nur kurz war so hat es mir immer mehr Spaß mit euch gemacht als ohne! Ich hoffe ihr könnt der Arbeitsgruppe, die während meiner Zeit durchaus Männerdominiert war, etwas Balance geben.

Meine ehemaligen Kollegen Dr. Kai Pachner, Dr. Anja Röder und Dr. Deb Pratim Mukhopadhyay sei an dieser Stelle ebenfalls gedankt. Kai, sich mit dir ein Büro zu teilen hat sich sofort ausgezahlt, da du dein Wissen jeden Tag mit mir geteilt hast und mir immer alle Fragen beantworten konntest. Anja deine Leidenschaft für die Wissenschaft habe ich von Anfang an bemerkt und es war immer eine Freude mit dir zu Arbeiten. Deb you supported us during our beamtimes and somehow always asked to right questions. Your curiosity taught me so much about what I did not yet know about my work, which kept me intrigued to find out more and more. Through your kind way it was always a pleasure talking to you and even after long and exhausting beamtimes we never argued with each other. Stay the way you are and I hope you find your dream job!

Darüber hinaus möchte ich noch die überaus produktiven Kooperationen mit Dr. Nancy Fassheber und Prof. Gernot Friedrichs von der Uni Kiel erwähnen, die für das Gelingen der Kinetikprojekte unverzichtbar gewesen ist. Vielen Dank für eure tatkräftige Unterstützung.

Natürlich wäre keine Messzeit so erfolgreich geworden ohne das jeweilige Team vor Ort: Dr. Patrick Hemberger und Dr. Andras Boedi bzw. Dr. Gustavo Garcia und Dr. Jean-Christophe Loison.

Ihr hattet quasi zu jeder Uhrzeit ein offenes Ohr für unsere Probleme, habt uns experimentell immer weitergeholfen und auch mal nach einem erfolgreichen Projekt mit uns angestoßen.

Patrick und Andras ihr habt uns nicht nur immer die perfekten Ausgangsbedingungen für Messzeiten geboten sondern uns stets bei allen Fragen weitergeholfen wo ihr nur konntet. Das Engagement, welches ihr an den Tag gelegt habt sucht seines Gleichen und ihr seid maßgeblich daran beteiligt, dass ich jedes mal mit Vorfreude in die Schweiz gefahren bin.

Jean-Christophe and Gustavo, you both made it incredibly easy for us to measure our data at SOLEIL. You were always a pleasure to talk to and you gladly helped us every time. Thank you both. Natürlich geht auch ein Dank an meine zwei Bachelorantinnen Luisa Martin und Dorothee

Schaffner. Ihr habt beide einen Arbeitseifer an den Tag gelegt, der es mir als Betreuer unglaublich einfach gemacht hat. Ich konnte euch hoffentlich helfen euren Weg für die Zukunft zu finden und ihr habt genauso von mir etwas lernen können wie ich von euch!

Natürlich geht mein Dank auch an die Praktikanten Bernhard Mahlmeister, Kathrin Meissel und alle die unser Team bei Messzeiten unterstützt haben wie Lisa Lummel und Max-Philipp Herbert.

Ohne die Werkstatt hätten wir unsere Forschung eigentlich schon einstellen können. Deswegen ein großer Dank an Wolfgang Liebler, Ralf Kohrmann, Katharina Schreckling, Peter Lang, Markus Keller, Reiner Eck und Uwe Reuss.

Da ich mit meinen meist luftinstabilen Verbindungen sehr anspruchsvolle Analytik gebraucht habe, geht ein riesengroßes Dankeschön an meine ehemaligen Komilitonen in der Anorganik, Dr. Fabian Keppner, Leon Schneider, Stefanie Kachel und Alexander Okorn. Ihr habt mir nicht nur bei jeder Synthese mit Rat und Tat beiseite gestanden sondern mir sehr oft verschiedenste NMRs gemessen, mir trockene Lösemittel ausgeliehen oder mir ein offenes Ohr geliehen wenn ich mich darüber beschwert habe wie undankbar die Synthese doch manchmal sein kann.

In diesem Zusammenhang sei auch meinen anderen Kommilitonen und guten Freunden, Peter Hentschel, Florian Geyer und Nicholas Scheuplein gedankt. Ihr alle habt die gesamten 10 Jahre an der Uni zu einer einzigartigen Zeit gemacht und ich hoffe wir bleiben auch weiter in Kontakt wenn wir nicht mehr zusammen in einer Stadt wohnen werden. Eine ganz besondere Rolle nimmt mein ehemaliger Mitbewohner und guter Freund Nicholas Stromer ein. Uns hat das Schicksal zusammen gebracht, was im Nachinein das beste war, das passieren konnte. Auch wenn wir uns jetzt nur noch selten sehen so hoffe ich doch, dass wir auf immer freundschaftlich miteinander verbunden bleiben.

Natürlich müssen auch noch weitere Personen erwähnt werden:

Thomas Steffenhagen, Sebastian Endres und Julian Glock sowie alle Mitglieder des JungChemikerForums Würzburg: Euer ehrenamtliches Engagement hat mir immer große Freude bereitet und es hat mir immer Spaß gemacht mit euch zusammen zu arbeiten!

Dr. Peter Fischer und Dr. Andreas Öchsner und Ute Link: Ihr habt mich in meiner Zeit in der Fachschaft und im JCF in vielen organisatorischen Bereichen unterstützt und habt die ein oder andere Veranstaltung erst ermöglicht.

Darüber hinaus möchte ich natürlich meiner Freundin Anne Dümichen

danken, die es aus bislang unerklärlichen Gründen nach wie vor mit mir aushält. Du hast mich immer auf meinem Weg unterstützt und warst immer für mich da. Danke!
Zuletzt möchte ich mich natürlich noch bei meiner Familie bedanken, ohne die ich heute nicht so wäre, wie ich bin und die mich während meines Weges immer unterstützt hat auch wenn ich mal weiter weg gewesen bin. Ich danke euch von ganzem Herzen.

Bibliography

[1] V. Masson-Delmotte, H.-O. P. P. Zhai, D. Roberts, J. Skea, P. Shukla, A. Pirani, W. Moufouma-Okia, C. Péan, R. Pidcock, S. Connors, J. Matthews, Y. Chen, X. Zhou, M. Gomis, E. Lonnoy, T. Maycock, M. Tignor, , T. Waterfield, „Global Warming of 1.5°C. An IPCC Special Report on the impacts of global warming of 1.5°C above pre-industrial levels and related global greenhouse gas emission pathways, in the context of strengthening the global response to the threat of climate change, sustainable development, and efforts to eradicate poverty.“ in *IPCC*, **2018**.

[2] S. A. Kulp, B. H. Strauss, *Nat. Commun.* **2019**, *10*, 4844.

[3] O. Bellprat, V. Guemas, F. Doblas-Reyes, M. G. Donat, *Nat. Commun.* **2019**, *10*, 1732.

[4] Eurostat, „Energieerzeugung und Energieeinfuhren“, **2020**, acessed 01.03.2021.

[5] A. Kwade, W. Haselrieder, R. Leithoff, A. Modlinger, F. Dietrich, K. Droeder, *Nat. Energy* **2018**, *3*, 290–300.

[6] P. Greim, A. Solomon, C. Breyer, *Nat. Commun.* **2020**, *11*, 4570.

[7] W. Lubitz, W. Tumas, *Chem. Rev.* **2007**, *107*, 3900–3903.

[8] K. Kohse-Höinghaus, *Proc. Combust. Inst.* **2021**, *38*, 1–56.

[9] M. V. Rodionova, R. S. Poudyal, I. Tiwari, R. A. Voloshin, S. K. Zharmukhamedov, H. G. Nam, B. K. Zayadan, B. D. Bruce, H. J. M. Hou, S. I. Allakhverdiev, *Int. J. Hydrog. Energy* **2017**, *42*, 8450–8461.

[10] K. Kohse-Höinghaus, P. Oßwald, T. Cool, T. Kasper, N. Hansen, F. Qi, C. Westbrook, P. Westmoreland, *Angw. Chem. Int. Ed.* **2010**, *49*, 3572–3597.

[11] R. Ahorsu, F. Medina, M. Constanti, *Energies* **2018**, *11*, 3366.

[12] C. B. Field, J. E. Campbell, D. B. Lobell, *Trends Ecol. Evol.* **2008**, *23*, 65–72.

[13] S. C. Pierobon, X. Cheng, P. J. Graham, B. Nguyen, E. G. Karakolis, D. Sinton, *Sustain. Energy Fuels* **2018**, *2*, 13–38.

[14] K. Hirano1, T. Hara1, Ardianor, R. A. Nugroho, H. Segah, N.Takayama, G. Sulmin, Y. Komai1, S. Okada, K. Kawamura, *Sci. Rep.* **2019**, *9*, 16974.

[15] M. A. Islam, M. Magnusson, R. J. Brown, G. A. Ayoko, M. N. Nabi, K. Heimann, *Energies* **2013**, *6*, 5676–5702.

[16] P. Metzger, C. Largeau, *Appl. Microbiol. Biotechnol.* **2005**, *66*, 486–496.

[17] H. Blanco, A. Faaij, *Renew. Sustain. Energy Rev.* **2018**, *81*, 1049–1086.

[18] H. Kobayashi, A. Hayakawa, K. K. A. Somarathne, E. C. Okafor, *Proc. Combust. Inst.* **2019**, *37*, 109–133.

[19] U. Eberle, M. Felderhoff, F. Schüth, *Angw. Chem. Int. Ed.* **2009**, *48*, 6608–6630.

[20] P. Jena, *J. Phys. Chem. Lett.* **2011**, *2*, 206–211.

[21] S. Gottesfeld, *J. Electrochem. Soc.* **2018**, *165*, J3405–J3412.

[22] Y. Zhao, B. P. Setzler, J. Wang, J. Nash, T. Wang, B. Xu, Y. Yan, *Joule* **2019**, *3*, 2472–2484.

[23] F. Obeid, T. C. Van, E. J. Horchler, Y. Guo, P. Verma, B. Miljevic, R. J. Brown, Z. Ristovski, T. A. Bodisco, T. Rainey, *Fuel* **2020**, *264*, 116805.

[24] Z. Tian, Y. Li, L. Zhang, P. Glarborg, F. Qi, *Combust. Flame* **2009**, *156*, 1413–1426.

[25] C. A. Pope III, R. T. Burnett, M. J. Thun, E. E. Calle, D. Krewski, K. Ito, G. D. Thurston, *JAMA* **2002**, *287*, 1132–1141.

[26] E. A. J. Bleeker, S. Wiegman, P. d. Voogt, M. Kraak, H. A. Leslie, E. d. Haas, W. Admiraal, *Reviews of Environmental Contamination and Toxicology*, Vol. 173, Springer, New York, **2002**.

[27] A. Hawliczek, B. Nota, P. Cenijn, J. Kamstra, B. Pieterse, R. Winter, K. Winkens, H. Hollert, H. Segner, J. Legler, *Reprod. Toxicol.* **2012**, *33*, 213–223.

[28] K. O. Johansson, M. P. Head-Gordon, P. E. Schrader, K. R. Wilson, H. A. Michelsen, *Science* **2018**, *361*, 997–1000.

[29] H. Junninen, J. Mønster, M. Rey, J. Cancelinha, K. Douglas, M. Duane, V. Forcina, A. Müller, F. Lagler, L. Marelli, A. Borowiak, J. Niedzialek, B. Paradiz, D. Mira-Salama, J. Jimenez, U. Hansen, C. Astorga, K. Stanczyk, M. Viana, X. Querol, R. M. Duvall, G. A. Norris, S. Tsakovski, P. Wåhlin, J. Horák, B. R. Larsen, *Environ. Sci. Technol* **2009**, *43*, 7964–7970.

[30] B. Shukla, M. Koshi, *Combust. Flame* **2012**, *159*, 3589–3596.

[31] A. Tielens, *Annu. Rev. Astron. Astrophys.* **2008**, *46*, 289–337.

[32] M. P. Bernstein, A. L. Mattioda, S. A. Sandford, D. M. Hudgins, *Astrophys. J.* **2005**, *626*, 909–918.

[33] I. Cherchneff, J. R. Barker, A. Tielens, *Astrophys. J.* **1992**, *401*, 269.

[34] F. Qi, *Proc. Combust. Inst.* **2013**, *34*, 33–63.

[35] D. L. Osborn, C. C. Hayden, P. Hemberger, A. Bodi, K. Voronova, B. Sztáray, *J. Chem. Phys.* **2016**, *145*, 164202.

[36] E. Reusch, F. Holzmeier, P. Constantinidis, P. Hemberger, I. Fischer, *Angw. Chem. Int. Ed.* **2017**, *56*, 8000–8003.

[37] T. Bierkandt, P. Hemberger, P. Oßwald, M. Köhler, T. Kasper, *Proc. Combust. Inst.* **2017**, *36*, 1223–1232.

[38] S. Feng, P. Hemberger, A. Bodi, X. Song, T. Yu, Z. Jiang, Y. Liu, Y. Ding, *J. Catal.* **2020**, *382*, 347–357.

[39] P. Hemberger, J. A. van Bokhoven, J. Pérez-Ramírez, A. Bodi, *Catal. Sci. Technol.* **2020**, *10*, 1975–1990.

[40] B. Sztáray, K. Voronova, K. G. Torma, K. J. Covert, A. Bodi, P. Hemberger, T. Gerber, D. L. Osborn, *J. Chem. Phys.* **2017**, *147*, 013944.

[41] D. Schleier, P. Constantinidis, N. Faßheber, I. Fischer, G. Friedrichs, P. Hemberger, E. Reusch, B. Sztáray, K. Voronova, *Phys. Chem. Chem. Phys.* **2018**, *20*, 10721–10731.

[42] D. Schleier, E. Reusch, M. Gerlach, T. Preitschopf, D. P. Mukhopadhyay, N. Faßheber, G. Friedrichs, P. Hemberger, I. Fischer, *Phys. Chem. Chem. Phys.* **2021**, *23*, 1539–1549.

[43] J. M. Dyke, *Phys. Chem. Chem. Phys.* **2019**, *21*, 9106–9136.

[44] M. Gomberg, *Ber. Dtsch. Chem. Ges.* **1900**, *33*, 3150–3163.

[45] M. Gomberg, *J. Am. Chem. Soc.* **1900**, *22*, 757–771.

[46] C. Wentrup, *Angw. Chem. Int. Ed.* **2017**, *56*, 14808–14835.

[47] M. N. McCabe, P. Hemberger, E. Reusch, A. Bodi, J. Bouwman, *J. Phys. Chem. Lett.* **2020**, *11*, 2859–2863.

[48] R. Hoffmann, *Angw. Chem. Int. Ed.* **1982**, *21*, 711–724.

[49] K. Fukui, *Science* **1982**, *218*, 747–754.

[50] T. A. Albright, J. K. Burdett, M.-H. Whangbo, *Orbital Interactions in Chemistry*, 2nd Ed., John Wiley & Sons Ltd., **2013**.

[51] H. A. Jahn, E. Teller, F. G. Donnan, *Proc. R. Soc. A* **1937**, *161*, 220–235.

[52] B. E. Applegate, T. A. Barckholtz, T. A. Miller, *Chem. Soc. Rev.* **2003**, *32*, 38–49.

[53] R. Renner, *Z. Physik* **1934**, 172–193.

[54] I. B. Bersuker, *Chem. Rev.* **2013**, *113*, 1351–1390.

[55] I. B. Bersuker, *Chem. Rev.* **2021**, *121*, 1463–1512.

[56] M. J. Paterson, M. J. Bearpark, M. A. Robb, L. Blancafort, G. A. Worth, *Phys. Chem. Chem. Phys.* **2005**, *7*, 2100–2115.

[57] R. Lindner, K. Müller-Dethlefs, E. Wedum, K. Haber, E. R. Grant, *Science* **1996**, *271*, 1698–1702.

[58] Y. Liu, I. B. Bersuker, W. Zou, J. E. Boggs, *Chem. Phys.* **2010**, *376*, 30–35.

[59] H. Kayi, I. B. Bersuker, J. E. Boggs, *J. Mol. Struct.* **2012**, *1023*, 108–114.

[60] P. Garcia-Fernandez, I. B. Bersuker, *Int. J. Quantum Chem.* **2012**, *112*, 3025–3032.

[61] J. Falta, T. Möller, *Forschung mit Synchrotronstrahlung: Eine Einführung in die Grundlagen und Anwendungen*, Vol. 1., Vieweg + Teubner, Wiesbaden, **2010**.

[62] K. Wille, *Physik der Teilchenbeschleuniger und Synchrotronstrahlungsquellen - Eine Einführung*, Vol. 2., B. G. Teubner, Stuttgart, **1996**.

[63] H. J. Kirkwood, R. Letrun, T. Tanikawa, J. Liu, M. Nakatsutsumi, M. Emons, T. Jezynski, G. Palmer, M. Lederer, R. Bean, J. Buck, S. D. D. Cafisio, R. Graceffa, J. Grünert, S. Göde, H. Höppner, Y. Kim, Z. Konopkova, G. Mills, M. Makita, A. Pelka, T. R. Preston, M. Sikorski, C. M. S. Takem, K. Giewekemeyer, M. Chollet, P. Vagovic, H. N. Chapman, A. P. Mancuso, T. Sato, *Opt. Lett.* **2019**, *44*, 1650–1653.

[64] J. D. Jackson, *Classical Electrodynamics*, Wiley, New York, **1975**.

[65] A. Lienard, *L'Eclairage Elec.* **1898**, *16*, 5.

[66] F. R. Elder, A. M. Gurewitsch, R. V. Langmuir, H. C. Pollock, *Nucl. Instrum. Methods Phys. Res., Sect. A* **1993**, *331*, 763–767.

[67] A. Britz, T. A. Assefa, A. Galler, W. Gawelda, M. Diez, P. Zalden, D. Khakhulin, B. Fernandes, P. Gessler, H. Sotoudi Namin, A. Beckmann, M. Harder, H. Yavaş, C. Bressler, *J. Synchrotron Radiat.* **2016**, *23*, 1409–1423.

[68] T. A. Carlson, *Annu. Rev. Phys. Chem.* **1975**, *26*, 211–234.

[69] I. Fischer, K. Müller-Dethlefs, *Phys. Unserer Zeit* **2000**, *31*, 168–176.

[70] W. Peatman, T. Borne, E. Schlag, *Chem. Phys. Lett.* **1969**, *3*, 492–497.

[71] T. Baer, W. Peatman, E. Schlag, *Chem. Phys. Lett.* **1969**, *4*, 243–247.

[72] K. Muller-Dethlefs, E. W. Schlag, *Annu. Rev. Phys. Chem.* **1991**, *42*, 109–136.

[73] E. R. Grant, M. G. White, *Nature* **1991**, *354*, 249–250.

[74] A. T. J. B. Eppink, D. H. Parker, *Rev. Sci. Instr.* **1997**, *68*, 3477–3484.

[75] T. Baer, Y. Li, *Int. J. Mass Spectrom.* **2002**, *219*, 381–389.

[76] B. Sztáray, T. Baer, *Rev. Sci. Instr.* **2003**, *74*, 3763–3768.

[77] K. Pachner, Dissertation, Universität Würzburg, **2018**.

[78] Z. Zhang, P. S. Monks, L. J. Stief, J. F. Liebman, R. E. Huie, S.-C. Kuo, R. B. Klemm, *J. Phys. Chem.* **1996**, *100*, 63–68.

[79] G. A. Garcia, L. Nahon, I. Powis, *Rev. Sci. Instr.* **2004**, *75*, 4989–4996.

[80] A. Röder, Dissertation, Universität Würzburg, Université Paris Sud, **2017**.

[81] R. L. Lord, L. Davis, E. L. Millam, E. Brown, C. Offerman, P. Wray, S. M. E. Green, *J. Chem. Edu.* **2008**, *85*, 1672.

[82] J. M. Standard, B. K. Clark, *J. Chem. Edu.* **1999**, *76*, 1363.

[83] R. L. Dunbrack, *J. Chem. Edu.* **1986**, *63*, 953.

[84] M. J. Thompson, M. Messina, *J. Chem. Edu.* **2019**, *96*, 1171–1177.

[85] M. J. Hollas, *Moderne Methoden in der Spektroskopie*, Springer-Verlag Berlin Heidelberg, **1995**.

[86] R. Signorell, F. Merkt, *Mole. Phys.* **1997**, *92*, 793–804.

[87] G. Wedler, H. J. Freund, *Lehrbuch der Physikalischen Chemie*, Vol. 6, Wiley-VCH, **2012**.

[88] S. Arrhenius, *Z. Phys. Chem.* **1889**, *4*, 226.

[89] J. Troe, *Chem. Rev.* **2003**, *103*, 4565–4576.

[90] R. A. Marcus, *J. Chem. Phys.* **1952**, *20*, 359–364.

[91] L. Nahon, N. de Oliveira, G. A. Garcia, J.-F. Gil, B. Pilette, O. Marcouillé, B. Lagarde, F. Polack, *J. Synchrotron Radiat.* **2012**, *19*, 508–520.

[92] G. A. Garcia, B. K. Cunha de Miranda, M. Tia, S. Daly, L. Nahon, *Rev. Sci. Instr.* **2013**, *84*, 053112.

[93] M. Johnson, A. Bodi, L. Schulz, T. Gerber, *Nucl. Instrum. Methods Phys. Res.* **2009**, *610*, 597–603.

[94] M. Lang, Dissertation, Universität Würzburg, **2015**.

[95] E. Reusch, Dissertation, Universität Würzburg, **2021**.

[96] D. W. Kohn, H. Clauberg, P. Chen, *Rev. Sci. Instr.* **1992**, *63*, 4003–4005.

[97] F. Holzmeier, Dissertation, Universität Würzburg, **2015**.

[98] M. J. Frisch, G. W. Trucks, H. B. Schlegel, G. E. Scuseria, M. A. Robb, J. R. Cheeseman, G. Scalmani, V. Barone, B. Mennucci, G. A. Petersson, H. Nakatsuji, M. Caricato, X. Li, H. P. Hratchian, A. F. Izmaylov, J. Bloino, G. Zheng, J. L. Sonnenberg, M. Hada, M. Ehara, K. Toyota, R. Fukuda, J. Hasegawa, M. Ishida, T. Nakajima, Y. Honda, O. Kitao, H. Nakai, T. Vreven, J. A. Montgomery, Jr., J. E. Peralta, F. Ogliaro, M. Bearpark, J. J. Heyd, E. Brothers, K. N. Kudin, V. N. Staroverov, R. Kobayashi, J. Normand, K. Raghavachari, A. Rendell, J. C. Burant, S. S. Iyengar, J. Tomasi, M. Cossi, N. Rega, J. M. Millam, M. Klene, J. E. Knox, J. B. Cross, V. Bakken, C. Adamo, J. Jaramillo, R. Gomperts, R. E. Stratmann, O. Yazyev, A. J. Austin, R. Cammi, C. Pomelli, J. W. Ochterski, R. L. Martin, K. Morokuma, V. G. Zakrzewski, G. A. Voth, P. Salvador, J. J. Dannenberg, S. Dapprich, A. D. Daniels, O. Farkas, J. B.

Foresman, J. V. Ortiz, J. Cioslowski, D. J. Fox, „Gaussian 09 Revision E.01“, gaussian Inc. Wallingford CT 2009.

[99] P. Hohenberg, W. Kohn, *Phys. Rev.* **1964**, *136*, B864–B871.

[100] W. Kohn, L. J. Sham, *Phys. Rev.* **1965**, *140*, A1133–A1138.

[101] P. W. Atkins, R. Friedman, *Molecular Quantum Mechanics*, Oxford University Press Inc., New York, **2011**.

[102] K. Burke, *J. Chem. Phys.* **2012**, *136*, 150901.

[103] A. D. Becke, *Phys. Rev. A* **1988**, *38*, 3098–3100.

[104] C. Lee, W. Yang, R. G. Parr, *Phys. Rev. B* **1988**, *37*, 785–789.

[105] P. J. Stephens, F. J. Devlin, C. F. Chabalowski, M. J. Frisch, *J. Phys. Chem.* **1994**, *98*, 11623–11627.

[106] J. A. Pople, M. Head-Gordon, D. J. Fox, K. Raghavachari, L. A. Curtiss, *J. Chem. Phys.* **1989**, *90*, 5622–5629.

[107] J. A. Montgomery, M. J. Frisch, J. W. Ochterski, G. A. Petersson, *J. Chem. Phys.* **1999**, *110*, 2822–2827.

[108] T. Schmidt, *Annu. Rev. Phys. Chem.* **2016**, *35*, 209–242.

[109] J. I. Moses, B. Bézard, E. Lellouch, G. Gladstone, H. Feuchtgruber, M. Allen, *Icarus* **2000**, *143*, 244–298.

[110] N. Hansen, J. Miller, S. Klippenstein, P. R. Westmoreland, K. Kohse-Höinghaus, *Combust. Explos. Shock Waves* **2012**.

[111] K. O. Johansson, M. P. Head-Gordon, P. E. Schrader, K. R. Wilson, H. A. Michelsen, *Science* **2018**, *361*, 997–1000.

[112] J. Bouwman, A. Bodi, J. Oomens, P. Hemberger, *Phys. Chem. Chem. Phys.* **2015**, *17*, 20508–20514.

[113] J. A. Miller, S. J. Klippenstein, Y. Georgievskii, L. B. Harding, W. D. Allen, A. C. Simmonett, *J. Phys. Chem. A* **2010**, *114*, 4881–4890.

[114] K. Wang, S. M. Villano, A. M. Dean, *Phys. Chem. Chem. Phys.* **2015**, *17*, 6255–6273.

[115] J. A. Zamet, S. L. Zeger, F. Dominici, F. Curriero, I. Coursac, D. W. Dockery, J. Schwartz, A. Zanobetti, *Res. Rep. Health Eff. Inst.* **2000**, *94*, 5–70.

[116] World Health Organization, **2014**, https://www.who.int/mediacentre/news/releases/2014/air-pollution/en/.

[117] I. Cherchneff, J. R. Barker, A. G. G. M. Tielens, *Astrophys. J.* **1992**, *401*, 269–287.

[118] A. Webster, *Mon. Not. R. Astron. Soc.* **1993**, *265*, 421–430.

[119] N. A. Porter, K. A. Mills, R. L. Carter, *J. Am. Chem. Soc.* **1994**, *116*, 6690–6696.

[120] D. W. Minsek, P. Chen, *J. Phys. Chem.* **1993**, *97*, 13375–13379.

[121] I. Fischer, P. Chen, *J. Phys. Chem. A* **2002**, *106*, 4291–4300.

[122] M. Gasser, A. M. Schulenburg, P. M. Dietiker, A. Bach, F. Merkt, P. Chen, *J. Chem. Phys.* **2009**, *131*, 014304.

[123] T. Schultz, J. S. Clarke, T. Gilbert, H.-J. Deyerl, I. Fischer, *Faraday Discuss.* **2000**, *115*, 17–31.

[124] H.-J. Deyerl, T. Gilbert, I. Fischer, P. Chen, *J. Chem. Phys.* **1997**, *107*, 3329–3332.

[125] D. Stranges, M. Stemmler, X. Yang, J. D. Chesko, A. G. Suits, Y. T. Lee, *J. Chem. Phys.* **1998**, *109*, 5372–5382.

[126] H. E. van den Bergh, A. B. Callear, *Trans. Faraday Soc.* **1970**, *66*, 2681–2684.

[127] J. M. Tulloch, M. T. Macpherson, C. A. Morgan, M. J. Pilling, *J. Phys. Chem.* **1982**, *86*, 3812–3819.

[128] A. A. Boyd, B. Noziere, R. Lesclaux, *J. Phys. Chem.* **1995**, *99*, 10815–10823.

[129] L. Seidel, K. Hoyermann, F. Mauß, J. Nothdurft, T. Zeuch, *Molecules* **2013**, *18*, 13608–13622.

[130] J. Lee, J. W. Bozzelli, *Proc. Combust. Inst.* **2005**, *30*, 1015 – 1022.

[131] C. A. Morgan, M. J. Pilling, J. M. Tulloch, R. P. Ruiz, K. D. Bayes, *J. Chem. Soc., Faraday Trans. 2* **1982**, *78*, 1323–1330.

[132] R. P. Ruiz, K. D. Bayes, M. T. Macpherson, M. J. Pilling, *J. Phys. Chem.* **1981**, *85*, 1622–1624.

[133] I. R. Slagle, E. Ratajczak, M. C. Heaven, D. Gutman, A. F. Wagner, *J. Am. Chem. Soc.* **1985**, *107*, 1838–1845.

[134] Z. H. Lodhi, R. W. Walker, *J. Chem. Soc., Faraday Trans.* **1991**, *87*, 2361–2365.

[135] N. D. Stothard, R. W. Walker, *J. Chem. Soc., Faraday Trans.* **1992**, *88*, 2621–2629.

[136] M. E. Jenkin, T. P. Murrells, S. J. Shalliker, G. D. Hayman, *J. Chem. Soc., Faraday Trans.* **1993**, *89*, 433–446.

[137] M. P. Rissanen, D. Amedro, A. J. Eskola, T. Kurten, R. S. Timonen, *J. Phys. Chem. A* **2012**, *116*, 3969–3978.

[138] P. Hemberger, M. Lang, B. Noller, I. Fischer, C. Alcaraz, B. K. Cunha de Miranda, G. A. Garcia, H. Soldi-Lose, *J. Phys. Chem. A* **2011**, *115*, 2225–2230.

[139] P. Hemberger, M. Steinbauer, M. Schneider, I. Fischer, M. Johnson, A. Bodi, T. Gerber, *J. Phys. Chem. A* **2010**, *114*, 4698–4703.

[140] M. Steinbauer, P. Hemberger, I. Fischer, A. Bodi, *ChemPhysChem* **2011**, *12*, 1795–1797.

[141] C. A. Taatjes, D. L. Osborn, T. A. Cool, K. Nakajima, *Chem. Phys. Lett.* **2004**, *394*, 19–24.

[142] C. A. Taatjes, N. Hansen, D. L. Osborn, K. Kohse-Höinghaus, T. A. Cool, P. R. Westmoreland, *Phys. Chem. Chem. Phys.* **2008**, *10*, 20–34.

[143] D. L. Osborn, P. Zou, H. Johnsen, C. C. Hayden, C. A. Taatjes, V. D. Knyazev, S. W. North, D. S. Peterka, M. Ahmed, S. R. Leone, *Rev. Sci. Instr.* **2008**, *79*, 104103.

[144] T. M. Selby, G. Meloni, F. Goulay, S. R. Leone, A. Fahr, C. A. Taatjes, D. L. Osborn, *J. Phys. Chem. A* **2008**, *112*, 9366–9373.

[145] R. J. Kee, F. M. Rupley, J. A. Miller, „Chemkin-II: A Fortrag chemical kinetics package for the analysis of gas-phase chemical kinetics.“, "Sandia National Laboratories, Livermore, CA, 1989, Report SAND89-8009, 1989".

[146] A. E. Lutz, R. J. Kee, J. A. Miller, „SENKIN: A Fortran program for predicting homogeneous gas phase chemical kinetics with sensitivity analysis.“, "Sandia National Laboratories, Livermore, CA, 1990, Report SAND87-8248, 1988".

[147] C. M. Leavitt, C. P. Moradi, B. W. Acrey, G. E. Douberly, *J. Chem. Phys.* **2013**, *139*, 234301.

[148] D. L. Baulch, J. Duxbury, S. J. Grant, D. C. Montague, *J. Phys. Chem. Ref. Data* **1981**, *10*, supplement 1.

[149] M. Ahmed, D. Blunt, D. Chen, A. G. Suits, *J. Chem. Phys.* **1997**, *106*, 7617–7624.

[150] N. Hemmi, A. G. Suits, *J. Phys. Chem. A* **1997**, *101*, 6633–6637.

[151] C.-Y. Wu, Y.-P. Lee, N. S. Wang, *J. Chem. Phys.* **2004**, *120*, 6957–6963.

[152] C.-Y. Wu, Y.-P. Lee, J. F. Ogilvie, N. S. Wang, *J. Phys. Chem. A* **2003**, *107*, 2389–2393.

[153] B. Ghosh, D. K. Papanastasiou, J. B. Burkholder, *J. Chem. Phys.* **2012**, *137*, 164315.

[154] A. V. Baklanov, L. N. Krasnoperov, *J. Phys. Chem. A* **2001**, *105*, 97–103.

[155] T.-K. Huang, B.-J. Chen, K.-C. Lin, L. Lin, B.-J. Sun, A. H. H. Chang, *J. Phys. Chem. A* **2017**, *121*, 2888–2895.

[156] S. Mohmand, T. Hirabayashi, H. Bock, *Chem. Ber.* **1981**, *114*, 2609–2621.

[157] E. W. Kaiser, T. J. Wallington, *J. Phys. Chem.* **1996**, *100*, 9788–9793.

[158] R. Atkinson, D. L. Baulch, R. A. Cox, J. N. Crowley, R. F. Hampson, R. G. Hynes, M. E. Jenkin, M. J. Rossi, J. Troe, *Atmos. Chem. Phys.* **2007**, *7*, 981–1191.

[159] T. Lenzer, K. Luther, D. Nilsson, S. Nordholm, *J. Phys. Chem. B* **2005**, *109*, 8325–8331.

[160] I. Oref, D. C. Tardy, *Chem. Rev.* **1990**, *90*, 1407–1445.

[161] M. Quack, J. Troe, „Unimolecular reactions and energy transfer of highly excited molecules“ in *Gas Kinetics and Energy Transfer: Volume 2*, *Vol. 2* (Edited by P. G. Ashmore, R. J. Donovan), The Royal Society of Chemistry, **1977**, Pp. 175–238.

[162] J. M. Ribeiro, A. M. Mebel, *J. Phys. Chem. A* **2016**, *120*, 1800–1812.

[163] C.-W. Zhou, Y. Li, E. O'Connor, K. P. Somers, S. Thion, C. Keesee, O. Mathieu, E. L. Petersen, T. A. DeVerter, M. A. Oehlschlaeger, G. Kukkadapu, C.-J. Sung, M. Alrefae, F. Khaled, A. Farooq, P. Dirrenberger, P.-A. Glaude, F. Battin-Leclerc, J. Santner, Y. Ju, T. Held, F. M. Haas, F. L. Dryer, H. J. Curran, *Combust. Flame* **2016**, *167*, 353–379.

[164] T. Zhang, J. Wang, T. Yuan, X. Hong, L. Zhang, F. Qi, *J. Phys. Chem. A* **2008**, *112*, 10487–10494.

[165] C. K. Westbrook, *Annu. Rev. Phys. Chem.* **2013**, *64*, 201–219.

[166] A. Röder, K. Issler, L. Poisson, A. Humeniuk, M. Wohlgemuth, M. Comte, F. Lepetit, I. Fischer, R. Mitric, J. Petersen, *J. Chem. Phys.* **2017**, *147*, 013902.

[167] M. Gasser, A. Bach, P. Chen, *Phys. Chem. Chem. Phys.* **2008**, *10*, 1133–1138.

[168] M. Lang, F. Holzmeier, P. Hemberger, I. Fischer, *J. Phys. Chem. A* **2015**, *119*, 3995–4000.

[169] S. Hartweg, J.-C. Loison, S. Boyé-Péronne, B. Gans, D. M. P. Holland, G. A. Garcia, L. Nahon, S. T. Pratt, *J. Phys. Chem. A* **2020**, *124*, 6050–6060.

[170] W. R. Roth, F. Bauer, A. Beitat, T. Ebbrecht, M. Wüstefeld, *Chem. Ber.* **1991**, *124*, 1453–1460.

[171] R. S. Tranter, A. W. Jasper, J. B. Randazzo, J. P. Lockhart, J. P. Porterfield, *Proc. Combust. Inst.* **2017**, *36*, 211–218.

[172] F. Bayrakceken, J. H. Brophy, R. D. Fink, J. E. Nicholas, *J. Chem. Soc., Faraday Trans. 1* **1973**, *69*, 228–235.

[173] C.-J. Chen, J. W. Bozzelli, *J. Phys. Chem. A* **2000**, *104*, 9715–9732.

[174] V. D. Knyazev, I. R. Slagle, *J. Phys. Chem. A* **1998**, *102*, 8932–8940.

[175] T. S. Dibble, Y. Sha, W. F. Thornton, F. Zhang, *J. Phys. Chem. A* **2012**, *116*, 7603–7614.

[176] T. Baer, R. P. Tuckett, *Phys. Chem. Chem. Phys.* **2017**, *19*, 9698–9723.

[177] K.-C. Lau, Y. Liu, L. J. Butler, *J. Chem. Phys.* **2006**, *125*, 144312.

[178] K. Voronova, K. M. Ervin, K. G. Torma, P. Hemberger, A. Bodi, T. Gerber, D. L. Osborn, B. Sztáray, *J. Phys. Chem. Lett.* **2018**, *9*, 534–539.

[179] M. A. Reza, H. Telfah, R. Xu, J. Liu, *J. Phys. Chem. A* **2019**, *123*, 3510–3517.

[180] K. A. Holbrook, M. J. Pilling, S. H. Robertson, *Unimolecular Reactions*, 2nd Ed., John Wiley & Sons: New York, **1996**.

[181] M. Olzmann, *Cleaner Combustion*, Pp. 549–576, Springer, London, **2013**.

[182] A. Miyoshi, *Int. J. Chem. Kinet.* **2012**, *44*, 59–74.

[183] S. M. Villano, L. K. Huynh, H.-H. Carstensen, A. M. Dean, *J. Phys. Chem. A* **2011**, *115*, 13425–13442.

[184] S. J. Klippenstein, *Proc. Combust. Inst.* **2017**, *36*, 77–111.

[185] B. M. Wong, D. M. Matheu, W. H. Green, *J. Phys. Chem. A* **2003**, *107*, 6206–6211.

[186] B. Alicke, K. Hebestreit, J. Stutz, U. Platt, *Nature* **1999**, *397*, 572–573.

[187] G. McFiggans, J. M. C. Plane, B. J. Allan, L. J. Carpenter, H. Coe, C. O'Dowd, *J. Geophys. Res.* **2000**, *105*, 14371–14385.

[188] A. Saiz-Lopez, J. M. C. Plane, A. R. Baker, L. J. Carpenter, R. von Glasow, J. C. Gómez Martín, G. McFiggans, R. W. Saunders, *Chem. Rev.* **2012**, *112*, 1773–1804.

[189] T. Sherwen, M. J. Evans, L. J. Carpenter, S. J. Andrews, R. T. Lidster, B. Dix, T. K. Koenig, R. Sinreich, I. Ortega, R. Volkamer, A. Saiz-Lopez, C. Prados-Roman, A. S. Mahajan, C. Ordóñez, *Atmos. Chem. Phys.* **2016**, *16*, 1161–1186.

[190] C. R. Thompson, P. B. Shepson, J. Liao, L. G. Huey, E. C. Apel, C. A. Cantrell, F. Flocke, J. Orlando, A. Fried, S. R. Hall, R. S. Hornbrook, D. J. Knapp, R. L. Mauldin III, D. D. Montzka, B. C. Sive, K. Ullmann, P. Weibring, A. Weinheimer, *Atmos. Chem. Phys.* **2015**, *15*, 9651–9679.

[191] B. Laszlo, M. J. Kurylo, R. E. Huie, *J. Phys. Chem.* **1995**, *99*, 11701–11707.

[192] M. E. Jenkin, R. A. Cox, *J. Phys. Chem.* **1985**, *89*, 192–199.

[193] A. Vipond, C. E. Canosa-Mas, M. L. Flugge, D. J. Gray, D. E. Shallcross, D. Shah, R. P. Wayne, *Phys. Chem. Chem. Phys.* **2002**, *4*, 3648–3658.

[194] M. E. Tucceri, T. J. Dillon, J. N. Crowley, *Phys. Chem. Chem. Phys.* **2005**, *7*, 1657–1663.

[195] C. D. O'Dowd, J. L. Jiminez, R. Bahreini, R. C. Flagan, J. H. Seinfeld, K. Hämeri, L. Pirjola, M. Kumala, S. G. Jennings, T. Hoffmann, *Nature* **2002**, *417*, 632–636.

[196] R. A. Durie, D. A. Ramsay, *Can. J. Phys.* **1958**, *36*, 35–53.

[197] I. Barnes, K. Becker, J. Starcke, *Chem. Phys. Lett.* **1992**, *196*, 578–582.

[198] N. Walker, D. E. Tevault, R. R. Smardzewski, *J. Chem. Phys.* **1978**, *69*, 564–568.

[199] J. Brown, C. Byfleet, B. Howard, D. Russell, *Mol. Phys.* **1972**, *23*, 457–468.

[200] S. Saito, *J. Mol. Spectrosc.* **1973**, *48*, 530–535.

[201] M. K. Gilles, M. L. Polak, W. C. Lineberger, *J. Chem. Phys.* **1992**, *96*, 8012–8020.

[202] J. C. Gómez Martín, O. Gálvez, M. T. Baeza-Romero, T. Ingham, J. M. C. Plane, M. A. Blitz, *Phys. Chem. Chem. Phys.* **2013**, *15*, 15612–15622.

[203] N. Wei, C. Hu, S. Zhou, Q. Ma, P. Mikuška, Z. Večeřa, Y. Gai, X. Lin, X. Gu, W. Zhao, B. Fang, W. Zhang, J. Chen, F. Liu, X. Shan, L. Sheng, *RSC Adv.* **2017**, *7*, 56779–56787.

[204] P. Hassanzadeh, K. K. Irikura, R. D. Johnson, *J. Phys. Chem. A* **1997**, *101*, 6897–6902.

[205] P. S. Monks, L. J. Stief, D. C. Tardy, J. F. Liebman, Z. Zhang, S.-C. Kuo, R. B. Klemm, *J. Phys. Chem.* **1995**, *99*, 16566–16570.

[206] L. Brewer, J. Tellinghuisen, *J. Chem. Phys.* **1972**, *56*, 3929–3938.

[207] L. Brewer, J. Tellinghuisen, *J. Chem. Phys.* **1972**, *56*, 3929–3938.

[208] K. A. Peterson, B. C. Shepler, D. Figgen, H. Stoll, *J. Phys. Chem. A* **2006**, *110*, 13877–13883.

[209] J. M. Dyke, S. D. Gamblin, N. Hooper, E. P. F. Lee, A. Morris, D. K. W. Mok, F. T. Chau, *J. Chem. Phys.* **2000**, *112*, 6262–6274.

[210] C. E. Miller, E. A. Cohen, *J. Chem. Phys.* **2001**, *115*, 6459–6470.

[211] N. Gilka, P. R. Taylor, C. M. Marian, *J. Chem. Phys.* **2008**, *129*, 044102.

[212] N. L. Ma, Y.-S. Cheung, C. Y. Ng, W.-K. Li, *Mol. Phys.* **1997**, *91*, 495–502.

[213] M. Abe, *Chem. Rev.* **2013**, *113*, 7011–7088.

[214] D. Kaiser, E. Reusch, P. Hemberger, A. Bodi, E. Welz, B. Engels, I. Fischer, *Phys. Chem. Chem. Phys.* **2018**, *20*, 3988–3996.

[215] J. C. Axtell, L. M. A. Saleh, E. A. Qian, A. I. Wixtrom, A. M. Spokoyny, *Inorg. Chem.* **2018**, *57*, 2333–2350.

[216] D. Auerhammer, M. Arrowsmith, P. Bissinger, H. Braunschweig, T. Dellermann, T. Kupfer, C. Lenczyk, D. K. Roy, M. Schäfer, C. Schneider, *Chem. Eur. J.* **2018**, *24*, 266–273.

[217] H. Braunschweig, P. Constantinidis, T. Dellermann, W. C. Ewing, I. Fischer, M. Hess, F. R. Knight, A. Rempel, C. Schneider, S. Ullrich, A. Vargas, J. D. Woollins, *Angw. Chem. Int. Ed.* **2016**, *55*, 5606–5609.

[218] Y. Wang, B. Quillian, P. Wei, C. S. Wannere, Y. Xie, R. B. King, H. F. Schaefer, P. v. R. Schleyer, G. H. Robinson, *J. Am. Chem. Soc.* **2007**, *129*, 12412–12413.

[219] M. Zhou, N. Tsumori, Z. Li, K. Fan, L. Andrews, Q. Xu, *J. Am. Chem. Soc.* **2002**, *124*, 12936–12937.

[220] H. Braunschweig, R. D. Dewhurst, K. Hammond, J. Mies, K. Radacki, A. Vargas, *Science* **2012**, *336*, 1420–1422.

[221] G. Frenking, N. Holzmann, *Science* **2012**, *336*, 1394–1395.

[222] J. Böhnke, H. Braunschweig, P. Constantinidis, T. Dellermann, W. C. Ewing, I. Fischer, K. Hammond, F. Hupp, J. Mies, H.-C. Schmitt, A. Vargas, *J. Am. Chem. Soc.* **2015**, *137*, 1766–1769.

[223] S.-D. Li, H.-J. Zhai, L.-S. Wang, *J. Am. Chem. Soc.* **2008**, *130*, 2573–2579.

[224] H. Braunschweig, R. Shang, *Inorg. Chem.* **2015**, *54*, 3099–3106.

[225] M. Soleilhavoup, G. Bertrand, *Angw. Chem. Int. Ed.* **2017**, *56*, 10282–10292.

[226] H. F. Bettinger, *J. Am. Chem. Soc.* **2006**, *128*, 2534–2535.

[227] J. Oliveira, M. Oliveira, O. Conde, *Surf. Coat. Technol.* **1996**, *80*, 100–104.

[228] R. Zan, A. Altuntepe, S. Erkan, *Physica E* **2021**, *128*, 114629.

[229] J. Xu, M. C. Granger, Q. Chen, J. W. Strojek, T. E. Lister, G. M. Swain, *Anal. Chemi.* **1997**, *69*, 591A–597A.

[230] P. L. Timms, *Acc. Chem. Res.* **1973**, *6*, 118–123.

[231] J. Böhnke, T. Dellermann, M. A. Celik, I. Krummenacher, R. D. Dewhurst, S. Demeshko, W. C. Ewing, K. Hammond, M. Heß, E. Bill, E. Welz, M. I. S. Röhr, R. Mitrić, B. Engels, F. Meyer, H. Braunschweig, *Nat. Commun.* **2018**, *9*, 1197.

[232] L. B. Knight, K. Kerr, P. K. Miller, C. A. Arrington, *J. Phys. Chem.* **1995**, *99*, 16842–16848.

[233] T. J. Tague, L. Andrews, *J. Am. Chem. Soc.* **1994**, *116*, 4970–4976.

[234] B. Engels, H. U. Suter, M. Perić, *J. Phys. Chem.* **1996**, *100*, 10121–10122.

[235] V. Brites, C. Léonard, *Comput. Theor. Chem.* **2013**, *1025*, 24–29.

[236] M. Perić, B. Ostojić, B. Engels, *J. Mol. Spectrosc.* **1997**, *182*, 295–308.

[237] M. Perić, B. Ostojić, B. Engels, *J. Mol. Spectrosc.* **1997**, *182*, 280–294.

[238] E. Miliordos, A. Mavridis, *J. Chem. Phys.* **2008**, *128*, 144308.

[239] K. A. Lundell, A. I. Boldyrev, *Chem. Phys. Lett.* **2018**, *699*, 85–87.

[240] B. Ruscic, R. E. Pinzon, M. L. Morton, G. von Laszevski, S. J. Bittner, S. G. Nijsure, K. A. Amin, M. Minkoff, A. F. Wagner, *J. Phys. Chem. A* **2004**, *108*, 9979–9997.

[241] B. Ruscic, R. E. Pinzon, G. von Laszewski, D. Kodeboyina, A. Burcat, D. Leahy, D. Montoy, A. F. Wagner, *J. Phys. Conf. Ser.* **2005**, *16*, 561–570.

[242] J. M. Dyke, C. Kirby, A. Morris, *J. Chem. Soc., Faraday Trans. 2* **1983**, *79*, 483–490.

[243] B. Ruščić, M. Schwarz, J. Berkowitz, *J. Chem. Phys.* **1989**, *91*, 4183–4188.

[244] B. Ruščic, M. Schwarz, J. Berkowitz, *J. Chem. Phys.* **1989**, *91*, 4576–4581.

[245] J. Baker, M. Barnes, M. Cockett, J. Dyke, A. Ellis, M. Fehér, E. Lee, A. Morris, H. Zamanpour, *J. Electron Spectros. Relat. Phenomena* **1990**, *51*, 487–511.

[246] J. Barr, L. Beeching, A. De Fanis, J. Dyke, S. Gamblin, N. Hooper, A. Morris, S. Stranges, J. West, A. Wright, T. Wright, *J. Electron Spectros. Relat. Phenomena* **2000**, *108*, 47–61.

[247] G. A. Garcia, B. Gans, J. Krüger, F. Holzmeier, A. Röder, A. Lopes, C. Fittschen, C. Alcaraz, J.-C. Loison, *Phys. Chem. Chem. Phys.* **2018**, *20*, 8707–8718.

[248] J. C. Poully, J. P. Schermann, N. Nieuwjaer, F. Lecomte, G. Grégoire, C. Desfrançois, G. A. Garcia, L. Nahon, D. Nandi, L. Poisson, M. Hochlaf, *Phys. Chem. Chem. Phys.* **2010**, *12*, 3566–3572.

[249] A. D. Walsh, *J. Chem. Soc.* **1953**, 2260–2266.

[250] G. Herzberg, J. W. T. Spinks, K. P. Huber, *Molecular spectra and molecular structure*, Vol. 4, Van Nostrand Reinhold, New York, **1974**.

[251] B. Jin, D. J. Clouthier, R. Tarroni, *J. Chem. Phys.* **2017**, *147*, 124303.

[252] F. X. Sunahori, M. Gharaibeh, D. J. Clouthier, R. Tarroni, *J. Chem. Phys.* **2015**, *142*, 174302.

[253] M. Kolbuszewski, *Mol. Phys.* **1996**, *88*, 105–124.

[254] M. Brommer, P. Rosmus, S. Carter, N. C. Handy, *Mol. Phys.* **1992**, *77*, 549–561.

[255] M. Perić, S. D. Peyerimhoff, R. J. Buenker, *Can. J. Chem.* **1981**, *59*, 1318–1327.

[256] G. Herzberg, J. W. C. Johns, *Proc. R. Soc. A* **1967**, *298*, 142–159.

[257] T. P. Fehlner, W. S. Koski, *J. Am. Chem. Soc.* **1964**, *86*, 2733–2734.

[258] J. H. Wilson, H. A. McGee, *J. Chem. Phys.* **1967**, *46*, 1444–1453.

[259] L. A. Curtiss, J. A. Pople, *J. Phys. Chem.* **1988**, *92*, 894–899.

[260] J. Koput, *J. Comput. Chem.* **2015**, *36*, 2219–2227.

[261] M. Krasowska, M. Edelmann, H. F. Bettinger, *J. Phys. Chem. A* **2016**, *120*, 6332–6341.

[262] I. Magoulas, A. Kalemos, A. Mavridis, *J. Chem. Phys.* **2013**, *138*, 104312.

[263] C. Ricardo Viteri, A. T. Gilkison, S. J. Rixon, E. R. Grant, *J. Chem. Phys.* **2006**, *124*, 144312.

[264] C. R. Viteri, A. T. Gilkison, S. J. Rixon, E. R. Grant, *Phys. Rev. A* **2007**, *75*, 013410.

[265] J. Clark, M. Konopka, L.-M. Zhang, E. R. Grant, *Chem. Phys. Lett.* **2001**, *340*, 45–54.

[266] C. Brazier, *J. Mol. Spectrosc.* **1996**, *177*, 90–105.

[267] K. Zhang, B. Guo, V. Braun, M. Dulick, P. Bernath, *J. Mol. Spectrosc.* **1995**, *170*, 82–93.

[268] W. Fernando, P. Bernath, *J. Mol. Spectrosc.* **1991**, *145*, 392–402.

[269] F. Pianalto, L. O'Brien, P. Keller, P. Bernath, *J. Mol. Spectrosc.* **1988**, *129*, 348–353.

[270] O. Gustafsson, M. Rittby, *J. Mol. Spectrosc.* **1988**, *131*, 325–339.

[271] W.-T. Luh, W. C. Stwalley, *J. Mol. Spectrosc.* **1983**, *102*, 212–223.

[272] J. Lebreton, J. Ferran, L. Marsigny, *J. Phys. B* **1975**, *8*, L465–L466.

[273] D. Hildebrand, *Int. J. Mass Spectrom. and Ion Phys.* **1971**, *7*, 255–260.

[274] S. Bauer, G. Herzberg, J. Johns, *J. Mol. Spectrosc.* **1964**, *13*, 256–280.

[275] D. W. Robinson, *J. Mol. Spectrosc.* **1963**, *11*, 275–300.

[276] F. J. Lovas, D. R. Johnson, *J. Chem. Phys.* **1971**, *55*, 41–44.

[277] R. B. Caton, A. E. Douglas, *Can. J. Phys.* **1970**, *48*, 432–452.

[278] R. F. Barrow, D. Premaswarup, J. Winternitz, P. B. Zeeman, *Proc. Phys. Soc.* **1958**, *71*, 61–64.

[279] A. S. Goldman, K. Krogh-Jespersen, *J. Am. Chem. Soc.* **1996**, *118*, 12159–12166.

[280] F. Dushinsky, *Acta Physicochim. USSR* **1937**, *7*, 441.

[281] G. B. Park, *J. Chem. Phys.* **2014**, *141*, 134304.

[282] G. B. Park, J. H. Baraban, R. W. Field, *J. Chem. Phys.* **2014**, *141*, 134305.

[283] F. Holzmeier, M. Lang, I. Fischer, P. Hemberger, G. A. Garcia, X. Tang, J.-C. Loison, *Phys. Chem. Chem. Phys.* **2015**, *17*, 19507–19514.

[284] T. Marder, *Angw. Chem. Int. Ed.* **2007**, *46*, 8116–8118.

[285] J. Andersson, S. Grönkvist, *Int. J. Hydrog. Energy* **2019**, *44*, 11901–11919.

[286] M. Hirscher, V. A. Yartys, M. Baricco, J. Bellosta von Colbe, D. Blanchard, R. C. Bowman, D. P. Broom, C. E. Buckley, F. Chang, P. Chen, Y. W. Cho, J.-C. Crivello, F. Cuevas, W. I. David, P. E. de Jongh, R. V. Denys, M. Dornheim, M. Felderhoff, Y. Filinchuk, G. E. Froudakis, D. M. Grant, E. M. Gray, B. C. Hauback, T. He, T. D. Humphries, T. R. Jensen, S. Kim, Y. Kojima, M. Latroche, H.-W. Li, M. V. Lototskyy, J. W. Makepeace, K. T. Møller, L. Naheed, P. Ngene, D. Noréus, M. M. Nygård, S. ichi Orimo, M. Paskevicius, L. Pasquini, D. B. Ravnsbæk, M. Veronica Sofianos, T. J. Udovic, T. Vegge, G. S. Walker, C. J. Webb, C. Weidenthaler, C. Zlotea, *J. Alloys Compd.* **2020**, *827*, 153548.

[287] V. A. Yartys, M. V. Lototsky, in *Hydrogen Materials Science and Chemistry of Carbon Nanomaterials* (Edited by T. N. Veziroglu, S. Yu. Zaginaichenko, D. V. Schur, B. Baranowski, A. P. Shpak, V. V. Skorokhod), Springer Netherlands, Dordrecht, **2005** Pp. 75–104.

[288] U. B. Demirci, *Int. J. Hydrog. Energy* **2017**, *42*, 9978–10013.

[289] U. B. Demirci, *Energies* **2020**, *13*, 3071.

[290] S. D. Peyerimhoff, R. J. Buenker, *J. Chem. Phys.* **1968**, *49*, 312–325.

[291] J. D. Dill, P. v. R. Schleyer, J. A. Pople, *J. Am. Chem. Soc.* **1975**, *97*, 3402–3409.

[292] J. S. Binkley, L. R. Thorne, *J. Chem. Phys.* **1983**, *79*, 2932–2940.

[293] P. Brint, B. Sangchakr, P. W. Fowler, *J. Chem. Soc., Faraday Trans. 2* **1989**, *85*, 29–37.

[294] H. Umeyama, K. Morokuma, *J. Am. Chem. Soc.* **1976**, *98*, 7208–7220.

[295] M. Dixon, W. E. Palke, *J. Chem. Phys.* **1974**, *61*, 2250–2254.

[296] R. H. Crabtree, P. E. M. Siegbahn, O. Eisenstein, A. L. Rheingold, T. F. Koetzle, *Acc. Chem. Res.* **1996**, *29*, 348–354.

[297] P. M. Mitrasinovic, *Chem. Phys. Lett.* **2004**, *392*, 419–427.

[298] F. Baitalow, J. Baumann, G. Wolf, K. Jaenicke-Rößler, G. Leitner, *Thermochim. Acta* **2002**, *391*, 159–168.

[299] R. Benzouaa, U. Demirci, R. Chiriac, F. Toche, P. Miele, *Thermochim. Acta* **2010**, *509*, 81–86.

[300] M. Hu, R. Geanangel, W. Wendlandt, *Thermochim. Acta* **1978**, *23*, 249–255.

[301] V. Sit, R. Geanangel, W. Wendlandt, *Thermochim. Acta* **1987**, *113*, 379–382.

[302] X. Kang, Z. Fang, L. Kong, H. Cheng, X. Yao, G. Lu, P. Wang, *Adv. Mater.* **2008**, *20*, 2756–2759.

[303] J. D. Carpenter, B. S. Ault, *Chem. Phys. Lett.* **1992**, *197*, 171–174.

[304] Y. Kawashima, K. Kawaguchi, E. Hirota, *J. Chem. Phys.* **1987**, *87*, 6331–6333.

[305] N. Patel, A. Kale, A. Miotello, *Appl. Catal. B Environ.* **2012**, *111-112*, 178–184.

[306] D. Neiner, A. Luedtke, A. Karkamkar, W. Shaw, J. Wang, N. D. Browning, T. Autrey, S. M. Kauzlarich, *J. Phys. Chem. C* **2010**, *114*, 13935–13941.

[307] I. H. T. Sham, C.-C. Kwok, C.-M. Che, N. Zhu, *Chem. Commun.* **2005**, 3547–3549.

[308] M. Bechelany, S. Bernard, A. Brioude, D. Cornu, P. Stadelmann, C. Charcosset, K. Fiaty, P. Miele, *J. Phys. Chem. C* **2007**, *111*, 13378–13384.

[309] T. Kar, P. Grüninger, S. Scheiner, H. F. Bettinger, A. K. Roy, *J. Phys. Chem. C* **2017**, *121*, 26044–26053.

[310] R. Sundaram, S. Scheiner, A. K. Roy, T. Kar, *J. Phys. Chem. C* **2015**, *119*, 3253–3259.

[311] R. C. Taylor, C. L. Cluff, *Nature* **1958**, *182*, 390–391.

[312] S. Trudel, D. F. R. Gilson, *Inorg. Chem.* **2003**, *42*, 2814–2816.

[313] R. Custelcean, Z. A. Dreger, *J. Phys. Chem. B* **2003**, *107*, 9231–9235.

[314] N. J. Hess, M. E. Bowden, V. M. Parvanov, C. Mundy, S. M. Kathmann, G. K. Schenter, T. Autrey, *J. Chem. Phys.* **2008**, *128*, 034508.

[315] J. Goubeau, E. Ricker, *Z. Anorg. Allg. Chem.* **1961**, *310*, 123–142.

[316] J. Smith, K. Seshadri, D. White, *J. Mol. Spectrosc.* **1973**, *45*, 327–337.

[317] E. C. Reynhardt, C. F. Hoon, *J. Phys. C Solid State Phys.* **1983**, *16*, 6137–6152.

[318] C. Gervais, F. Babonneau, J. Maquet, C. Bonhomme, D. Massiot, E. Framery, M. Vaultier, *Magn. Reson. Chem.* **1998**, *36*, 407–414.

[319] G. H. Penner, Y. C. P. Chang, J. Hutzal, *Inorg. Chem.* **1999**, *38*, 2868–2873.

[320] O. Gunaydin-Sen, R. Achey, N. S. Dalal, A. Stowe, T. Autrey, *J. Phys. Chem. B* **2007**, *111*, 677–681.

[321] D. G. Allis, M. E. Kosmowski, B. S. Hudson, *J. Am. Chem. Soc.* **2004**, *126*, 7756–7757.

[322] C. F. Hoon, E. C. Reynhardt, *J. Phys. C Solid State Phys.* **1983**, *16*, 6129–6136.

[323] W. T. Klooster, T. F. Koetzle, P. E. M. Siegbahn, T. B. Richardson, R. H. Crabtree, *J. Am. Chem. Soc.* **1999**, *121*, 6337–6343.

[324] D. R. Lloyd, N. Lynaugh, *J. Chem. Soc. D* **1970**, 1545–1546.

[325] R. L. Sams, S. S. Xantheas, T. A. Blake, *J. Phys. Chem. A* **2012**, *116*, 3124–3136.

[326] D. R. Lloyd, N. Lynaugh, *J. Chem. Soc., Faraday Trans. 2* **1972**, *68*, 947–958.

[327] R. Suenram, L. Thorne, *Chem. Phys. Lett.* **1981**, *78*, 157–160.

[328] L. R. Thorne, R. D. Suenram, F. J. Lovas, *J. Chem. Phys.* **1983**, *78*, 167–171.

[329] K. Vormann, H. Dreizler, *Z. Naturforsch. A* **1991**, *46*, 1060–1062.

[330] J. Smith, K. Seshadri, D. White, *J. Mol. Spectrosc.* **1973**, *45*, 327–337.

[331] B. R. Westbrook, E. M. Valencia, S. C. Rushing, G. S. Tschumper, R. C. Fortenberry, *J. Chem. Phys.* **2021**, *154*, 041104.

[332] N. C. Baird, R. K. Datta, *Inorg. Chem.* **1972**, *11*, 17–19.

[333] D. Armstrong, D. Clark, *Theoret. Chim. Acta* **1972**, *24*, 307–316.

[334] E. R. Lory, R. F. Porter, *J. Am. Chem. Soc.* **1973**, *95*, 1766–1770.

[335] F. Zhang, P. Maksyutenko, R. I. Kaiser, A. M. Mebel, A. Gregušová, S. A. Perera, R. J. Bartlett, *J. Phys. Chem. A* **2010**, *114*, 12148–12154.

[336] D. Schleier, A. Humeniuk, E. Reusch, F. Holzmeier, D. Nunez-Reyes, C. Alcaraz, G. A. Garcia, J.-C. Loison, I. Fischer, R. Mitric, *J. Phys. Chem. Lett.* **2018**, *9*, 5921–5925.

[337] R. Boese, A. H. Maulitz, P. Stellberg, *Chem. Ber.* **1994**, *127*, 1887–1889.

[338] B. Kiran, A. K. Phukan, E. D. Jemmis, *Inorg. Chem.* **2001**, *40*, 3615–3618.

[339] E. D. Jemmis, B. Kiran, *Inorg. Chem.* **1998**, *37*, 2110–2116.

[340] A. Stock, E. Pohland, *Ber. Dtsch. Chem. Ges.* **1926**, *59*, 2210–2215.

[341] S. F. Parker, *RSC Adv.* **2018**, *8*, 23875–23880.

[342] D. Frost, F. Herring, C. McDowell, I. Stenhouse, *Chem. Phys. Let.* **1970**, *5*, 291–292.

[343] D. R. Lloyd, N. Lynaugh, W. C. Price, D. W. Turner, *Philos. Trans. R. Soc. A* **1970**, *268*, 97–109.

[344] H. Kato, K. Hirao, M. Sano, *J. Mol. Struct.* **1983**, *104*, 489–494.

[345] R. Rüede, H. Troxler, C. Beglinger, M. Jungen, *Chem. Phys. Lett.* **1993**, *203*, 477–481.

[346] B. Niu, D. A. Shirley, Y. Bai, *J. Chem. Phys.* **1993**, *98*, 4377–4390.

[347] U. Jacovella, C. J. Stein, M. Grütter, L. Freitag, C. Lauzin, M. Reiher, F. Merkt, *Phys. Chem. Chem. Phys.* **2018**, *20*, 1072–1081.

[348] J. Dyke, E. Lee, M. Zamanpour Niavaran, *Int. J. Mass Spectrom. and Ion Proc.* **1989**, *94*, 221–235.

[349] S. Lias, J. Bartmess, J. Liebman, J. Holmes, R. Levin, W. Mallard, *J. Phys. Chem. Ref. Data, Suppl. 1* **1988**, *17*, 1–861.

[350] G. Reiser, W. Habenicht, K. Müller-Dethlefs, E. W. Schlag, *Chem. Phys. Lett.* **1988**, *152*, 119–123.

[351] S. S. Mallajosyula, A. Datta, S. K. Pati, *J. Phys. Chem. A* **2006**, *110*, 5156–5163.

[352] K. L. K. Lee, S. M. Rabidoux, J. F. Stanton, *J. Phys. Chem. A* **2016**, *120*, 7548–7553.

[353] H. M. Sulzbach, D. Graham, J. C. Stephens, H. F. Schaefer III, *Acta Chim. Scand.* **1997**, *51*, 547–555.

[354] K. Toriyama, K. Nunome, M. Iwasaki, *J. Chem. Phys.* **1982**, *77*, 5891–5912.

[355] M. Iwasaki, K. Toriyama, K. Nunome, *Radiat. Phys. Chem.* **1983**, *21*, 147–156.

[356] A. Ioffe, S. Shaik, *J. Chem. Soc., Perkin Trans. 2* **1993**, 1461–1473.

[357] M. H. Matus, D. J. Grant, M. T. Nguyen, D. A. Dixon, *J. Phys. Chem. C* **2009**, *113*, 16553–16560.

[358] A. Baker, C. Baker, C. Brundle, D. Turner, *Int. J. Mass Spectrom. and Ion Phys.* **1968**, *1*, 285–301.

[359] B. Yuan, J.-W. Shin, E. R. Bernstein, *J. Chem. Phys.* **2016**, *144*, 144315.

[360] T. Wideman, P. J. Fazen, A. T. Lynch, K. Su, E. E. Remsen, L. G. Sneddon, T. Chen, R. T. Paine, *Borazine, Polyborazylene, β-Vinylborazine, and Poly(β-Vinylborazine)*, Pp. 232–242, John Wiley & Sons, Ltd, **1998**.

[361] J. Li, C. Zhang, B. Li, F. Cao, S. Wang, *Eur. J. Inorg. Chem.* **2010**, *2010*, 1763–1766.

[362] A. Candian, J. Bouwman, P. Hemberger, A. Bodi, A. G. G. M. Tielens, *Phys. Chem. Chem. Phys.* **2018**, *20*, 5399–5406.

[363] A. J. Yencha, R. I. Hall, L. Avaldi, G. Dawber, A. G. McConkey, M. A. MacDonald, G. C. King, *Can. J. Chem.* **2004**, *82*, 1061–1066.

[364] J. Eiding, R. Schneider, W. Domcke, H. Köppel, W. von Niessen, *Chem. Phys. Lett.* **1991**, *177*, 345–351.

[365] P. Baltzer, L. Karlsson, B. Wannberg, G. Öhrwall, D. Holland, M. MacDonald, M. Hayes, W. von Niessen, *Chem. Phys.* **1997**, *224*, 95–119.

[366] M. Epshtein, V. Scutelnic, Z. Yang, T. Xue, M. L. Vidal, A. I. Krylov, S. Coriani, S. R. Leone, *J. Phys. Chem. A* **2020**, *124*, 9524–9531.

[367] R. Kadam, R. Erickson, K. Komaguchi, M. Shiotani, A. Lund, *Chem. Phys. Lett.* **1998**, *290*, 371–378.

[368] M. K. Carter, G. Vincow, *J. Chem. Phys.* **1967**, *47*, 292–302.

[369] J. Miller, L. Andrews, *Chem. Phys. Lett.* **1980**, *72*, 90–93.

[370] O. Braitbart, E. Castellucci, G. Dujardin, S. Leach, *J. Phys. Chem.* **1983**, *87*, 4799–4804.

[371] H. Tachikawa, *J. Phys. Chem. A* **2018**, *122*, 4121–4129.

[372] M. Döscher, H. Köppel, P. G. Szalay, *J. Chem. Phys.* **2002**, *117*, 2645–2656.

[373] M. L. Vidal, M. Epshtein, V. Scutelnic, Z. Yang, T. Xue, S. R. Leone, A. I. Krylov, S. Coriani, *J. Phys. Chem. A* **2020**, *124*, 9532–9541.

[374] V. Mozhayskiy, A. Krylov, *Mol. Phys.* **2009**, *107*, 929–938.

[375] P. A. Pieniazek, S. E. Bradforth, A. I. Krylov, *J. Chem. Phys.* **2008**, *129*, 074104.

[376] M. Shahbaz, S. Urano, P. R. LeBreton, M. A. Rossman, R. S. Hosmane, N. J. Leonard, *J. Am. Chem. Soc.* **1984**, *106*, 2805–2811.

[377] J. V. Ortiz, *J. Chem. Phys.* **1996**, *104*, 7599–7605.

[378] M. C. E. Galbraith, S. Scheit, N. V. Golubev, G. Reitsma, N. Zhavoronkov, V. Despré, F. Lépine, A. I. Kuleff, M. J. J. Vrakking, O. Kornilov, H. Köppel, J. Mikosch, *Nat. Commun.* **2018**, *8*, 1018.

[379] L. Avaldi, G. Dawber, R. Hall, G. King, A. McConkey, M. MacDonald, G. Stefani, *J. Electron Spectros. Relat. Phenomena* **1995**, *71*, 93–105.

[380] A. P. Scott, L. Radom, *J. Phys. Chem.* **1996**, *100*, 16502–16513.

[381] P. Paetzold, „Iminoboranes“, Academic Press, **1987**, Pp. 123–170.

[382] J. Böhnke, T. Brückner, A. Hermann, O. F. González-Belman, M. Arrowsmith, J. O. C. Jiménez-Halla, H. Braunschweig, *Chem. Sci.* **2018**, *9*, 5354–5359.

[383] V. Domnich, S. Reynaud, R. A. Haber, M. Chhowalla, *J. Am. Ceram. Soc.* **2011**, *94*, 3605–3628.

[384] L. Souqui, H. Högberg, H. Pedersen, *Chem. Mater.* **2019**, *31*, 5408–5412.

[385] K. Higuchi, K. Tabuchi, K. S. Lim, M. Konagai, K. Takahashi, *Jpn. J. Appl. Phys.* **1991**, *30*, 1635–1640.

[386] J. S. Lewis, S. Vaidyaraman, W. Lackey, P. K. Agrawal, G. B. Freeman, E. Barefield, *Mater. Lett.* **1996**, *27*, 327–332.

[387] M. Imam, C. Höglund, J. Jensen, S. Schmidt, I. G. Ivanov, R. Hall-Wilton, J. Birch, H. Pedersen, *J. Phys. Chem. C* **2016**, *120*, 21990–21997.

[388] M. Imam, L. Souqui, J. Herritsch, A. Stegmüller, C. Höglund, S. Schmidt, R. Hall-Wilton, H. Högberg, J. Birch, R. Tonner, H. Pedersen, *J. Phys. Chem. C* **2017**, *121*, 26465–26471.

[389] P. R. Rablen, J. F. Hartwig, *J. Am. Chem. Soc.* **1996**, *118*, 4648–4653.

[390] P. Hassanzadeh, Y. Hannachi, L. Andrews, *J. Phys. Chem.* **1993**, *97*, 6418–6424.

[391] L. Andrews, D. V. Lanzisera, P. Hassanzadeh, Y. Hannachi, *J. Phys. Chem. A* **1998**, *102*, 3259–3267.

[392] P. v. R. Schleyer, B. T. Luke, J. A. Pople, *Organometallics* **1987**, *6*, 1997–2000.

[393] D. P. Mukhopadhyay, D. Schleier, S. Wirsing, J. Ramler, D. Kaiser, E. Reusch, P. Hemberger, T. Preitschopf, I. Krummenacher, B. Engels, I. Fischer, C. Lichtenberg, *Chem. Sci.* **2020**, *11*, 7562–7568.

[394] J. Berkowitz, J. P. Greene, H. Cho, B. Ruscić, *J. Chem. Phys.* **1987**, *86*, 674–676.

[395] P. R. Rablen, J. F. Hartwig, *J. Am. Chem. Soc.* **1996**, *118*, 4648–4653.

[396] B. A. Williams, T. A. Cool, *J. Chem. Phys.* **1991**, *94*, 6358–6366.

[397] M. K. Murphy, J. L. Beauchamp, *J. Am. Chem. Soc.* **1976**, *98*, 1433–1440.

[398] R. W. Law, J. L. Margrave, *J. Chem. Phys.* **1956**, *25*, 1086–1087.

[399] N. Galland, Y. Hannachi, D. V. Lanzisera, L. Andrews, *Chem. Phys.* **2000**, *255*, 205–215.

[400] F. Holzmeier, M. Lang, K. Hader, P. Hemberger, I. Fischer, *J. Chem. Phys.* **2013**, *138*, 214310.

[401] S. J. Kim, T. P. Hamilton, H. F. Schaefer, *J. Phys. Chem.* **1993**, *97*, 1872–1877.

[402] A. Thon, D. Saulys, S. A. Safvi, D. F. Games, T. F. Kuech, *J. Electrochem. Soc.* **1997**, *144*, 1127–1130.

[403] P. A. Arnold, B. R. Cosofret, S. M. Dylewski, P. L. Houston, B. K. Carpenter, *J. Phys. Chem. A* **2001**, *105*, 1693–1701.

[404] S. M. Clegg, B. F. Parsons, S. J. Klippenstein, D. L. Osborn, *J. Chem. Phys.* **2003**, *119*, 7222–7236.

[405] P. S. Engel, G. A. Bodager, *J. Org. Chem.* **1988**, *53*, 4748–4758.

[406] W. E. Farneth, M. W. Thomsen, *J. Am. Chem. Soc.* **1983**, *105*, 1843–1848.

[407] J. D. Nieto, O. S. Herrera, S. I. Lane, E. V. Oexler, *Int. J. Chem. Kinet.* **1993**, *25*, 63–66.

[408] L. J. Johnston, J. C. Scaiano, K. U. Ingold, *J. Am. Chem. Soc.* **1984**, *106*, 4877–4881.

[409] J. Dyke, A. Ellis, N. Jonathan, A. Morris, *J. Chem. Soc., Faraday Trans. 2* **1985**, *81*, 1573–1586.

[410] J. D. DeSain, S. J. Klippenstein, C. A. Taatjes, M. D. Hurley, T. J. Wallington, *J. Phys. Chem. A* **2003**, *107*, 1992–2002.

[411] Y. Li, Y. Han, H. Xiong, N. Zhu, B. Qian, C. Ye, E. A. B. Kantchev, H. Bao, *Org. Lett.* **2016**, *18*, 392–395.

[412] L. A. Singer, N. P. Kong, *J. Am. Chem. Soc.* **1966**, *88*, 5213–5219.

[413] S. Pospiech, S. Brough, M. Bolte, H.-W. Lerner, H. F. Bettinger, M. Wagner, *Chem. Commun.* **2012**, *48*, 5886–5888.

[414] B. Ruščić, C. A. Mayhew, J. Berkowitz, *J. Chem. Phys.* **1988**, *88*, 5580–5593.

[415] M. E. Garabedian, S. W. Benson, *J. Am. Chem. Soc.* **1964**, *86*, 176–182.

[416] J. K. Rice, C. Douglass, H. Nelson, *Chem. Phys.* **1990**, *143*, 109–121.

[417] C. H. Douglass, H. H. Nelson, J. K. Rice, *J. Chem. Phys.* **1989**, *90*, 6940–6948.

[418] L. Pasternack, B. Weiner, A. Baronavski, *Chem. Phys. Lett.* **1989**, *154*, 121–125.

[419] B. R. Weiner, L. Pasternack, H. H. Nelson, K. A. Prather, R. N. Rosenfeld, *J. Phys. Chem.* **1990**, *94*, 4138–4142.

[420] A. B. Burg, H. I. Schlesinger, *J. Am. Chem. Soc.* **1937**, *59*, 780–787.

[421] L. J. Malone, R. W. Parry, *Inorg. Chem.* **1967**, *6*, 817–822.

[422] R. Alberto, K. Ortner, N. Wheatley, R. Schibli, A. P. Schubiger, *J. Am. Chem. Soc.* **2001**, *123*, 3135–3136.

[423] G. A. Garcia, X. Tang, J.-F. Gil, L. Nahon, M. Ward, S. Batut, C. Fittschen, C. A. Taatjes, D. L. Osborn, J.-C. Loison, *J. Chem. Phys.* **2015**, *142*, 164201.

[424] P. C. Tellinghuisen, J. Tellinghuisen, J. A. Coxon, J. E. Velazco, D. W. Setser, *J. Chem. Phys.* **1978**, *68*, 5187–5198.

[425] D. F. Halpern, G. Tavcar, M. Tramček, *Xenon(II) Fluoride*, Pp. 1–5, American Cancer Society, **2017**.

[426] F. Schreiner, G. N. McDonald, C. L. Chernick, *J. Phys. Chem.* **1968**, *72*, 1162–1166.

[427] J. Bott, R. Heidner, J. Holloway, J. Koffend, *Chem. Phys.* **1990**, *148*, 411–416.

[428] E. Assaf, B. Song, A. Tomas, C. Schoemaecker, C. Fittschen, *J. Phys. Chem. A* **2016**, *120*, 8923–8932.

[429] E. Assaf, C. Schoemaecker, L. Vereecken, C. Fittschen, *Int. J. Chem. Kinet.* **2018**, *50*, 670–680.

[430] E. Assaf, C. Schoemaecker, L. Vereecken, C. Fittschen, *Phys. Chem. Chem. Phys.* **2018**, *20*, 10660–10670.

[431] L. H. Jones, R. C. Taylor, R. T. Paine, *J. Chem. Phys.* **1979**, *70*, 749–757.